Modeling and simulation in photoacoustics

Vincent Jugnon

THÈSE

Présentée pour obtenir
LE GRADE DE DOCTEUR DE L'ÉCOLE POLYTECHNIQUE
Spécialité : Mathématiques Appliquées
par
M. Vincent JUGNON

Modélisation et Simulation en Photo-acoustique

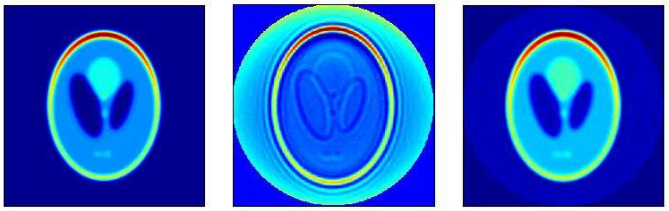

Soutenue le 9 décembre 2010 devant le jury composé de:

M. Habib AMMARI	*Directeur de Thèse*
M. Martin HANKE	*Rapporteur*
M. John SCHOTLAND	*Rapporteur*
M. Hongkai ZHAO	*Rapporteur*
M. Josselin GARNIER	*Examinateur*
M. François JOUVE	*Examinateur*
M. George PAPANICOLAOU	*Examinateur*

Modeling and Simulation in Photoacoustics

Vincent JUGNON
Centre de Mathématiques Appliquées, Ecole Polytechnique,
91128 Palaiseau, France
e-mail address : **jugnon@cmap.polytechnique.fr**

Contents

Acknowledgment

I first want to thank Habib for his guidance and his friendliness. I am profoundly grateful to him for keeping the right balance between supervision and autonomy. I have learnt so much from him, and not only from a scientific point of view. In particular, he made possible numerous great journeys and meetings with wonderful people. I hope our collaboration will continue long after this thesis.

My longest trip was a six month visit to Columbia University where Guillaume Bal was in charge of me. With him, I had the chance to work on more theoretical problems and to manipulate notions I was not familiar with. I want to thank him for his patience and his kind welcome.

I also had the great opportunity to travel to South Korea several times, to visit Hyeonbae Kang. Each time I received the warmest welcome possible. I want to express my deepest gratitude to him.

Numerics were an important part of my work as a Ph.D student. Working with Mark Asch was extremely formative from this point of view. He also came to Wuhan and supported me for my first talk in an international conference. I thank him for his kindness and his insight.

Understanding of the physics underlying the problems I treated was of utmost importance. I want to thank Emannuel Bossy and his student Arik Funke from Institute Langevin for the exciting discussions and their essential explanations. I hope our collaboration was as fruitful for them as it was for me.

Three whole chapters of this manuscript wouldn't be there without the help and work of two post-doc students, Alexandre Jollivet and Elie Bretin. I am indebted to them both.

I am honored to defend my thesis before such an impressive jury. I thank Hongkai Zhao, John Schotland and Martin Hanke who agreed to be referees of this manuscript and George Papanicolaou, Francois Jouve and Josselin Garnier, who accepted to be examinators.

This thesis has been supported by the Doctoral School of Ecole Polytechnique and was conducted in the best environment at the Center of Applied Mathematics of Ecole Polytechnique (CMAP).

Introduction

Non-invasive medical imaging is a field in constant development, in which scientists make use of various physical phenomena to reconstruct inner properties of a patient. Today, mainly three techniques dominate the field, each coming with its advantages and its drawbacks.

- Magnetic Resonance Imaging (MRI) produces very high resolution images, with not so bad contrast (it images proton density), but is very expensive, and has a long acquisition time.
- X-ray based techniques (radiography and the more advanced CT-scan) have good resolution too, and similar contrast (they image X-ray absorption that can be linked to density information). Their main drawback is their health hazard : X-ray exposure is harmful and has to be limited to its minimum.
- Ultrasound techniques are cheap and achieve sub-millimetric resolution but with quite poor contrast.

For decades, researchers have been investigating how other phenomena can be used to produce cheaper, faster, harmless, highly resolved, more differential images.

Optical contrast is very good in biological tissues and the use of visual diagnostics (biopsies) is a common practice in medicine. This comes from the fact that optical parameters (absorption, scattering coefficients) have important variations in tissues. Moreover, the possibility to use several wavelength for the light adds a dimension to the images and allows for functional imaging.

Optical imaging is thus being actively studied. Unfortunately, although light can penetrate easily in tissues (especially in the near infra-red domain), the inverse problem that has to be solved from such measurements is highly ill-posed due to strong scattering. The achieved resolution with pure optical imaging gets poorer and poorer with depth.

Among the other directions being followed is the so-called multiphysics imaging, in which people use one phenomenon to image another. There are different ways to play with this concept. First, one can use one phenomenon to perturb the other. This is the idea used for example in Electrical Impedance Tomography (EIT) by Elastic Deformation [**4**]. Another way to perform multiphysics imaging is to trigger one phenomenon with the other. This is the idea used in photoacoustic imaging. Enlighting a medium with an electromagnetic wave (light, radio-frequency or microwave) can trigger an acoustic (ultrasonic) wave of very low amplitude. This is the photoacoustic effect, that will be explained briefly in the next paragraph. In this setting the source of the acoustic wave is the deposition of electromagnetic energy in the medium, that depends on its **optical** properties and the illumination conditions.

Ultrasounds are then measured on the boundary of the medium and the image is produced using these **acoustic** data.

We thus get a cheap (laser illumination, acoustic measures) and fast technique that images optical contrast with ultrasound resolution.

Passing through the medium, the electromagnetic waves interact with it, and deposit energy. This results in a slight heating of the medium (in the range of the milliKelvin), which locally dilates, and due to stress constraints, ultrasounds are emitted.

To state the problem mathematically, one has to write :

- a mass conservation equation
- a momentum conservation equation (Navier-Stokes)
- a heat equation.

Then using reasonable assumptions :

- different time scales between the electromagnetic, thermal and acoustic phenomena (thermal and stress confinement assumptions)
- small amplitude acoustic waves (linearization)
- adiabatic process.

one arrives at the scalar wave equation for the pressure [**75**] :

$$\frac{1}{c_s^2}\frac{\partial^2 p}{\partial t^2}(x,t) - \Delta p(x,t) = \Gamma \frac{\partial H}{\partial t}(x,t)$$

with zero intial conditions. Here the source term $H(x,t)$ comes for the electromagnetic energy deposit, and Γ is the constant Grüneisen coefficient. If the light pulse is short, one can separate variables and write $H(x,t) = \delta(t)A(x)$, and so the problem becomes :

$$\begin{cases} \dfrac{1}{c_s^2}\dfrac{\partial^2 p}{\partial t^2}(x,t) - \Delta p(x,t) = 0 \\ p(x,0) := p_0(x) = \Gamma A(x) \quad \dfrac{\partial p}{\partial t}(x,t) = 0 \end{cases}$$

When the medium is acoustically non-attenuating, homogeneous and has the same acoustic properties as the free space, the absorbed energy density $A(x)$ can be recovered from pressure measurements by inverting a spherical Radon transform. The problem has been thoroughly studied and numerous inversion methods are available.

The assumptions underlying this approach are valid most of the time. Nonetheless, if we stray from them, a reconstruction using the inverse spherical Radon transform may fail.

In the first main part of this thesis, we study the mathematical problems arising when we try to relax these assumptions. Our main findings in this direction are as follows.

- Free space assumption: When boundary conditions are imposed on the medium, one cannot link the measured waves with the spherical Radon transform of the unknown initial condition. However, using a dual approach, we show that it is still possible to reconstruct the initial pressure. We also give results in the case of asymptotically small inclusions.

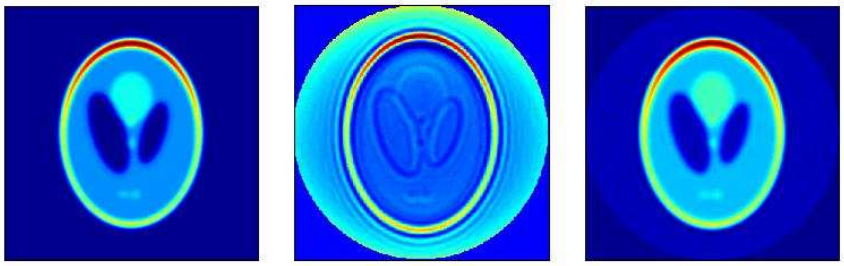

Photoacoustics with boundary conditions.
Left : true energy distribution. Center : reconstruction using spherical Radon transform. Right : reconstruction using our dual approach.

- View-limited data: Using geometric control tools, we show that, even with measurements taken only on part of the boundary, one can reconstruct the initial distribution theoretically with the same precision as in the full-view case.

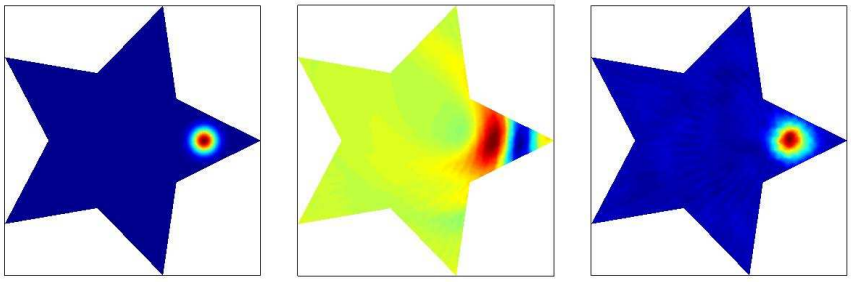

Photoacoustics with boundary conditions and limited view.
Left : true energy distribution. Center : reconstruction using the dual approach proposed in 4. Right : reconstruction using our control algorithm.

- Acoustic attenuation: We consider acoustic attenuation, with power-law models (and their thermo-viscous approximation). Unaccounted for, it can generate serious blurring in the reconstruction. We propose, for both the free-space and the boundary conditions case, a correction based on the asymptotic development of the attenuation effect (with respect to attenuation intensity).

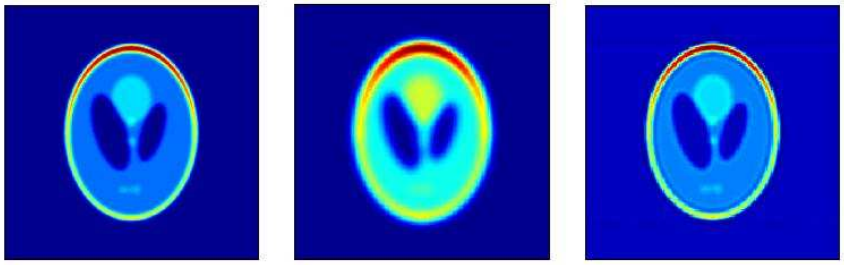

Photoacoustics with attenuation.
Left : true energy distribution. Center : reconstruction using the dual approach proposed in 4. Right : reconstruction using our asymptotic correction.

- Random fluctuation of sound speed (around a constant): If the medium is not acoustically homogeneous, we follow the approach proposed by G. Papanicolaou and his co-authors. We develop a coherent interferometric-like algorithm adapted to photoacoustics to correct the effect of medium heterogeneity on photoacoustic image reconstruction.

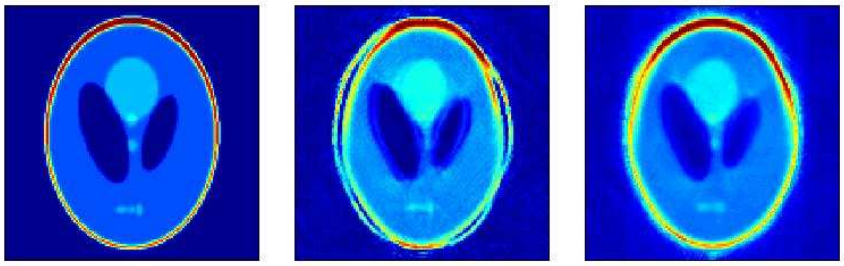

Photoacoustics with cluttered sound speed.
Left : true energy distribution. Center : reconstruction using the dual approach proposed in 4. Right : reconstruction using our CINT-like algorithm.

In a second time, we also deal with another inverse problem concerning light propagation. The initial condition reconstructed solving the *wave* inverse problem is easily linked to the absorbed EM energy density. It holds information on both the intrinsic optical parameters of the medium and the illumination conditions/light propagation. To obtain a more relevant image, we have to extract the intrinsic information. To proceed, we can model light propagation in different ways. Our main results in this second direction are as follows.

- Radiative transfer model: We prove stability estimates on the optical coefficients given the Albedo operator which maps illumination conditions to absorbed energy density (solution of the wave inverse problem).
- Diffusion model: We propose a method to estimate the size and absorption coefficient of small inclusions from the absorbed energy.

The thesis is organized as follows. In Chapter 1 we focus on imaging of small absorbers. In the time domain, we develop an original algorithm to estimate accurately the positions of the inclusions. We then develop asymptotic formulae to get the product of the size of the inclusions times the absorbed energy.In the Fourier doamin, we propose two methods for reconstructing small absorbing regions inside a bounded domain from boundary measurements of the induced acoustic signal. The first method consists of a MUltiple SIgnal Classification (MUSIC)-type algorithm and the second one uses a multi-frequency approach. We also show results of computational experiments to demonstrate efficiency of the algorithms. In Chapter 2 we propose, in the context of small-volume absorbers, two methods for reconstructing the optical absorption coefficient from the absorbed energy density. In Chapter 3 we consider the inverse problem of identifying locations of point sources and dipoles from limited-view data, for the wave equation . Using as weights particular background solutions constructed by the geometrical control method, we recover Kirchhoff-, back-propagation-, MUSIC-, and arrival time-type algorithms by appropriately averaging limited-view data. We show both analytically and numerically that if one can construct accurately the geometric control, then one can perform imaging with the same resolution using limited-view as using full-view data. Chapter 4 is devoted to photo-acoustic imaging of extended absorbers. We provide algorithms to correct the effects of imposed boundary conditions and that of attenuation as well on imaging extended absorbers. By testing our measurements against an appropriate family of functions, we show that we can access the Radon transform of the initial condition of the acoustic wave equation, and thus recover quantitatively the absorbed energy density. We also show how to compensate the effect of acoustic attenuation on image quality by using the stationary phase theorem. Chapter 5 presents a coherent interferometric strategy for photo-acoustic imaging in the presence of random fluctuations of the speed of sound. Chapter 6 develops an inverse transport theory with internal measurements to extract information on the optical coefficient from knowledge of the absorbed energy density. It provides stability estimates for the reconstruction. Chapter 7 investigates a topological derivative based anomaly detection algorithm. A stability analysis with respect to both medium and measurement noises as well as a resolution analysis are derived.

The seven chapters of this thesis are self-contained and can be read independently. Results in this thesis will appear in [**7, 8, 6, 9, 10, 27, 11**].

CHAPTER 1

Mathematical Modelling in Photo-Acoustic Imaging of Small Absorbers

1.1. Introduction

The photo-acoustic effect is the physical basis for photo-acoustic imaging; it refers to the generation of acoustic waves by the absorption of optical energy [**135, 72**]. In photo-acoustic imaging, energy absorption causes thermo-elastic expansion of the tissue, which in turn leads to propagation of a pressure wave. This signal is measured by transducers distributed on the boundary of the object, which is in turn used for imaging optical properties of the object.

In the last decade or so, work on photo-acoustic imaging in biomedical applications has come a long way. The motivation is to combine ultrasonic resolution with high contrast due to optical absorption. In pure optical imaging, optical scattering in soft tissues degrades spatial resolution significantly with depth. Pure optical imaging is very sensitive to optical absorption but can only provide a spatial resolution on the order of 1 cm at cm depths. Pure conventional ultrasound imaging is based on the detection of mechanical properties (acoustic impedance) in biological soft tissues. It can provide good spatial resolution because of its millimetric wavelength and weak scattering at MHz frequencies. The significance of photo-acoustic imaging combines both approaches to provide images of *optical* contrasts (based on the optical absorption) with the *ultrasound* resolution.

In this chapter, we propose a new approach for reconstructing small absorbing regions and absorbing energy density inside a bounded domain from boundary data. We also consider a problem of selective detection, which is to locate a targeted optical absorber among several absorbers from boundary measurements of the induced acoustic signal.

We first consider the problem of identifying absorbing regions from boundary measurements. It turns out that the spherical waves centered at some points, which we call probe waves, may serve as solutions to adjoint problems to the wave equation for the photo-acoustic phenomena. By integrating the boundary measurements against such a spherical wave, we can estimate the duration of the wave on the absorber. Then, by choosing a few waves centered at different points and taking the intersection of durations of these waves, we can estimate the location and size of the absorber pretty accurately.

We then turn our attention to selective detection and propose two methods to localize the targeted absorber. The first method is based on a MUltiple SIgnal Classification (MUSIC)-type algorithm in conjunction with a time reversal technique, namely, back-propagation of the acoustic signal [**62, 63, 71, 4**]. This method works when the absorbing coefficient of the targeted absorber is in contrast with those of

other absorbers. We also investigate the focusing property of the back-propagated acoustic signal. An alternative method of selective detection is based on the fact that the absorbing coefficient may vary depending on the frequencies. Some absorbers are transparent at a certain frequency, while they are quite absorbing at other frequencies. This phenomenon causes a multi-frequency approach to detect a targeted absorber. We propose a detailed implementation of this multi-frequency approach.

These methods are tested numerically using simulation data. Computational results clearly exhibit their accuracy and efficiency. It should be emphasized that all the methods proposed in this chapter are derived using approximations which are valid under the assumption that the optical absorbers are of small size.

The chapter is organized as follows: In Section 1.2, we formulate the mathematical problems (in a bounded domain) and review known results of reconstruction using the spherical Radon transform in free space. In Section 1.3 we propose a reconstruction method using probe waves. Section 1.4 investigates the focusing property of the back-projected signal. Section 1.5 is devoted to the selective detection. Section 1.6 presents the results of computational experiments, and the chapter ends with a short discussion.

1.2. Mathematical Formulation

Let $D_l, l = 1, \ldots, m$, be m absorbing domains inside the non-absorbing background bounded medium $\Omega \subset \mathbb{R}^d, d = 2$ or 3. In an acoustically homogeneous medium, the photo-acoustic effect is described by the following equation:

$$\frac{\partial^2 p}{\partial t^2}(x,t) - c^2 \Delta p(x,t) = \gamma \frac{\partial H}{\partial t}(x,t), \quad x \in \Omega, \quad t \in]-\infty, +\infty[, \tag{1.1}$$

where c is the acoustic speed in Ω, γ is the dimensionless Grüneisen coefficient in Ω, and $H(x,t)$ is a heat source function (absorbed energy per unit time per unit volume).

Assuming the stress-confinement condition, the source term can be modelled as $\gamma H(x,t) = \delta(t) \sum_l \chi_{D_l}(x) A_l(x)$. Here and throughout this chapter χ_{D_l} is the indicator function of D_l. Under this assumption, the pressure in an acoustically homogeneous medium obeys the following wave equation:

$$\frac{\partial^2 p}{\partial t^2}(x,t) - c^2 \Delta p(x,t) = 0, \quad x \in \Omega, \quad t \in]0, T[, \tag{1.2}$$

for some final observation time T. The pressure satisfies either the Dirichlet or the Neumann boundary condition

$$p = 0 \quad \text{or} \quad \frac{\partial p}{\partial \nu} = 0 \quad \text{on } \partial\Omega \times]0, T[\tag{1.3}$$

and the initial conditions

$$p|_{t=0} = \sum_{l=1}^{m} \chi_{D_l}(x) A_l(x) \quad \text{and} \quad \frac{\partial p}{\partial t}\Big|_{t=0} = 0 \quad \text{in } \Omega. \tag{1.4}$$

Here and throughout this chapter, ν denotes the outward normal to $\partial\Omega$. It is worth emphasizing that both the Dirichlet and Neumann boundary conditions in (1.3) yield good mathematical models in practice.

The inverse problem in photo-acoustic imaging is to determine the supports of nonzero optical absorption $(D_l,\, l = 1, \ldots, m)$ in Ω and the absorbed optical energy density times the Grüneisen coefficient, $A(x) = \sum_{l=1}^{m} A_l(x)\chi_{D_l}(x)$, from boundary measurements of $\frac{\partial p}{\partial \nu}$ on $\partial\Omega\times]0,T[$ if p satisfies the Dirichlet boundary condition, and p on $\partial\Omega\times]0,T[$ if p satisfies the Neumann boundary condition. We will assume that T is large enough that

$$T > \frac{\mathrm{diam}(\Omega)}{c}, \tag{1.5}$$

which says that the observation time is long enough for the wave initiated inside Ω to reach the boundary $\partial\Omega$.

The density $A(x)$ is related to the optical absorption coefficient distribution $\mu_a(x) = \sum_{l=1}^{m} \mu_l(x)\chi_{D_l}(x)$ by the equation $A(x) = \gamma\mu_a(x)\Phi(x)$, where Φ is the light fluence. The function Φ depends on the distribution of scattering and absorption within Ω, as well as the light sources. The reconstruction of the optical absorption coefficient distribution $\mu_a(x)$ from $A(x)$ is therefore a non trivial task. It will be considered in Chapter 2.

Suppose $d = 3$ and consider the wave equation

$$\frac{\partial^2 p}{\partial t^2}(x,t) - c^2\Delta p(x,t) = 0$$

in free space with the initial conditions $p = \sum_{l=1}^{m} \chi_{D_l} A_l(x)$ and $\partial_t p = 0$ at $t = 0$. The pressure p in this case can be written explicitly as

$$p(x,t) = \frac{d}{dt}\left[\sum_{l=1}^{m} \int_{|x-x'|=ct} \frac{\chi_{D_l}(x')A_l(x')}{4\pi|x-x'|}\, dS(x')\right],$$

or, equivalently,

$$p(x,t) = \frac{c}{4\pi}\frac{d}{dt}\left[t\sum_{l=1}^{m} \int_{|x'|=1} \chi_{D_l}(x+ctx')A_l(x+ctx')\, dS(x')\right], \tag{1.6}$$

where dS is the surface area element on the unit sphere, since $c^2t^2dS(x') = d\sigma(x')$. Formula (1.6) says that $c^{-1}t^{-1}\int_0^t p(x,\tau)d\tau$ is the spherical Radon transform of $A(x)$. Hence, we can reconstruct A by inverting the spherical Radon transform. We refer the reader to the papers [**1, 2, 96, 133, 80, 81, 3**] for uniqueness of the reconstruction and back-projection inversion procedures. See also [**110**] and [**131**], where the half-space problem has been considered.

The main purpose of this chapter is to deal with the difficulty caused by imposing boundary conditions and to develop new methods to reconstruct absorbing regions and their densities. We propose a method related to the time-reversal technique [**71**] for reconstructing A. We will also show the focusing property of the back-propagated acoustic signal and provide two different methods for locating a targeted optical absorber from boundary measurements of the induced acoustic signal. The first method consists of a MUSIC-type algorithm, while the second one uses a multi-frequency approach. It is worth mentioning, in connection with our reconstruction methods, the nice analysis of the sensitivity of a photo-acoustic wave to the presence of small absorbing objects in [**72**].

1.3. A Reconstruction Method

The algorithms available in the literature are limited to unbounded media. They use the inversion of the spherical Radon transform. However, since the pressure field p is significantly affected by the acoustic boundary conditions at the tissue-air interface, where the pressure must vanish, we cannot base photo-acoustic imaging on pressure measurements made over a free surface. Instead, we propose the following algorithm.

Let v satisfy

$$\frac{\partial^2 v}{\partial t^2} - c^2 \Delta v = 0 \quad \text{in } \Omega \times]0, T[, \tag{1.7}$$

with the final conditions

$$v|_{t=T} = \frac{\partial v}{\partial t}\Big|_{t=T} = 0 \quad \text{in } \Omega, \tag{1.8}$$

which is an adjoint problem to (1.2)-(1.4). We will refer to v as a probe function or a probe wave.

Multiply both sides of (1.2) by v and integrate them over $\Omega \times [0, T]$. After some integrations by parts, this leads to the following identity:

$$\int_0^T \int_{\partial\Omega} \frac{\partial p}{\partial \nu}(x,t) v(x,t)\, d\sigma(x)\, dt = \frac{1}{c^2} \sum_{l=1}^{m} \int_{D_l} A_l(x) \partial_t v(x,0) dx. \tag{1.9}$$

Here we assume that p satisfies the Dirichlet boundary condition.

Suppose first that $d = 3$. For $y \in \mathbb{R}^3 \setminus \overline{\Omega}$, let

$$v_y(x,t;\tau) := \frac{\delta\left(t + \tau - \frac{|x-y|}{c}\right)}{4\pi|x-y|} \quad \text{in } \Omega \times]0, T[, \tag{1.10}$$

where δ is the Dirac mass at 0 and $\tau > \frac{\operatorname{dist}(y,\partial\Omega)}{c}$ is a parameter. It is easy to check that v_y satisfies (1.7) (see, e.g., [**76**, p. 117]). Moreover, since

$$|x - y| \leq \operatorname{diam}(\Omega) + \operatorname{dist}(y, \partial\Omega)$$

for all $x \in \Omega$, v_y satisfies (1.8) provided that the condition (1.5) is fulfilled.

We write

$$D_l = z_l + \varepsilon B_l,$$

where z_l is the "center" of D_l, B_l contains the origin and plays the role of a reference domain, and ε is the common order of magnitude of the diameters of the D_l. Throughout this chapter, we assume that z_l's are well-separated, *i.e.*,

$$|z_i - z_j| > C_0 \quad \forall i \neq j \tag{1.11}$$

for some positive constant C_0. Suppose that

$$A_l(x) = \sum_{|j|=0}^{N} \frac{1}{j!} a_j^{(l)} \cdot (x - z_l)^j, \tag{1.12}$$

which is reasonable as D_l is small. Here, $j = (j_1, \ldots, j_d)$, $x^j = x_1^{j_1} \cdots x_d^{j_d}$, and $j! = j_1! \cdots j_d!$. Equation (1.12) corresponds to a multipolar expansion up to order N of the optical effect of D_l.

Choosing v_y as a probe function in (1.9), we obtain the new identity

(1.13)
$$\frac{1}{c^2}\sum_{l=1}^{m}\sum_{|j|=0}^{N}\frac{1}{j!}a_j^{(l)}\int_{D_l}(x-z_l)^j\partial_t v_y(x,0;\tau)dx=\int_0^T\int_{\partial\Omega}\frac{\partial p}{\partial\nu}(x,t)v_y(x,t;\tau)\,d\sigma(x)\,dt.$$

Determination of location. Suppose for simplicity that there is only one absorbing object ($m=1$), which we denote by $D(=z+\varepsilon B)$. Identity (1.13) shows that

$$\tau\mapsto\int_0^T\int_{\partial\Omega}\frac{\partial p}{\partial\nu}(x,t)v_y(x,t;\tau)\,d\sigma(x)\,dt \tag{1.14}$$

is nonzero only on the interval $]\tau_a,\tau_e[$, where $\tau_a=\operatorname{dist}(y,D)/c$ is the first τ at which the sphere of center y and radius τ hits D and τ_e is the last τ at which that sphere hits D. This gives a simple way to detect the location (by changing the source point y and taking the intersection of spheres). The quantity $\int_0^T\int_{\partial\Omega}\frac{\partial p}{\partial\nu}(x,t)v_y(x,t;\tau)\,d\sigma(x)\,dt$ can be used to probe the medium as a function of τ and y. For fixed y, it is a one-dimensional function and it is related to time reversal in the sense that it is a convolution with a reversed wave.

Let us now compute $\int_D(x-z)^j\partial_t v_y(x,0;\tau)dx$ for $\tau\in]\tau_a,\tau_e[$. Note that, in a distributional sense,

$$\partial_t v_y(x,0;\tau)=\frac{\delta'\left(\tau-\frac{|x-y|}{c}\right)}{4\pi|x-y|}. \tag{1.15}$$

Thus we have

$$\int_D(x-z)^j\partial_t v_y(x,0;\tau)dx=\int_D\frac{(x-z)^j}{4\pi|x-y|}\,\delta'\left(\tau-\frac{|x-y|}{c}\right)dx.$$

Letting $s=|x-y|$ and $\sigma=\frac{x-y}{|x-y|}$, we get by a change of variables

(1.16)
$$\int_D(x-z)^j\partial_t v_y(x,0;\tau)dx=\frac{1}{4\pi}\int_0^{+\infty}s\int_{S^2}\chi_D(s\sigma+y)(s\sigma+y-z)^j\delta'(\tau-\frac{s}{c})\,ds\,d\sigma,$$

where S^2 is the unit sphere.

Define for multi-indices j,

$$b_j(D,t;\tau)=\int_{S^2}\chi_D(c(\tau-t)\sigma+y)(c(\tau-t)\sigma+y-z)^j d\sigma.$$

Note that the function $b_j(D,t;\tau)$ is dependent on the shape of D (b_j is related to the moment of order j of the domain D). If we take D to be a sphere of radius r (its center is z), then one can compute $b_j(D,t;\tau)$ explicitly using the spherical coordinates.

Since

$$\int_0^{+\infty}s\int_{S^2}\chi_D(s\sigma+y)(s\sigma+y-z)^j\delta'(\tau-\frac{s}{c})\,ds\,d\sigma=-c^2\frac{d}{dt}\left[(\tau-t)b_j(D,t;\tau)\right]\Big|_{t=0},$$

it follows from (1.16) that

$$\int_D(x-z)^j\partial_t v_y(x,0;\tau)dx=\frac{c^2}{4\pi}(b_j(D,0;\tau)-\tau b_j'(D,0;\tau)),$$

where b_j' is the derivative with respect to t. We then obtain the following theorem from (1.13).

THEOREM 1.1. *For* $\tau \in]\tau_a, \tau_e[$,

(1.17)
$$\frac{1}{4\pi}\sum_{|j|=0}^{N}\frac{a_j}{j!}\cdot(b_j(D,0;\tau)-\tau b_j'(D,0;\tau))=\int_0^T\int_{\partial\Omega}\frac{\partial p}{\partial\nu}(x,t)v_y(x,t;\tau)\,d\sigma(x)\,dt.$$

If the Dirichlet boundary condition (1.3) is replaced by the Neumann boundary condition

$$\frac{\partial p}{\partial\nu}=0\quad\text{on }\partial\Omega\times]0,T[, \tag{1.18}$$

then (1.17) should be replaced by

(1.19)
$$\frac{1}{4\pi}\sum_{|j|=0}^{N}\frac{a_j}{j!}\cdot(b_j(D,0;\tau)-\tau b_j'(D,0;\tau))=-\int_0^T\int_{\partial\Omega}\frac{\partial v_y}{\partial\nu}(x,t;\tau)p(x,t)\,d\sigma(x)\,dt.$$

Estimation of absorbing energy. Now we show how to use (1.17) for estimating $a^{(j)}$ and some geometric features of D when the location z of D has been determined by the variations of the function in (1.14). Suppose that $N=0$, *i.e.*, A is constant on D. Then (1.17) reads

$$\frac{1}{4\pi}a_0\cdot(b_0(D,0;\tau)-\tau b_0'(D,0;\tau))=\int_0^T\int_{\partial\Omega}\frac{\partial p}{\partial\nu}(x,t)v_y(x,t;\tau)\,d\sigma(x)\,dt.$$

Note that $b_0(D,0;\tau)-\tau b_0'(D,0;\tau)$ for $\tau>0$ is supported in $[\tau_a,\tau_e]$. We then have

$$\begin{aligned}&\frac{|a_0|}{4\pi}\cdot\int_{\tau_a}^{\tau_e}\Big|b_0(D,0;\tau)-\tau b_0'(D,0;\tau)\Big|\,d\tau\\ &=\int_{\tau_a}^{\tau_e}\left|\int_0^T\int_{\partial\Omega}\frac{\partial p}{\partial\nu}(x,t)v_y(x,t;\tau)\,d\sigma(x)\,dt\right|d\tau.\end{aligned} \tag{1.20}$$

If we further assume that $D=z+\varepsilon B$ for small ε and a sphere B of radius 1, then we can compute $b_0(D,t;\tau)$ explicitly. In fact, one can show that

(1.21)
$$b_0(D,t,\tau)=\begin{cases}\pi\dfrac{\varepsilon^2-(|z-y|-c|\tau-t|)^2}{c|z-y||\tau-t|} & \text{if } -\varepsilon<|z-y|-c|\tau-t|<\varepsilon,\\ 0 & \text{otherwise,}\end{cases}$$

and hence we deduce $c\tau_a=|z-y|-\varepsilon$, $c\tau_e=|z-y|+\varepsilon$, and

$$b_0(D,0,\tau)-\tau b_0'(D,0,\tau)=\frac{2\pi(|z-y|-c\tau)}{|z-y|}$$

for $\tau>0$. Therefore, easy computations show that

$$|a_0|\varepsilon^2\approx c|z-y|\int_{\tau_a}^{\tau_e}\left|\int_0^T\int_{\partial\Omega}\frac{\partial p}{\partial\nu}(x,t)v_y(x,t;\tau)\,d\sigma(x)\,dt\right|d\tau, \tag{1.22}$$

which gives an approximation of $|a_0|\varepsilon^2$. Higher-order approximations can be obtained from (1.17) as well.

Suppose now $d = 2$. Due to the two-dimensional nature of the Green function, we consider a new probe wave given by

$$v_\theta(x,t;\tau) = \delta\left(t + \tau - \frac{\langle x,\theta\rangle}{c}\right) \tag{1.23}$$

where $\theta \in S^1$, $\langle\cdot,\cdot\rangle$ denotes the Euclidean scalar product, and τ is a parameter satisfying

$$\tau > \max_{x\in\Omega}\left(\frac{\langle x,\theta\rangle}{c}\right).$$

We can still use the function

$$\tau \mapsto \int_0^T \int_{\partial\Omega} \frac{\partial p}{\partial \nu}(x,t) v_\theta(x,t;\tau)\, d\sigma(x)\, dt$$

to probe the medium as a function of τ. This quantity is non-zero on the interval $]\tau_a, \tau_e[$, where τ_a and τ_e are defined such that planes $\langle x,\theta\rangle = c\tau$ for $\tau = \tau_a$ and τ_e hit D. Changing the direction θ and intersecting stripes gives us an efficient way to reconstruct the inclusions.

By exactly the same arguments as in three dimensions, one can show that

$$\frac{1}{c}\sum_{|j|=0}^{N} \frac{a_j}{j!}\cdot b_j'(D,0;\tau) = \int_0^T \int_{\partial\Omega} \frac{\partial p}{\partial \nu}(x,t) v_\theta(x,t;\tau)\, d\sigma(x)\, dt, \tag{1.24}$$

where

$$b_j(D,t;\tau) := \int_{\mathbb{R}} \chi_D(c(\tau-t)\theta + u\theta^\perp)(c(\tau-t)\theta + u\theta^\perp - z)^j du. \tag{1.25}$$

Assuming $N = 0$ and $D = z + \epsilon B$, we can compute b_0 explicitly. We have

$$b_0(D,t;\tau) = \begin{cases} 2\sqrt{\epsilon^2 - (c|\tau-t| - \langle z,\theta\rangle)^2} & \text{if } -\epsilon < \langle z,\theta\rangle - c|\tau-t| < \epsilon, \\ 0 & \text{otherwise.} \end{cases} \tag{1.26}$$

Since $c\tau_a = \langle z,\theta\rangle - \epsilon$, $c\tau_0 = \langle z,\theta\rangle$, and $c\tau_b = \langle z,\theta\rangle + \epsilon$, we get

$$|a_0|\epsilon = \frac{c}{4}\int_{\tau_a}^{\tau_e} \left| \int_0^T \int_{\partial\Omega} \frac{\partial p}{\partial \nu}(x,t) v_\theta(x,t;\tau)\, d\sigma(x)\, dt \right| d\tau. \tag{1.27}$$

The above formula can be used to estimate $|a_0|\epsilon$.

In the case when there are m inclusions, we first compute for each l the quantity

$$\theta_{l,best} = \operatorname*{argmax}_{\theta\in[0,\pi]} \left(\min_{j\neq l} |\langle z_j - z_l, \theta\rangle| \right) \tag{1.28}$$

and then, since along the direction $\theta_{l,best}$, the inclusion D_l is well separated from all the other inclusions, we can use (1.27) to estimate its $|a_0|\epsilon$.

To conclude this section, we make a few remarks. We first emphasize that probe functions other than those in (1.10) and (1.23) can be used.

If the medium contains small acoustic anomalies, then the effect of the inhomogeneity of acoustic speed can be neglected when the anomalies are away from the optical absorbing domains. However, we need to correct this effect when the anomalies are close to or on the absorbing region. In this case, the probe function v_y has to be corrected and this correction can be constructed by using the inner expansions derived in [**15**]. See also [**4**].

Let us digress a little to the problem posed in free space. Let Ω be a large domain containing the support D of the nonzero absorption. We can check from the explicit formula (1.6) for p that

$$\int_0^T \int_{\partial\Omega} \left(\frac{\partial p}{\partial \nu}(x,t) v_y(x,t;\tau) - p(x,t) \frac{\partial v_y}{\partial \nu}(x,t;\tau) \right) d\sigma(x)\, dt$$
$$= \frac{1}{4\pi} \sum_{|j|=0}^{N} \frac{a_j}{j!} \cdot (b_j(D,0;\tau) - \tau b_j'(D,0;\tau)),$$

which shows the consistency of our approach with the free space problem.

1.4. Back-Propagation of the Acoustic Signals

If we separate out the time dependence of p, the solution to (1.2)-(1.4), by expanding $p(x,t)$ into a set of harmonic modes, then, for a given frequency ζ, the harmonic mode $\hat{p}(x,\zeta)$ satisfies the Helmholtz equation

$$-(\zeta^2 + c^2\Delta)\hat{p}(x,\zeta) = i\zeta(\sum_{l=1}^{m} \chi_{D_l} A_l(x)) \quad \text{in } \Omega, \tag{1.29}$$

with the boundary condition

$$\hat{p} = 0 \quad \text{or} \quad \frac{\partial \hat{p}}{\partial \nu} = 0 \quad \text{on } \partial\Omega.$$

Suppose that $-\zeta^2/c^2$ is not an eigenvalue of Δ in Ω with the Dirichlet or the Neumann boundary condition. The inverse problem we consider in this section is to reconstruct $A = \sum_{l=1}^{m} \chi_{D_l} A_l$ from the measurements of $\frac{\partial \hat{p}}{\partial \nu}$ or $\hat{p}$ on $\partial\Omega$.

In this section, we show the focusing properties of the back-propagated acoustic signals. To do so, let $\Gamma_y(x)$, for $y \in \mathbb{R}^d \setminus \overline{\Omega}$, be the fundamental outgoing solution of $-(\zeta^2 + c^2\Delta)$ in $\mathbb{R}^d$, *i.e.*,

$$-(\zeta^2 + c^2\Delta_x)\Gamma_y(x) = \delta_{x=y}$$

subject to the outgoing radiation condition. It then follows from the divergence theorem that

$$i\zeta \sum_{l=1}^{m} \int_{D_l} A_l(x)\Gamma_y(x)dx = c^2 \int_{\partial\Omega} \hat{p}(x,\zeta) \frac{\partial \Gamma_y}{\partial \nu}(x) d\sigma(x) - c^2 \int_{\partial\Omega} \frac{\partial \hat{p}}{\partial \nu_x}(x,\zeta)\Gamma_y(x)\, d\sigma(x).$$

As before, suppose that $D_l = z_l + \varepsilon B_l$, where ε is small. Then, we have

$$i\zeta \sum_{l=1}^{m} |D_l| A_l(z_l)\Gamma_y(z_l) \approx \begin{cases} c^2 \displaystyle\int_{\partial\Omega} \hat{p}(x,\zeta) \frac{\partial \Gamma_y}{\partial \nu}(x) d\sigma(x) & \text{if } \dfrac{\partial \hat{p}}{\partial \nu} = 0 \quad \text{on } \partial\Omega, \\ -c^2 \displaystyle\int_{\partial\Omega} \frac{\partial \hat{p}}{\partial \nu}(x,\zeta)\Gamma_y(x)\, d\sigma(x) & \text{if } \hat{p} = 0 \quad \text{on } \partial\Omega. \end{cases} \tag{1.30}$$

For R large enough, let $S_R := \{|y| = R\}$. Set

$$H(y) := -\frac{ic^2}{\zeta} \times \begin{cases} \displaystyle\int_{\partial\Omega} \hat{p}(x,\zeta) \frac{\partial \Gamma_y}{\partial \nu}(x) d\sigma(x) & \text{if } \dfrac{\partial \hat{p}}{\partial \nu} = 0 \quad \text{on } \partial\Omega, \\ -\displaystyle\int_{\partial\Omega} \frac{\partial \hat{p}}{\partial \nu}(x,\zeta)\Gamma_y(x)\, d\sigma(x) & \text{if } \hat{p} = 0 \quad \text{on } \partial\Omega, \end{cases} \tag{1.31}$$

and $\alpha_l = |D_l| A_l(z_l)$. Note that, for any $y \in \mathbb{R}^d \setminus \overline{\Omega}$, the function $H(y)$ can be computed from the boundary measurements of p.

Back-propagating p corresponds to computing

$$W(z) := \int_{S_R} \left[\frac{\partial \Gamma_z}{\partial \nu}(y) \overline{H}(y) - \frac{\partial \overline{H}}{\partial \nu}(y) \Gamma_z(y) \right] d\sigma(y), \quad z \in \Omega, \tag{1.32}$$

where H is defined in (1.31) (see, e.g., [**4**]). Since from (1.30)

$$H(y) \approx \sum_{l=1}^{m} \alpha_l \Gamma_y(z_l)$$

for y in a neighborhood of S_R, we have

$$W(z) \approx \sum_{l=1}^{m} \overline{\alpha_l} \int_{S_R} \left[\frac{\partial \Gamma_z}{\partial \nu}(y) \overline{\Gamma_{z_l}}(y) - \frac{\partial \overline{\Gamma_{z_l}}}{\partial \nu}(y) \Gamma_z(y) \right] d\sigma(y) = 2 \sum_{l=1}^{m} \overline{\alpha_l} \Im m \Gamma_{z_l}(z). \tag{1.33}$$

Thus it is now easy to find the locations z_l, $l = 1, \ldots, m$, as the points where the functional W has its maximum. Equation (1.33) shows that the reversed signal focuses on the locations of the absorbers with a resolution determined by the behavior of the imaginary part of the Green function.

1.5. Selective Detection

The purpose of selective detection is to focus high-intensity ultrasound toward a targeted optical absorber in biological tissue, based on the back-propagation of photo-acoustic waves generated by this optical absorber [**74**]. The main difficulty in focusing toward a targeted optical absorber is that photo-acoustic waves are generated by other optical absorbers in the medium as well. In this section we propose two methods of different natures to overcome this difficulty.

1.5.1. MUSIC Algorithm. Here, we use the same notation as in Section 4. Suppose that, for some l_0, D_{l_0} is a targeted optical absorber and its coefficient α_{l_0} is known. However, its location z_{l_0} is not known. Suppose also that

$$|\alpha_{l_0}| \geq C, \quad |\alpha_{l_0} - \alpha_l| \geq C, \quad \forall\, l \neq l_0, \tag{1.34}$$

for some positive constant C. This means that α_{l_0} is significantly different from the coefficients associated with all the other absorbers in the medium. The locations and the α_l's of all the other absorbing inclusions (D_l for $l \neq l_0$) are not known.

To localize the absorbing object D_{l_0} without knowing any of the others, we compute the following quantity for $z \in \Omega$:

$$W_{l_0}(z) := \frac{1}{\overline{\alpha_{l_0}} - 4\pi c^4 \int_{S_R} \Gamma_y(z) \overline{H}(y)\, d\sigma(y)}. \tag{1.35}$$

Let $k = \frac{\zeta}{c}$ for simplicity of notation. Recall that in three dimensions

$$\Gamma_y(z) = \frac{e^{ik|y-z|}}{4\pi c^2 |y-z|} \approx \frac{e^{ik|y|}}{4\pi c^2 |y|} e^{-ik \frac{y}{|y|} \cdot z},$$

if $|y|$ is sufficiently large, while in the two-dimensional case

$$\Gamma_y(z) = \frac{i}{4c^2} H_0^{(1)}(k|y-z|) \approx \frac{e^{ik|y|+i\pi/4}}{2c^2\sqrt{2k\pi|y|}} e^{-ik \frac{y}{|y|} \cdot z}.$$

Therefore, in three dimensions we have for large R

$$\int_{S_R} \Gamma_y(z)\overline{\Gamma_y}(z_l)\, d\sigma(y) \approx \frac{1}{(4\pi R c^2)^2} \int_{S_R} e^{-ik\frac{y}{|y|}\cdot(z-z_l)}\, d\sigma(y) = \frac{1}{4\pi c^4}\frac{\sin k|z-z_l|}{k|z-z_l|},$$

and hence

$$4\pi c^4 \int_{S_R} \Gamma_y(z)\overline{H}(y)\, d\sigma(y) \approx \sum_{l=1}^{m} \overline{\alpha_l}\frac{\sin k|z-z_l|}{k|z-z_l|}.$$

This yields

$$W_{l_0}(z) \approx \frac{1}{\overline{\alpha_{l_0}} - \sum_l \overline{\alpha_l}\frac{\sin k|z-z_l|}{k|z-z_l|}}.$$

Therefore, thanks to assumption (1.11), we have

$$W_{l_0}(z) \approx \frac{1}{\sum_{l\neq l_0} \overline{\alpha_l}\frac{\sin k|z-z_l|}{k|z-z_l|}} \gg 1 \quad \text{for } z \text{ near } z_{l_0}. \tag{1.36}$$

We also have from assumption (1.34)

$$W_{l_0}(z) \approx \frac{1}{\overline{\alpha_{l_0}} - \sum_l \overline{\alpha_l}\frac{\sin k|z-z_l|}{k|z-z_l|}} = O(1) \quad \text{for } z \text{ away from } z_{l_0}. \tag{1.37}$$

It then follows that z_{l_0} can be detected as the point where the functional W_{l_0} has a peak. This is a MUSIC-type algorithm for locating the anomalies.

In the two-dimensional case, we compute for large R

$$\int_{S_R} \Gamma_y(z)\overline{\Gamma_y}(z_l)\, d\sigma(y) \approx \frac{1}{8k\pi R c^4} \int_{S_R} e^{-ik\frac{y}{|y|}\cdot(z-z_l)}\, d\sigma(y) = \frac{1}{4kc^4} J_0(k|z-z_l|),$$

where J_0 is the Bessel function of the first kind of order zero. It then follows that

$$4kc^4 \int_{S_R} \Gamma_y(z)\overline{H}(y)\, d\sigma(y) \approx \sum_{l=1}^{m} \overline{\alpha_l} J_0(k|z-z_l|).$$

In two dimensions, define W_{l_0} by

$$W_{l_0}(z) := \frac{1}{\overline{\alpha_{l_0}} - 4kc^4 \int_{S_R} \Gamma_y(z)\overline{H}(y)\, d\sigma(y)}.$$

As in the three-dimensional case, the behavior of the function J_0 yields

$$W_{l_0}(z) \approx \frac{1}{\sum_{l\neq l_0} \overline{\alpha_l} J_0(k|z-z_l|)} \gg 1 \quad \text{for } z \text{ near } z_{l_0}$$

and

$$W_{l_0}(z) \approx \frac{1}{\overline{\alpha_{l_0}} - \sum_l \overline{\alpha_l} J_0(k|z-z_l|)} = O(1) \quad \text{for } z \text{ away from } z_{l_0}.$$

Therefore, exactly as in three dimensions, z_{l_0} can be detected as the point where the functional W_{l_0} has a peak.

Note that one does not need the exact value of α_{l_0}. One can get an approximation of α_{l_0} by looking numerically for the maximum of the function $F(z) = \int_{S_R} \Gamma_y(z)\bar{H}(y)d\sigma(y)$.

1.5.2. Multi-Frequency Approach. An alternative method for isolating the photo-acoustic signal generated by the targeted optical absorber from those generated by the others is to make use of two light pulses with slightly different excitation wavelengths, ω_1 and ω_2, tuned to the absorption spectrum of the targeted optical absorber. If the wavelengths are such that ω_1 corresponds to a low value (that can be neglected) of the absorption coefficient of the optical target and ω_2 to a high value of the absorption coefficient of the optical target, then the only difference in photo-acoustic waves generated in the medium by the two different pulses corresponds to the photo-acoustic waves generated by the light pulse selectively absorbed by the optical target (see, e.g., [**74, 130**]). Back-propagating this signal will focus on the location of the optical target [**74**].

Suppose that there are two absorbers, say, D_1 and D_2, and assume that

$$|D_2| \ll 1, \tag{1.38}$$

$$\mathrm{dist}(D_1, D_2) \geq C > 0, \tag{1.39}$$

which means that D_2 is small and D_1 and D_2 are apart from each other.

Let Φ_1 and Φ_2 be the light fluences corresponding, respectively, to illuminating the medium with excitation wavelengths ω_1 and ω_2. If we take ω_2 close to ω_1, then due to the assumptions (1.38) and (1.39) we have

$$\mu_1(x,\omega_1)\Phi_1(x) \approx \mu_1(x,\omega_2)\Phi_2(x) \quad \text{in } D_1. \tag{1.40}$$

The pressures generated by the photo-acoustic effect are given by

$$\begin{cases} \dfrac{\partial^2 p_1}{\partial t^2}(x,t) - c^2\Delta p_1(x,t) = 0, \quad x \in \Omega, \quad t \in]0,T[, \\ p_1 = 0 \quad \text{or} \quad \dfrac{\partial p_1}{\partial \nu} = 0 \quad \text{on } \partial\Omega\times]0,T[, \\ p_1|_{t=0} = \mu_1(x,\omega_1)\chi_{D_1}\Phi_1 \quad \text{and} \quad \dfrac{\partial p_1}{\partial t}\Big|_{t=0} = 0 \quad \text{in } \Omega, \end{cases}$$

and

$$\begin{cases} \dfrac{\partial^2 p_2}{\partial t^2}(x,t) - c^2\Delta p_2(x,t) = 0, \quad x \in \Omega, \quad t \in]0,T[, \\ p_2 = 0 \quad \text{or} \quad \dfrac{\partial p_2}{\partial \nu} = 0 \quad \text{on } \partial\Omega\times]0,T[, \\ p_2|_{t=0} = (\mu_1(x,\omega_2)\chi_{D_1} + \mu_2(x,\omega_2)\chi_{D_2})\Phi_2 \quad \text{and} \quad \dfrac{\partial p_2}{\partial t}\Big|_{t=0} = 0 \quad \text{in } \Omega. \end{cases}$$

For the sake of simplicity we work in the frequency domain. In view of (1.29), the difference between the generated pressures $\hat{p}_2 - \hat{p}_1$ at frequency ζ can be approximated for $x \in \Omega$ as follows:

$$(\hat{p}_2 - \hat{p}_1)(x,\zeta) \approx i\zeta|D_2|\mu_2(z,\omega_2)\Phi_2(z) \times \begin{cases} G(x,z) & \text{in the case of the} \\ & \text{Dirichlet boundary condition,} \\ N(x,z) & \text{in the case of the} \\ & \text{Neumann boundary condition,} \end{cases}$$

where G is the Dirichlet function

$$\begin{cases} -(\zeta^2 + c^2\Delta)G(x,z) = \delta_z & \text{in } \Omega, \\ G = 0 & \text{on } \partial\Omega, \end{cases}$$

and N is the Neumann function

$$\begin{cases} -(\zeta^2 + c^2\Delta)N(x,z) = \delta_z & \text{in } \Omega, \\ \dfrac{\partial N}{\partial \nu} = 0 & \text{on } \partial\Omega. \end{cases}$$

Here we assume that $-\zeta^2$ is not an eigenvalue of Δ in Ω with Dirichlet or Neumann boundary condition.

Define, as in (1.31), H by

$$H(y) := -\frac{ic^2}{\zeta} \begin{cases} \displaystyle\int_{\partial\Omega} (\hat{p}_2 - \hat{p}_1)(x) \frac{\partial \Gamma_y}{\partial \nu}(x) d\sigma(x) & \text{in the case of the Neumann} \\ & \text{boundary condition,} \\ \displaystyle -\int_{\partial\Omega} \frac{\partial(\hat{p}_2 - \hat{p}_1)}{\partial \nu}(x) \Gamma_y(x)\, d\sigma(x) & \text{in the case of the Dirichlet} \\ & \text{boundary condition.} \end{cases}$$

Back-propagating $\hat{p}_2 - \hat{p}_1$ yields

$$2|D_2|\mu_2(z,\omega_2)\Phi_2(z)\Im m\Gamma_z(x) \approx \int_{S_R} \left[\frac{\partial \Gamma_z}{\partial \nu}(y)\overline{H}(y) - \frac{\partial \overline{H}}{\partial \nu}(y)\Gamma_z(y) \right] d\sigma(y) \quad \text{for } x \in \Omega.$$

Here, R is large enough and $S_R = \{|x| = R\}$, as before. This equation shows that the reversed frequency-difference signal focuses on the location z of the targeted optical absorber. Using the equation we can reconstruct the location z with a resolution given by the behavior of the imaginary part of the Green function and a signal-to-noise ratio function of the quantity $|D_2|\mu_2(z,\omega_2)\Phi_2(z)$.

1.6. Numerical Examples

1.6.1. Reconstruction Algorithm. We have performed numerical simulations to validate our approach. Data used were obtained by numerically solving the two-dimensional photo-acoustic equation (1.1) (with the Dirichlet boundary condition) with a finite-difference in time-domain method. The modelled medium was an acoustically homogeneous square (40 mm×40 mm) with $c = 1.5\text{mms}^{-1}$. The spatial step was 10 μm, and the temporal step was 9.3 ns. These steps were chosen to allow the modelling of the temporal Dirac in the heat function by a gaussian impulse with full width at half maximum of 250 ns. In order to have accurate Neumann boundary data on the time interval $]0,T[$, 4000 captors (spatial step=10 μm) were aligned on each edge of the square, taking 7500 measures of $\frac{\partial p}{\partial \nu}$ over a total time length T of 70μs (time step=9.3 ns). In our further computations, derivatives were obtained using the finite difference approximation, integrals using the trapezium approximation, and we approximated $\int f(t)\delta(t-t_0)dt$ by the nearest discrete value of $f(t_0)$. Note also that the 7500 measures of $\frac{\partial p}{\partial \nu}$ were only used to interpolate very accurately the integral in the quantity defined by (1.14). It has

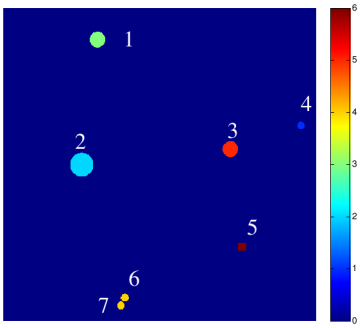

(a) Real configuration of the medium. There are seven optical inclusions.

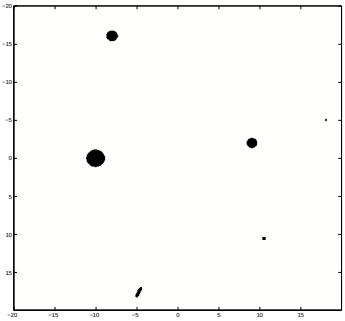

(b) Reconstructed image of the medium. Inclusions 6 and 7 are reconstructed as a single inclusion.

FIGURE 1.1. Real and reconstructed configurations of the medium.

been checked that using 1/1000 of the data (1/10 in time and 1/10 in each space component) still yields satisfactory reconstruction results.

A first set of data was used to validate the reconstruction algorithm. Inside the medium were several unknown inclusions of various size and absorption. The initial situation is shown in Figure 1(a).

We computed the probe function for K=360 values of θ and L=800 values of τ. Then, taking the intersection of all the zero-stripes, we obtained a binary image of the medium. We also determined the gravity centers of the inclusions. The reconstructed image is shown in Figure 1(b). Gravity centers of the real and reconstructed inclusions are shown in Figure 1.2. First we notice that our reconstruction method cannot distinguish between the too-close inclusions 6 and 7.

As can be observed, results are quite accurate. Ignoring inclusions 6-7, the mean error on the positions is less than the pixel size of our image (0.074 vs. 0.08).

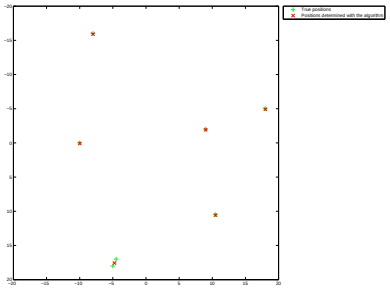

FIGURE 1.2. Gravity centers of actual and reconstructed inclusions.

1.6.2. Back-Propagation Algorithm. To test the back-propagation algorithm, we simulated data based on the Helmholtz equation (1.29) by using a finite

element method. For all the simulations, we used frequency $\zeta = 5\text{Mrads}^{-1}$. Note that we could not use the same space-time data as in the reconstruction algorithm since the time length of these data is limited. Because we have only access to $p(x,t)$ for $t \in]0;T[$, taking the discrete Fourier transform of these data would not give $\hat{p}(x,\zeta)$, but $\hat{p}$ is acquired by convolution with the *sinc* function.

We first applied the back-propagation algorithm on data generated by seven inclusions of radius 1mm. Each inclusion has a similar absorbed energy $a_0 = 1$. The actual configuration and the resulting image of $W(z)$ are shown in Figure 1.3.

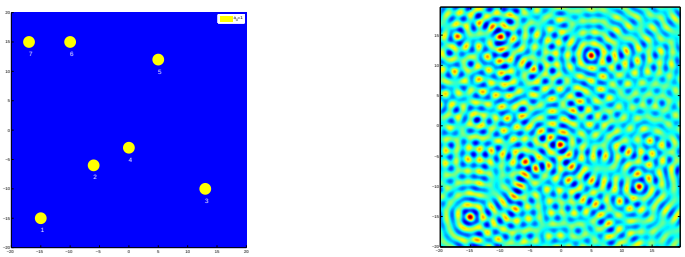

FIGURE 1.3. Back-propagation simulation. Left: Actual configuration. Right: Plot of $W(z)$.

1.6.3. Selective Detection.

1.6.3.1. *MUSIC Algorithm.* We first tested the MUSIC algorithm on a simple situation with only one inclusion. In Figure 1.4, we give the initial situation, the reconstruction function $F(z) = \int_{S_R} \Gamma_y(z)\bar{H}(y)d\sigma(y)$, which is close to the time-reversal philosophy [**4**], and the MUSIC function $W_{l_0}(z)$, which has a sharp peak around the inclusion.

We then simulated data with different energies to verify that the MUSIC algorithm could selectively distinguish an inclusion whose absorbed energy is very different to that of any other inclusion. Results, shown in Figures 1.5 and 1.6, are quite satisfying since we could separate the contrasted inclusion among seven inclusions, even with contrast equal to two.

1.6.3.2. *Multi-Frequency Approach.* We simulated 2 sets of data corresponding to the situation described in Section 1.5.2. We assumed that inclusion six was totally transparent at wavelength ω_1 but appeared just like the other inclusions at ω_2. As expected, one can see in Figure 1.7 that the algorithm managed to isolate inclusion 6.

1.7. Concluding Remarks and Extensions

In this chapter, we have provided a new method for reconstructing small absorbing inclusions inside a bounded medium where boundary conditions are imposed. Because of the acoustic boundary conditions, the spherical Radon inverse transform cannot be applied. Our approach is to make an appropriate averaging of the measurements by using particular solutions to the wave equation. It is related to time reversal in the sense that it is a convolution with a reversed wave. It has been validated by numerical simulations.

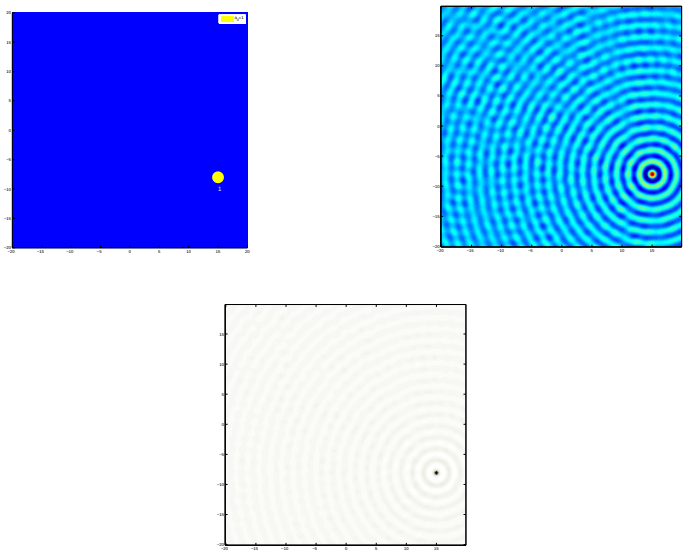

FIGURE 1.4. Selective detection: MUSIC simulation with a single inclusion. Top left: actual configuration. Top right: plot of $F(z)$. Bottom: plot of $W_{l_0}(z)$.

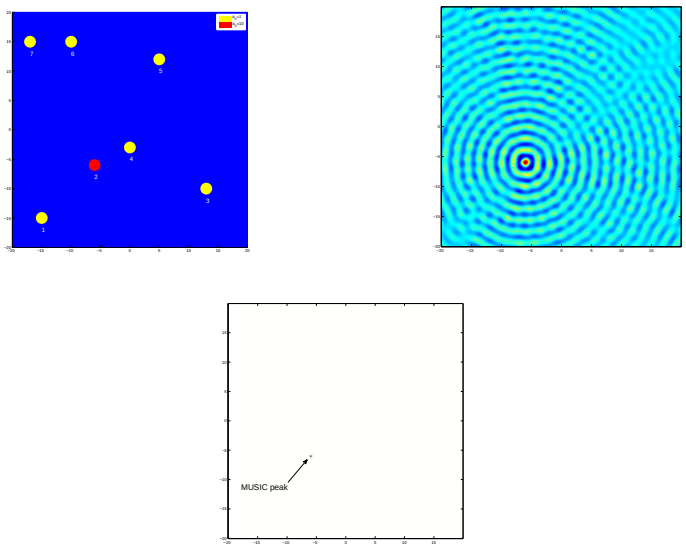

FIGURE 1.5. Selective detection: MUSIC simulation with seven inclusions, and contrast=10.

In the case where the time-dependence of the induced pressure by the photo-acoustic effect can be separated out, we have designed a back-propagation algorithm to detect the absorbers. Its resolution is determined by the behavior of the

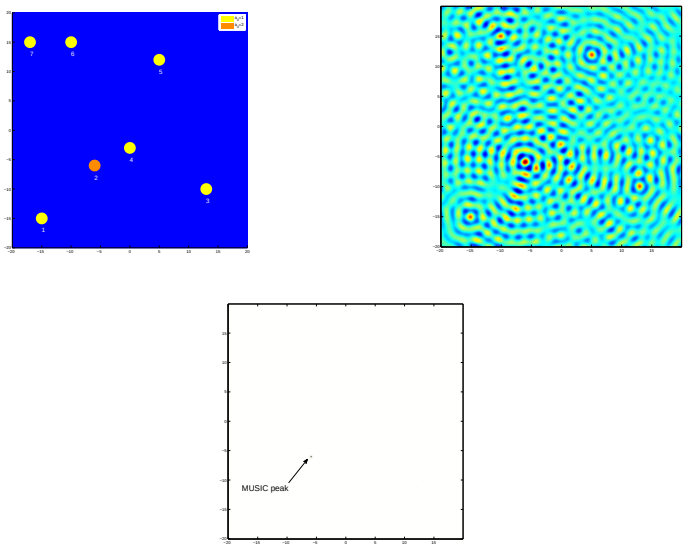

FIGURE 1.6. Selective detection: MUSIC simulation with seven inclusions, and contrast=2.

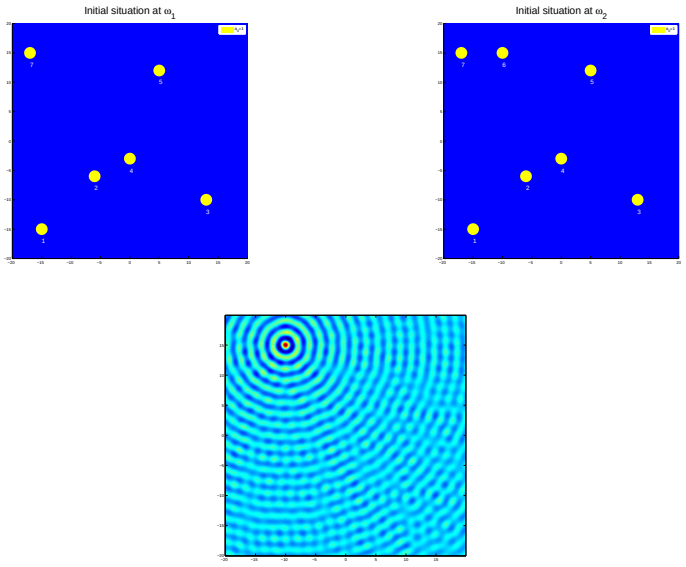

FIGURE 1.7. Selective detection: Multi-frequency approach results. Inclusion 6 is transparent at one frequency (top left), is seen at other frequency (top right), and hence is separated (bottom).

imaginary part of the Green function of the acoustic medium. To isolate the photo-acoustic signal generated by a targeted optical absorber from those generated by

the others, we developed two different approaches: the first approach is of MUSIC-type and the second one is a multi-frequency approach. These two approaches have the same resolution.

All the algorithms designed in this paper can be extended to the case where the acoustic background medium is heterogeneous but known.

An important problem is to develop a stable and accurate method for reconstructing the optical absorption coefficient from the absorbed energy. This will be the aim of Chapter 2.

Our approach extends to the case where only a part of the boundary is accessible. If we suppose that the measurements are only made on a part Γ of the boundary $\partial\Omega$, then the detection of the absorbers from these partial measurements holds only under an extra assumption on T and Γ. The geometric control theory [**28**] can be used to construct an appropriate probe function in the limited-view data case. This will be discussed in Chapter 3. We also intend to generalize in Chapters 4 and 5 our inversion formula to the case where the medium is acoustically inhomogeneous (contains small acoustical scatterers and/or in the presence of attenuation).

CHAPTER 2

Reconstruction of the Optical Absorption Coefficient of a Small Absorber from the Absorbed Energy Density

2.1. Problem Formulation

Photo-acoustic imaging is an emerging imaging technique that combines high optical contrast and high ultrasound resolution in a single modality. It is based on the photo-acoustic effect which refers to the generation of acoustic waves by the absorption of the optical energy. See, for instance, [**135, 72, 110, 112**].

In photo-acoustic imaging, the absorbed energy density can be reconstructed from boundary measurements of the induced pressure wave; see Chapter 1. However, in general, it is not possible to infer physiological parameters from the absorbed energy density. It is the optical absorption coefficient that directly correlates with tissue structural and functional information such as blood oxygenation. See [**139, 99, 129**].

Let D be an absorbing domain inside the non-absorbing background bounded medium $\Omega \subset \mathbb{R}^3$. Let χ_D be the characteristic function of D. The absorbed energy density $A(x)$ is related to the optical absorption coefficient distribution $\mu_a(x) = \mu_a \chi_D(x)$, where μ_a is a constant, by the equation $A(x) = \mu_a(x)\Phi(x)$, where Φ is the fluence. The function Φ depends on the distribution of scattering and absorption within Ω, as well as the light sources. Suppose that μ_s, the reduced scattering coefficient in Ω, is constant. Based on the diffusion approximation to the transport equation, Φ satisfies

$$\left(\mu_a(x) - \frac{1}{3}\nabla \cdot \frac{1}{\mu_a(x) + \mu_s}\nabla\right)\Phi(x) = 0 \quad \text{in } \Omega, \tag{2.1}$$

with the boundary condition

$$\frac{\partial \Phi}{\partial \nu} + l\Phi = g \quad \text{on } \partial\Omega. \tag{2.2}$$

See, for instance, [**22, 89**]. Here, ν denotes the outward normal to $\partial\Omega$ and g denotes the light source and l a positive constant; $1/l$ being an extrapolation length.

Since A is a nonlinear function of μ_a, the reconstruction of μ_a from A is therefore a non-trivial task and of considerable practical interest.

In [**112**], a formula to reconstruct small changes in the absorption coefficient is given. A fixed-point algorithm has been designed in [**58, 57**] in a more general case. The algorithm starts with an initial guess for the absorption coefficient. Then, when the (reduced) scattering coefficient distribution is known *a priori*, the light fluence Φ is calculated using the diffusion approximation to the light transport model. As long as the calculated and reconstructed absorption densities differ, these steps are

repeated with an assumed absorption coefficient calculated from the quotient of the reconstructed absorption density and the computed fluence distribution. When the reduced scattering coefficient distribution is unknown, an optimal control approach for estimating the absorption and reduced scattering coefficient distributions from absorbed energies obtained at multiple optical wavelengths has been developed in [**56**]. See, for instance, [**99**] for the validity of a multi-wavelength approach.

However, such iterative approaches are not appropriate to reconstruct the absorption coefficient of a small absorber. Suppose that the absorbing object D is small. We write

$$D = z + \varepsilon B,$$

where z is the "center" of D, B is a reference domain which contains the origin, and ε is a small parameter. In this case, only the normalized energy density of the absorber, $\varepsilon^2 A$ with ε being the radius of D, can be reconstructed from pressure measurements; see Chapter 1.

The main purpose of this chapter is to develop, in the context of small-volume absorbers, new efficient methods to recover μ_a of the absorber D from the normalized energy density $\varepsilon^2 A$. We distinguish two cases. The first case is the one where the reduced scattering coefficient μ_s inside the background medium is known *a priori*. In this case we develop an asymptotic approach to recover the normalized absorption coefficient, $\varepsilon^2\mu_a$, from the normalized energy density using multiple measurements. We make use of inner expansions of the fluence distribution Φ in terms of the size of the absorber. We also provide an approximate formula to separately recover ε from μ_a. However, this requires boundary measurements of Φ. The feasibility of combining photo-acoustic and diffusing light measurements has been demonstrated in [**136, 137**].

The second case is when the reduced scattering coefficient μ_s is unknown. We use multiple optical wavelength data. We assume that the optical wavelength dependence of the scattering and absorption coefficients are known. In tissues, the wavelength-dependence of the scattering often approximates to a power law. We propose a formula to extract the absorption coefficient μ_a from multiple optical wavelength data. In fact, we combine multiple optical wavelength measurements to separate the product of absorption coefficient and optical fluence. Note that the approximate model we use in this case for the light transport, which is based on the diffusion approximation, allows us to estimate $|D|$ independently from A and therefore, the multi-wavelength approach yields the absolute absorption coefficient.

The chapter is organized as follows. In Section 2.2, assuming that μ_s is known *a priori*, we develop a method for reconstructing $\varepsilon^2\mu_a(z)$ from $\varepsilon^2 A(z)$. Then we show how to separate ε from $\mu_a(z)$. In Section 2.3, we provide in the case where μ_s is unknown (and possibly varies in Ω) an algorithm to extract the absorption coefficient μ_a from absorbed energies obtained at multiple optical wavelengths. Numerical results are presented in Section 2.4 to show the validity of our inversion algorithms. The chapter ends with a short discussion. For the sake of simplicity, we only consider the three-dimensional problem but stress that the techniques developed here apply directly to the two-dimensional case.

2.2. Asymptotic Approach

In this section, we consider a slightly more general equation than (2.1) and provide an asymptotic expansion of its solution as the size of the absorbing object D goes to zero.

Recall that the fluence Φ is the integral over time of the fluence rate Ψ which satisfies

$$\left(\frac{1}{c}\partial_t + \mu_a(x) - \frac{1}{3}\nabla\cdot\frac{1}{\mu_a(x)+\mu_s}\nabla\right)\Psi(x) = 0 \quad \text{in } \Omega\times\mathbb{R}, \tag{2.3}$$

where c is the speed of light. Taking the Fourier transform of (2.3) yields that $\Phi = \Phi_{\omega=0}$, where, for a given frequency ω, Φ_ω is the solution to

$$\left(\frac{i\omega}{c} + \mu_a(x) - \frac{1}{3}\nabla\cdot\frac{1}{\mu_a(x)+\mu_s}\nabla\right)\Phi_\omega(x) = 0 \quad \text{in } \Omega, \tag{2.4}$$

with the boundary condition

$$\frac{\partial\Phi_\omega}{\partial\nu} + l\Phi_\omega = g \quad \text{on } \partial\Omega. \tag{2.5}$$

In the sequel, for any fixed $\omega \geq 0$ we rigorously derive an asymptotic expansion of $\Phi_\omega(z)$ as ϵ goes to zero, where z is the location of the absorbing object D. The results for nonzero ω have their own mathematical and physical interests [**72**].

For simplicity, we assume that $l \leq C\sqrt{\mu_s}$ for some constant C and drop in the notation the dependence with respect to ω.

2.2.1. Asymptotic Formula. In this section we assume that μ_s is a constant and known *a priori*. Recall that the space dimension is taken as 3. Define $\Phi^{(0)}$ by

$$\left(\frac{i\omega}{c} - \frac{1}{3\mu_s}\Delta\right)\Phi^{(0)}(x) = 0 \quad \text{in } \Omega,$$

subject to the boundary condition

$$\frac{\partial\Phi^{(0)}}{\partial\nu} + l\Phi^{(0)} = g \quad \text{on } \partial\Omega,$$

where g is a bounded function on $\partial\Omega$.

Throughout this chapter we assume that the location z of the anomaly is away from the boundary $\partial\Omega$, namely

$$\operatorname{dist}(z,\partial\Omega) \geq C_0 \tag{2.6}$$

for some constant C_0.

Let N be the Neumann function, that is, the solution to

$$\begin{cases} \left(\dfrac{i\omega}{c} - \dfrac{1}{3\mu_s}\Delta_x\right)N(x,y) = -\delta_y \quad \text{in } \Omega, \\ \dfrac{\partial N}{\partial\nu} + lN = 0 \quad \text{on } \partial\Omega. \end{cases} \tag{2.7}$$

Note that

$$N(x,y) = N(y,x), \quad x,y\in\Omega, \quad x\neq y. \tag{2.8}$$

Note also that

$$\Phi^{(0)}(x) = -\frac{1}{3\mu_s}\int_{\partial\Omega} g(y)N(x,y)\,d\sigma(y), \quad x\in\Omega. \tag{2.9}$$

Thus, multiplying (2.4) by N, using the symmetry property (2.8) and integrating by parts, we readily get the following lemma.

LEMMA 2.1. *For any $x \in \Omega$, the following representation formula of $\Phi(x)$ holds:*

$$\begin{aligned}(\Phi - \Phi^{(0)})(x) &= \mu_a \int_D \Phi(y) N(x,y)\, dy \\ &\quad + \frac{1}{3}\left(\frac{1}{\mu_a + \mu_s} - \frac{1}{\mu_s}\right) \int_D \nabla\Phi(y) \cdot \nabla_y N(x,y)\, dy.\end{aligned} \tag{2.10}$$

We now derive an asymptotic expansion of $(\Phi - \Phi^{(0)})(z)$, where z is the location of D, as the size ε of D goes to zero. The asymptotic expansion also takes the smallness of μ_a/μ_s into account. Note that if the anomaly approaches $\partial\Omega$, then the expansion is not valid since the interaction between D and $\partial\Omega$ becomes significant.

Let us first recall that the (outgoing) fundamental solution to the operator $\frac{i\omega}{c} - \frac{1}{3\mu_s}\Delta$ is given by

$$G(x,y) := \frac{3\mu_s}{4\pi} \frac{e^{-k|x-y|}}{|x-y|} \tag{2.11}$$

where

$$k = \exp(\frac{\pi}{4} i) \sqrt{\frac{3\mu_s \omega}{c}}. \tag{2.12}$$

In particular, we have

$$\left(\frac{i\omega}{c} - \frac{1}{3\mu_s}\Delta_x\right) G(x,y) = -\delta_y(x), \quad x \in \mathbb{R}^3.$$

Thus, the function $R_1(x,y) := N(x,y) - G(x,y)$ is the solution to

$$\begin{cases} \left(\dfrac{i\omega}{c} - \dfrac{1}{3\mu_s}\Delta_x\right) R_1(x,y) = 0, \quad x \in \Omega, \\ \dfrac{\partial R_1}{\partial \nu} + l R_1 = -\dfrac{\partial G}{\partial \nu} - lG \quad \text{on } \partial\Omega. \end{cases}$$

Observe that if $y \in D$, then

$$l \left\| G(\cdot,y) \right\|_{L^\infty(\partial\Omega)} + \left\| \frac{\partial G}{\partial \nu_x}(\cdot,y) \right\|_{L^\infty(\partial\Omega)} \leq C\mu_s^{3/2},$$

since, by assumption, $l \leq C'\sqrt{\mu_s}$ for some constant C'.

It then follows from Lemma 2.7 in Appendix A that

$$\sup_{x,y \in D} \left(\mu_s^{-3/2} |R_1(x,y)| + C_1 \mu_s^{-2} |\nabla R_1(x,y)| + C_2 \mu_s^{-5/2} |\nabla\nabla R_1(x,y)| \right) \leq C_3 \tag{2.13}$$

for some constants (with different dimensions) $C_i, i = 1,2,3$, independent of μ_s. Note that if $\omega = 0$ then

$$\begin{aligned} &\sup_{x,y \in D} \left(|R_1(x,y)| + C_1 |\nabla R_1(x,y)| + C_2 |\nabla\nabla R_1(x,y)| \right) \\ &\qquad \leq C_3 \left(l \left\| G(\cdot,y) \right\|_{L^\infty(\partial\Omega)} + \left\| \frac{\partial G}{\partial \nu_x}(\cdot,y) \right\|_{L^\infty(\partial\Omega)} \right) \\ &\qquad \leq C_4 l, \end{aligned} \tag{2.14}$$

where $C_i, i = 1, \dots, 4$, are independent of μ_s, provided that (2.6) holds. See, for instance, [**67**] for basic facts on the function spaces used throughout this chapter.

Let $\Gamma(x) := -1/(4\pi|x|)$ be a fundamental solution of the Laplacian in three dimensions and let

$$R(x,y) = N(x,y) - 3\mu_s\Gamma(x-y). \tag{2.15}$$

Writing

$$R(x,y) = R_1(x,y) + (G(x,y) - 3\mu_s\Gamma(x-y)),$$

we obtain the following lemma as an immediate consequence of (2.13).

LEMMA 2.2. *Let $R(x,y)$ be defined by (2.15). There are constants $C_i, i = 1, \dots, 6$ (with different dimensions) depending on C_0 given in (2.6) such that for all $x, y \in D$,*

$$|R(x,y)| \le C_1\mu_s^{3/2}, \tag{2.16}$$

$$|\nabla_x R(x,y)| \le C_2\mu_s^2 + C_3\frac{\mu_s^{3/2}}{|x-y|}, \tag{2.17}$$

$$|\nabla_x\nabla_x R(x,y)| \le C_4\mu_s^{5/2} + C_5\frac{\mu_s^2}{|x-y|} + C_6\frac{\mu_s^{3/2}}{|x-y|^2}, \tag{2.18}$$

provided that $\varepsilon\sqrt{\mu_s}$ is sufficiently small.

Let us now introduce some notation. Let

$$n(x) := \int_D N(x,y)\,dy, \quad x \in D, \tag{2.19}$$

and define a multiplier $\mathcal{M}$ by

$$\mathcal{M}[f](x) := \mu_a n(x) f(x). \tag{2.20}$$

We then define two operators $\mathcal{N}$ and $\mathcal{R}$ by

$$\begin{aligned}\mathcal{N}[f](x) &:= 3\mu_a\mu_s\int_D (f(y)-f(x))\Gamma(x-y)\,dy \\ &\quad + \mu_s\Big(\frac{1}{\mu_a+\mu_s} - \frac{1}{\mu_s}\Big)\int_D \nabla f(y)\cdot\nabla_y\Gamma(x-y)\,dy,\end{aligned} \tag{2.21}$$

$$\begin{aligned}\mathcal{R}[f](x) &:= \mu_a\int_D (f(y)-f(x))R(x,y)\,dy \\ &\quad + \frac{1}{3}\Big(\frac{1}{\mu_a+\mu_s} - \frac{1}{\mu_s}\Big)\int_D \nabla f(y)\cdot\nabla_y R(x,y)\,dy.\end{aligned} \tag{2.22}$$

In view of Lemma 2.2, the equation (2.10) then can be rewritten as

$$(I-\mathcal{M})[\Phi] - (\mathcal{N}+\mathcal{R})[\Phi] = \Phi^{(0)} \quad \text{on } D, \tag{2.23}$$

where I is the identity operator.

The following lemma is proved in Appendix B.

LEMMA 2.3. *Let $p > 3$ and q be its conjugate exponent, i.e., $1/p + 1/q = 1$. Then there is a constant C depending on C_0 given in (2.6) such that*

$$\|\mathcal{N}[f]\|_{L^p(D)} \leq C\varepsilon \left(\varepsilon^2 \mu_a \mu_s + \frac{\mu_a}{\mu_s}\right) \|\nabla f\|_{L^p(D)}, \tag{2.24}$$

$$\|\nabla \mathcal{N}[f]\|_{L^p(D)} \leq C \left(\varepsilon^2 \mu_a \mu_s + \frac{\mu_a}{\mu_s}\right) \|\nabla f\|_{L^p(D)}, \tag{2.25}$$

$$\|\mathcal{R}[f]\|_{L^p(D)} \leq C\varepsilon^2 \sqrt{\mu_s} \left(\mu_a \mu_s \varepsilon^2 + \frac{\mu_a}{\mu_s}\right) \|\nabla f\|_{L^p(D)}, \tag{2.26}$$

$$\|\nabla \mathcal{R}[f]\|_{L^p(D)} \leq C\varepsilon \sqrt{\mu_s} \left(\mu_a \mu_s \varepsilon^2 + \frac{\mu_a}{\mu_s}\right) \|\nabla f\|_{L^p(D)}. \tag{2.27}$$

Note that

$$\|n\|_{L^\infty(D)} = O(\varepsilon^2 \mu_s) \quad \text{and} \quad \|\nabla n\|_{L^\infty(D)} = O(\varepsilon \mu_s). \tag{2.28}$$

We also note the simple fact that

$$(I - \mathcal{M})^{-1}[f](x) = \frac{f(x)}{1 - \mu_a n(x)}.$$

We may rewrite (2.23) as

$$\Phi - (I - \mathcal{M})^{-1}(\mathcal{N} + \mathcal{R})[\Phi] = (I - \mathcal{M})^{-1}[\Phi^{(0)}] \quad \text{on } D. \tag{2.29}$$

Moreover, one can see from Lemma 2.3 that

$$\|(I - \mathcal{M})^{-1}\mathcal{N}[f]\|_{W^{1,p}(D)} \leq C \left(\varepsilon^2 \mu_a \mu_s + \frac{\mu_a}{\mu_s}\right) \|f\|_{W^{1,p}(D)}$$

and

$$\|(I - \mathcal{M})^{-1}\mathcal{R}[f]\|_{W^{1,p}(D)} \leq C\varepsilon \sqrt{\mu_s} \left(\varepsilon^2 \mu_a \mu_s + \frac{\mu_a}{\mu_s}\right) \|f\|_{W^{1,p}(D)}.$$

Here, $W^{1,p}(D) := \{f \in L^p(D), \nabla f \in L^p(D)\}$. So, if $\varepsilon^2 \mu_a \mu_s$ and $\frac{\mu_a}{\mu_s}$ are sufficiently small, then the integral equation (2.29) can be solved by the Neumann series

$$\Phi = \sum_{j=0}^{\infty} \left((I - \mathcal{M})^{-1}(\mathcal{N} + \mathcal{R})\right)^j (I - \mathcal{M})^{-1}[\Phi^{(0)}], \tag{2.30}$$

which converges in $W^{1,p}(D)$. It then follows from above two estimates that

$$\Phi = (I - \mathcal{M})^{-1}[\Phi^{(0)}] + (I - \mathcal{M})^{-1}(\mathcal{N} + \mathcal{R})(I - \mathcal{M})^{-1}[\Phi^{(0)}] + E_1, \tag{2.31}$$

where the error term E_1 satisfies

$$\|E_1\|_{W^{1,p}(D)} \leq C \left(\varepsilon^2 \mu_a \mu_s + \frac{\mu_a}{\mu_s}\right)^2 \|\Phi^{(0)}\|_{W^{1,p}(D)}.$$

We further have from (2.24), (2.26), and (2.28) that

$$\|\mathcal{M}(\mathcal{N} + \mathcal{R})[f]\|_{W^{1,p}(D)} \leq C\varepsilon \mu_a \mu_s (1 + \varepsilon \sqrt{\mu_s}) \left(\varepsilon^2 \mu_a \mu_s + \frac{\mu_a}{\mu_s}\right) \|f\|_{W^{1,p}(D)}.$$

Thus we get the following asymptotic expansion:

LEMMA 2.4. *The following estimate holds:*

$$\Phi(x) = (I-\mathcal{M})^{-1}[\Phi^{(0)}](x) + (\mathcal{N}+\mathcal{R})(I-\mathcal{M})^{-1}[\Phi^{(0)}](x) + E(x), \quad x \in D, \tag{2.32}$$

where the error term E satisfies

$$\|E\|_{W^{1,p}(D)} \leq C\varepsilon\mu_a\mu_s(1+\varepsilon\sqrt{\mu_s})\left(\varepsilon^2\mu_a\mu_s + \frac{\mu_a}{\mu_s}\right)\|\Phi^{(0)}\|_{W^{1,p}(D)}. \tag{2.33}$$

It is worth mentioning that since $p > 3$, $W^{1,p}(D)$ is continuously imbedded in $L^\infty(D)$ by the Sobolev imbedding theorem, and hence the asymptotic formula (2.32) holds uniformly in D.

Note that

$$\begin{aligned}
&(I-\mathcal{M})^{-1}[\Phi^{(0)}](x) + (\mathcal{N}+\mathcal{R})(I-\mathcal{M})^{-1}[\Phi^{(0)}](x) \\
&= \frac{\Phi^{(0)}(x)}{1-\mu_a n(x)} + \mu_a\int_D \frac{\Phi^{(0)}(y)}{1-\mu_a n(y)} N(x-y)\,dy - \frac{\mu_a n(x)\Phi^{(0)}(x)}{1-\mu_a n(x)} \\
&\quad + \frac{1}{3}\Big(\frac{1}{\mu_a+\mu_s} - \frac{1}{\mu_s}\Big)\int_D \nabla\left(\frac{\Phi^{(0)}(y)}{1-\mu_a n(y)}\right)\cdot\nabla_y N(x-y)\,dy \\
&\approx \Phi^{(0)}(x) + 3\mu_a\mu_s\int_D \Phi^{(0)}(y)\Gamma(x-y)\,dy \\
&\quad + \mu_s\Big(\frac{1}{\mu_a+\mu_s} - \frac{1}{\mu_s}\Big)\int_D \nabla\Phi^{(0)}(y)\cdot\nabla_y\Gamma(x-y)\,dy
\end{aligned}$$

where the error of the approximation satisfies (2.33). We then get for $x \in D$,

$$\int_D \Phi^{(0)}(y)\Gamma(x-y)\,dy = \Phi^{(0)}(x)\int_D \Gamma(x-y)\,dy + O(\varepsilon^3\|\nabla\Phi^{(0)}\|_{L^\infty(D)})$$

and

$$\begin{aligned}
&\mu_s\Big(\frac{1}{\mu_a+\mu_s} - \frac{1}{\mu_s}\Big)\int_D \nabla\Phi^{(0)}(y)\cdot\nabla_y\Gamma(x-y)\,dy \\
&= \frac{\mu_a}{\mu_s}\nabla\Phi^{(0)}(x)\cdot\int_D \nabla_y\Gamma(x-y)\,dy + O\Big(\varepsilon^2\frac{\mu_a}{\mu_s}\|\nabla\nabla\Phi^{(0)}\|_{L^\infty(D)} + \varepsilon\Big(\frac{\mu_a}{\mu_s}\Big)^2\|\nabla\Phi^{(0)}\|_{L^\infty(D)}\Big).
\end{aligned}$$

Let $\hat{N}_B$ be the Newtonian potential of B, which is given by

$$\hat{N}_B(x) := \int_B \Gamma(x-y)\,dy, \quad x \in \mathbb{R}^3, \tag{2.34}$$

and let $\mathcal{S}_B$ be the single layer potential associated to B, which are given for a density $\psi \in L^2(\partial B)$ by

$$\mathcal{S}_B[\psi](x) := \int_{\partial B} \Gamma(x-y)\psi(y)\,d\sigma(y), \quad x \in \mathbb{R}^3.$$

Then one can see by scaling $x = \varepsilon x' + z$ that

$$\int_D \Gamma(x-y)\,dy = \varepsilon^2\hat{N}_B(x'), \quad x' \in B,$$

and

$$\begin{aligned}
&\int_D \nabla_y\Gamma(x-y)\,dy = \varepsilon\int_B \nabla_y\Gamma(x'-y')\,dy' \\
&= -\varepsilon\int_{\partial B} \Gamma(x'-y')\nu(y')\,d\sigma(y') = -\varepsilon\mathcal{S}_B[\nu](x')
\end{aligned}$$

where $\nu(y)$ the outward normal to ∂B at y. Therefore we have

(2.35)
$$\Phi(x) \approx \Phi^{(0)}(x) + 3\varepsilon^2\mu_a\mu_s\Phi^{(0)}(z)\hat{N}_B\left(\frac{x-z}{\varepsilon}\right) - \varepsilon\frac{\mu_a}{\mu_s}\mathcal{S}_B[\nu]\left(\frac{x-z}{\varepsilon}\right)\cdot\nabla\Phi^{(0)}(z)$$

with the approximation error satisfying (2.33). Since this approximation holds in $W^{1,p}(D)$, we have

(2.36)
$$\nabla\Phi(x) \approx 3\varepsilon\mu_a\mu_s\Phi^{(0)}(z)\nabla\hat{N}_B\left(\frac{x-z}{\varepsilon}\right) + \left(I - \frac{\mu_a}{\mu_s}\nabla\mathcal{S}_B[\nu]\left(\frac{x-z}{\varepsilon}\right)\right)\nabla\Phi^{(0)}(z).$$

Note that, again by Lemma 2.7,

$$\|\Phi^{(0)}\|_{W^{1,p}(D)} \leq \varepsilon^{1/p}\sup_{x\in D}(|\Phi^{(0)}(x)| + |\nabla\Phi^{(0)}(x)|) \leq C\varepsilon^{1/p}\sqrt{\mu_s},$$

and

$$\|\nabla\nabla\Phi^{(0)}\|_{L^\infty(D)} \leq C\mu_s.$$

Thus we have the following asymptotic formula, which is the main result of this section.

Proposition 2.5. *We have*

$$(\Phi - \Phi^{(0)})(z) \approx 3\varepsilon^2\mu_a\mu_s\Phi^{(0)}(z)\hat{N}_B(0) - \varepsilon\frac{\mu_a}{\mu_s}\mathcal{S}_B[\nu](0)\cdot\nabla\Phi^{(0)}(z), \tag{2.37}$$

where the error of the approximation is less than

$$C_1\varepsilon^{1+1/p}\mu_a\mu_s^{3/2}(1+\varepsilon\sqrt{\mu_s})\left(\varepsilon^2\mu_a\mu_s + \frac{\mu_a}{\mu_s}\right) + C_2\mu_s^{1/2}\left(\varepsilon^3\mu_a\mu_s + \varepsilon(\frac{\mu_a}{\mu_s})^2\right) + C_3\varepsilon^2\mu_a$$

for $p > 3$ and some constants C_1, C_2, and C_3 (with different dimensions) depending on C_0 given in (2.6) and on g.

Note that the first term in (2.37) is a point source type approximation while the second term is a dipole approximation. Formula (2.37) also shows that if $\varepsilon\Phi^{(0)}(z)$ is of the same order as $(1/\mu_s^2(z))\nabla\Phi^{(0)}(z)$ then we have two contributions in the leading-order term of the perturbations in Φ that are due to D. The first contribution is coming from the source term $\mu_a(x,\omega)$ and the second one from the jump conditions. If $\varepsilon\Phi^{(0)}(z)$ is much larger than $(1/\mu_s^2(z))\nabla\Phi^{(0)}(z)$ then we can neglect the second contribution. It is worth emphasizing that formula (2.37) holds for any fixed $\omega \geq 0$ as ε goes to zero.

Remark. If the reduced scattering coefficient μ_s is not constant, then the expected asymptotic formula would be

$$(\Phi - \Phi^{(0)})(z) \approx 3\varepsilon^2\mu_a\mu_s(z)\Phi^{(0)}(z)\hat{N}_B(0) - \varepsilon\frac{\mu_a}{\mu_s(z)}\mathcal{S}_B[\nu](0)\cdot\nabla\Phi^{(0)}(z). \tag{2.38}$$

To prove it, one needs to prove (2.16) - (2.18) with variable μ_s. Even though these estimates are most likely true, we do not attempt to prove them since this is out of scope of the chapter.

2.2.2. Reconstruction of the Absorption Coefficient. We now turn to the reconstruction of the absorption coefficient. Given the light source g, it has been shown in Chapter 1 that the location z and $\alpha := \varepsilon^2\mu_a\Phi(z)$ can be reconstructed from photo-acoustic measurements. Here $\Phi = \Phi_{\omega=0}$.

Suppose that B is the unit sphere. Since $\mathcal{S}_B[\nu](0) = 0$, formula (2.37) reads

$$(\Phi - \Phi^{(0)})(z) \approx 3\varepsilon^2\mu_a\mu_s\Phi^{(0)}(z)\hat{N}_B(0) \approx 3\alpha\mu_s\hat{N}_B(0). \tag{2.39}$$

Thus one can easily see that

$$\varepsilon^2\mu_a \approx \frac{\alpha}{3\alpha\mu_s\hat{N}_B(0) + \Phi^{(0)}(z)}. \tag{2.40}$$

Let us see how one may separate ε from μ_a. Because of (2.9), it follows from (2.10) that

$$-\frac{1}{3\mu_s}\int_{\partial\Omega} g(\Phi-\Phi^{(0)})\,d\sigma \approx \mu_a\Phi(z)\Phi^{(0)}(z)|D| + \frac{1}{3}\left(\frac{1}{\mu_s+\mu_a} - \frac{1}{\mu_s}\right)\int_D \nabla\Phi(y)\cdot\nabla\Phi^{(0)}(y)dy.$$

Thus we get from (2.36) that

$$\begin{aligned}
&-\frac{1}{3\mu_s}\int_{\partial\Omega} g(\Phi - \Phi^{(0)})\,d\sigma \\
&\approx \mu_a\Phi(z)\Phi^{(0)}(z)|D| - \frac{\mu_a}{3\mu_s^2}\nabla\Phi^{(0)}(z)\cdot\left[3\varepsilon^4\mu_a\mu_s\Phi^{(0)}(z)\int_B \nabla\hat{N}_B(y)\,dy + \right. \\
&\qquad \left. + \varepsilon^3\int_B \big(I - \frac{\mu_a}{\mu_s}\nabla\mathcal{S}_B[\nu]\big)(y)\,dy\nabla\Phi^{(0)}(z)\right] \\
&\approx \varepsilon\alpha|B|\Phi^{(0)}(z) - \frac{\mu_a\varepsilon^3}{3\mu_s^2}\nabla\Phi^{(0)}(z)\cdot\left[3\varepsilon\mu_a\mu_s\Phi^{(0)}(z)\int_B \nabla\hat{N}_B(y)\,dy + \right. \\
&\qquad \left. + \int_B \big(I - \frac{\mu_a}{\mu_s}\nabla\mathcal{S}_B[\nu]\big)(y)\,dy\nabla\Phi^{(0)}(z)\right].
\end{aligned} \tag{2.41}$$

One may use this approximation to separately recover ε from μ_a even in the general case, where B not necessary a unit sphere by combining (2.41) together with (2.37). However, this approach requires boundary measurements of Φ on $\partial\Omega$.

2.3. Multi-Wavelength Approach

We now deal with the problem of estimating both the absorption coefficient μ_a and the reduced scattering coefficient μ_s from $A = \mu_a\Phi$ where Φ satisfies (2.4) and the boundary condition (2.5). It is known that this problem at fixed optical wavelength λ is a severely ill-posed problem. However, if the optical wavelength dependence of both the scattering and the absorption are known, then the ill-posedness of the inversion can be dramatically reduced.

Let $\mu_s(x,\lambda_j)$ and $\mu_a(x,\lambda_j)$ be the reduced scattering and absorption coefficients at the optical wavelength λ_j for $j = 1, 2$, respectively. Note that $\mu_a(\cdot,\lambda_j)$ is supported in the absorbing region D which is of the form $D = z + \varepsilon B$ for ε of small magnitude. We assume that $\mu_s(x,\lambda)$ and $\mu_a(x,\lambda)$ depend on the wavelength in the following way:

$$\mu_s(x,\lambda) = f_s(x)g_s(\lambda), \tag{2.42}$$

and

$$\mu_a(x,\lambda) = f_a(x)g_a(\lambda), \tag{2.43}$$

for some functions f_a, f_s, g_a, g_s. Denote

$$C_s := \frac{\mu_s(x,\lambda_1)}{\mu_s(x,\lambda_2)} = \text{constant in the } x \text{ variable in } \Omega,$$

and

$$C_a := \frac{\mu_a(x,\lambda_1)}{\mu_a(x,\lambda_2)} = \text{constant in the } x \text{ variable in } D.$$

Assumptions (2.42) and (2.43) are physically acceptable. See, for instance, [**56**].

Let A_j be the optical absorption density at $\lambda_j, j = 1, 2$. Let l_1', l_2' be two positive constants. Let Φ_j be the solution of

$$\left(\mu_a(x,\lambda_j) - \frac{1}{3}\nabla\cdot\frac{1}{\mu_s(x,\lambda_j)}\nabla\right)\Phi_j(x) = 0, \tag{2.44}$$

with the boundary condition

$$\frac{1}{\mu_s(x,\lambda_j)}\frac{\partial\Phi_j}{\partial\nu}(x) + l_j'\Phi_j(x) = g_j'(x) \quad \text{on } \partial\Omega. \tag{2.45}$$

Note that the boundary condition (2.45) is slightly different from (2.2) because μ_s is assumed variable possibly up to the boundary. Moreover, in order to simplify the derivations below we neglect μ_a in the denominator in the second term of (2.44).

Multiplying (2.44) for $j = 1$ by Φ_2 and integrating by parts over Ω, we obtain that

$$\begin{aligned}
0 &= \int_\Omega \left(\mu_a(x,\lambda_1) - \frac{1}{3}\nabla\cdot\frac{1}{\mu_s(x,\lambda_1)}\nabla\right)\Phi_1(x)\Phi_2(x)dx \\
&= \int_\Omega \mu_a(x,\lambda_1)\Phi_1\Phi_2 dx - \frac{1}{3}\int_{\partial\Omega}(g_1'\Phi_2 - l_1'\Phi_1\Phi_2)\,d\sigma \\
&+ \frac{1}{3}\int_\Omega \frac{1}{\mu_s(x,\lambda_1)}\nabla\Phi_1(x)\cdot\nabla\Phi_2(x)dx.
\end{aligned}$$

We then replace $\mu_s(x,\lambda_1)$ by $C_s\mu_s(x,\lambda_2)$ and integrate by parts further to obtain

$$\begin{aligned}
&\frac{1}{3}\int_{\partial\Omega}\left(g_1'\Phi_2 - \frac{1}{C_s}g_2'\Phi_1\right)(x)\,d\sigma(x) + \frac{1}{3}\int_{\partial\Omega}\left(\frac{l_2'}{C_s} - l_1'\right)\Phi_1(x)\Phi_2(x)\,d\sigma(x) \\
&= \int_D (-\frac{\mu_a(x,\lambda_2)}{C_s} + \mu_a(x,\lambda_1))\Phi_1(x)\Phi_2(x)\,dx.
\end{aligned}$$

Since $D = z + \varepsilon B$, we have the following proposition.

Proposition 2.6. *The following approximation holds:*

$$\begin{aligned}
|D|(1+o(1))\left(-\frac{1}{C_sC_a}+1\right)\frac{A_1(z)A_2(z)}{\mu_a(x,\lambda_2)} &= \frac{1}{3}\int_{\partial\Omega}\left(g_1'\Phi_2 - \frac{1}{C_s}g_2'\Phi_1\right)d\sigma \\
&+ \frac{1}{3}\int_{\partial\Omega}\left(\frac{l_2'}{C_s} - l_1'\right)\Phi_1\Phi_2\,d\sigma.
\end{aligned} \tag{2.46}$$

Proposition 2.6 yields approximations of $\mu_a(z,\lambda_2)$ and $\mu_a(z,\lambda_1) = C_a\mu_a(z,\lambda_2)$ from A_1 and A_2 provided that $|D|$ is known. To estimate $|D|$ one can use the following identity

$$\int_D \mu_a(x,\lambda_j)\Phi_j(x)\,dx = \frac{1}{3}\int_{\partial\Omega}\left(g_j' - l_j'\Phi_j\right)d\sigma. \tag{2.47}$$

2.4. Numerical Examples

To explore the performances of approaches in the previous sections, we run numerical simulations in a simple 3D setting. The medium we considered is a cube in $\mathbb{R}^3$ of edge 4cm ($[0\text{cm}, 4\text{cm}]^3$), containing a small spherical inclusion D located at $(1.7\text{cm}, 2.5\text{cm}, 0.8\text{cm})$. The background medium was assumed to be non-absorbing and to have a constant realistic reduced scattering coefficient $\mu_s = 10\text{cm}^{-1}$. The absorption coefficient $\mu_a|_D$ inside the inclusion was set to different (positive) values, from asymptotically small to realistic ones ($\mu_a = 0.01$, 0.05 and 0.1cm^{-1}). The inclusion radius ε ranges from 0.03cm to 0.3cm (to 0.5cm in the multi-wavelength setting).

We assume pure Neumann conditions ($l = 0$), with a focused laser beam at the center of one edge of the square and of normalized intensity (g is a Gaussian with full width at half maximum $\approx$ 2mm). The working frequency ω was set to 30Mhz so that $k = \frac{\omega}{c} = 0.001\text{cm}^{-1}$.

Simulations were conducted using FreeFEM++ (http://www.freefem.org). We solved the direct problem (2.4)-(2.5) using P1-elements on an adapted mesh (characteristic size of the mesh $h \approx 0.1$cm on the boundary of the medium; $h \approx \dfrac{\varepsilon}{100}$ in the neighborhood of the inclusion).

2.4.1. Asymptotic Approach. Following Chapter 1, we assumed that we can accurately estimate the position z of the inclusion and the quantity $\alpha = \mu_a\varepsilon^2\Phi(z)$ from photoacoustic inversion. Both quantities, along with the reduced scattering coefficient μ_s were assumed to be known with no error.

We computed $\Phi^{(0)}$ solving (2.9) on the same mesh. Applying formula (2.40), we obtained an estimate on $\mu_a\varepsilon^2$. The error on this estimate for the values of the parameters can be seen in Fig.2.1.

To separate size from attenuation, we furthermore assumed that we could access total boundary measurements $\Phi|_{\partial\Omega}$. Using the leading-order term in (2.41), we can write

$$\frac{1}{3\mu_s}\int_{\partial\Omega} g(\Phi - \Phi^{(0)})d\sigma \approx -\frac{4}{3}\pi\varepsilon\alpha\Phi^{(0)}(z),$$

which yields a direct estimation for ε. Using both estimates, we derived an estimation of μ_a. Errors on these estimates are given in Figs. 2.2 and 2.3.

As expected, reconstruction is very accurate in the asymptotic limit and degrades as μ_a and/or ε increase.

We mention that the asymptotic estimations of ε and $\mu_a\varepsilon^2$ are independent. The latter is only based on the photoacoustic measurements. The former requires also diffusing light measurements and seems to be more accurate (error $< 3\%$ in the range of our parameters vs. $< 30\%$ for the estimation of $\mu_a\varepsilon^2$).

The estimate on μ_a is obtained using these two estimates, thus the quality of the attenuation reconstruction is limited by the least-quality estimate, *i.e.*, $\mu_a\varepsilon^2$.

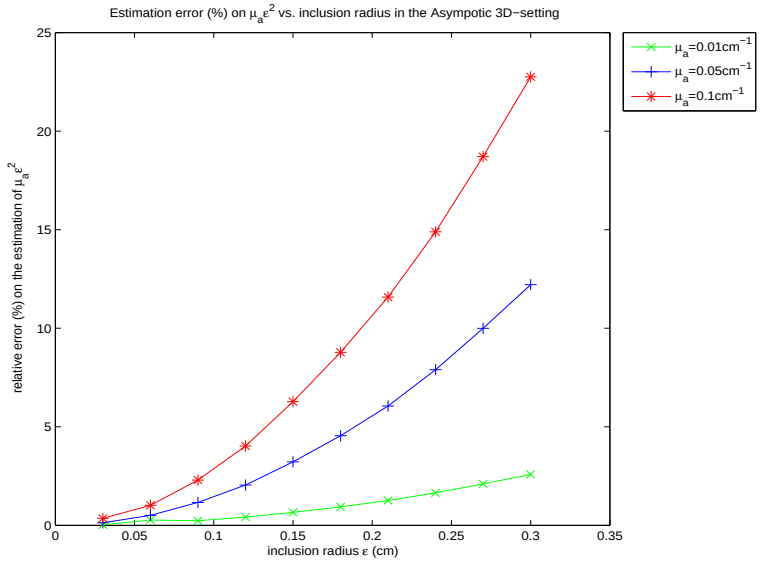

FIGURE 2.1. Error on the first estimate $\mu_a\varepsilon^2$ using the asymptotic approach.

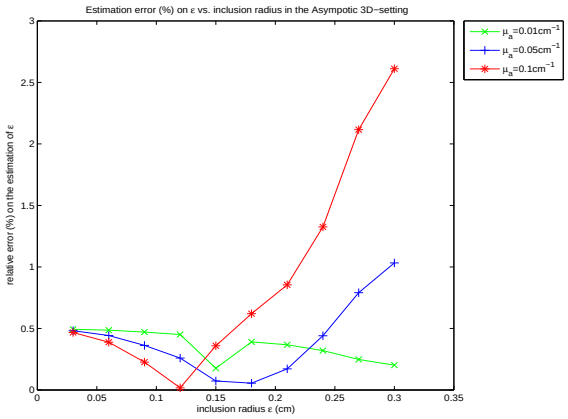

FIGURE 2.2. Error on the reconstruction of ε using the asymptotic approach.

2.4.2. Multi-Wavelength Approach. In this setting, we assumed that we could access the position z of the inclusion, the quantities $\alpha_j = \mu_a(\lambda_j)\varepsilon^2\Phi_j(z)$ and the factors C_s and C_a, with no error. The factors C_s and C_a were arbitrarily fixed at values 1.1 and 1.25 and $l'_j, j = 1, 2$, set to 0.

We first used identity (2.47) to get estimations of ε. Indeed, if we assume that μ_a is independent of x, then, in an asymptotic setting, (2.47) can be written as follows:

$$\frac{4}{3}\pi\varepsilon^3\mu_a(\lambda_j)\Phi_j(z) = \frac{4}{3}\pi\varepsilon\alpha_j \approx \frac{1}{3}\int_{\partial\Omega} g'_j.$$

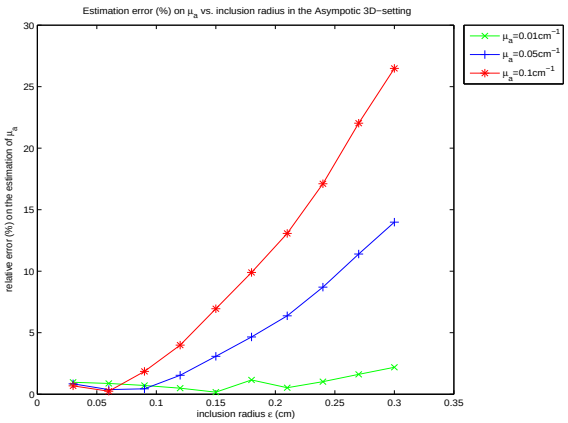

FIGURE 2.3. Error on the reconstruction of μ_a using the asymptotic approach.

This way to estimate the inclusion size ε is slightly different from the one used in the previous subsection.

Assuming we had total boundary measurements, we applied formula (2.46) to extract an estimation on μ_a. Errors on the estimations in this multi-wavelength setting are given in Figs. 2.4 and 2.5.

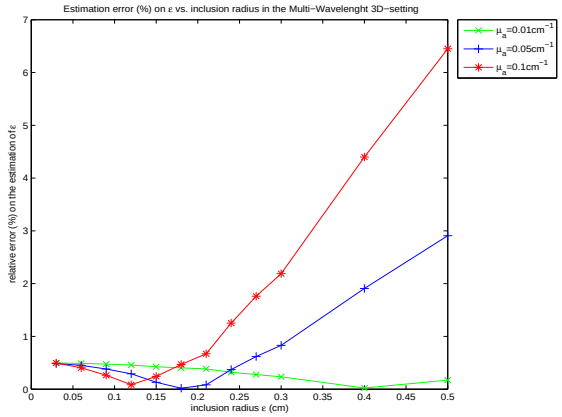

FIGURE 2.4. Error on the reconstruction of ε in the multi-wavelength setting.

2.5. Concluding Remarks

Assuming that the reduced scattering coefficient is known, we have provided an asymptotic approach to estimate the normalized absorption coefficient of a small absorber from the normalized absorbed energy. We have also shown how to separate the size of the absorber from the absolute absorption coefficient by combining

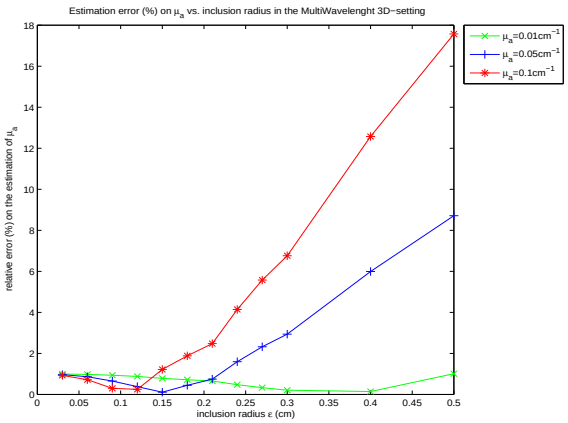

FIGURE 2.5. Error on the reconstruction of μ_a in the multi-wavelength setting.

photo-acoustic and diffusing light measurements. In the case where the reduced scattering coefficient is unknown, we have developed a multi-wavelength approach to estimate the absolute absorption coefficient. Finally, it would be of interest to use the radiative transfer equation as a light transport model when the diffusion approximation breaks down. Another subject of future work is to develop a method, similar to the one derived in this chapter, to estimate the normalized absorption coefficient from the normalized absorbed energy for the half-space problem. The Half-space model is of considerable practical interest in photo-acoustic imaging of the skin. See [**46, 127**].

Appendix A: Proof of Estimate (2.13)

In this section we prove estimate (2.13). To this end, we consider

$$\begin{cases} \Delta u - i\alpha u = 0, & \text{in } \Omega, \\ \dfrac{\partial u}{\partial \nu} + \beta u = g & \text{on } \partial\Omega, \end{cases} \tag{2.48}$$

where $\alpha \geq 0$ and $\beta > 0$. The estimate (2.13) is an easy consequence of the following lemma.

LEMMA 2.7. *Let $y \in \Omega$ and $r > 0$ be such that $B_{3r} := B_{3r}(y)$ is a subset of Ω with dist$(B_{3r}, \partial\Omega) > c_0$ for some positive constant c_0. Here $B_r(y)$ denotes the ball of radius r centered at y. The following estimates hold:*

- *If $\alpha > 1$, then there is a constant C independent of α such that if u be the solution to (2.48), then*

$$\|u\|_{L^\infty(B_r)} + \alpha^{-1/2}\|\nabla u\|_{L^\infty(B_r)} + \alpha^{-1}\|\nabla\nabla u\|_{L^\infty(B_r)} \leq C\|g\|_{L^\infty(\partial\Omega)}. \tag{2.49}$$

- *If $0 \leq \alpha \leq 1$, then there is a constant C independent of α such that if u be the solution to (2.48), then*

$$\|u\|_{L^\infty(B_r)} + \|\nabla u\|_{L^\infty(B_r)} + \|\nabla\nabla u\|_{L^\infty(B_r)} \leq C\|g\|_{L^\infty(\partial\Omega)}. \tag{2.50}$$

Proof. Multiplying both sides of the equation in (2.48) by $\overline{u}$ and integrating by parts yield

$$\beta \int_{\partial\Omega} |u|^2 + \int_\Omega |\nabla u|^2 dx + i\alpha \int_\Omega |u|^2 dx = \int_{\partial\Omega} g\overline{u}.$$

By taking the real and imaginary parts of the above identity and using the inequality $ab < a^2/\eta + \eta b^2$, we have

$$\beta \int_{\partial\Omega} |u|^2 + \int_\Omega |\nabla u|^2 dx + \alpha \int_\Omega |u|^2 dx \le \frac{C}{\eta} \|g\|^2_{L^\infty(\partial\Omega)} + C\eta \|u\|^2_{L^1(\partial\Omega)} \tag{2.51}$$

for some constant C where η is a small constant to be determined later. Since

$$\|u\|^2_{L^1(\partial\Omega)} \le |\partial\Omega| \|u\|^2_{L^2(\partial\Omega)},$$

then by choosing η so small that $C\eta|\partial\Omega| < \frac{\beta}{2}$, we have

$$\frac{\beta}{2} \int_{\partial\Omega} |u|^2 d\sigma(x) + \int_\Omega |\nabla u|^2 dx + \alpha \int_\Omega |u|^2 dx \le C\|g\|^2_{L^\infty(\partial\Omega)}. \tag{2.52}$$

Let φ be a smooth function with a support in B_{3r} such that $\varphi \equiv 1$ on B_{2r}, and let $w := \varphi u$. Then w is a smooth function (with a compact support) satisfying

$$(\Delta - i\alpha)w = 2\nabla\varphi \cdot \nabla u + \Delta\varphi u.$$

Recall that the fundamental solution to the operator $\Delta - i\alpha$ is given by

$$\Gamma_\alpha(x) := \frac{\exp(-e^{\frac{\pi}{4}i}\sqrt{\alpha}|x|)}{4\pi|x|}, \quad x \neq 0.$$

Therefore, we have

$$w(x) = \int_\Omega \Gamma_\alpha(x-y)(2\nabla\varphi \cdot \nabla u + \Delta\varphi u)(y)dy, \quad x \in \Omega.$$

Note that $2\nabla\varphi\cdot\nabla u + \Delta\varphi u$ is supported in $B_{3r} \setminus B_{2r}$. So (2.49) and (2.50) for $\alpha \neq 0$ follow immediately. For $\alpha = 0$, we shall make use of the inequality

$$\left\| u - \frac{1}{|\partial\Omega|} \int_{\partial\Omega} u \, d\sigma \right\|_{L^2(\Omega)} \le C\|\nabla u\|_{L^2(\Omega)}$$

to obtain the desired estimate. This completes the proof. □

Appendix B: Proof of Lemma 2.3

We first note that since $p > 3$, $q = \frac{p}{p-1} < \frac{3}{2}$. For $-1 \le \alpha \le 2$, define

$$T_\alpha[f](x) = \int_D \frac{f(y)}{|x-y|^\alpha} dy, \quad x \in D.$$

By Hölder's inequality, we have

$$|T_\alpha[f](x)| \le \|f\|_{L^p(D)} \left(\int_D \frac{1}{|x-y|^{\alpha q}} dy \right)^{1/q} \le C\varepsilon^{\frac{3}{q}-\alpha} \|f\|_{L^p(D)}.$$

It then follows that

$$\|T_\alpha[f]\|_{L^p(D)} \le C\varepsilon^{3-\alpha} \|f\|_{L^p(D)}. \tag{2.53}$$

Let us set

$$\mathcal{N}_1[f](x) := \int_D (f(y) - f(x))\Gamma(x-y)\, dy,$$
$$\mathcal{N}_2[f](x) := \int_D \nabla f(y) \cdot \nabla_y \Gamma(x-y)\, dy,$$
$$\mathcal{R}_1[f](x) := \int_D (f(y) - f(x))R(x,y)\, dy,$$
$$\mathcal{R}_2[f](x) := \int_D \nabla f(y) \cdot \nabla_y R(x,y)\, dy,$$

so that

$$\mathcal{N} = 3\mu_a\mu_s\mathcal{N}_1 - \frac{\mu_a}{\mu_a+\mu_s}\mathcal{N}_2 \quad \text{and} \quad \mathcal{R} = \mu_a\mathcal{R}_1 - \frac{\mu_a}{3(\mu_a+\mu_s)\mu_s}\mathcal{R}_2.$$

Note that

$$\mathcal{N}_1[f](x) = \int_D \frac{f(y)-f(x)}{|y-x|}|y-x|\Gamma(x-y)\, dy.$$

Since $|y-x|\Gamma(x-y) \le C$, we have as in (2.53)

$$\|\mathcal{N}_1[f]\|_{L^p(D)} \le C\varepsilon^{\frac{3}{q}} \left(\int_D \int_D \frac{|f(y)-f(x)|^p}{|y-x|^p} dxdy \right)^{1/p} \le C\varepsilon^3 \|\nabla f\|_{L^p(D)}.$$

Similarly, we have

$$\|\nabla\mathcal{N}_1[f]\|_{L^p(D)} \le C\varepsilon^2 \|\nabla f\|_{L^p(D)}.$$

We also have

$$\|\mathcal{N}_2[f]\|_{L^p(D)} \le C\varepsilon \left\|\nabla f\right\|_{L^p(D)}.$$

Note that $\nabla_x\nabla_y\Gamma(x-y)$ is a Calderón-Zygmund kernel [**122**] and hence the operator $\nabla\mathcal{N}_2$ is bounded on L^p, $1 < p < \infty$. Therefore, we have

$$\|\nabla\mathcal{N}_2[f]\|_{L^p(D)} \le C \left\|\nabla f\right\|_{L^p(D)}.$$

Therefore, we obtain (2.24) and (2.25).

Similarly, we have using (2.16)-(2.18) that

$$\|\mathcal{R}_1[f]\|_{L^p(D)} \le C\mu_s^{3/2}\varepsilon^4 \|\nabla f\|_{L^p(D)},$$
$$\|\nabla\mathcal{R}_1[f]\|_{L^p(D)} \le C(\mu_s^2\varepsilon^4 + \mu_s^{3/2}\varepsilon^3) \|\nabla f\|_{L^p(D)},$$
$$\|\mathcal{R}_2[f]\|_{L^p(D)} \le C(\mu_s^2\varepsilon^3 + \mu_s^{3/2}\varepsilon^2) \|\nabla f\|_{L^p(D)},$$
$$\|\nabla\mathcal{R}_2[f]\|_{L^p(D)} \le C(\mu_s^{5/2}\varepsilon^3 + \mu_s^2\varepsilon^2 + \mu_s^{3/2}\varepsilon) \|\nabla f\|_{L^p(D)}.$$

Therefore we get

$$\|\mathcal{R}[f]\|_{L^p(D)} \le C\left(\mu_a\mu_s^{3/2}\varepsilon^4 + \frac{\mu_a}{\mu_s^2}(\mu_s^2\varepsilon^3 + \mu_s^{3/2}\varepsilon^2)\right) \|\nabla f\|_{L^p(D)},$$
$$\|\nabla\mathcal{R}[f]\|_{L^p(D)} \le C\left(\mu_a(\mu_s^2\varepsilon^4 + \mu_s^{3/2}\varepsilon^3) + \frac{\mu_a}{\mu_s^2}(\mu_s^{5/2}\varepsilon^3 + \mu_s^2\varepsilon^2 + \mu_s^{3/2}\varepsilon)\right) \|\nabla f\|_{L^p(D)}.$$

Suppose that $\varepsilon\sqrt{\mu_s}$ is small. We obtain

$$\mu_a\mu_s^{3/2}\varepsilon^4 + \frac{\mu_a}{\mu_s^2}(\mu_s^2\varepsilon^3 + \mu_s^{3/2}\varepsilon^2) \le \varepsilon^2\sqrt{\mu_s}\left(\mu_a\mu_s\varepsilon^2 + \frac{\mu_a}{\mu_s}\right)$$

and

$$\mu_a(\mu_s^2\varepsilon^4 + \mu_s^{3/2}\varepsilon^3) + \frac{\mu_a}{\mu_s^2}(\mu_s^{5/2}\varepsilon^3 + \mu_s^2\varepsilon^2 + \mu_s^{3/2}\varepsilon) \leq \varepsilon\sqrt{\mu_s}\left(\mu_a\mu_s\varepsilon^2 + \frac{\mu_a}{\mu_s}\right),$$

which yields (2.27) and (2.26) and thus completes the proof. □

CHAPTER 3

Transient Wave Imaging with Limited-View Data

3.1. Introduction

In Chapter 1 and the recent works [**15, 14**], the imaging of small anomalies using transient wave boundary measurements has been investigated. We have designed different approaches for locating them and reconstructing some information about their sizes and physical parameters. Our algorithms make use of complete boundary measurements. They are of Kirchhoff-, back-propagation, MUSIC-, and arrival time-types. The resolution of those algorithms in the time-harmonic domain is finite. It is essentially of order one-half the wavelength. See, for instance, [**4**].

In this work, we extend those algorithms to the case with limited-view measurements. For simplicity, we model here the small anomalies as point sources or dipoles. We refer the reader to [**15, 14**] and Chapter 1 for rigorous derivations of these approximate models and their higher-order corrections. It is worth mentioning that in order to model a small anomaly as a point source or a dipole, one has to truncate the high-frequency component of the transient incident and reflected waves.

By using the geometrical control method [**28**], we show how to recover all the classical algorithms that have been used to image point sources and dipole locations. Our main finding in this chapter is that if one can construct accurately the geometric control then one can perform imaging with the same resolution using partial data as using complete data. Our algorithms apply equally well to the case of many source points or dipole locations and are robust with respect to perturbations of the boundary. This is quite important in real experiments since one does not necessarily know the non-accessible part of the boundary with good accuracy.

The chapter is organized as follows. In Section 3.2 we provide a key identity based on the averaging of the limited-view data, using weights constructed by the geometrical control method. Section 3.3 is devoted to developing, for different choices of weights, Kirchhoff-, back-propagation-, MUSIC-, and arrival time-type algorithms for transient imaging with limited-view data. In Section 3.4 we discuss potential applications of the method in emerging biomedical imaging. In Section 3.5 we present results of numerical experiments and comparisons among the proposed algorithms.

3.2. Geometric Control

The basic model to be considered in this chapter is the following wave equation:

$$\frac{\partial^2 p}{\partial t^2}(x,t) - c^2 \Delta p(x,t) = 0, \quad x \in \Omega, \quad t \in]0,T[, \tag{3.1}$$

for some final observation time T, with the Dirichlet boundary conditions

$$p(x,t) = 0 \quad \text{on } \partial\Omega\times]0,T[, \tag{3.2}$$

the initial conditions

$$p(x,t)|_{t=0} = 0 \quad \text{in } \Omega, \tag{3.3}$$

and

$$\partial_t p(x,t)|_{t=0} = \delta_{x=z} \quad \text{or} \quad \partial_t p(x,t)|_{t=0} = m_0 \cdot \nabla\delta_{x=z} \quad \text{in } \Omega. \tag{3.4}$$

Here c is the acoustic speed in Ω which we assume to be constant, and m_0 is a constant nonzero vector. We suppose that T is large enough so that

$$T > \frac{\operatorname{diam}(\Omega)}{c}. \tag{3.5}$$

The purpose of this chapter is to design efficient algorithms for reconstructing the location z from boundary measurements of $\frac{\partial p}{\partial \nu}$ on $\Gamma\times]0,T[$, where $\Gamma \subset \partial\Omega$.

Suppose that T and Γ are such that they geometrically control Ω, which roughly means that every geometrical optic ray, starting at any point $x \in \Omega$, at time $t = 0$, hits Γ before time T at a nondiffractive point; see [**28, 100**]. Let $\beta \in \mathcal{C}_0^\infty(\Omega)$ be a cutoff function such that $\beta(x) \equiv 1$ in a sub-domain Ω' of Ω, which contains the source point z.

For a given function w which will be specified later, we construct by the geometrical control method a function $v(x,t)$ satisfying

$$\frac{\partial^2 v}{\partial t^2} - c^2\Delta v = 0 \quad \text{in } \Omega\times]0,T[, \tag{3.6}$$

with the initial condition

$$v(x,0) = c^2\beta(x)w(x), \quad \partial_t v(x,0) = 0, \tag{3.7}$$

the boundary condition $v = 0$ on $\partial\Omega \setminus \overline{\Gamma}$, and the final conditions

$$v|_{t=T} = \frac{\partial v}{\partial t}\Big|_{t=T} = 0 \quad \text{in } \Omega. \tag{3.8}$$

Let

$$g_w(x,t) := v(x,t) \quad \text{on } \Gamma\times]0,T[. \tag{3.9}$$

Multiplying (3.1) by v and integrating over $\Omega \times [0,T]$ lead to the following key identity of this chapter:

$$\int_0^T \int_\Gamma \frac{\partial p}{\partial \nu}(x,t) g_w(x,t)\, d\sigma(x)\, dt = w(z) \quad \text{or} \quad -m_0 \cdot \nabla w(z). \tag{3.10}$$

Note that the probe function constructed in [**7**] corresponds to one of the following choices for w in Ω:

$$w(x) := \frac{\delta\left(\tau - \frac{|x-y|}{c}\right)}{4\pi|x-y|} \quad \text{in three dimensions} \tag{3.11}$$

or

$$w(x) := \delta\left(\tau - \frac{1}{c}\theta\cdot x\right) \quad \text{in two dimensions,} \tag{3.12}$$

where θ is a unit vector.

The reader is referred, for instance, to [**23, 140, 87**] for numerical investigations of the geometrical control method.

3.3. Imaging Algorithms

In this section, we only consider the initial condition $\partial_t p(x,t)|_{t=0} = \delta_{x=z}$ in Ω. One can treat the case of the initial data $\partial_t p(x,t)|_{t=0} = m_0 \cdot \nabla \delta_{x=z}$ in the exactly same way. Using the functions v constructed by the geometrical control method with different choices of initial data w, one recovers several classical algorithms for imaging point sources. For simplicity, we only consider a single point source, but the derived algorithms are efficient for locating multiple sources as well. The reader is referred to [**53**] for a review on source localization methods.

3.3.1. Kirchhoff Algorithm. Let $y \in \mathbb{R}^d \setminus \overline{\Omega}, d = 2, 3$, and $\omega \in \mathbb{R}$. Set

$$w(x) = e^{i\omega|x-y|}, \quad x \in \Omega.$$

Then, for a given search point z^S in Ω, we have from (3.10)

$$\int_{\mathbb{R}} e^{-i\omega|z^S-y|} \int_0^T \int_\Gamma \frac{\partial p}{\partial \nu}(x,t) g_w(x,t)\, d\sigma(x)\, dt\, d\omega = \int_{\mathbb{R}} e^{-i\omega(|z^S-y|-|z-y|)}\, d\omega = \delta_{|z^S-y|-|z-y|=0},$$

where δ is the Dirac mass. Taking a (virtual) planar array of receivers y outside Ω yields then a Kirchhoff-type algorithm for finding z.

In fact, let $\omega_k, k = 1, \ldots, K$, be a set of frequencies and let $y_1, \ldots, y_N$, be a set of virtual receivers. To find the location z one maximizes over z^S the following imaging functional:

$$\mathcal{I}_{\mathrm{KI}}(z^S) := \frac{1}{K} \Re e \sum_{\omega_k} \sum_{y_n} e^{-i\omega|z^S-y_n|} \int_0^T \int_\Gamma \frac{\partial p}{\partial \nu}(x,t) g_{w_{k,n}}(x,t)\, d\sigma(x)\, dt,$$

where $w_{k,n}(x) = e^{i\omega_k|x-y_n|}$.

3.3.2. Back-propagation Algorithm. If one takes w to be a plane wave:

$$w(x) = e^{i\omega\theta\cdot x}, \quad \theta \in S^{d-1},$$

where S^{d-1} is the unit sphere in $\mathbb{R}^d$, then one computes for a given search point $z^S \in \Omega$,

$$\int_{S^{d-1}} e^{-i\omega\theta\cdot z^S} \int_0^T \int_\Gamma \frac{\partial p}{\partial \nu}(x,t) g_w(x,t)\, d\sigma(x)\, dt\, d\sigma(\theta) = \int_{S^{d-1}} e^{i\omega\theta\cdot(z-z^S)}\, d\sigma(\theta).$$

But

$$\int_{S^{d-1}} e^{i\omega\theta\cdot(z-z^S)}\, d\sigma(\theta) = \begin{cases} j_0(\omega|z-z^S|) & \text{for } d=3, \\ J_0(\omega|z-z^S|) & \text{for } d=2, \end{cases}$$

where j_0 is the spherical Bessel function of order zero and J_0 is the Bessel function of the first kind and of order zero.

This is a back-propagation algorithm. Let $\theta_1, \ldots, \theta_N$, be a discretization of the unit sphere S^{d-1}. One plots at each point z^S in the search domain the following imaging functional:

$$\mathcal{I}_{\mathrm{BP}}(z^S) := \frac{1}{N} \Re e \sum_{\theta_n} e^{-i\omega\theta_n \cdot z^S} \int_0^T \int_\Gamma \frac{\partial p}{\partial \nu}(x,t) g_{w_n}(x,t)\, d\sigma(x)\, dt,$$

where $w_n(x) = e^{i\omega\theta_n \cdot x}$. The resulting plot will have a large peak at z. Note that the higher the frequency ω is, the better is the resolution. However, high frequency oscillations cause numerical instabilities. There is a trade-off between resolution and stability.

3.3.3. MUSIC Algorithm. Take

$$w(x) = e^{i\omega(\theta+\theta')\cdot x}, \quad \theta, \theta' \in S^{d-1}.$$

It follows from (3.10) that

$$\int_0^T \int_\Gamma \frac{\partial p}{\partial \nu}(x,t) g_w(x,t)\, d\sigma(x)\, dt = e^{i\omega(\theta+\theta')\cdot z}.$$

Therefore, one can design a multiple signal classification (MUSIC) algorithm for locating z. For doing so, let $\theta_1, \ldots, \theta_N$ be N unit vectors in $\mathbb{R}^d$. Define the matrix $A = (A_{nn'})_{n,n'=1}^N$ by

$$A_{nn'} := \int_0^T \int_\Gamma \frac{\partial p}{\partial \nu}(x,t) g_{w_{n,n'}}(x,t)\, d\sigma(x)\, dt,$$

with

$$w_{n,n'}(x) = e^{i\omega(\theta_n+\theta_{n'})\cdot x}.$$

Let P be the orthogonal projection onto the range of A. Given any point z^S in the search domain form the vector

$$h(z^S) := (e^{i\omega\theta_1 \cdot z^S}, \ldots, e^{i\omega\theta_N \cdot z^S})^T,$$

where T denotes the transpose. Then plot the MUSIC imaging functional:

$$\mathcal{I}_{\mathrm{MU}}(z^S) := \frac{1}{||(I-P)h(z^S)||}.$$

The resulting plot will have a large peak at z. Again, the higher the frequency ω is, the better is the resolution.

3.3.4. Arrival Time and Time-Delay of Arrival Algorithms. Taking w to be a distance function,

$$w(x) = |y - x|,$$

to a virtual receiver y on a planar array outside Ω yields arrival-time and time-delay of arrival algorithms. In fact, we have

$$\int_0^T \int_\Gamma \frac{\partial p}{\partial \nu}(x,t) g_w(x,t)\, d\sigma(x)\, dt = |y - z|.$$

Let $y_1, \ldots, y_N$ be N receivers and compute

$$r_n := \int_0^T \int_\Gamma \frac{\partial p}{\partial \nu}(x,t) g_{w_n}(x,t)\, d\sigma(x)\, dt,$$

with $w_n(x) = |y_n - x|$. Then, the point z can be found as the intersection of spheres of centers y_n and radii r_n.

Using time-of-arrival differences instead of arrival times would improve the robustness of the algorithm. Introduce the time-of-arrival difference, $t_{n,n'}$, between the receiver y_n and $y_{n'}$ as follows:

$$t_{n,n'} := \int_0^T \int_\Gamma \frac{\partial p}{\partial \nu}(x,t)(g_{w_n} - g_{w_{n'}})(x,t)\, d\sigma(x)\, dt.$$

At least $N = 4$ sources are required to locate z. The location z can be found as the intersection of three sets of hyperboloids. See, for instance, [**47, 132, 117, 50, 86, 31, 53**].

3.4. Applications to Emerging Biomedical Imaging

In this section we show how to apply the designed algorithms to emerging biomedical imaging. Of particular interest are radiation force imaging, magneto-acoustic current imaging, and photo-acoustic imaging.

3.4.1. Radiation Force Imaging. In radiation force imaging, one generates vibrations inside the organ, and acquires a spatio-temporal sequence of the propagation of the induced transient wave to estimate the location and the viscoelastic parameters of a small anomaly inside the medium. See, for instance, [**32, 33, 15**].

Let z be the location of the anomaly. Let Ω be a large ball englobing the anomaly. In the far-field, the problem, roughly speaking, reduces to finding the location of the anomaly from measurements of the pressure p on $\partial\Omega\times]0,T[$, that is, the solution to (3.1) with the initial conditions

$$p(x,t)|_{t=0} = 0 \quad \text{and} \quad \partial_t p(x,t)|_{t=0} = m_0 \cdot \nabla \delta_{x=z} \quad \text{in } \Omega. \tag{3.13}$$

A time-reversal technique can be designed to locate the anomaly. Suppose that one is able to measure p and its normal derivative at any point x on $\partial\Omega$. If both p and its normal derivative on $\partial\Omega$ are time-reversed and emitted from $\partial\Omega$, then the time-reversed wave travels back to the location z of the anomaly. See [**15**].

Suppose now that the measurements of p and its normal derivative are only done on the part Γ of $\partial\Omega$. Note first that

$$\frac{\partial p}{\partial \nu}|_{\partial\Omega\times]0,T[} = \Lambda_{\mathrm{DtN}}[p|_{\partial\Omega\times]0,T[}],$$

where Λ_{DtN} is the Dirichlet-to-Neumann operator for the wave equation in $\mathbb{R}^3 \setminus \Omega$. For any function v satisfying (3.6), (3.7), and (3.8), integrating by parts yields

$$\int_0^T \int_{\partial\Omega} p(x,t)(\Lambda^*_{\mathrm{DtN}}[v] + \frac{\partial v}{\partial \nu})(x,t)\, d\sigma(x)\, dt = m_0 \cdot \nabla w(z),$$

where Λ^*_{DtN} denotes the adjoint of Λ_{DtN}. Next, constructing by the geometrical control method, g_w such that v satisfies (3.6), (3.7), and (3.8), together with the boundary condition

$$\Lambda^*_{\mathrm{DtN}}[v] + \frac{\partial v}{\partial \nu} = \begin{cases} 0 & \text{on } \partial\Omega \setminus \overline{\Gamma} \times]0,T[\\ g_w & \text{on } \Gamma\times]0,T[, \end{cases}$$

one obtains

$$\int_0^T \int_\Gamma p(x,t) g_w(x,t)\, d\sigma(x)\, dt = m_0 \cdot \nabla w(z).$$

Making similar choices for w to those in the previous section provide different algorithms for locating the anomaly.

3.4.2. Magneto-Acoustic Current Imaging. In magneto-acoustic current imaging, one detects a pressure signal created in the presence of a magnetic field by electrically active tissues [**88, 115, 116**]. In the presence of an externally applied magnetic field, biological action currents, arising from active nerve or muscle fibers, experience a Lorentz force. The resulting pressure or tissue displacement contains information about the action current distribution.

Let $z \in \Omega$ be the location of an electric dipole, which represents an active nerve or muscle fiber, with strength c. The wave equation governing the induced pressure distribution p is (3.1), with the boundary condition (3.2), the initial conditions (3.3), and

$$\partial_t p(x,t)|_{t=0} = \delta_{x=z} \quad \text{in } \Omega. \tag{3.14}$$

The algorithms constructed in the previous section apply immediately to finding z from partial boundary measurements of the normal derivative of p.

3.4.3. Photo-Acoustic Imaging. The photo-acoustic effect refers to the generation of acoustic waves by the absorption of optical energy [**135, 72**]. In photo-acoustic imaging, energy absorption causes thermo-elastic expansion of the tissue, which in turn leads to propagation of a pressure wave. This signal is measured by transducers distributed on the boundary of the organ, which is in turn used for imaging optical properties of the organ. Mathematically, the pressure p satisfies (3.1) with the boundary condition (3.2) and the initial conditions

$$p(x,t)|_{t=0} = a\delta_{x=z} \quad \text{in } \Omega, \tag{3.15}$$

and

$$\partial_t p(x,t)|_{t=0} = 0 \quad \text{in } \Omega. \tag{3.16}$$

Here a is the absorbed energy.

Construct by the geometrical control method a function $v(x,t)$ satisfying (3.6), the initial condition (3.7), the boundary condition $v = 0$ on $\partial\Omega \setminus \overline{\Gamma}$, and the final conditions (3.8). Choosing w as in Section 3.3 yields different detection algorithms.

3.5. Numerical Illustrations

To test the geometrical control imaging approach, we implemented numerical simulations of both the forward problem, the wave equation (3.1)-(3.4), and the inverse problem where we compute the geometrical control function (3.6)-(3.9) and implement the inversion algorithms of Section 3.3.

To simulate the wave equation, we used a standard P1-finite elements discretization in space and a finite difference scheme in time. For time-cost considerations, we settled with an explicit (leap-frog) scheme along with the use of mass lumping (row-sum technique).

The method we present here has been implemented and tested on various types of two-dimensional meshes. We will present results obtained on three different sets of meshes (see Figure 3.1 and Table 3.1):

- squareReg0 and squareReg2 are regular meshes of the unit square $[-0.5\ 0.5]^2$.
- circle are unstructured meshes of the unit disc.

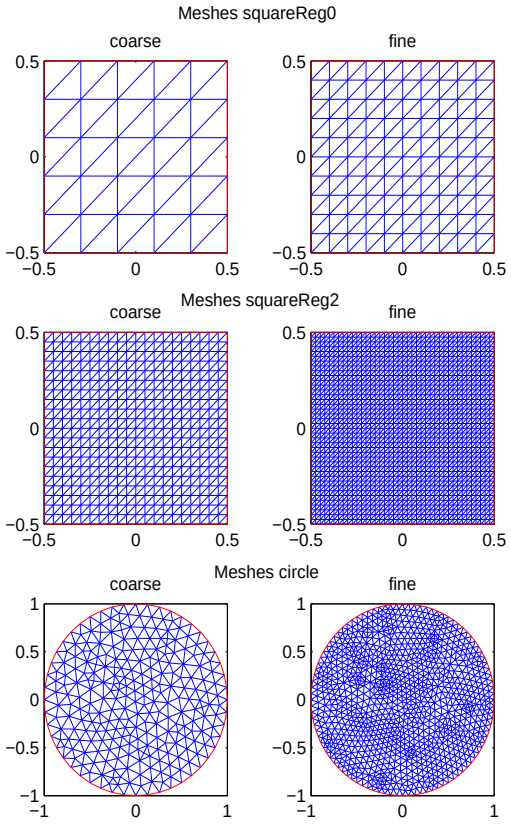

FIGURE 3.1. The coarse and fine meshes used on the square and circular geometries.

Set name	Coarse mesh			Fine mesh		
	# of nodes	# of elements	h	# of nodes	# of elements	$2h$
squareReg0	36	50	0.2	121	200	0.1
squareReg2	441	800	0.05	1681	3200	0.025
circle	270	490	0.0672	1029	1960	0.0336

TABLE 3.1. Geometries and meshes.

For computation of imaging functionals of Kirchhoff-, back-propagation-, and MUSIC-types, one has to be very careful with the spatial frequency ω. One has to make sure that the function $w(x;\omega)$ is accurately represented on the meshes we use. This imposes strict limitations on the range of frequencies that can be used.

Finally, the considered initial conditions for the simulated measurements are $p(x,0) = 0$ and $\frac{\partial p}{\partial t}(x,0) = \delta_h(x_0)$, where δ_h is a Gaussian approximation of the Dirac distribution and $x_0 = [0.21 \ -0.17]$ (see Figure 3.2).

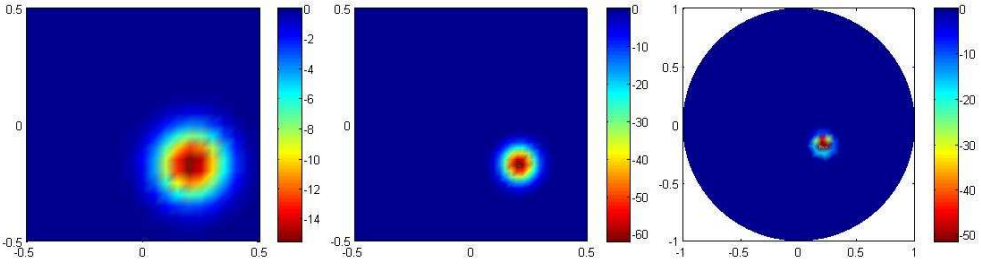

FIGURE 3.2. Initial time derivative, for the three geometries, used for the simulated measures.

To illustrate the performance of our approach with regards to limiting the view, we applied the algorithm to both a full and a partial view setting.

For the square medium, we assumed measurements were taken only on two adjacent edges - this corresponds to the theoretical (and practical) limit that still ensures geometric controllability. For the circular medium, we assumed measurements between angles $\frac{\pi}{4}$ and $\frac{3\pi}{2}$, as shown in Figure 3.4.

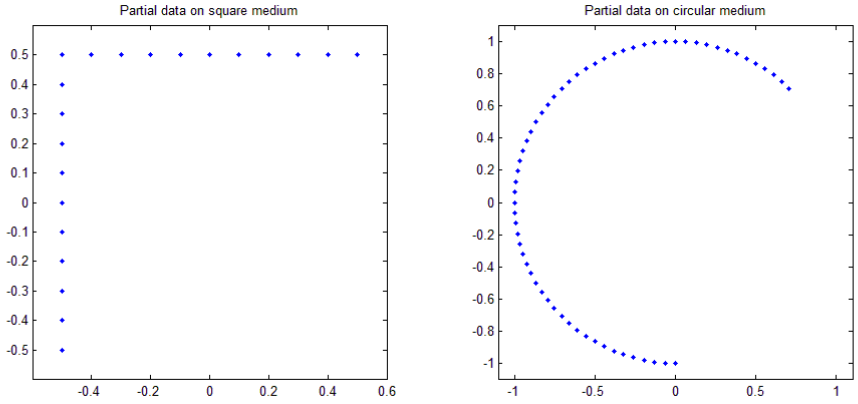

FIGURE 3.3. Limited-view observation boundaries for square and disc.

Before presenting the numerical results, we describe the numerical method used for computing the geometrical control, which is based on the Hilbert Uniqueness Method (HUM) of Lions.

3.5.1. Geometrical Control: HUM Using Conjugate Gradient Iteration on a Bi-Grid Mesh. The solution g_w of (3.6)-(3.9) has been shown to be unique provided that T and the control boundary Γ geometrically control Ω [**28**]. A systematic and constructive method for computing such a control is given by the Hilbert Uniqueness Method (HUM) of Lions [**102**]. A detailed study of the algorithm can be found in [**77**], [**23**], and [**140**]. The method applies a conjugate gradient algorithm as follows:

- Let $e_0, e_1 \in \mathrm{H}_0^1(\Omega) \times \mathrm{L}^2(\Omega)$, where $\mathrm{H}_0^1(\Omega)$ is the standard Sobolev space with zero boundary values;
- Solve forwards on $(0,T)$ the wave equation

$$\left\{\begin{array}{l} \dfrac{\partial^2\phi}{\partial t^2}(x,t) - c^2\Delta\phi(x,t) = 0, \\ \\ \phi(x,t) = 0 \qquad \text{on } \partial\Omega, \\ \\ \phi(x,0) = e_0(x), \qquad \dfrac{\partial\phi}{\partial t}(x,0) = e_1(x); \end{array}\right. \tag{3.17}$$

- Solve backwards the wave equation

$$\left\{\begin{array}{l} \dfrac{\partial^2\psi}{\partial t^2}(x,t) - c^2\Delta\psi(x,t) = 0, \\ \\ \psi(x,t) = \left\{\begin{array}{ll} 0 & \text{on } \partial\Omega\backslash\bar{\Gamma}, \\ \\ \frac{\partial\phi}{\partial\nu}(x,t) & \text{on } \Gamma, \end{array}\right. \\ \\ \psi(x,T) = 0, \qquad \dfrac{\partial\psi}{\partial t}(x,T) = 0; \end{array}\right. \tag{3.18}$$

- Set

$$\Lambda(e_0,e_1) = \left\{\frac{\partial\psi}{\partial t}(x,0), -\psi(x,0)\right\}; \tag{3.19}$$

- The solution v of (3.6)-(3.8) can be identified with ψ when

$$\Lambda(e_0,e_1) = \left\{0, -c^2\beta(x)w(x)\right\}$$

and $g_w(x,t) = \psi(x,t)$ on Γ.

Remark 3.1. *In the case where the initial condition is a pressure field (e.g., photo-acoustics)* $p(x,0) = p_0(x)$, $\frac{\partial p}{\partial t}(x,0) = 0$, *we need to have* $v(x,0) = 0$, $\frac{\partial v}{\partial t}(x,0) = c^2\beta(x)w(x)$. *This can be easily obtained by solving :* $\Lambda(e_0,e_1) = \left\{c^2\beta(x)w(x), 0\right\}$.

To proceed, we used a conjugate gradient algorithm on a discretized version Λ_h of the operator defined in (3.19), where we solve the wave equation using the finite-element finite-difference discretization described previously. To deal with unwanted effects linked with high spatial frequencies, we used a bi-grid method of Glowinski [**77**] based on a fine mesh with discretization length h and a coarse mesh with length $2h$. The wave equation is solved on the fine mesh and the residuals of Λ_h are computed after projection onto the coarse mesh.

Let us define I_h^{2h} and I_{2h}^h to be the projectors from the fine mesh to the coarse mesh and vice versa. The conjugate gradient algorithm is now as follows:

- Let e_0^0, e_1^0 be given initial guesses on the coarse mesh;

- Solve numerically (3.17) forwards with initial conditions $I_{2h}^h e_0^0$, $I_{2h}^h e_1^0$ and solve (3.18) backwards, both on the fine grid;
- Compute the initial residuals $g^0 = \{g_0^0, g_1^0\}$ on the coarse grid as follows:

$$\begin{cases} -\Delta g_0^0 = I_h^{2h} \dfrac{\psi^1 - \psi^{-1}}{2\Delta t} - I_h^{2h} u_1 & \text{in } \Omega, \\ g_0^0 = 0 & \text{on } \partial\Omega, \end{cases}$$

  and

$$g_1^0 = \psi^0 - I_h^{2h} u_0;$$

- If the norm of the residuals

$$\|\{g_0^0, g_1^0\}\|_h^2 = \int_{\mathcal{T}_h} |g_1^0|^2 + |\nabla g_0^0|^2$$

  is small enough, we have our solution, else we set the first search direction $w^0 = g^0$ and start the conjugate gradient;
- Suppose we know $e^k = \{e_0^k, e_1^k\}$, $g^k = \{g_0^k, g_1^k\}$and $w^k = \{w_0^k, w_1^k\}$;
- Solve numerically (3.17) forwards with initial conditions $I_{2h}^h w_0^k$, $I_{2h}^h w_1^k$ and solve (3.18) backwards both on the fine grid;
- Compute the remaining residuals $\xi^k = \{\xi_0^k, \xi_1^k\}$ on the coarse grid as follows:

$$\begin{cases} -\Delta_h \xi_0^k = I_h^{2h} \dfrac{\psi^1 - \psi^{-1}}{2\Delta t}, \\ \xi_0^k = 0 & \text{on } \partial\Omega, \end{cases}$$

  and

$$\xi_1^k = \psi^0;$$

- Calculate the length of the step in the w^k direction

$$\rho^k = \frac{\|g^k\|_h}{\langle \xi^k, w^k \rangle_h},$$

  where $\langle \xi^k, w^k \rangle_h = \displaystyle\int_{\mathcal{T}_h} \nabla \xi_0^k \nabla w_0^k + \xi_1^k w_1^k$;
- Update the quantities

$$e^{k+1} = e^k - \rho^k w^k,$$

$$g^{k+1} = g^k - \rho^k \xi^k;$$

- If $\|g^{k+1}\|_h$ is small, then e^{k+1} is our solution, else compute

$$\gamma^k = \frac{\|g^{k+1}\|_h}{\|g^k\|_h},$$

  and set the new descent direction

$$w^{k+1} = g^{k+1} + \gamma^k w^k.$$

REMARK 3.2 (Remarks on the numerical convergence). *The numerical procedure described in the previous section has been proved to converge in the case of finite difference method on the unit square* [**87**]. *This result can be easily extended in the case of a finite element method on a regular mesh. Convergence results for more general meshes are not available yet. They will be the subject of a future study.*

3.5.2. Reconstruction Results. We present here some results obtained by algorithms presented in Section 3.3. For each algorithm we will consider both the full view and the partial view cases.

- **Kirchhoff algorithm.** We limited ourselves to the frequency range : $W = [-\omega_{\max}, \omega_{\max}]$ with a step-size $\Delta\omega = \omega_{\max}/n_\omega$ where $\omega_{\max}$ and n_ω depend on the mesh coarseness.

  For time considerations we chose a reduced array of three virtual receivers
  - $Y = \{[0.6\ \ -0.6],\ [0.6\ 0],\ [0.6\ 0.6]\}$ for the square medium.
  - $Y = \{[1\ \ -1],\ [1\ 0],\ [1\ 1]\}$ for the circular medium.

  We compute and represent the function $\mathcal{I}_{\mathrm{KI}}(z^S)$ for z^S on the fine mesh. The estimated position is at the maximum of $\mathcal{I}_{\mathrm{KI}}(z^S)$. Reconstruction results are given in Figure 3.4.
- **Back-propagation algorithm.** We chose frequencies well represented on the mesh ($\omega = 9$ for squareReg0, $\omega = 30$ for squareReg2 and $\omega = 20$ for circle) and a 30-point discretization of the unit circle for θ.

  We compute and represent the function $\mathcal{I}_{\mathrm{BP}}(z^S)$ for z^S on the fine mesh. The estimated position is at the maximum of $\mathcal{I}_{\mathrm{BP}}(z^S)$. Results are given in Figure 3.5.
- **Arrival-time algorithm.** We considered minimal arrays of two virtual receivers $Y = \{[0\ 0.6]; [0.6\ 0]\}$ for the square medium. For each receiver we computed the value of $r_k = d(x_0, y_k)$, where x_0 is the position of the source and y_k the position of the receiver. We represent the circles $\mathcal{C}(y_k, r_k)$ and their intersections. Results are given in Figure 3.6.
- **MUSIC algorithm.** Working with the same parameters, we compute and represent the function $\mathcal{I}_{\mathrm{MU}}(z^S)$ for z^S on the fine mesh. The estimated position is at the maximum of $\mathcal{I}_{\mathrm{MU}}(z^S)$. Reconstruction results are given in Figure 3.7.

In Table 3.2 we give the estimations x_{est} of the source location $x_0 = [0.21 - 0.17]$ for each algorithm, and the error $d(x_0, x_{\mathrm{est}})$. For comparison, we give $h_{\min}$, the smallest distance between 2 points in the fine mesh.

3.5.3. Case of Multiple Sources. Except for the arrival-time algorithm, all the methods presented in this chapter are well-suited for identifying several point-like sources. To illustrate this, we simulated measurements on squareReg2 with three sources located at $[0.21\ \ -0.17]$, $[-0.22\ \ -0.3]$ and $[0.05\ 0.27]$.

- We applied the Kirchhoff imaging algorithm with a different set of virtual receivers:

  $$Y = \{[0.6\ 0],\ [0.6\ 0.6],\ [0\ 0.6],\ [-0.6\ 0.6],\ [-0.6\ 0]\}\,.$$

  The reason for taking more virtual receivers is that Kirchhoff works on intersecting circles centered at the receivers and passing through the sources. Too few receivers can generate false positives. Results are given in Figure 3.10.
- We ran the back-propagation and MUSIC algorithms with exactly the same parameters as previously. Results are given in Figures 3.11 and 3.12 respectively.

Algorithm	Mesh	View	x_{est}	$h_{\min}$	$d(x_0, x_{\text{est}})$
Kirchhoff	squareReg0	Full	[0.2 -0.15]	0.1	0.0224
		Partial	[0.2 -0.15]		0.0224
	squareReg2	Full	[0.2 -0.175]	0.025	0.0112
		Partial	[0.2 -0.175]		0.0112
	circle	Full	[0.1949 -0.1619]	0.0336	0.0171
		Partial	[0.1949 -0.1619]		0.0171
Back-propagation	squareReg0	Full	[0.2 -0.15]	0.1	0.0224
		Partial	[0.2 -0.15]		0.0224
	squareReg2	Full	[0.2125 -0.175]	0.025	0.0056
		Partial	[0.2125 -0.175]		0.0056
	circle	Full	[0.1949 -0.1619]	0.0336	0.0171
		Partial	[0.1949 -0.1619]		0.0171
Arrival time	squareReg0	Full	[0.1877 -0.1433]	0.1	0.0348
		Partial	[0.1882 -0.1314]		0.0444
	squareReg2	Full	[0.2050 -0.1768]	0.025	0.0085
		Partial	[0.2048 -0.1774]		0.009
	circle	Full	[0.1802 -0.2196]	0.0336	0.0579
		Partial	[0.1790 -0.2119]		0.0522
MUSIC	squareReg0	Full	[0.15 -0.2]	0.1	0.0671
		Partial	[0.15 -0.2]		0.0671
	squareReg2	Full	[0.175 -0.1625]	0.025	0.0358
		Partial	[0.175 -0.175]		0.0354
	circle	Full	[0.2804 -0.139]	0.0336	0.0769
		Partial	[0.2416 -0.0974]		0.0792

TABLE 3.2. Numerical results for localization of the source at $x_0 = [0.21, -0.17]$ using four algorithms and three geometries.

3.5.4. Boundary Perturbation. In real experiments, one does not necessarily know the uncontrolled part of the boundary with good accuracy. A major concern for real applications of the method is thus its robustness with respect to perturbations of the boundary.

We tested our algorithms by perturbing the boundary nodes outwards

$$x_{i,\text{perturbed}} = x_i + \epsilon U n_{x_i},$$

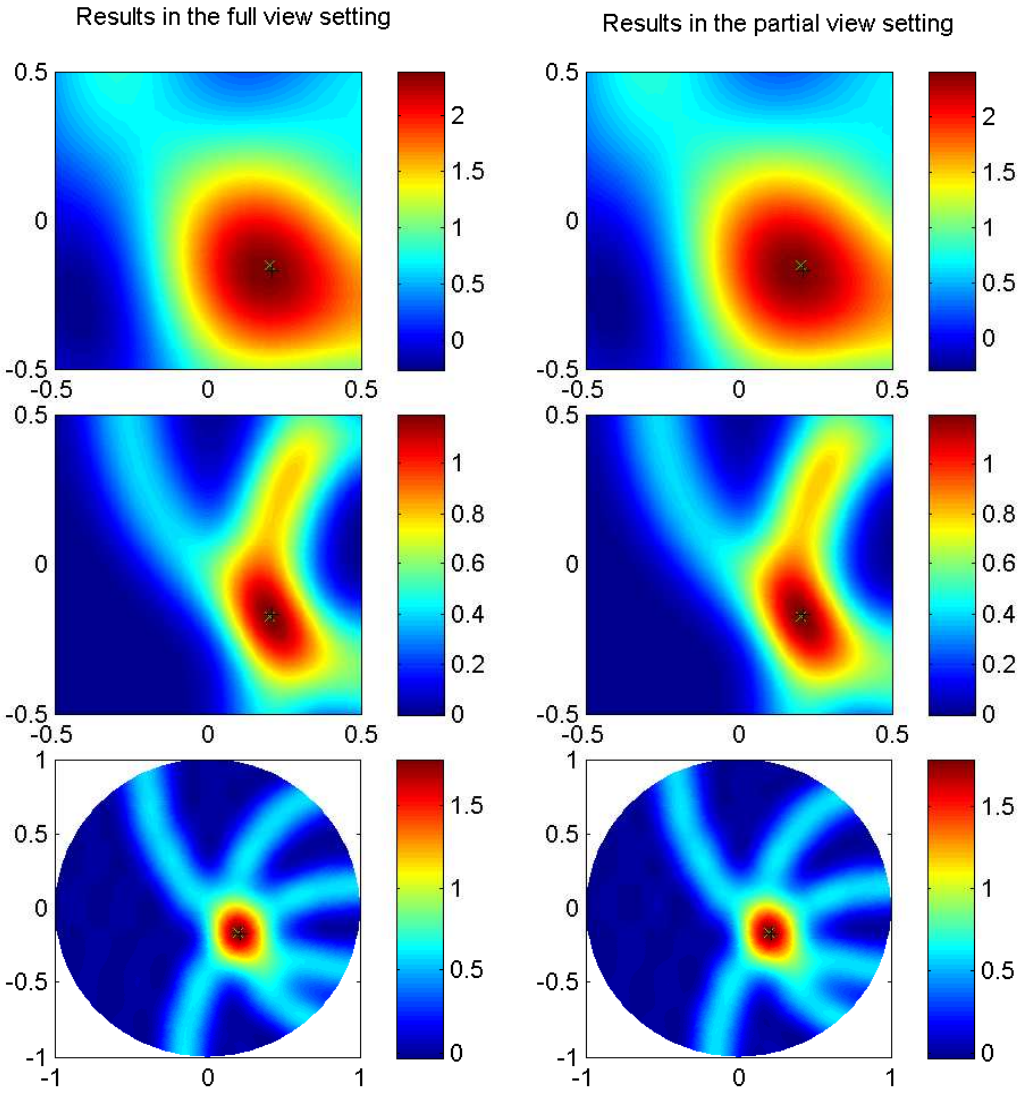

FIGURE 3.4. Kirchhoff results for the geometries of Table 3.1 - from top to bottom: squareReg0, squareReg2, circle. The (black/white) x denotes the (numerical/theoretical) center of the source.

where ϵ is an amplitude factor, U is a uniform random variable in [0 1] and n_{x_i} is the outward normal at the point x_i. We simulated measurements on the perturbed mesh, which is then supposed unknown since we computed the geometric control on the unperturbed mesh.

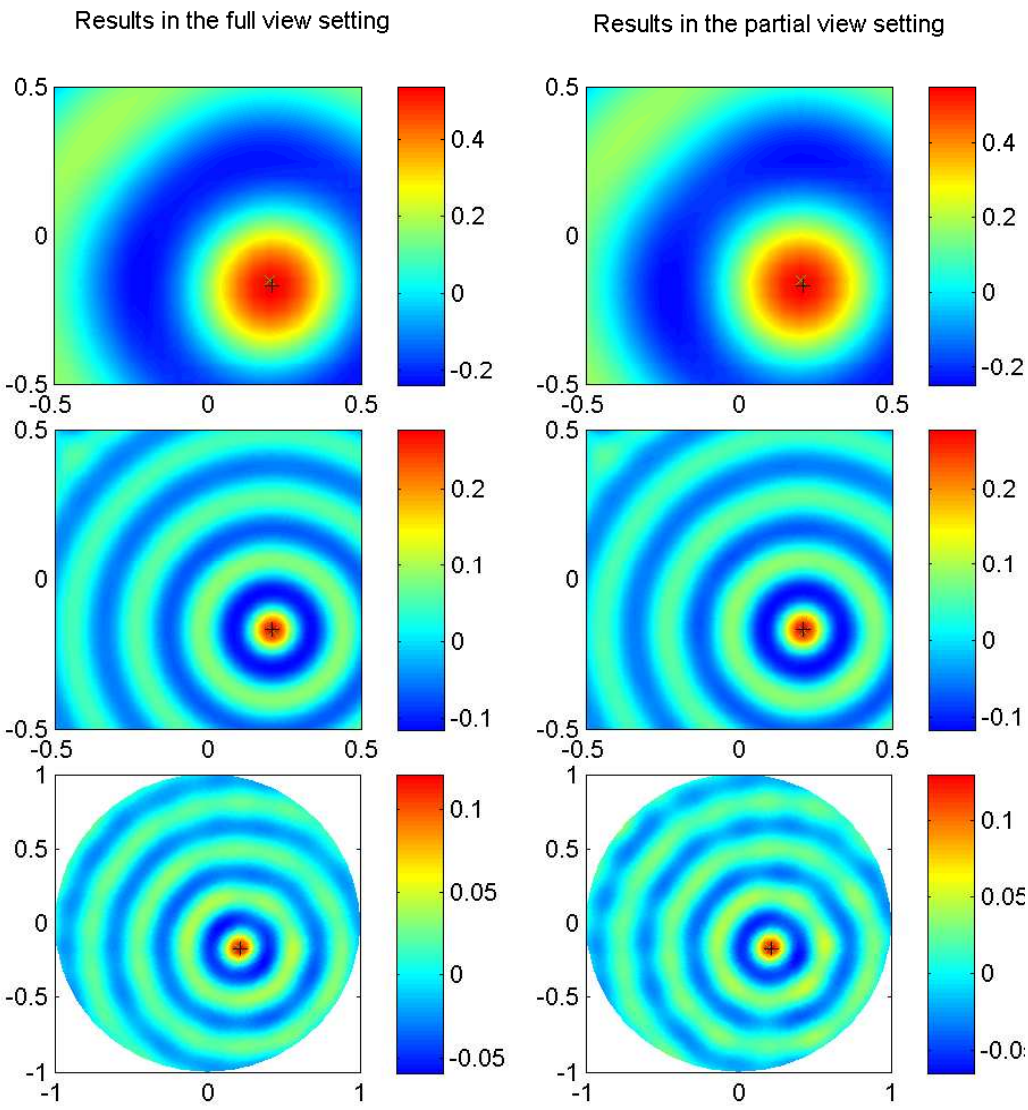

FIGURE 3.5. Back-propagation results for the geometries of Table 3.1 - from top to bottom: squareReg0, squareReg2, circle. The (black/white) x denotes the (numerical/theoretical) center of the source.

To illustrate the results, we used squareReg2 with three levels of perturbation, $\epsilon = 0.01$, 0.025 and 0.05 (see Figure 3.5.4) and the same initial condition as before, that is a Dirac approximation located at $[0.21 \ -0.17]$.

We give the results, with the three perturbations, for the Kirchhoff (Figure 3.13), the back-propagation (Figure 3.14) and the arrival-time (Figure 3.15) algorithms. Modifying the mesh as we did generates smaller elements and thus changes

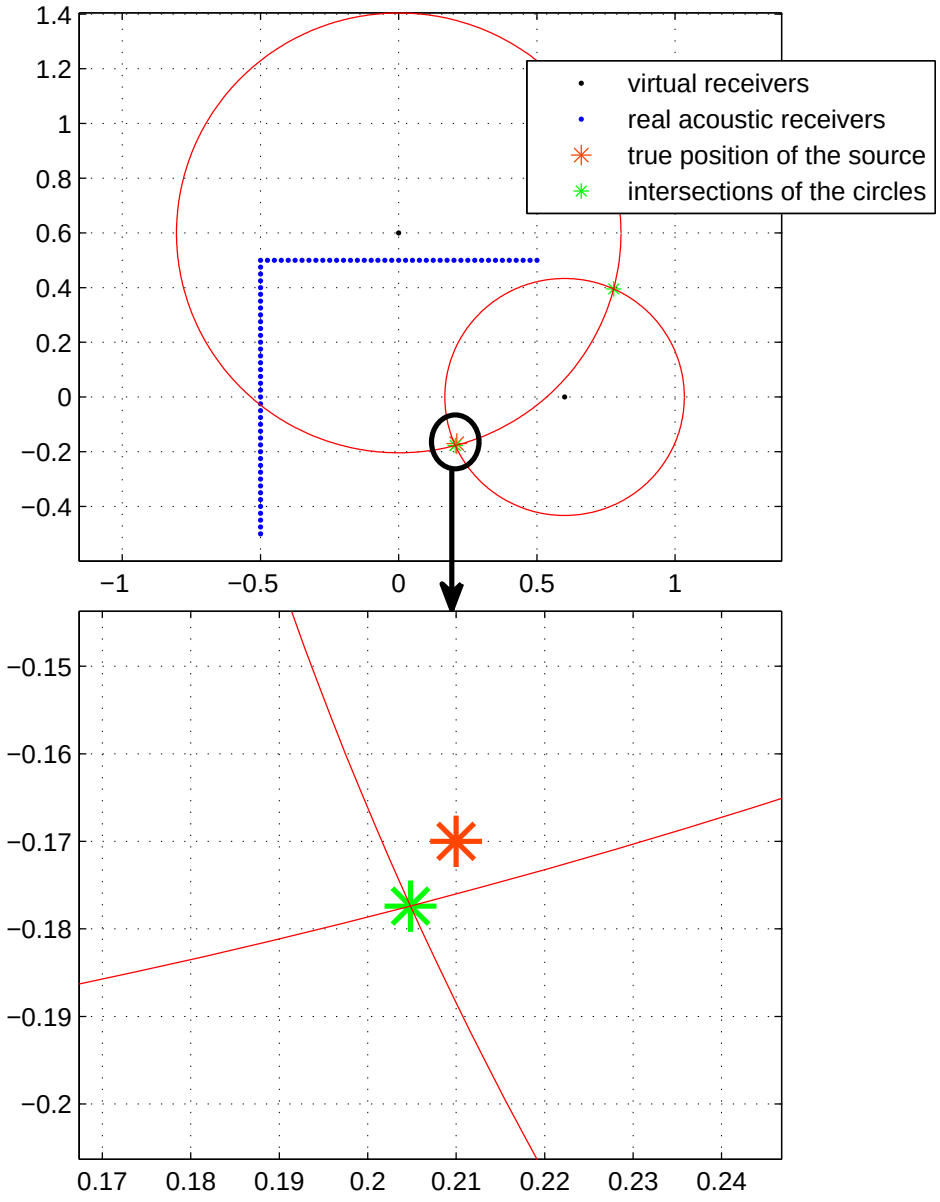

FIGURE 3.6. Example of arrival time results for squareReg2 geometry.

the CFL condition for the wave-equation solver. Computation time becomes too expensive for the MUSIC algorithm. For this reason we do not present MUSIC results here.

As expected the estimation of the source position deteriorates as we increase the boundary uncertainty. The errors are summarized in Table 3.5.4.

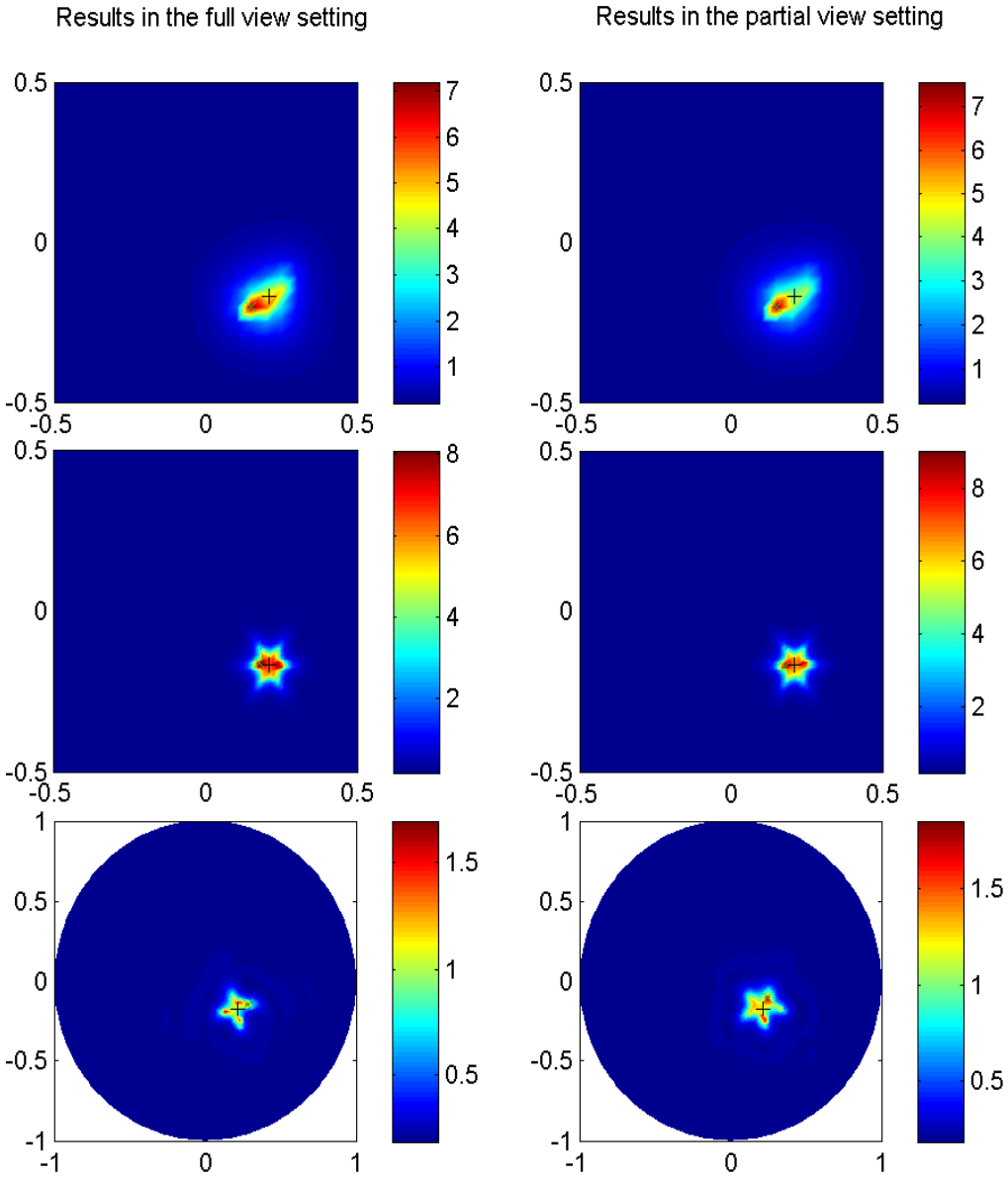

FIGURE 3.7. MUSIC results for the geometries of Table 3.1 - from top to bottom: sqReg0, sqReg2, circle. The (black/white) x denotes the (numerical/theoretical) center of the source.

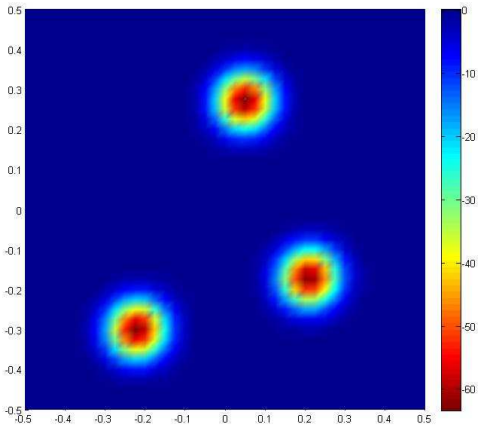

FIGURE 3.8. Initial time derivative for the case of multiple sources.

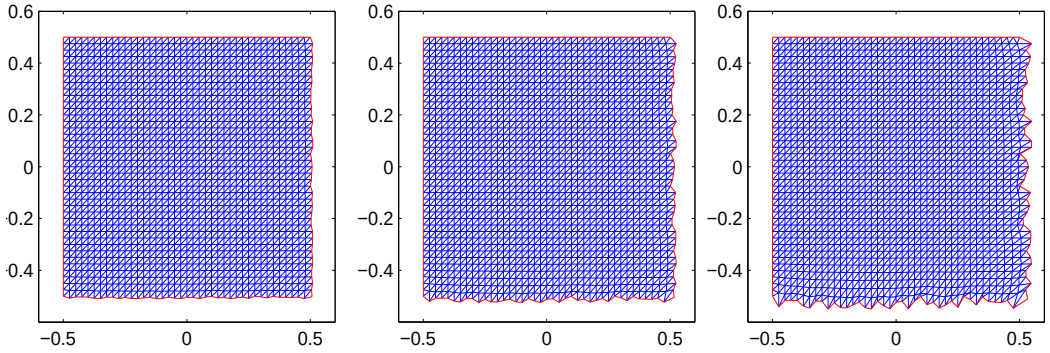

FIGURE 3.9. Perturbation of the mesh for $\epsilon = 0.01$, 0.025 and 0.05.

3.6. Concluding Remarks

In this chapter we have constructed Kirchhoff-, back-propagation-, MUSIC-, and arrival time-type algorithms for imaging point sources and dipoles from limited-view data. Our approach is based on averaging of the limited-view data, using weights constructed by the geometrical control method. It is quite robust with respect to perturbations of the non-accessible part of the boundary. We have shown that if one can construct accurately the geometric control then one can perform imaging with the same resolution using partial data as using complete data. The

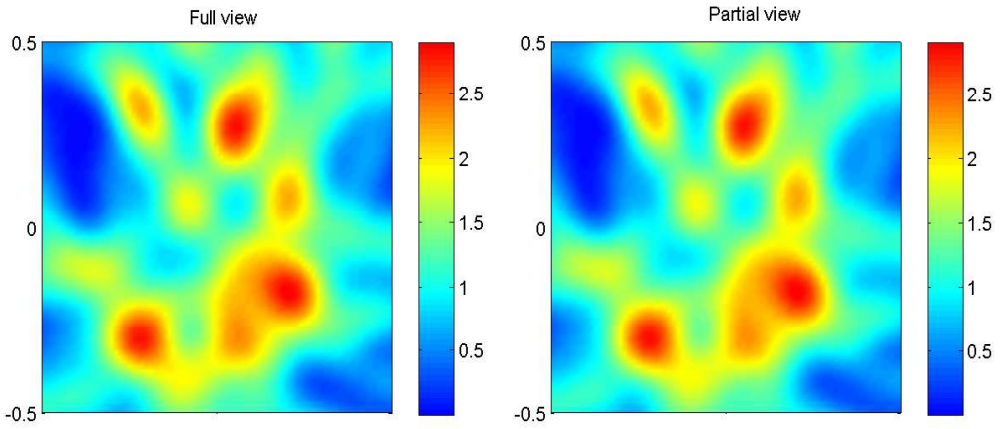

FIGURE 3.10. Kirchhoff results for the geometry sqReg2 with several inclusions.

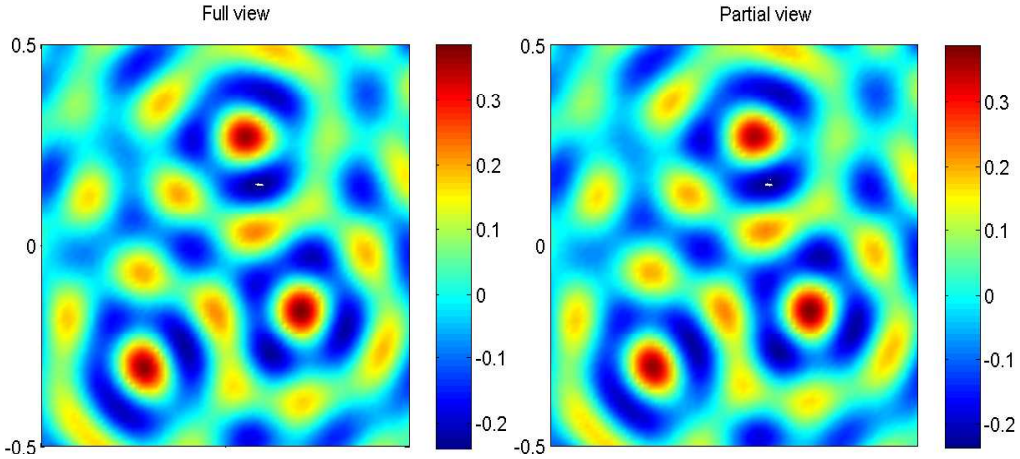

FIGURE 3.11. Back-propagation results for the geometry sqReg2 with several inclusions.

generalization of the proposed algorithms to the case where the speed of sound has random fluctuations will be considered in Chapter 5.

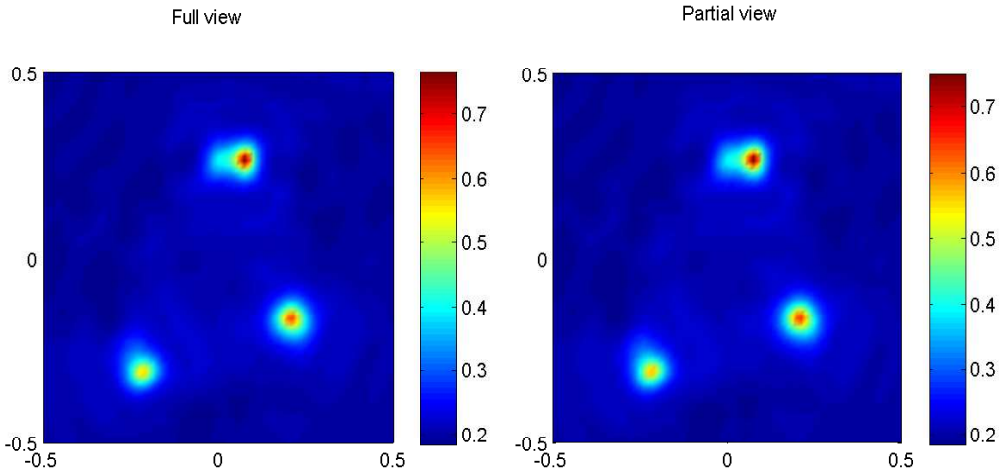

FIGURE 3.12. MUSIC results for the geometry sqReg2 with several inclusions.

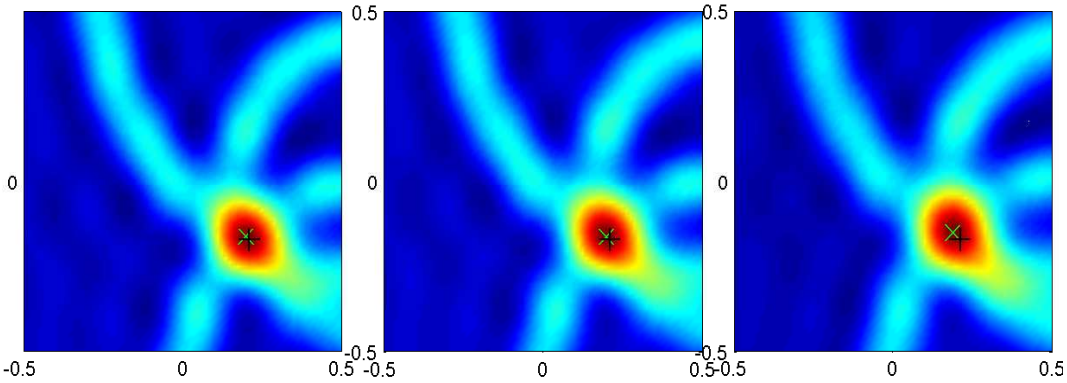

FIGURE 3.13. Kirchhoff results for the geometry sqReg2 with perturbed boundary (from left-to-right,$\epsilon = 0.01$, 0.025 and 0.05). The (black/white) x denotes the (numerical/theoretical) center of the source.

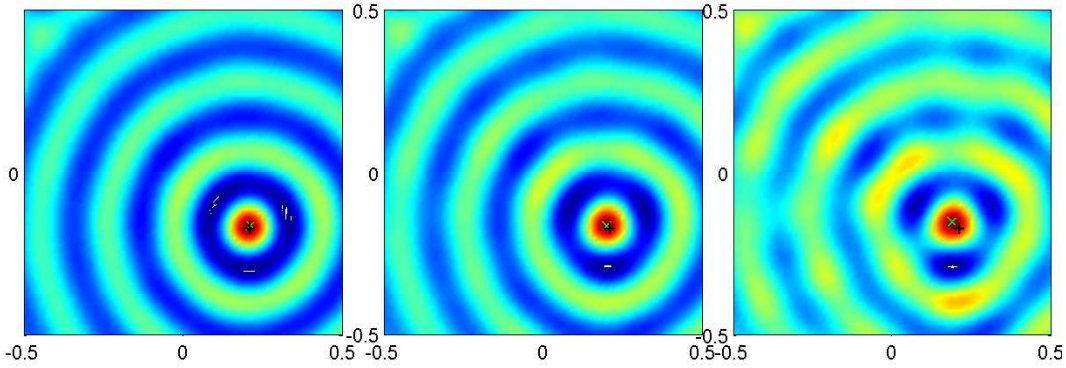

FIGURE 3.14. Back-propagation results for the geometry sqReg2 with perturbed boundary (from left-to-right, $\epsilon = 0.01$, 0.025 and 0.05). The (black/white) x denotes the (numerical/theoretical) center of the source.

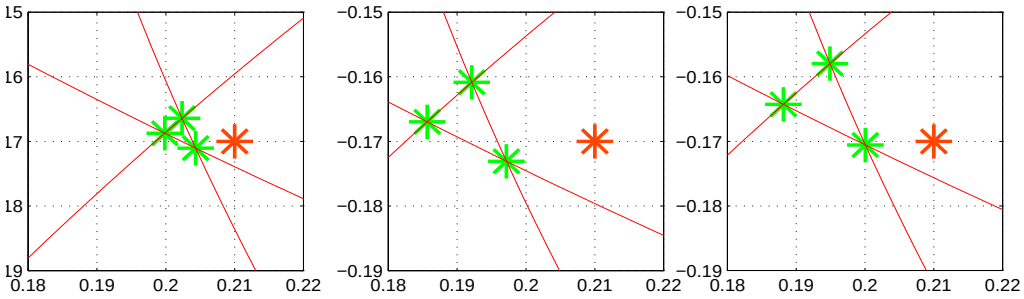

FIGURE 3.15. Arrival-time results for the geometry sqReg2 with perturbed boundary (from left-to-right, $\epsilon = 0.01$, 0.025 and 0.05)

Algorithm	Perturbation amplitude ϵ	x_{est}	$d(x_0, x_{\text{est}})$
Kirchhoff	0.01	[0.2 -0.1625]	0.0125
	0.025	[0.2 -0.1625]	0.0125
	0.05	[0.1875 -0.15]	0.03
Back-propagation	0.01	[0.2125 -0.1625]	0.0079
	0.025	[0.2 -0.1625]	0.0125
	0.05	[0.1875 -0.15]	0.03
Arrival time	0.01	[0.2022 -0.1687]	0.0079
	0.025	[0.1917 -0.167]	0.0186
	0.05	[0.1944 -0.1643]	0.0166

TABLE 3.3. Numerical results for localization of the source at $x_0 = [0.21 \ -0.17]$ using sqReg2 geometry with boundary perturbations.

CHAPTER 4

Photoacoustic Imaging of Extended Absorbers in Attenuating Acoustic Media

4.1. Introduction

In photo-acoustic imaging, optical energy absorption causes thermo-elastic expansion of the tissue, which leads to the propagation of a pressure wave. This signal is measured by transducers distributed on the boundary of the object, which in turn is used for imaging optical properties of the object. The major contribution of photo-acoustic imaging is to provide images of optical contrasts (based on the optical absorption) with the resolution of ultrasound [**135**].

If the medium is acoustically homogeneous and has the same acoustic properties as the free space, then the boundary of the object plays no role and the optical properties of the medium can be extracted from measurements of the pressure wave by inverting a spherical Radon transform [**96**].

A first challenging problem in photo-acoustic imaging is to take into account the issue of modelling the acoustic attenuation and its compensation. This subject is addressed in [**113, 45, 110, 92, 94, 104, 124, 126**]. The reader is in particular referred to [**93**] for a very nice discussion on the attenuation models and their causality properties.

Moreover, in some settings, free space assumptions does not hold. For example, in brain imaging, the skull plays an important acoustic role, and in small animal imaging devices, the metallic chamber may have a strong acoustic effect. In those cases, one has to account for boundary conditions. If a boundary condition has to be imposed on the pressure field, then an explicit inversion formula no longer exists. However, using a quite simple duality approach, one can still reconstruct the optical absorption coefficient. In fact, in Chapters 1 and 2, we have investigated quantitative photoacoustic imaging in the case of a bounded medium with imposed boundary conditions. In Chapter 3, we proposed a geometric-control approach to deal with the case of limited view measurements. In both cases, we focused on a situation with small optical absorbers in a non-absorbing background and proposed adapted algorithms to locate the absorbers and estimate their absorbed energy.

In this chapter, we propose a new approach to image extended optical sources from photo-acoustic data and to correct the effect of acoustic attenuation. By testing our measurements against an appropriate family of functions, we show that we can access the Radon transform of the initial condition, and thus recover quantitatively any initial condition for the photoacoustic problem. We also show how to compensate the effect of acoustic attenuation on image quality by using the stationary phase theorem. We use a frequency power-law model for the attenuation losses.

The chapter is organized as follows. In Section 4.2 we consider the photo-acoustic imaging problem in free space. We first propose three algorithms to recover the absorbing energy density from limited-view and compare their speeds of convergence. We then present two approaches to correct the effect of acoustic attenuation. We use a power-law model for the attenuation. We test the singular value decomposition approach proposed in [**113**] and provide a new a technique based on the stationary phase theorem. Section 4.3 is devoted to correct the effect of imposed boundary conditions. By testing our measurements against an appropriate family of functions, we show how to obtain the Radon transform of the initial condition in the acoustic wave equation, and thus recover quantitatively the absorbing energy density. We also show how to compensate the effect of acoustic attenuation on image quality by using again the stationary phase theorem. The chapter ends with a discussion.

4.2. Photo-Acoustic Imaging in Free Space

In this section, we first formulate the imaging problem in free space and present a simulation for the reconstruction of the absorbing energy density using the spherical Radon transform. Then, we provide a total variation regularization to find a satisfactory solution of the imaging problem with limited-view data. Finally, we present algorithms for compensating the effect of acoustic attenuation. The main idea is to express the effect of attenuation as a convolution operator. Attenuation correction is then achieved by inverting this operator. Two strategies are used for such deconvolution. The first one is based on the singular value decomposition of the operator and the second one uses its asymptotic expansion based on the stationary phase theorem. We compare the performances of the two approaches.

4.2.1. Mathematical Formulation. We consider the wave equation in $\mathbb{R}^d$,

$$\frac{1}{c_0^2}\frac{\partial^2 p}{\partial t^2}(x,t) - \Delta p(x,t) = 0 \quad \text{in } \mathbb{R}^d \times (0,T),$$

with

$$p(x,0) = p_0 \quad \text{and} \quad \frac{\partial p}{\partial t}(x,0) = 0.$$

Here c_0 is the phase velocity in a non-attenuating medium.

Assume that the support of p_0, the absorbing energy density, is contained in a bounded set Ω of $\mathbb{R}^d$. Our objective in this part is to reconstruct p_0 from the measurements $g(y,t) = p(y,t)$ on $\partial\Omega \times (0,T)$, where $\partial\Omega$ denotes the boundary of Ω.

The problem of reconstructing p_0 is related to the inversion of the spherical Radon transform given by

$$\mathcal{R}_\Omega[f](y,r) = \int_S r f(y + r\xi)\, d\sigma(\xi), \quad (y,r) \in \partial\Omega \times \mathbb{R}^+,$$

where S denotes the unit sphere. It is known that in dimension 2, Kirchhoff's formula implies that [**70**]

$$\begin{cases} p(y,t) = \dfrac{1}{2\pi}\partial_t \displaystyle\int_0^t \frac{\mathcal{R}_\Omega[p_0](y, c_0 r)}{\sqrt{t^2 - r^2}}\, dr, \\ \mathcal{R}_\Omega[p_0](y,r) = 4r \displaystyle\int_0^r \frac{p(y, t/c_0)}{\sqrt{r^2 - t^2}}\, dt. \end{cases}$$

Let the operator $\mathcal{W}$ be defined by

$$\mathcal{W}[g](y,r) = 4r \int_0^r \frac{g(y,t/c_0)}{\sqrt{r^2-t^2}}\,dt \quad \text{for all } g : \partial\Omega \times \mathbb{R}^+ \to \mathbb{R}. \tag{4.1}$$

Then, it follows that

$$\mathcal{R}_\Omega[p_0](y,r) = \mathcal{W}[p](y,r). \tag{4.2}$$

In recent works, a large class of inversion retroprojection formulae for the spherical Radon transform have been obtained in even and odd dimensions when Ω is a ball, see for instance [**70, 97, 69, 108**]. In dimension 2 when Ω is the unit disk, it turns out that

$$p_0(x) = \frac{1}{(4\pi^2)} \int_{\partial\Omega} \int_0^2 \left[\frac{d^2}{dr^2}\mathcal{R}_\Omega[p_0](y,r)\right] \ln|r^2-(y-x)^2|\,dr\,d\sigma(y). \tag{4.3}$$

This formula can be rewritten as follows:

$$p_0(x) = \frac{1}{4\pi^2}\mathcal{R}_\Omega^*\mathcal{B}\mathcal{R}_\Omega[p_0](x), \tag{4.4}$$

where $\mathcal{R}_\Omega^*$ is the adjoint of $\mathcal{R}_\Omega$,

$$\mathcal{R}_\Omega^*[g](x) = \int_{\partial\Omega} g(y,|y-x|)\,d\sigma(y),$$

and $\mathcal{B}$ is defined by

$$\mathcal{B}[g](x,t) = \int_0^2 \frac{d^2 g}{dr^2}(y,r)\ln(|r^2-t^2|)\,dr$$

for $g : \Omega \times \mathbb{R}^+ \to \mathbb{R}$.

In Figure 4.1, we give a numerical illustration for the reconstruction of p_0 using the spherical Radon transform. We adopt the same approach as in [**69**] for the discretization of formulae (4.1) and (4.3). Note that in the numerical examples presented in this section, N_θ denotes the number of equally spaced angles on $\partial\Omega$, the pressure signals are uniformly sampled at N time steps, and the phantom (the initial pressure distribution p_0) is sampled on a uniform Cartesian grid with $N_R \times N_R$ points.

4.2.2. Limited-View Data. In many situations, we have only at our disposal data on $\Gamma \times (0,T)$, where $\Gamma \subset \partial\Omega$. As illustrated in Figure 4.2, restricting the integration in formula (4.3) to Γ as follows:

$$p_0(x) \simeq \frac{1}{(4\pi^2)} \int_{\Gamma} \int_0^2 \left[\frac{d^2}{dr^2}\mathcal{R}_\Omega[p_0](y,r)\right] \ln|r^2-(y-x)^2|\,dr\,d\sigma(y), \tag{4.5}$$

is not stable enough to give a correct reconstruction of p_0.

The inverse problem becomes severely ill-posed and needs to be regularized (see for instance [**134, 79**]). We apply here a Tikhonov regularization with a total variation term, which is well adapted to the reconstruction of smooth solutions with front discontinuities. We then introduce the function $p_{0,\eta}$ as the minimizer of

$$J[f] = \frac{1}{2}\|Q\left[\mathcal{R}_\Omega[f]-g\right]\|^2_{L^2(\partial\Omega\times(0,2))} + \eta\|\nabla f\|_{L^1(\Omega)},$$

where Q is a positive weight operator.

Direct computation of $p_{0,\eta}$ can be complicated as the TV term is not smooth (not of class $\mathcal{C}^1$). Here, we obtain an approximation of $p_{0,\eta}$ via an iterative

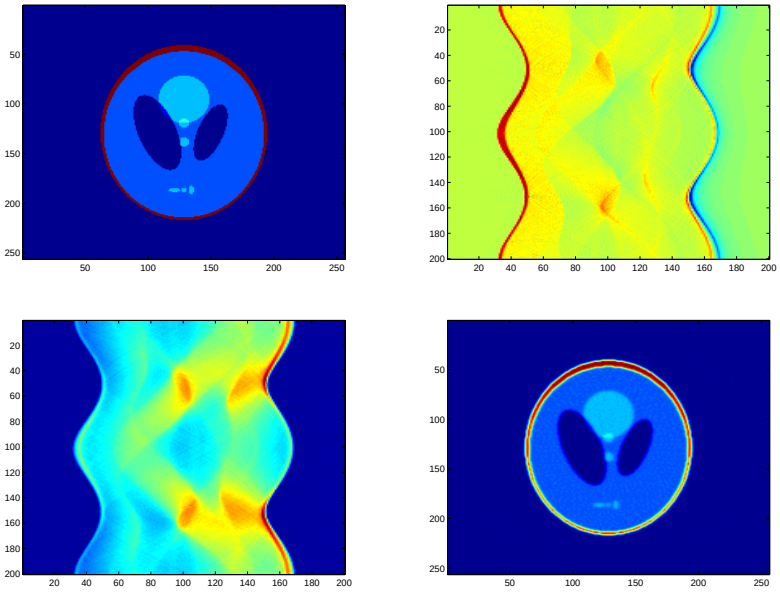

FIGURE 4.1. Numerical inversion using (4.3) with $N = 256$, $N_R = 200$ and $N_\theta = 200$. Top left: p_0 ; Top right: $p(y,t)$ with $(y,t) \in \partial\Omega \times (0,2)$; Bottom left: $\mathcal{R}_\Omega[p_0](y,t)$ with $(y,t) \in \partial\Omega \times (0,2)$; Bottom right: $\frac{1}{4\pi^2}\mathcal{R}_\Omega^*\mathcal{B}\mathcal{R}_\Omega[p_0]$.

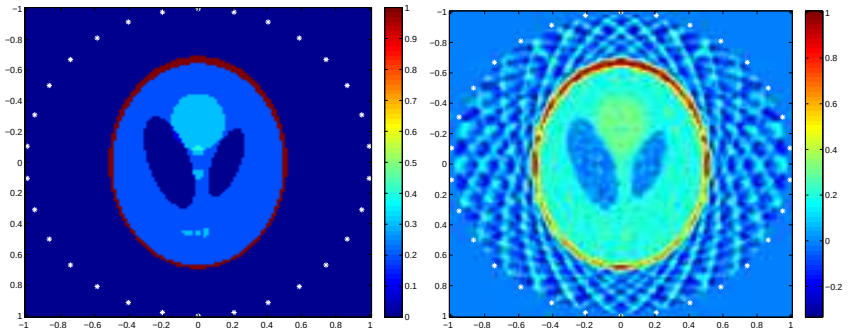

FIGURE 4.2. Numerical inversion with truncated (4.3) formula with $N = 128$, $N_R = 128$, and $N_\theta = 30$. Left: p_0; Right: $\frac{1}{4\pi^2}\mathcal{R}_\Omega^*\mathcal{B}\mathcal{R}_\Omega[p_0]$.

shrinkage-thresholding algorithm [**60, 55**]. This algorithm can be viewed as a split, gradient-descent, iterative scheme:

- Data g, initial solution $f_0 = 0$;
- *(1) Data link step:* $f_{k+1/2} = f_k - \gamma\mathcal{R}_\Omega^* Q^* Q\left[\mathcal{R}_\Omega[f_k] - g\right]$;
- *(2) Regularization step:* $f_k = T_{\gamma\eta}[f_{k+1/2}]$,

where γ is a virtual descent time step and the operator T_η is given by

$$T_\eta[y] = \arg\min_x \left\{ \frac{1}{2}\|y-x\|_{L^2}^2 + \eta\|\nabla x\|_{L^1} \right\}.$$

Note that T_η defines a proximal point method. One advantage of the algorithm is to minimize implicitly the TV term using the duality algorithm of Chambolle [**49**]. This algorithm converges [**60, 55**] under the assumption $\gamma\|\mathcal{R}_\Omega^* Q^* Q \mathcal{R}_\Omega\| \leq 1$, but its rate of convergence is known to be slow. Thus, in order to accelerate the convergence rate, we will also consider the variant algorithm of Beck and Teboulle [**29**] defined as

- Data g, initial set: $f_0 = x_0 = 0$, $t_1 = 1$;
- *(1)* $x_k = T_{\gamma\eta}\left(f_k - \gamma\mathcal{R}_\Omega^* Q^* Q\left[\mathcal{R}_\Omega[f_k] - g\right]\right)$;
- *(2)* $f_{k+1} = x_k + \frac{t_k - 1}{t_{k+1}}(x_k - x_{k-1})$ with $t_{k+1} + \frac{1+\sqrt{1+4t_k^2}}{2}$.

The standard choice of Q is the identity, Id, and then it is easy to see that $\|R_\Omega R_\Omega^*\| \simeq 2\pi$. It will also be interesting to use $Q = \frac{1}{2\pi}\mathcal{B}^{1/2}$, which is well defined since $\mathcal{B}$ is symmetric and positive. In this case, $\mathcal{R}_\Omega^* Q^* Q \simeq \mathcal{R}_\Omega^{-1}$ and we can hope to improve the convergence rate of the regularized algorithm.

We compare three algorithms of this kind in Figure 4.3. The first and the second one correspond to the simplest algorithm with respectively $Q = \mathrm{Id}$ and $Q = \frac{1}{2\pi}\mathcal{B}^{1/2}$. The last method uses the variant of Beck and Teboulle with $Q = \frac{1}{2\pi}\mathcal{B}^{1/2}$. The speed of convergence of each of these algorithms is plotted in Figure 4.3. Clearly, the third method is the best and after 30 iterations, a very good approximation of p_0 is reconstructed.

Two limited-angle experiments are presented in Figure 4.4 using the third algorithm.

4.2.3. Compensation of the Effect of Acoustic Attenuation. Our aim in this section is to compensate for the effect of acoustic attenuation. The pressures $p(x,t)$ and $p_a(x,t)$ are respectively solutions of the following wave equations:

$$\frac{1}{c_0^2}\frac{\partial^2 p}{\partial t^2}(x,t) - \Delta p(x,t) = \frac{1}{c_0^2}\delta'_{t=0} p_0(x),$$

and

$$\frac{1}{c_0^2}\frac{\partial^2 p_a}{\partial t^2}(x,t) - \Delta p_a(x,t) - L(t) * p_a(x,t) = \frac{1}{c_0^2}\,\delta'_{t=0} p_0(x),$$

where L is defined by

$$L(t) = \frac{1}{\sqrt{2\pi}}\int_{\mathbb{R}} \left(K^2(\omega) - \frac{\omega^2}{c_0^2} \right) e^{i\omega t} d\omega. \tag{4.6}$$

Many models exist for $K(\omega)$. Here we use the power-law model. Then $K(\omega)$ is the complex wave number, defined by

$$K(\omega) = \frac{\omega}{c(\omega)} + ia|\omega|^\zeta, \tag{4.7}$$

where ω is the frequency, $c(\omega)$ is the frequency dependent phase velocity and $1 \leq \zeta \leq 2$ is the power of the attenuation coefficient. See [**125**]. A common model, known as the thermo-viscous model, is given by $K(\omega) = \frac{\omega}{c_0\sqrt{1 - ia\omega c_0}}$ and corresponds approximately to $\zeta = 2$ with $c(\omega) = c_0$.

Our strategy is now to:

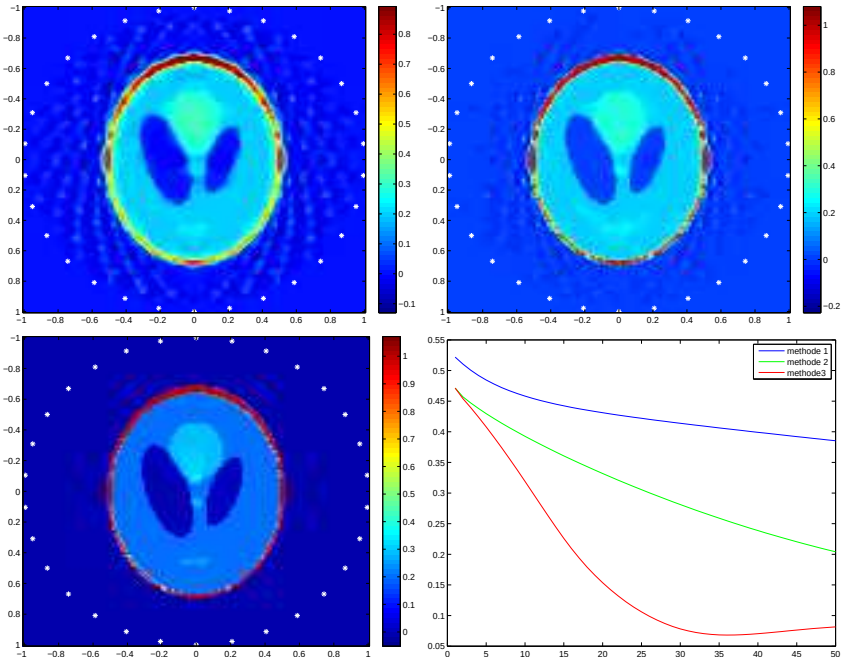

FIGURE 4.3. Iterative shrinkage-thresholding solution after 30 iterations with $\eta = 0.01$, $N = 128$, $N_R = 128$, and $N_\theta = 30$. Top left: simplest algorithm with $Q = \mathrm{Id}$ and $\mu = 1/(2\pi)$; Top right: simplest algorithm with $Q = \frac{1}{2\pi}\mathcal{B}^{1/2}$ and $\mu = 0.5$; Bottom left: Beck and Teboulle variant with $Q = \frac{1}{2\pi}\mathcal{B}^{1/2}$ and $\mu = 0.5$; Bottom right: error $k \to \|f_k - p_0\|_\infty$ for each of the previous situations.

Test 1:

Test 2:

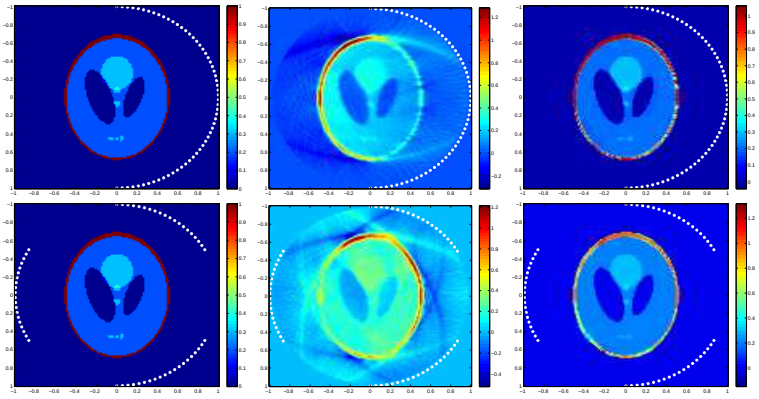

FIGURE 4.4. Case of limited angle with Beck and Teboulle iterative shrinkage-thresholding after 50 iterations, with parameters equal to $\eta = 0.01$, $N = 128$, $N_R = 128$, $N_\theta = 64$ and $Q = \frac{1}{2\pi}\mathcal{B}^{1/2}$. Left: p_0; Center: $\frac{1}{4\pi^2}\mathcal{R}_\Omega^*\mathcal{B}\mathcal{R}_\Omega[p_0]$; Right: f_{50}.

- Estimate $p(y,t)$ from $p_a(y,t)$ for all $(y,t) \in \partial\Omega \times \mathbb{R}^+$.
- Apply the inverse formula for the spherical Radon transform to reconstruct p_0 from the non-attenuated data.

A natural definition of an attenuated spherical Radon transform $\mathcal{R}_{a,\Omega}$ is

$$\mathcal{R}_{a,\Omega}[p_0] = \mathcal{W}[p_a]. \tag{4.8}$$

4.2.4. Relationship Between p and p_a. Recall that the Fourier transforms of p and p_a satisfy

$$\left(\Delta + (\frac{\omega}{c_0})^2\right)\hat{p}(x,\omega) = \frac{i\omega}{\sqrt{2\pi}c_0^2}p_0(x) \quad \text{and} \quad \left(\Delta + K(\omega)^2\right)\hat{p_a}(x,\omega) = \frac{i\omega}{\sqrt{2\pi}c_0^2}p_0(x),$$

which implies that

$$\hat{p}(x, c_0K(\omega)) = \frac{c_0K(\omega)}{\omega}\hat{p}_a(x,\omega).$$

The issue is to estimate p from p_a using the relationship $p_a = \mathcal{L}[p]$, where $\mathcal{L}$ is defined by

$$\mathcal{L}[\phi](s) = \frac{1}{2\pi}\int_{\mathbb{R}} \frac{\omega}{c_0K(\omega)}e^{-i\omega s}\int_0^\infty \phi(t)e^{ic_0K(\omega)t}\,dt\,d\omega.$$

The main difficulty is that $\mathcal{L}$ is not well conditioned. We will compare two approaches. The first one uses a regularized inverse of $\mathcal{L}$ via a singular value decomposition (SVD), which has been recently introduced in [**113**]. The second one is based on the asymptotic behavior of $\mathcal{L}$ as the attenuation coefficient a tends to zero.

Figure 4.5 gives some numerical illustrations of the inversion of the attenuated spherical Radon transform without a correction of the attenuation effect, where a thermo-viscous attenuation model is used with $c_0 = 1$.

4.2.5. A SVD Approach. La Rivière, Zhang, and Anastasio have recently proposed in [**113**] to use a regularized inverse of the operator $\mathcal{L}$ obtained by a standard SVD approach:

$$\mathcal{L}[\phi] = \sum_l \sigma_l \langle \phi, \tilde{\psi_l}\rangle \psi_l,$$

where $(\tilde{\psi_l})$ and (ψ_l) are two orthonormal bases of $L^2(0,T)$ and σ_l are positives eigenvalues such that

$$\begin{cases} \mathcal{L}^*[\phi] & = \sum_l \sigma_l \langle \phi, \psi_l\rangle \tilde{\psi_l}, \\ \mathcal{L}^*\mathcal{L}[\phi] & = \sum_l \sigma_l^2 \langle \phi, \tilde{\psi_l}\rangle \tilde{\psi_l}, \\ \mathcal{L}\mathcal{L}^*[\phi] & = \sum_l \sigma_l^2 \langle \phi, \psi_l\rangle \psi_l. \end{cases}$$

An ϵ-approximation inverse of $\mathcal{L}$ is then given by

$$\mathcal{L}^{-1}_{1,\epsilon}[\phi] = \sum_l \frac{\sigma_l}{\sigma_l^2 + \epsilon^2}\langle \phi, \psi_l\rangle \tilde{\psi_l},$$

where $\epsilon > 0$.

In Figure 4.6 we present some numerical inversions of the thermo-viscous wave equation with $a = 0.0005$ and $a = 0.0025$. We first obtain the ideal measurements from the attenuated ones and then apply the inverse formula for the spherical Radon transform to reconstruct p_0 from the ideal data. We take ϵ respectively equal to 0.01, 0.001 and 0.0001. The operator $\mathcal{L}$ is discretized to obtain an $N_R \times N_R$ matrix

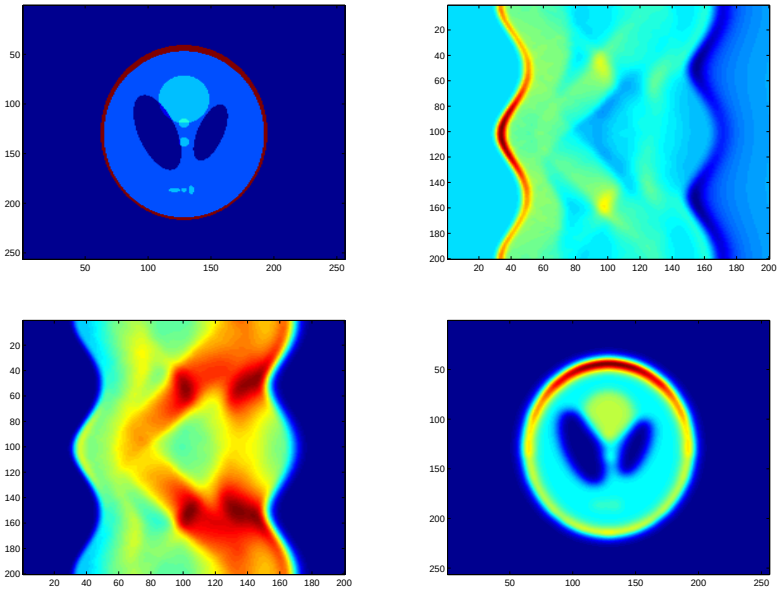

FIGURE 4.5. Numerical inversion of attenuated wave equation with $K(\omega) = \frac{\omega}{c_0} + ia\omega^2/2$ and $a = 0.001$. Here $N = 256$, $N_R = 200$ and $N_\theta = 200$. Top left: p_0; Top right: $p_a(y,t)$ with $(y,t) \in \partial\Omega \times (0,2)$; Bottom left: $\mathcal{W}p_a(y,t)$ with $(y,t) \in \partial\Omega \times (0,2)$; Bottom right: $\frac{1}{4\pi^2}\mathcal{R}_\Omega^* \mathcal{B}\left(\mathcal{W}[p_a](y,t)\right)$.

to which we apply an SVD decomposition. A regularization of the SVD allows us to construct $\mathcal{L}_{1,\epsilon}^{-1}$.

As expected, this algorithm corrects a part of the attenuation effect but is unstable when ϵ tends to zero.

4.2.6. Asymptotics of $\mathcal{L}$. In physical situations, the coefficient of attenuation a is very small. We will take into account this phenomenon and introduce an approximation of $\mathcal{L}$ and $\mathcal{L}^{-1}$ as a goes to zero:

$$\mathcal{L}_k[\phi] = \mathcal{L}[\phi] + o(a^{k+1}) \quad \text{and} \quad \mathcal{L}_{2,k}^{-1}[\phi] = \mathcal{L}^{-1}[\phi] + o(a^{k+1}),$$

where k represents an order of approximation.

4.2.6.1. *Thermo-viscous case:* $K(\omega) = \frac{\omega}{c_0} + ia\omega^2/2$. Let us consider in this section the attenuation model $K(\omega) = \frac{\omega}{c_0} + ia\omega^2/2$ at low frequencies $\omega \ll \frac{1}{a}$, such that

$$\frac{1}{1 + iac_0\omega/2} \simeq 1 - i\frac{ac_0}{2}\omega.$$

The operator $\mathcal{L}$ is approximated as follows

$$\mathcal{L}[\phi](s) \simeq \frac{1}{2\pi}\int_0^\infty \phi(t) \int_{\mathbb{R}} \left(1 - i\frac{ac_0}{2}\omega\right) e^{-\frac{1}{2}c_0 a\omega^2 t} e^{i\omega(t-s)}\, d\omega\, dt.$$

Since

$$\frac{1}{\sqrt{2\pi}}\int_{\mathbb{R}} e^{-\frac{1}{2}c_0 a\omega^2 t} e^{i\omega(t-s)} d\omega = \frac{1}{\sqrt{c_0 at}} e^{-\frac{1}{2}\frac{(s-t)^2}{c_0 at}},$$

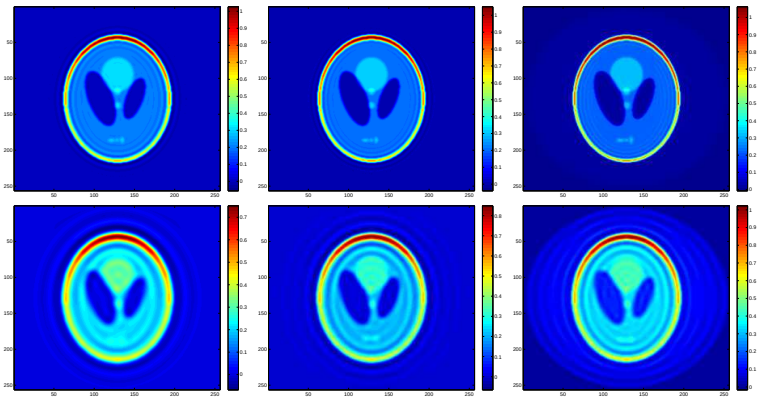

FIGURE 4.6. Compensation of acoustic attenuation with SVD regularization: $N = 256$, $N_R = 200$ and $N_\theta = 200$. First line: $a = 0.0005$; second line: $a = 0.0025$. Left to right: using $\mathcal{L}_{1,\epsilon}^{-1}$ respectively with $\epsilon = 0.01$, $\epsilon = 0.001$ and $\epsilon = 0.0001$.

and

$$\frac{1}{\sqrt{2\pi}} \int_{\mathbb{R}} \frac{-iac_0\omega}{2} e^{-\frac{1}{2}c_0 a\omega^2 t} e^{i\omega(t-s)} d\omega = \frac{ac_0}{2}\partial_s \left(\frac{1}{\sqrt{c_0 at}} e^{-\frac{1}{2}\frac{(s-t)^2}{c_0 at}} \right),$$

it follows that

$$\mathcal{L}[\phi] \simeq \left(1 + \frac{ac_0}{2}\partial_s\right) \left(\frac{1}{\sqrt{2\pi}} \int_0^{+\infty} \phi(t) \frac{1}{\sqrt{c_0 at}} e^{-\frac{1}{2}\frac{(s-t)^2}{c_0 at}} dt \right).$$

We then investigate the asymptotic behavior of $\tilde{\mathcal{L}}$ defined by

$$\tilde{\mathcal{L}}[\phi] = \frac{1}{\sqrt{2\pi}} \int_0^{+\infty} \phi(t) \frac{1}{\sqrt{c_0 at}} e^{-\frac{1}{2}\frac{(s-t)^2}{c_0 at}} dt. \tag{4.9}$$

Since the phase in (4.9) is quadratic and a is small, by the stationary phase theorem we can prove that

$$\tilde{\mathcal{L}}[\phi](s) = \sum_{i=0}^{k} \frac{(c_0 a)^i}{2^i i!} D_i[\phi](s) + o(a^k), \tag{4.10}$$

where the differential operators D_i satisfy $D_i[\phi](s) = (t^i \phi(t))^{(2i)}(s)$. See Appendix B. We can also deduce the following approximation of order k of $\tilde{\mathcal{L}}^{-1}$

$$\tilde{\mathcal{L}}_k^{-1}[\psi] = \sum_{j=0}^{k} a^j \psi_{k,j}, \tag{4.11}$$

where $\psi_{k,j}$ are defined recursively by

$$\psi_{k,0} = \psi \quad \text{and} \quad \psi_{k,j} = -\sum_{i=1}^{j} \frac{1}{i!} D_i[\psi_{k,j-i}], \text{ for all } j \leq k.$$

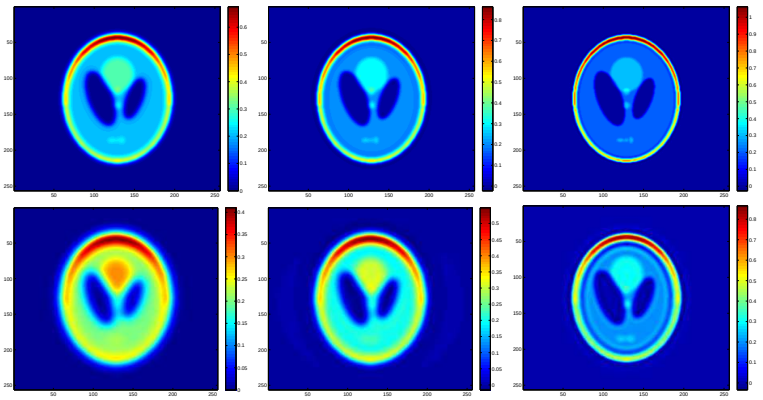

FIGURE 4.7. Compensation of acoustic attenuation with formula (4.12): $N = 256$, $N_R = 200$ and $N_\theta = 200$. First line: $a = 0.0005$; second line: $a = 0.0025$. Left: $\tilde{\mathcal{L}}_k^{-1}$ with $k = 0$; Center: $\tilde{\mathcal{L}}_k^{-1}$ with $k = 1$; Right: $\tilde{\mathcal{L}}_k^{-1}$ with $k = 8$.

Finally, we define

$$\mathcal{L}_k = \left(1 + \frac{ac_0}{2}\partial_s\right)\tilde{\mathcal{L}}_k \quad \text{and} \quad \mathcal{L}_{2,k}^{-1} = \tilde{\mathcal{L}}_k^{-1}\left(1 + \frac{ac_0}{2}\partial_t\right)^{-1}. \tag{4.12}$$

We plot in Figure 4.6 some numerical reconstructions of p_0 using a thermo-viscous wave equation with $a = 0.0005$ and $a = 0.0025$. We take the value of k respectively equal to $k = 0$, $k = 1$ and $k = 8$. These reconstructions seem to be as good as those obtained by the SVD regularization approach. Moreover, this new algorithm has better stability properties.

4.2.6.2. *General case:* $K(\omega) = \omega + ia|\omega|^\zeta$ *with* $1 \leq \zeta < 2$. We now consider the attenuation model $K(\omega) = \frac{\omega}{c_0} + ia|\omega|^\zeta$ with $1 \leq \zeta < 2$. We first note that this model is not causal but can be changed to a causal one [**93, 52**]. However, since our main purpose here is to give insights for the compensation of the effect of attenuation on image reconstruction, we work with this quite general model because of its simplicity. As before, the problem can be reduced to the approximation of the operator $\tilde{\mathcal{L}}$ defined by

$$\tilde{\mathcal{L}}[\phi](s) = \int_0^\infty \phi(t) \int_{\mathbb{R}} e^{i\omega(t-s)} e^{-|\omega|^\zeta c_0 a t}\, d\omega dt.$$

It is also interesting to see that its adjoint $\tilde{\mathcal{L}}^*$ satisfies

$$\tilde{\mathcal{L}}^*[\phi](s) = \int_0^\infty \phi(t) \int_{\mathbb{R}} e^{i\omega(s-t)} e^{-|\omega|^\zeta c_0 a s}\, d\omega dt.$$

Suppose for the moment that $\zeta = 1$, and working with the adjoint operator $\mathcal{L}^*$, we see that

$$\tilde{\mathcal{L}}^*[\phi](s) = \frac{1}{\pi}\int_0^\infty \frac{c_0 a s}{(c_0 a s)^2 + (s-t)^2}\phi(t)dt.$$

Invoking the dominated convergence theorem, we have

$$\lim_{a\to 0} \tilde{\mathcal{L}}^*[\phi](s) = \lim_{a\to 0} \frac{1}{\pi}\int_{-\frac{1}{ac_0}}^\infty \frac{1}{1+y^2}\phi(s + c_0 a y s)dy = \frac{1}{\pi}\int_{-\infty}^\infty \frac{1}{1+y^2}\phi(s)dy = \phi(s).$$

More precisely, introducing the fractional Laplacian $\Delta^{1/2}$ as follows

$$\Delta^{1/2}\phi(s) = \frac{1}{\pi}\,\text{p.v.}\int_{-\infty}^{+\infty}\frac{\phi(t)-\phi(s)}{(t-s)^2}\,dt,$$

where p.v. stands for the Cauchy principal value, we get

$$\begin{aligned}
\frac{1}{a}\big(\tilde{\mathcal{L}}^*[\phi](s)-\phi(s)\big) &= \frac{1}{a}\int_{-\infty}^{\infty}\frac{1}{\pi c_0 a s}\frac{1}{1+\left(\frac{s-t}{c_0 a s}\right)^2}\left(\phi(t)-\phi(s)\right)dt\\
&= \int_{-\infty}^{\infty}\frac{1}{\pi}\frac{c_0 s}{(c_0 a s)^2+(s-t)^2}\left(\phi(t)-\phi(s)\right)dt\\
&= \lim_{\epsilon\to 0}\int_{\mathbb{R}\setminus[s-\epsilon,s+\epsilon]}\frac{1}{\pi}\frac{c_0 s}{(c_0 a s)^2+(s-t)^2}\left(\phi(t)-\phi(s)\right)dt\\
&\to \lim_{\epsilon\to 0}\int_{\mathbb{R}\setminus[s-\epsilon,s+\epsilon]}\frac{1}{\pi}\frac{c_0 s}{(s-t)^2}\left(\phi(t)-\phi(s)\right)dt\\
&= c_0 s\Delta^{1/2}\phi(s),
\end{aligned}$$

as a tends to zero. We therefore deduce that

$$\tilde{\mathcal{L}}^*[\phi](s)=\phi(s)+c_0 a s\Delta^{1/2}\phi(s)+o(a)\quad\text{ and }\quad\tilde{\mathcal{L}}^*[\phi](s)=\phi(s)+c_0 a\Delta^{1/2}\left(s\phi(s)\right)+o(a).$$

Applying exactly the same argument for $1<\zeta<2$, we obtain that

$$\mathcal{L}[\phi](s)=\phi(s)+Cc_0 a\Delta^{\zeta/2}(s\phi(s))+o(a),$$

where C is a constant, depending only on ζ and $\Delta^{\zeta/2}$, defined by

$$\Delta^{\zeta/2}\phi(s)=\frac{1}{\pi}\,\text{p.v.}\int_{-\infty}^{+\infty}\frac{\phi(t)-\phi(s)}{(t-s)^{1+\zeta}}\,dt.$$

4.2.7. Iterative Shrinkage-Thresholding Algorithm with Correction of Attenuation. The previous correction of attenuation is not so efficient for a large attenuation coefficient a. In this case, to improve the reconstruction, we may use again a Tikhonov regularization. Let $\mathcal{R}^{-1}_{\Omega,a,k}$ be an approximate inverse of the attenuated spherical Radon transform $\mathcal{R}_{\Omega,a}$:

$$\mathcal{R}^{-1}_{\Omega,a,k}=\mathcal{R}_{\Omega^{-1}}\mathcal{W}\mathcal{L}^{-1}_{2,k}\mathcal{W}^{-1}.$$

Although its convergence is not clear, we will now consider the following iterative shrinkage-thresholding algorithm:

- Data g, initial set: $f_0=x_0=0$, $t_1=1$;
- *(1)* $x_j=T_{\gamma\eta}\left(f_j-\gamma\mathcal{R}^{-1}_{\Omega,a,k}\left(\mathcal{R}_{\Omega,a}f_j-g\right)\right)$;
- *(2)* $f_{j+1}=x_j+\frac{t_j-1}{t_{j+1}}\left(x_j-x_{j-1}\right)\quad$ with $\quad t_{j+1}+\frac{1+\sqrt{1+4t_j^2}}{2}$.

Figure 4.8 shows the efficiency of this algorithm.

4.3. Photo-Acoustic Imaging with Imposed Boundary Conditions

In this section, we consider the case where a boundary condition has to be imposed on the pressure field. We first formulate the photo-acoustic imaging problem in a bounded domain before reviewing the reconstruction procedures. We refer the reader to [**131**] where the half-space problem has been considered. We then introduce a new algorithm which reduces the reconstruction problem to the inversion of a Radon transform. This procedure is particularly well-suited for extended

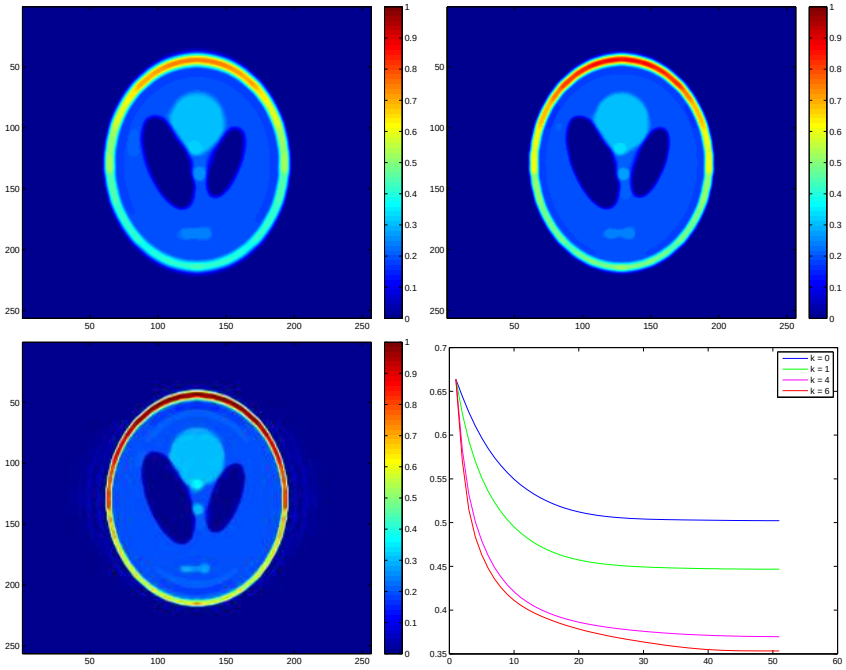

FIGURE 4.8. Numerical results using iterative shrinkage-thresholding algorithm with $\eta = 0.001$ and $a = 0.0025$. Left up: f_{50} with $k = 0$; Top right: f_{50} with $k = 1$; Bottom left: f_{50} with $k = 6$; Bottom right: error $j \to \|f_j - p_0\|$ for different values of k.

absorbers. Finally, we discuss the issue of correcting the attenuation effect and propose an algorithm analogous to the one described in the previous section.

4.3.1. Mathematical Formulation. Let Ω be a bounded domain. We consider the wave equation in the domain Ω:

$$\begin{cases} \dfrac{1}{c_0^2}\dfrac{\partial^2 p}{\partial t^2}(x,t) - \Delta p(x,t) = 0 & \text{in } \Omega \times (0,T), \\ p(x,0) = p_0(x) & \text{in } \Omega, \\ \dfrac{\partial p}{\partial t}(x,0) = 0 & \text{in } \Omega, \end{cases} \tag{4.13}$$

with the Dirichlet (resp. the Neumann) imposed boundary conditions:

$$p(x,t) = 0 \qquad \left(\text{resp. } \frac{\partial p}{\partial \nu}(x,t) = 0\right) \qquad \text{on } \partial\Omega \times (0,T). \tag{4.14}$$

Our objective in the next subsection is to reconstruct $p_0(x)$ from the measurements of $\dfrac{\partial p}{\partial \nu}(x,t)$ (resp. $p(x,t)$) on the boundary $\partial\Omega \times (0,T)$.

4.3.2. Inversion Algorithms. Consider probe functions satisfying

$$\begin{cases} \dfrac{1}{c_0^2}\dfrac{\partial^2 v}{\partial t^2}(x,t) - \Delta v(x,t) = 0 & \text{in } \Omega \times (0,T), \\ v(x,T) = 0 & \text{in } \Omega, \\ \dfrac{\partial v}{\partial t}(x,T) = 0 & \text{in } \Omega. \end{cases} \tag{4.15}$$

Multiplying (4.13) by v and integrating by parts yields (in the case of Dirichlet boundary conditions):

$$\int_0^T \int_{\partial\Omega} \frac{\partial p}{\partial \nu}(x,t) v(x,t) d\sigma(x) dt = \int_\Omega p_0(x) \frac{\partial v}{\partial t}(x,0) dx. \tag{4.16}$$

Choosing a probe function v with proper initial time derivative allows us to infer information on p_0 (right-hand side in (4.16)) from our boundary measurements (left-hand side in (4.16)).

In Chapter 1, considering a full view setting, we used a 2-parameter travelling plane wave given by

$$v^{(1)}_{\tau,\theta}(x,t) = \delta\left(\frac{x\cdot\theta}{c_0} + t - \tau\right), \tag{4.17}$$

and we determined the inclusions' characteristic functions by varying (θ,τ). We also used in three dimensions the spherical waves given by

$$w_{\tau,y}(x,t) = \frac{\delta\left(t + \tau - \frac{|x-y|}{c_0}\right)}{4\pi|x-y|}, \tag{4.18}$$

for $y \in \mathbb{R}^3 \setminus \Omega$, to probe the medium.

In Chapter 3, we assumed that measurements are only made on a part of the boundary $\Gamma \subset \partial\Omega$. Using geometric control, we could choose the form of $\dfrac{\partial v}{\partial t}(x,0)$ and design a probe function v satisfying (4.15) together with

$$v(x,t) = 0 \qquad \text{on } \partial\Omega\backslash\bar{\Gamma},$$

so that we had

$$\int_0^T \int_\Gamma \frac{\partial p}{\partial \nu}(x,t) v(x,t) d\sigma(x) dt = \int_\Omega p_0(x) \frac{\partial v}{\partial t}(x,0) dx. \tag{4.19}$$

Varying our choice of $\dfrac{\partial v}{\partial t}(x,0)$, we could adapt classical imaging algorithms (MUSIC, back-propagation, Kirchhoff migration, arrival-time) to the case of limited view data.

Now simply consider the 2-parameter family of probe functions:

$$v^{(2)}_{\tau,\theta}(x,t) = 1 - H\left(\frac{x\cdot\theta}{c_0} + t - \tau\right), \tag{4.20}$$

where H is the Heaviside function. The probe function $v^{(2)}_{\tau,\theta}(x,t)$ is an incoming plane wavefront. Its equivalent, still denoted by $v^{(2)}_{\tau,\theta}$, in the limited-view setting satisfies the initial conditions

$$v^{(2)}_{\tau,\theta}(x,0) = 0 \quad \text{and} \quad \frac{\partial v^{(2)}_{\tau,\theta}}{\partial t}(x,0) = \delta\left(\frac{x\cdot\theta}{c_0} - \tau\right), \tag{4.21}$$

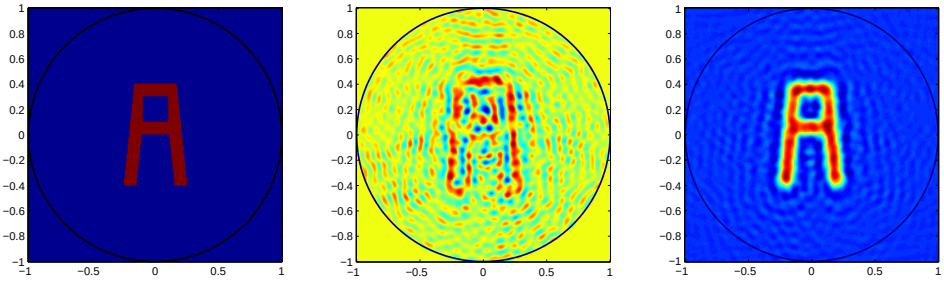

FIGURE 4.9. Reconstruction in the case of homogeneous Dirichlet boundary conditions. Left: initial condition p_0; Center: reconstruction using spherical Radon transform; Right: reconstruction using probe functions algorithm.

together with the boundary condition $v^{(2)}_{\tau,\theta} = 0$ on $\partial\Omega \setminus \Gamma \times (0,T)$.

Note that if $T \geq \frac{\mathrm{diam}(\Omega)}{c_0}$ in the full-view setting, our test functions $v^{(1)}_{\tau,\theta}$, $v^{(2)}_{\tau,\theta}$ and $w_{\tau,y}$ vanish at $t = T$. In the limited-view case, under the geometric controllability conditions [**28**] on Γ and T, existence of the test function v is guaranteed.

In both the full- and the limited-view cases, we get

$$\int_0^T \int_{\partial\Omega \text{ or } \Gamma} \frac{\partial p}{\partial \nu}(x,t) v^{(2)}_{\tau,\theta}(x,t) d\sigma(x) dt = \mathrm{R}[p_0](\theta,\tau), \tag{4.22}$$

where $\mathrm{R}[f]$ is the (line) Radon transform of f. Applying a classical filtered back-projection algorithm to the data (4.22), one can reconstruct $p_0(x)$.

To illustrate the need of this approach, we present in Figure 4.9 the reconstruction results from data with homogeneous Dirchlet boundary conditions. We compare the reconstruction using the inverse spherical Radon transform with the duality approach presented above. It appears that not taking boundary conditions into account leads to important errors in the reconstruction.

We then tested this approach on the Shepp-Logan phantom, using the family of probe functions $v^{(2)}_{\tau,\theta}$. Reconstructions are given in Figure 4.10. We notice numerical noise due to the use of discontinuous (Heaviside) test functions against discrete measurements.

The numerical tests were conducted using Matlab. Three different forward solvers have been used for the wave equation:

- a FDTD solver, with Newmark scheme for time differentiation;
- a space-Fourier solver, with Crank-Nicholson finite difference scheme in time;
- a space-(P1) FEM-time finite difference solver.

Measurements were supposed to be obtained on equi-distributed captors on a circle or a square. The use of integral transforms (line or spherical Radon transform) avoids inverse crime since such transforms are computed on a different class of parameters (center and radius for spherical Radon transforms, direction and shift for line Radon transform). Indeed, their numerical inversions (achieved using formula

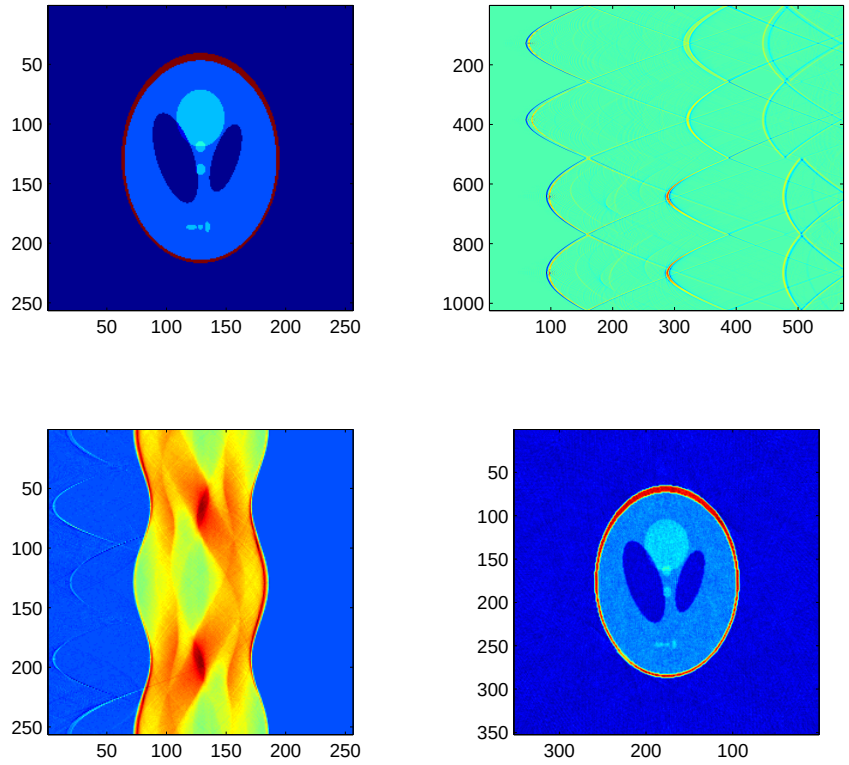

FIGURE 4.10. Numerical inversion in the case of homogeneous Dirichlet boundary conditions. Here, $N = 256$, $N_R = 200$ and $N_\theta = 200$. Top left: p_0; Top right: $p(y,t)$ with $(y,t) \in \partial\Omega \times (0,3)$; Bottom left: $\mathcal{R}[p_0]$; Bottom right: reconstruction using probe functions algorithm.

(4.3) or the iradon function of Matlab) are not computed on the same grid as the one for the forward solvers.

4.3.3. Compensation of the Effect of Acoustic Attenuation. Our aim in this section is to compensate the effect of acoustic attenuation. Let $p_a(x,t)$ be the solution of the wave equation in a dissipative medium:

(4.23)
$$\frac{1}{c_0^2}\frac{\partial^2 p_a}{\partial t^2}(x,t) - \Delta p_a(x,t) - L(t) * p_a(x,t) = \frac{1}{c_0^2}\delta'_{t=0} p_0(x) \qquad \text{in } \Omega \times \mathbb{R},$$

with the Dirichlet (resp. the Neumann) imposed boundary conditions:

(4.24)
$$p_a(x,t) = 0 \qquad \left(\text{resp. } \frac{\partial p_a}{\partial \nu}(x,t) = 0\right) \qquad \text{on } \partial\Omega \times \mathbb{R},$$

where L is defined by (4.6).

We want to recover $p_0(x)$ from boundary measurements of $\dfrac{\partial p_a}{\partial \nu}(x,t)$ (resp. $p_a(x,t)$). Again, we assume that a is small.

Taking the Fourier transform of (4.23) yields

$$\begin{cases} (\Delta + K^2(\omega))\hat{p}_a(x,\omega) = \dfrac{i\omega}{\sqrt{2\pi}c_0^2}p_0(x) \quad \text{in } \Omega, \\ \hat{p}_a(x,\omega) = 0 \qquad \left(\text{resp. } \dfrac{\partial \hat{p}_a}{\partial \nu}(x,\omega) = 0\right) \qquad \text{on } \partial\Omega, \end{cases} \tag{4.25}$$

where $\hat{p}_a$ denotes the Fourier transform of p_a.

4.3.4. Case of a Spherical Wave as a Probe Function. By multiplying (4.25) by the Fourier transform, $\hat{w}_{0,y}(x,\omega)$, of $w_{\tau=0,y}$ given by (4.18), we arrive at, for any τ,

$$\frac{i}{\sqrt{2\pi}}\int_\Omega p_0(x)\Big(\int_{\mathbb{R}} \omega e^{i\omega\tau}\hat{w}_{0,y}(x,K(\omega))\,d\omega\Big)\,dx = \int_{\mathbb{R}} e^{i\omega\tau}\int_{\partial\Omega}\frac{\partial \hat{p}_a}{\partial\nu}(x,\omega)\hat{w}_{0,y}(x,K(\omega))\,d\omega, \tag{4.26}$$

for the Dirichlet problem and

$$\frac{i}{\sqrt{2\pi}}\int_\Omega p_0(x)\Big(\int_{\mathbb{R}} \omega e^{i\omega\tau}\hat{w}_{0,y}(x,K(\omega))\,d\omega\Big)\,dx = -\int_{\mathbb{R}} e^{i\omega\tau}\int_{\partial\Omega}\hat{p}_a(x,\omega)\frac{\partial \hat{w}_{0,y}}{\partial\nu}(x,K(\omega))\,d\omega, \tag{4.27}$$

for the Neumann problem.

Next we compute $\int_{\mathbb{R}} \omega e^{i\omega\tau}\hat{w}_{0,y}(x,K(\omega))\,d\omega$ for the thermo-viscous model. Recall that in this case,

$$K(\omega) \approx \frac{\omega}{c_0} + \frac{ia\omega^2}{2}.$$

We have

$$\int_{\mathbb{R}} \omega e^{i\omega\tau}\hat{w}_{0,y}(x,K(\omega))\,d\omega \approx \frac{1}{4\pi|x-y|}\int_{\mathbb{R}} \omega e^{i\omega(\tau-\frac{|x-y|}{c_0})}e^{-a\omega^2\frac{|x-y|}{c_0}}\,d\omega, \tag{4.28}$$

and again, the stationary phase theorem can then be applied to approximate the inversion procedure for $p_0(x)$.

Note that if we use the Fourier transform $\hat{v}$ of (4.17) or (4.20) as a test function then we have to truncate the integral in (4.26) since $\hat{v}(x,K(\omega))$ is exponentially growing in some regions of Ω.

4.3.5. Case of a Plane Wave as a Probe Function. Let us first introduce the function $\tilde{K}(\omega)$ defined by $\tilde{K}(\omega) = \sqrt{\overline{K(\omega)^2}}$ and consider a solution of the Helmholtz equation

$$\left(\Delta + \tilde{K}^2(\omega)\right)\hat{v}_a(x,\omega) = 0$$

of the form

$$\hat{v}_a(x,\omega) = e^{-i\omega(x\cdot\theta - c_0\tau)}g(\omega), \tag{4.29}$$

where $g(\omega)$ decays sufficiently fast.

Multiplying (4.25) by $\overline{\hat{v}_a(x,\omega)}$, we obtain

$$\frac{i}{\sqrt{2\pi}}\int_\Omega p_0(x)\left(\int_{\mathbb{R}}\omega\overline{\hat{v}_a(x,\omega)}d\omega\right)dx = \int_{\mathbb{R}}\int_{\partial\Omega}\frac{\partial\hat{p}_a}{\partial\nu}(x,\omega)\overline{\hat{v}_a(x,\omega)}d\sigma(x)d\omega. \tag{4.30}$$

Since $\tilde{K}(\omega) \simeq \frac{\omega}{c_0} - \frac{ia\omega^2}{2}$, then by taking in formula (4.29)

$$g(\omega) = e^{-\frac{1}{2}\omega^2 a c_0 T} \quad \text{and} \quad g(\omega) = \frac{1}{i\omega} e^{-\frac{1}{2}\omega^2 a c_0 T},$$

we can use the plane waves $\hat{v}_a^{(1)}$ and $\hat{v}_a^{(2)}$ given by

$$\hat{v}_a^{(1)}(x,\omega) = e^{-i\omega(x\cdot\theta - c_0\tau)} e^{-\frac{1}{2}\omega^2 a c_0 (T + \frac{x\cdot\theta}{c_0} - \tau)},$$

and

$$\hat{v}_a^{(2)}(x,\omega) = \frac{1}{i\omega} e^{-i\omega(x\cdot\theta - c_0\tau)} e^{-\frac{1}{2}\omega^2 a c_0 (T + \frac{x\cdot\theta}{c_0} - \tau)},$$

as approximate probe functions.

Take T sufficiently large such that $\left(T + \frac{x\cdot\theta}{c_0} - \tau\right)$ stays positive for all $x \in \Omega$. Thus,

$$v_a^{(1)}(x,t) \simeq \frac{1}{\sqrt{ac_0\left(T + \frac{x\cdot\theta}{c_0} - \tau\right)}} e^{-\frac{(x\cdot\theta - c_0\tau + t)^2}{2ac_0\left(T + \frac{x\cdot\theta}{c_0} - \tau\right)}},$$

and

$$v_a^{(2)}(x,t) \simeq \operatorname{erf}\left(\frac{x\cdot\theta - c_0\tau + t}{\sqrt{ac_0\left(T + \frac{x\cdot\theta}{c_0} - \tau\right)}}\right).$$

Now using $v_a^{(2)}$in formula (4.30) leads to the convolution of the Radon transform of p_0 with a quasi-Gaussian kernel. Indeed, the left hand-side of (4.30) satisfies

$$\begin{aligned}
&\frac{i}{\sqrt{2\pi}} \int_\Omega p_0(x) \left(\int_{\mathbb{R}} \omega \overline{\hat{v}_a^{(2)}(x,w))} d\omega \right) dx \\
&\qquad \simeq \int_\Omega p_0(x) \frac{1}{\sqrt{ac_0\left(T + \frac{x\cdot\theta}{c_0} - \tau\right)}} e^{-\frac{(x\cdot\theta - c_0\tau)^2}{2ac_0\left(T + \frac{x\cdot\theta}{c_0} - \tau\right)}} dx \\
&\qquad = \int_{s_{\min}}^{s_{\max}} R[p_0](\theta,s) \frac{1}{\sqrt{ac_0\left(T + \frac{s}{c_0} - \tau\right)}} e^{-\frac{(s - c_0\tau)^2}{2ac_0\left(T + \frac{s}{c_0} - \tau\right)}} ds,
\end{aligned}$$

and the right hand-side is explicitly estimated by

$$\int_{\mathbb{R}} \int_{\partial\Omega} \frac{\partial \hat{p}_a}{\partial \nu}(x,\omega) \overline{\hat{v}_a^{(2)}(x,\omega)} d\sigma(x) d\omega \simeq \int_0^T \int_{\partial\Omega} \frac{\partial p_a}{\partial \nu}(x,t) \operatorname{erf}\left(\frac{x\cdot\theta - c_0\tau + t}{\sqrt{ac_0\left(T + \frac{x\cdot\theta}{c_0} - \tau\right)}}\right) d\sigma(x) dt.$$

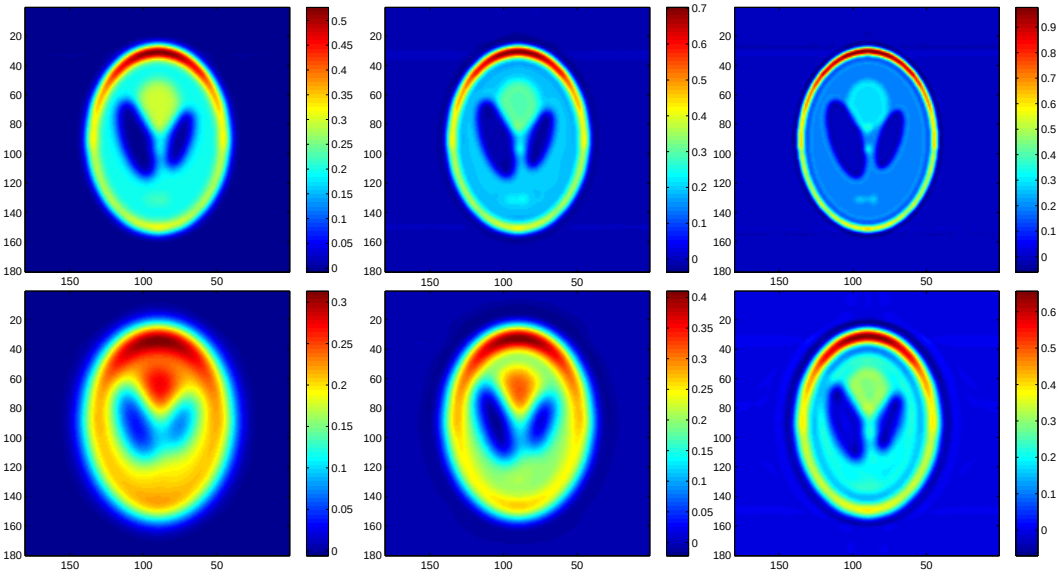

FIGURE 4.11. Compensation of acoustic attenuation with formula (4.31) in the case of homogeneous Dirichlet boundary conditions. Here, $N = 256$, $N_R = 200$ and $N_\theta = 200$. First line: $a = 0.0005$; Second line: $a = 0.0025$. Left: $\tilde{\mathcal{L}}_k^{-1}$ with $k = 0$; Center: $\tilde{\mathcal{L}}_k^{-1}$ with $k = 1$; Right: $\tilde{\mathcal{L}}_k^{-1}$ with $k = 8$.

As previously, we can compensate the effect of attenuation using the stationary phase theorem for the operator $\tilde{\mathcal{L}}$,

$$\tilde{\mathcal{L}}[\phi](\tau) = \int_{s_{\min}}^{s_{\max}} \phi(s) \frac{1}{\sqrt{ac_0\left(T + \frac{s}{c_0} - \tau\right)}} e^{-\frac{(s - c_0\tau)^2}{2ac_0\left(T + \frac{s}{c_0} - \tau\right)}} ds,$$

which reads

$$\tilde{\mathcal{L}}[\phi](\tau) \simeq \phi(c_0\tau) + \frac{ac_0T}{2}\left(\phi''(c_0\tau) + \frac{2\phi'(c_0\tau)}{c_0T}\right). \tag{4.31}$$

See Appendix C. More generally,

$$\tilde{\mathcal{L}}[\phi](\tau) = \sum_{i=0}^{k} \frac{(c_0a)^i}{2^i i!} D_i[\phi] + o(a^k), \tag{4.32}$$

where the differential operators D_i satisfy

$$D_i[\phi] = ((T + \frac{s}{c_0} - \tau)^i [\phi](s))^{(2i)}_{|_{s=c_0\tau}}.$$

Define $\tilde{\mathcal{L}}_k^{-1}$ as in (4.11). Using (4.32), we reconstructed the line Radon transform of p_0 correcting the effect of attenuation. We then applied a standard filtered back-projection algorithm to inverse the Radon transform. Results are given in Figure 4.11.

4.4. Conclusion

In this chapter we have provided new approaches to correct the effect of imposed boundary conditions as well as the effect of acoustic attenuation for imaging extended absorbers.

It would be very interesting to analytically investigate their robustness with respect to measurement noise and medium noise. In this connection, we refer to Chapter 5 for a coherent interferometric strategy for photo-acoustic imaging in the presence of microscopic random fluctuations of the speed of sound.

Another important problem is to *a priori* estimate the attenuation coefficient a and the frequency power ζ.

Finally, it is worth emphasizing that it is the absorption coefficient, not the absorbed energy, that is a fundamental physiological parameter. The absorbed energy density is in fact the product of the optical absorption coefficient and the light fluence which depends on the distribution of scattering and absorption within the domain, as well as the light sources. In Chapter 2, methods for reconstructing the normalized optical absorption coefficient of small absorbers from the absorbed density are proposed. Multi-wavelength acoustic measurements are combined with diffusing light measurements to separate the product of absorption coefficient and optical fluence. In the case of extended absorbers, multi-wavelength photo-acoustic imaging is also expected to lead to a satisfactory solution [**59**].

Stationary Phase Theorem and Proofs of (4.10) and (4.31)

Appendix A: Stationary Phase Theorem.

THEOREM 4.1. **(Stationary Phase [85])** *Let $K \subset [0,\infty)$ be a compact set, X an open neighborhood of K and k a positive integer. If $\psi \in \mathcal{C}_0^{2k}(K)$, $f \in \mathcal{C}^{3k+1}(X)$ and $Im(f) \geq 0$ in X, $Im(f(t_0)) = 0$, $f'(t_0) = 0$, $f''(t_0) \neq 0$, $f' \neq 0$ in $K \setminus \{t_0\}$ then for $\epsilon > 0$*

$$\left| \int_K \psi(t) e^{if(t)/\epsilon} dt - e^{if(t_0)/\epsilon} \left(\epsilon^{-1} f''(t_0)/2\pi i\right)^{-1/2} \sum_{j<k} \epsilon^j L_j[\psi] \right| \leq C\epsilon^k \sum_{\alpha \leq 2k} \sup |\psi^{(\alpha)}(x)|.$$

Here C is bounded when f stays in a bounded set in $\mathcal{C}^{3k+1}(X)$ and $|t-t_0|/|f'(t)|$ has a uniform bound. With,

$$g_{t_0}(t) = f(t) - f(t_0) - \frac{1}{2} f''(t_0)(t-t_0)^2,$$

which vanishes up to third order at t_0, and

$$L_j[\psi] = \sum_{\nu-\mu=j} \sum_{2\nu \geq 3\mu} i^{-j} \frac{2^{-\nu}}{\nu!\mu!} (-1)^\nu f''(t_0)^{-\nu} (g_{t_0}^\mu \psi)^{(2\nu)}(t_0).$$

We will use this theorem with $k = 2$. Note that L_1 can be expressed as the sum $L_1[\psi] = L_1^{(1)}[\psi] + L_1^{(2)}[\psi] + L_1^{(3)}[\psi]$, where $L_1^{(j)}$ is respectively associated to the couple $(\nu_j, \mu_j) = (1,0), (2,1), (3,2)$ and is identified as

$$\begin{cases} L_1^{(1)}[\psi] & = -\frac{1}{2i} f''(t_0)^{-1} \psi^{(2)}(t_0), \\ L_1^{(2)}[\psi] & = \frac{1}{2^2 2! i} f''(t_0)^{-2} (g_{t_0}\psi)^{(4)}(t_0) = \frac{1}{8i} f''(t_0)^{-2} \left(g_{t_0}^{(4)}(t_0)\psi(t_0) + 4 g_{t_0}^{(3)}(t_0)\psi'(t_0) \right), \\ L_1^{(3)}[\psi] & = \frac{-1}{2^3 2! 3! i} f''(t_0)^{-3} (g_{t_0}^2 \psi)^{(6)}(t_0) = \frac{-1}{2^3 2! 3! i} f''(t_0)^{-3} (g_{t_0}^2)^{(6)}(t_0)\psi(t_0). \end{cases}$$

Appendix B: Proof of Approximation (4.10). Let us now apply the stationary phase theorem to the operator $\tilde{\mathcal{L}}$

$$\tilde{\mathcal{L}}[\phi] = \frac{1}{\sqrt{2\pi}} \int_0^{+\infty} \phi(t) \frac{1}{\sqrt{c_0 a t}} e^{-\frac{1}{2}\frac{(s-t)^2}{c_0 a t}}\, dt.$$

Note that the integral

$$J(s) = \int_0^{\infty} \psi(t) e^{if(t)/\epsilon} dt,$$

with $\psi(t) = \frac{\phi(t)}{\sqrt{t}}$, $\epsilon = c_0 a$, $f(t) = i\frac{(t-s)^2}{2t}$, satisfies $J(s) = \sqrt{c_0 a 2\pi}\tilde{\mathcal{L}}[\phi]$. The phase f vanishes at $t = s$ and satisfies

$$f'(t) = i\frac{1}{2}\left(1 - \frac{s^2}{t^2}\right), \quad f''(t) = i\frac{s^2}{t^3}, \quad f''(s) = i\frac{1}{s}.$$

The function $g_s(t)$ is given by

$$g_s(t) = i\frac{1}{2}\frac{(t-s)^2}{t} - i\frac{1}{2}\frac{(t-s)^2}{s} = i\frac{1}{2}\frac{(s-t)^3}{ts}.$$

We can deduce that

$$\begin{cases} (g_s\psi)^{(4)}(s) &= \left(g_{x_0}^{(4)}(s)\psi(s) + 4g_{x_0}^{(3)}(s)\psi'(s)\right) = i\frac{1}{2}\left(\frac{24}{s^3}\psi(s) - \frac{24}{s^2}\psi'(s)\right), \\ (g_s^2\psi)^{(6)}(s) &= (g_{x_0}^2)^{(6)}(s)\psi(s) = -\frac{1}{4}\frac{6!}{s^4}\psi(s), \end{cases}$$

and then, with the same notation as in Theorem 4.1,

$$\begin{cases} L_1^{(1)}[\psi] = -\frac{1}{i}\left(\frac{1}{2}(f''(s))^{-1}\psi''(s)\right) = \frac{1}{2}s\left(\frac{\phi}{\sqrt{s}}\right)'' = \frac{1}{2}\left(\sqrt{s}\phi''(s) - \frac{\phi'(s)}{\sqrt{s}} + \frac{3}{4}\frac{\phi}{s^{3/2}}\right), \\ L_1^{(2)}[\psi] = \frac{1}{8i}f''(s)^{-2}\left(g_s^{(4)}(s)\psi(s) + 4g_s^{(3)}(s)\psi'(s)\right) = \frac{1}{2}\left(3\left(\frac{\phi(s)}{\sqrt{s}}\right)' - 3\frac{\phi(s)}{s^{3/2}}\right) \\ \qquad\qquad = \frac{1}{2}\left(3\frac{\phi'(s)}{\sqrt{s}} - \frac{9}{2}\frac{\phi(s)}{s^{3/2}}\right), \\ L_1^{(3)}[\psi] = \frac{-1}{2^3 2! 3! i}f''(s)^{-3}(g_s^2)^{(6)}(s)\psi(s) = \frac{1}{2}\left(\frac{15}{4}\frac{\phi(s)}{s^{3/2}}\right). \end{cases}$$

The operator L_1 is given by

$$\begin{aligned} L_1[\psi] &= L_1^{(1)}[\psi] + L_1^{(2)}[\psi] + L_1^{(3)}[\psi] \\ &= \frac{1}{2}\left(\sqrt{s}\phi''(s) + (3-1)\frac{\phi'(s)}{\sqrt{s}} + \left(\frac{3}{4} - \frac{9}{2} + \frac{15}{4}\right)\frac{\phi(s)}{s^{3/2}}\right) = \frac{1}{2\sqrt{s}}\left(s\phi(s)\right)'', \end{aligned}$$

and so,

$$\left| J(s) - \sqrt{2\pi a c_0 s}\left(\frac{\phi(s)}{\sqrt{s}} + a\frac{1}{2\sqrt{s}}\left(s\phi(s)\right)''\right)\right| \leq Ca^2 \sum_{\alpha\leq 4} \sup|\phi^{(\alpha)}(x)|.$$

Finally, we arrive at

$$\left|\frac{1}{\sqrt{2\pi}}\int_0^{\infty} \phi(t)\frac{1}{\sqrt{ac_0 t}} e^{-\frac{(t-s)^2}{2ac_0 t}} dt - \left(\phi(s) + \frac{a}{2}\left(s\phi(s)\right)''\right)\right| \leq Ca^{3/2} \sum_{\alpha\leq 4} \sup|\phi^{(\alpha)}(t)|.$$

Appendix C: Proof of Approximation (4.31)**.** Let us now apply the stationary phase theorem to the operator $\mathcal{L}$ defined by

$$\begin{aligned}\tilde{\mathcal{L}}[\phi](\tau) &= \frac{1}{\sqrt{2\pi}}\int_{s_{\min}}^{s_{\max}}\left[\phi(s)\left(a\left(c_0T+s-c_0\tau\right)\right)^{-\frac{1}{2}}e^{-\frac{\left(s-c_0\tau\right)^2}{2a\left(c_0T+s-c_0\tau\right)}}\right]ds\\ &= \frac{1}{\sqrt{2\pi}}\int_{s_{\min}-c_0\tau}^{s_{\max}-c_0\tau}\left[\phi(t+c_0\tau)\left(a\left(\tilde{T}+t\right)\right)^{-\frac{1}{2}}e^{-\frac{t^2}{2a\left(\tilde{T}+t\right)}}\right]dt,\end{aligned}$$

where $\tilde{T}=c_0T$. Note that the integral

$$J(\tau)=\int_{s_{\min}-c_0\tau}^{s_{\max}-c_0\tau}\psi(t)e^{if(t)/\epsilon}dt,$$

with $\psi(t)=\frac{\phi(t+c_0\tau)}{\sqrt{\tilde{T}+t}}$, $\epsilon=a$, $f(s)=i\frac{t^2}{2\left(\tilde{T}+t\right)}$, satisfies $J(\tau)=\sqrt{a2\pi}\tilde{\mathcal{L}}[\phi]$.
The phase f vanishes at $t=0$ and satisfies

$$f'(t)=i\frac{1}{2}\frac{t(t+2\tilde{T})}{(t+\tilde{T})^2},\quad f''(t)=i\frac{\tilde{T}^2}{(t+\tilde{T})^3},\quad f''(0)=i\frac{1}{\tilde{T}}.$$

The function $g_0(t)$ is identified as

$$g_0(t)=-i\frac{1}{2}\frac{t^3}{\tilde{T}(\tilde{T}+t)}.$$

We have

$$\begin{cases}(g_0\psi)^{(4)}(0) &= \left(g_0^{(4)}(0)\psi(0)+4g_0^{(3)}(0)\psi'(0)\right)=i\frac{1}{2}\left(\frac{24}{\tilde{T}^3}\psi(0)-\frac{24}{\tilde{T}^2}\psi'(0)\right),\\ (g_0^2\psi)^{(6)}(0) &= (g_0^2)^{(6)}(0)\psi(0)=-\frac{1}{4}\frac{6!}{\tilde{T}^4}\psi(0),\end{cases}$$

and

$$\psi(0)=\frac{\phi(c_0\tau)}{\tilde{T}^{1/2}},\quad \psi'(0)=\frac{\phi'(c_0\tau)}{\tilde{T}^{1/2}}-\frac{1}{2}\frac{\phi(c_0\tau)}{\tilde{T}^{3/2}},\quad \psi''(0)=\frac{\phi''(c_0\tau)}{\tilde{T}^{1/2}}-\frac{\phi'(c_0\tau)}{\tilde{T}^{3/2}}+\frac{3}{4}\frac{\phi(c_0\tau)}{\tilde{T}^{5/2}}.$$

Therefore, again with the same notation as in Theorem 4.1,

$$\begin{cases}L_1^{(1)}[\psi]=-\frac{1}{i}\left(\frac{1}{2}(f''(0))^{-1}\psi''(0)\right)=\frac{1}{2}\left(\sqrt{\tilde{T}}\phi''(c_0\tau)-\frac{\phi'(c_0\tau)}{\tilde{T}^{1/2}}+\frac{3}{4}\frac{\phi(c_0\tau)}{\tilde{T}^{3/2}}\right),\\ L_1^{(2)}[\psi]=\frac{1}{8i}f''(0)^{-2}\left(g_0^{(4)}(0)\psi(0)+4g_0^{(3)}(0)\psi'(0)\right)=\frac{1}{2}\left(3\psi'(0)-3\frac{\psi(0)}{\tilde{T}}\right)\\ \qquad=\frac{1}{2}\left(3\frac{\phi'(c_0\tau)}{\tilde{T}^{1/2}}-\frac{9}{2}\frac{\phi(c_0\tau)}{\tilde{T}^{3/2}}\right),\\ L_1^{(3)}[\psi]=-\frac{1}{2^3 2!3!i}f''(0)^{-3}(g_0^2)^{(6)}(0)\psi(0)=\frac{1}{2}\left(\frac{15}{4}\frac{\phi(c_0\tau)}{\tilde{T}^{3/2}}\right),\end{cases}$$

and L_1 is given by

$$\begin{aligned}L_1[\psi] &= L_1^{(1)}[\psi]+L_1^{(2)}[\psi]+L_1^{(3)}[\psi]=\frac{1}{2\sqrt{\tilde{T}}}\left(\tilde{T}\phi''(c_0\tau)+2\phi'(c_0\tau)\right)\\ &= \frac{1}{2\sqrt{\tilde{T}}}\left((s-c_0\tau+\tilde{T})\phi(s)\right)''_{\lfloor s=c_0\tau},\end{aligned}$$

which yields

$$\left|J(\tau) - \sqrt{2\pi a}\left(\phi(c_0\tau) + a/2\left((s - c_0\tau + c_0T)\phi(s)\right)''_{\lfloor s=c_0\tau}\right)\right| \leq Ca^2 \sum_{\alpha\leq 4} \sup|\phi^{(\alpha)}(x)|.$$

Hence,

$$\left|\tilde{\mathcal{L}}[\phi] - \left(\phi(c_0\tau) + \frac{ac_0T}{2}\left(\phi''(c_0\tau) + \frac{2\phi'(c_0\tau)}{c_0T}\right)\right)\right| \leq Ca^{3/2} \sum_{\alpha\leq 4} \sup|\phi^{(\alpha)}(t)|.$$

CHAPTER 5

Coherent Interferometric Strategy for Photoacoustic Imaging

5.1. Introduction

In the previous chapters, we developed a variety of inversion approaches which can be extended to the case of variable but known sound speed and can correct the effect of attenuation on image reconstructions. However, the situation of interest for medical applications is the case where the sound speed is perturbed by an unknown clutter noise. This means that the speed of sound of the medium is randomly fluctuating around a known value. In this situation, waves experience partial coherence loss [**73**] and the designed algorithms assuming a constant sound speed may fail.

Interferometric methods for imaging have been considered in [**51, 120, 119**]. Coherent interferometry (CINT) was introduced and analyzed in [**39, 40**]. While classical methods back-propagate the recorded signals directly, CINT is an array imaging method that first computes cross-correlations of the recorded signals over appropriately chosen space-frequency windows and then back-propagates the local cross-correlations. As shown in [**39, 40, 41, 42**], CINT deals well with partial loss of coherence in cluttered environments.

In this chapter, combining the CINT method for imaging in clutter together with a reconstruction approach for extended targets by Radon inversions, we propose CINT-Radon algorithms for photoacoustic imaging in the presence of random fluctuations of the sound speed. We show that these new algorithms provide statistically stable photoacoustic images. We provide a detailed analysis for their stability and resolution and numerically illustrate their performance.

The chapter is organized as follows. In Section 5.2 we formulate the inverse problem of photoacoustics and describe the clutter noise considered for the sound speed. In Section 5.3 we recall the reconstruction using the circular Radon transform when the sound speed is constant and describe the original CINT algorithm. We then propose a new CINT approach which consists in pre-processing the data (in the same way as for the circular Radon inversion) before back-projecting their correlations. Section 5.4 is devoted to the stability analysis of this new algorithm. Section 5.5 adapts the results presented in Sections 5.3 and 5.4 to the case of a bounded domain. We make a parallel between the filtered back-projection of the *circular* Radon inversion in free space and of the *line* Radon inversion when we have boundary conditions. Both algorithms end with a back-projection step. We propose to back-project the correlations between the (pre-processed) data in the same way as in Section 5.3. The chapter ends with a short discussion.

5.2. Problem Formulation

In photoacoustics, a pressure wave $p(\mathbf{x},t)$ is generated by an electromagnetic energy deposit $p_0(\mathbf{x})$:

$$\begin{cases} \dfrac{\partial^2 p}{\partial t^2}(\mathbf{x},t) - c(\mathbf{x})^2 \Delta p(\mathbf{x},t) = 0, \\ p(\mathbf{x},0) = p_0(\mathbf{x}), \quad \dfrac{\partial p}{\partial t}(\mathbf{x},0) = 0. \end{cases}$$

The imaging problem is to reconstruct the initial value of the pressure p_0 from boundary measurements. Most of the reconstruction algorithms assume constant (or known) sound speed. However, in real applications, the sound speed is not perfectly known. It seems more relevant to consider that it fluctuates randomly around a known distribution. For simplicity, we will consider the model with random fluctuations around a constant:

$$\frac{1}{c(\mathbf{x})^2} = \frac{1}{c_0^2}\Big(1 + \sigma_c \mu\big(\frac{\mathbf{x}}{x_c}\big)\Big), \tag{5.1}$$

where μ is a normalized stationary random process, x_c is the correlation length of the fluctuations of c and σ_c is their relative standard deviation.

5.3. Imaging Algorithms

Consider the two-dimensional case. Define the Fourier transform by

$$\hat{f}(\omega) = \int_{\mathbb{R}} f(t) e^{i\omega t}\, dt, \qquad f(t) = \frac{1}{2\pi}\int_{\mathbb{R}} \hat{f}(\omega) e^{-i\omega t}\, d\omega. \tag{5.2}$$

In free space, it is possible to link the measurements of the pressure waves $p(\mathbf{y},t)$ on the boundary $\partial\Omega$ to the circular Radon transform of the initial condition $p_0(\mathbf{x})$ as follows [**70**]:

$$\mathcal{R}_\Omega[p_0](\mathbf{y},r) = \mathcal{W}[p](\mathbf{y},r), \quad \mathbf{y}\in\partial\Omega, \quad r\in\mathbb{R}^+,$$

where the circular Radon transform is defined by

$$\mathcal{R}_\Omega[p_0](\mathbf{y},r) := \int_{\mathbb{S}^1} r p_0(\mathbf{y}+r\boldsymbol{\theta}) d\sigma(\boldsymbol{\theta}), \quad \mathbf{y}\in\partial\Omega, \quad r\in\mathbb{R}^+,$$

and

$$\mathcal{W}[p](\mathbf{y},r) := 4r\int_0^s \frac{p(\mathbf{y},t/c_0)}{\sqrt{s^2-t^2}}\, dt, \quad \mathbf{y}\in\partial\Omega, \quad r\in\mathbb{R}^+.$$

Here $\mathbb{S}^1$ denotes the unit circle. When Ω is the unit disk with center at $\mathbf{0}$ and radius $X_0 = 1$, in order to find p_0 we can use the following exact inversion formula [**108**]:

$$p_0 = \frac{1}{4\pi^2}\mathcal{R}_\Omega^\star \mathcal{B}\mathcal{W}[p], \tag{5.3}$$

where $\mathcal{R}_\Omega^\star$ (the adjoint of the circular Radon transform) is a backprojection operator given by

$$\mathcal{R}_\Omega^\star[f](\mathbf{x}) = \int_{\partial\Omega} f(\mathbf{y}, |\mathbf{x}-\mathbf{y}|) d\sigma(\mathbf{y}) = \frac{1}{2\pi}\int_{\partial\Omega}\int_{\mathbb{R}} \hat{f}(\mathbf{y},\omega) e^{-i\omega|\mathbf{x}-\mathbf{y}|} d\omega d\sigma(\mathbf{y}), \quad \mathbf{x}\in\Omega,$$

and $\mathcal{B}$ is a filter defined by

$$\mathcal{B}[g](\mathbf{y},t) = \int_0^2 \frac{d^2 g}{dr^2}(\mathbf{y},r)\ln(|r^2-t^2|)\, dr, \quad \mathbf{y}\in\partial\Omega.$$

Note that (5.3) holds only in two dimensions. Moreover, in the Fourier domain, it reads

$$p_0(\mathbf{x}) = \frac{1}{(2\pi)^3} \int_{\partial\Omega} \int_{\mathbb{R}} \widehat{\mathcal{BW}[p]}(\mathbf{y},\omega) e^{-i\omega|\mathbf{x}-\mathbf{y}|} d\omega d\sigma(\mathbf{y}), \quad \mathbf{x} \in \Omega.$$

Hence, we introduce the Kirchhoff-Radon migration imaging functional:

$$\mathcal{I}_{\mathrm{KRM}}(\mathbf{x}) = \frac{1}{4\pi^2} \mathcal{R}^\star_\Omega \mathcal{BW}[p](\mathbf{x}) = \frac{1}{2\pi} \int_{\partial\Omega} \int_{\mathbb{R}} \hat{q}(\mathbf{x},\omega) e^{-i\omega|\mathbf{x}-\mathbf{y}|} d\omega d\sigma(\mathbf{y}), \tag{5.4}$$

where

$$q = \frac{1}{4\pi^2} \mathcal{BW}[p] \tag{5.5}$$

is the pre-processed data.

A second imaging functional is to simply back-project the raw data [**36**]:

$$\mathcal{I}_{\mathrm{KM}}(\mathbf{x}) = \mathcal{R}^\star_\Omega[p](\mathbf{x}) = \frac{1}{2\pi} \int_{\partial\Omega} \int_{\mathbb{R}} \hat{p}(\mathbf{y},\omega) e^{-i\omega|\mathbf{x}-\mathbf{y}|} d\omega d\sigma(\mathbf{y}), \quad \mathbf{x} \in \Omega. \tag{5.6}$$

When the sound speed varies, the phases of the measured waves are shifted according to the unknown clutter. To correct this effect, the idea of the original CINT algorithm is to back-project the space and frequency correlations between the data [**40**]:

$$\begin{aligned} \mathcal{I}_{\mathrm{CI}}(\mathbf{x}) = \; & \frac{1}{(2\pi)^2} \int_{\partial\Omega} \int_{|\mathbf{y}_2-\mathbf{y}_1|\le X_d} \int_{\mathbb{R}} \int_{|\omega_2-\omega_1|\le \Omega_d} \hat{p}(\mathbf{y}_1,\omega_1) e^{-i\omega_1|\mathbf{x}-\mathbf{y}_1|} \\ & \times \overline{\hat{p}}(\mathbf{y}_2,\omega_2) e^{i\omega_2|\mathbf{x}-\mathbf{y}_2|} d\omega_1 d\omega_2 d\sigma(\mathbf{y}_1) d\sigma(\mathbf{y}_2). \end{aligned} \tag{5.7}$$

As will be shown later, $\mathcal{I}_{\mathrm{CI}}$ is quite efficient in localizing point sources but not in finding the true value of p_0. Moreover, when the support of the initial pressure p_0 is extended, $\mathcal{I}_{\mathrm{CI}}$ may fail in recovering a good photoacoustic image. We propose two things. First, in order to avoid numerical oscillatory effects, we replace the sharp cut-offs in the integral by Gaussian convolutions. Then instead of taking the correlations between the back-projected raw data, we pre-process them like we do for the Radon inversion. We thus get the following CINT-Radon imaging functional:

$$\begin{aligned} \mathcal{I}_{\mathrm{CIR}}(\mathbf{x}) = \; & \frac{1}{(2\pi)^2} \int_{\partial\Omega} \int_{\partial\Omega} \int_{\mathbb{R}} \int_{\mathbb{R}} e^{-\frac{(\omega_2-\omega_1)^2}{2\Omega_d^2}} e^{-\frac{|\mathbf{y}_1-\mathbf{y}_2|^2}{2X_d^2}} \\ & \times \widehat{q}(\mathbf{y}_1,\omega_1) e^{-i\omega_1|\mathbf{x}-\mathbf{y}_1|} \overline{\widehat{q}}(\mathbf{y}_2,\omega_2) e^{i\omega_2|\mathbf{x}-\mathbf{y}_2|} d\omega_1 d\omega_2 d\sigma(\mathbf{y}_1) d\sigma(\mathbf{y}_2), \end{aligned} \tag{5.8}$$

where q is given by (5.5).

Note that, when $\Omega_d \to \infty$ and $X_d \to \infty$, then $\mathcal{I}_{\mathrm{CIR}}$ is the square of the Kirchhoff-Radon migration functional:

$$\mathcal{I}_{\mathrm{CIR}}(\mathbf{x}) = |\mathcal{I}_{\mathrm{KRM}}(\mathbf{x})|^2.$$

The purpose of the CINT-Radon imaging functional is to keep in (5.8) the pairs $(\mathbf{y}_1,\omega_1)$ and $(\mathbf{y}_2,\omega_2)$ for which the pre-processed data $\hat{q}(\mathbf{y}_1,\omega_1)$ and $\hat{q}(\mathbf{y}_2,\omega_2)$ are coherent, and to remove the pairs that do not bring information.

5.4. Stability and Resolution Analysis

5.4.1. Noise Model. We assume that the operating bandwidth of the sensors is of the form $[\omega_0 - B/2, \omega_0 + B/2]$ with $B \ll \omega_0$ and consider the following noise model. We assume that there is an error $\nu(\mathbf{x}, \mathbf{y})$ between the theoretical travel time $\tau_0(\mathbf{x}, \mathbf{y})$ with the background velocity c_0 and the real travel time $\tau(\mathbf{x}, \mathbf{y})$ where $\mathbf{y}$ is a point of the surface of the observation disk $\partial\Omega$ and $\mathbf{x}$ is a point of the search domain. Therefore, we have

$$\tau(\mathbf{x}, \mathbf{y}) = \tau_0(\mathbf{x}, \mathbf{y}) + \nu(\mathbf{x}, \mathbf{y}),$$

where $\nu(\mathbf{x}, \mathbf{y})$ is a random process. This model can be used in the presence of low-frequency (*i.e.*, $x_c \gg (2\pi)/\omega_0$) cluttered noise $\mu(\mathbf{x})$ in (5.1) which induces perturbations to travel times up to leading order:

$$\nu(\mathbf{x}, \mathbf{y}) = \frac{\sigma_c |\mathbf{y} - \mathbf{x}|}{2c_0} \int_0^1 \mu\Big(\frac{\mathbf{x} + (\mathbf{y} - \mathbf{x})s}{x_c}\Big) ds.$$

Assuming that the search window is relatively small we can assume that ν depends only on the sensor position $\mathbf{y}$ and we can neglect the variations of ν with respect to $\mathbf{x}$. This is perfectly correct if we analyze the expectations and the variances of the imaging functionals for a fixed test point $\mathbf{x}$ (then the search region is just one point). This is still correct if we analyze the covariance of the imaging functional for a pair of test points $\mathbf{x}$ and $\mathbf{x}'$ that are close to each other (closer than the correlation radius x_c of the clutter noise). This model can also be used when the positions of the sensors are poorly characterized.

We assume that the random process μ is a random process with Gaussian statistics, mean zero, and covariance function:

$$\mathbb{E}\big[\sigma\mu\big(\frac{\mathbf{x}}{x_c}\big)\sigma\mu\big(\frac{\mathbf{x}'}{x_c}\big)\big] = \sigma_c^2 \exp\Big(-\frac{|\mathbf{x} - \mathbf{x}'|^2}{2x_c^2}\Big).$$

Then ν is a random process with Gaussian statistics, mean zero, and covariance function:

$$\mathbb{E}[\nu(\mathbf{y})\nu(\mathbf{y}')] = \tau_c^2 \psi\big(\frac{|\mathbf{y} - \mathbf{y}'|}{x_c}\big), \qquad \psi(r) = \frac{1}{r}\int_0^r \exp\big(-\frac{s^2}{2}\big) ds, \tag{5.9}$$

where $\tau_c^2 = \sqrt{2\pi}\sigma_c^2 l X_0/(4c_0^2)$ is the variance of the fluctuations of the travel times. Here $\mathbb{E}$ stands for the expectation (mean value) and we have assumed that $x_c \ll X_0$.

Using the Gaussian statistics it is straightforward to compute the moments

$$\begin{aligned}
\mathbb{E}[e^{i\omega\nu(\mathbf{y})}] &= \exp\Big(-\frac{\omega^2\tau_c^2}{2}\Big), \\
\mathbb{E}[e^{i\omega\nu(\mathbf{y}) - i\omega'\nu(\mathbf{y}')}] &= \exp\Big(-\frac{(\omega - \omega')^2\tau_c^2}{2} - \omega\omega'\tau_c^2\big(1 - \psi\big(\frac{|\mathbf{y} - \mathbf{y}'|}{x_c}\big)\big)\Big).
\end{aligned}$$

If we assume that $\omega_0\tau_c \gg 1$, then for $\omega, \omega' \in [\omega_0 - B/2, \omega_0 + B/2]$, we have

$$\mathbb{E}[e^{i\omega\nu(\mathbf{y})}] \simeq \exp\Big(-\frac{\omega_0^2\tau_c^2}{2}\Big), \tag{5.10}$$

$$\mathbb{E}[e^{i\omega\nu(\mathbf{y}) - i\omega'\nu(\mathbf{y}')}] \simeq \exp\Big(-\frac{(\omega - \omega')^2\tau_c^2}{2} - \frac{|\mathbf{y} - \mathbf{y}'|^2}{2X_c^2}\Big), \tag{5.11}$$

with $X_c^2 = 3x_c^2/(2\omega_0^2\tau_c^2)$.

5.4.2. Kirchhoff-Radon Migration. Recall that the Kirchhoff-Radon migration functional is

$$\mathcal{I}_{\rm KRM}(\mathbf{x}) \quad = \quad \frac{1}{2\pi}\int_{\partial\Omega}\int_{\mathbb{R}}\hat{q}(\mathbf{y},\omega)e^{-i\omega|\mathbf{y}-\mathbf{x}|}d\omega d\sigma(\mathbf{y}) = \int_{\partial\Omega} q(\mathbf{y},|\mathbf{y}-\mathbf{x}|)d\sigma(\mathbf{y}), \tag{5.12}$$

where $q = \mathcal{BW}[p]/(4\pi^2)$. The functional applied to the perfect pre-processed data

$$q^{(0)} = \frac{1}{4\pi^2}\mathcal{BW}[p^{(0)}] \tag{5.13}$$

is

$$\mathcal{I}^{(0)}_{\rm KRM}(\mathbf{x}) = \frac{1}{2\pi}\int_{\partial\Omega}\int_{\mathbb{R}}\hat{q}^{(0)}(\mathbf{y},\omega)e^{-i\omega|\mathbf{y}-\mathbf{x}|}d\omega d\sigma(\mathbf{y}) = \int_{\partial\Omega} q^{(0)}(\mathbf{y},|\mathbf{y}-\mathbf{x}|)d\sigma(\mathbf{y}), \tag{5.14}$$

and it is equal to the initial condition $p_0(\mathbf{x})$.

We consider the random travel time model to describe the recorded data set:

$$q(\mathbf{y},t) = q^{(0)}(\mathbf{y},t-\nu(\mathbf{y})). \tag{5.15}$$

We first consider the expectation of the functional. Using (5.10) we find that

$$\mathbb{E}[\mathcal{I}_{\rm KRM}(\mathbf{x})] \quad = \quad \exp\Big(-\frac{\omega_0^2\tau_c^2}{2}\Big)\mathcal{I}^{(0)}_{\rm KRM}(\mathbf{x}),$$

which shows that the mean functional undergoes a strong damping compared to the unperturbed functional $\mathcal{I}^{(0)}_{\rm KRM}(\mathbf{x})$.

The statistics of the fluctuations can be characterized by the covariance

$$\begin{aligned}\mathbb{E}[\mathcal{I}_{\rm KRM}(\mathbf{x})\overline{\mathcal{I}_{\rm KRM}(\mathbf{x}')}] \quad &= \quad \frac{1}{(2\pi)^2}\iint_{\partial\Omega\times\partial\Omega}\hat{q}^{(0)}(\mathbf{y}_1,\omega_1)\overline{\hat{q}^{(0)}(\mathbf{y}_2,\omega_2)}e^{-i\omega_1|\mathbf{y}_1-\mathbf{x}|}e^{i\omega_2|\mathbf{y}_2-\mathbf{x}'|}\\ &\quad\times\exp\Big(-\frac{(\omega_1-\omega_2)^2\tau_c^2}{2}-\frac{|\mathbf{y}_1-\mathbf{y}_2|^2}{2X_c^2}\Big)d\omega_1 d\sigma(\mathbf{y}_1)d\omega_2 d\sigma(\mathbf{y}_2).\end{aligned}$$

In the regime in which $\tau_c^{-1} > B$ and $X_c > X_0$ we find that the amplitude of the fluctuations is of the order of

$$\mathrm{Var}\big(\mathcal{I}_{\rm KRM}(\mathbf{x})\big) \sim (\mathcal{I}^{(0)}_{\rm KRM}(\mathbf{x}))^2.$$

Here, Var stands for the variance. In the regime in which $\tau_c^{-1} < B$ and $X_c < X_0$ we find that

$$\mathrm{Var}\big(\mathcal{I}_{\rm KRM}(\mathbf{x})\big) \sim (\mathcal{I}^{(0)}_{\rm KRM}(\mathbf{x}))^2\Big(\frac{1}{B\tau_c}\Big)\Big(\frac{X_c}{X_0}\Big).$$

Define the signal-to-noise ratio (SNR) by

$$\mathrm{SNR}_{\rm KRM} = \frac{\mathbb{E}[\mathcal{I}_{\rm KRM}(\mathbf{x})]}{\mathrm{Var}(\mathcal{I}_{\rm KRM}(\mathbf{x}))^{1/2}}. \tag{5.16}$$

The following holds.

PROPOSITION 5.4.1. *We have*

$$\mathrm{SNR}_{\rm KRM} \sim \exp\Big(-\frac{\omega_0^2\tau_c^2}{2}\Big)\Big(1+B\tau_c\Big)^{\frac{1}{2}}\Big(1+\frac{X_0}{X_c}\Big)^{\frac{1}{2}}.$$

Note that $\mathrm{SNR}_{\rm KRM}$ is very small in this regime ($\omega_0\tau_c \gg 1$).

5.4.3. CINT-Radon. We consider the random travel time model (5.15). We first note that coherence in (5.8) is maintained as long as $\exp(i\omega_2\nu(\mathbf{y}_2) - i\omega_1\nu(\mathbf{y}_1))$ is close to one. From (5.11) this requires that $|\omega_1 - \omega_2| < \tau_c^{-1}$ and $|\mathbf{y}_1 - \mathbf{y}_2| < X_c$. We can therefore anticipate that the cut-off parameters X_d and Ω_d should be related to the coherence parameters X_c and τ_c^{-1}. In the following we study the role of the cut-off parameters X_d and Ω_d for resolution and stability. For doing so, we compute the expectation and variance of the imaging functional $\mathcal{I}_{\rm CIR}$.

We have

$$\mathbb{E}[\mathcal{I}_{\rm CIR}(\mathbf{x})] = \frac{1}{(2\pi)^2}\iint d\omega_1 d\omega_2 \iint_{\partial\Omega\times\partial\Omega} d\sigma(\mathbf{y}_1)d\sigma(\mathbf{y}_2)\hat{q}^{(0)}(\mathbf{y}_1,\omega_1)\overline{\hat{q}^{(0)}(\mathbf{y}_2,\omega_2)}$$
$$\times e^{-i\omega_1|\mathbf{y}_1-\mathbf{x}|}e^{i\omega_2|\mathbf{y}_2-\mathbf{x}|}\exp\Big(-\frac{(\omega_1-\omega_2)^2}{2}(\tau_c^2+\frac{1}{\Omega_d^2}) - \frac{|\mathbf{y}_1-\mathbf{y}_2|^2}{2}(\frac{1}{X_d^2}+\frac{1}{X_c^2})\Big),$$

where $q^{(0)}$ is the perfect pre-processed data defined by (5.13). Using the change of variables

$$\omega_1 = \omega_a + \frac{h_a}{2}, \quad \omega_2 = \omega_a - \frac{h_a}{2}, \qquad \mathbf{y}_1 = \mathbf{Y}_a + \frac{\mathbf{y}_a}{2}, \quad \mathbf{y}_2 = \mathbf{Y}_a - \frac{\mathbf{y}_a}{2},$$

the expectation of the CINT-Radon functional can be written as

$$\begin{aligned}\mathbb{E}[\mathcal{I}_{\rm CIR}(\mathbf{x})] &= \frac{1}{(2\pi)^2}\int_{\partial\Omega} d\sigma(\mathbf{Y}_a)\int dh_a \int_{\mathbf{Y}_a^\perp} d\sigma(\mathbf{y}_a)\hat{Q}(\mathbf{Y}_a,h_a,\mathbf{y}_a;\mathbf{x})\\ &\quad\times\exp\Big(-\frac{h_a^2}{2}(\tau_c^2+\frac{1}{\Omega_d^2}) - \frac{|\mathbf{y}_a|^2}{2}(\frac{1}{X_d^2}+\frac{1}{X_c^2})\Big),\end{aligned} \tag{5.17}$$

where

$$\mathbf{Y}_a^\perp = \Big\{\mathbf{y}_a\in\mathbb{R}^2\,,\ \mathbf{Y}_a - \frac{\mathbf{y}_a}{2}\in\partial\Omega \text{ and } \mathbf{Y}_a + \frac{\mathbf{y}_a}{2}\in\partial\Omega\Big\}$$

and

$$\begin{aligned}\hat{Q}(\mathbf{Y}_a,h_a,\mathbf{y}_a;\mathbf{x}) &= \int d\omega_a \hat{q}^{(0)}(\mathbf{Y}_a+\frac{\mathbf{y}_a}{2},\omega_a+\frac{h_a}{2})\overline{\hat{q}^{(0)}(\mathbf{Y}_a-\frac{\mathbf{y}_a}{2},\omega_a-\frac{h_a}{2})}\\ &\quad\times e^{-i(\omega_a+\frac{h_a}{2})|\mathbf{Y}_a+\frac{\mathbf{y}_a}{2}-\mathbf{x}|}e^{i(\omega_a-\frac{h_a}{2})|\mathbf{Y}_a-\frac{\mathbf{y}_a}{2}-\mathbf{x}|}.\end{aligned}$$

We assume that X_d is much smaller than X_0, so that $\mathbf{y}_1 - \mathbf{y}_2$ is approximately orthogonal to $(\mathbf{y}_1+\mathbf{y}_2)/2$ when $\mathbf{y}_1,\mathbf{y}_2\in\partial\Omega$ and $|\mathbf{y}_1-\mathbf{y}_2|\le X_d$. Then

$$\mathbf{Y}_a^\perp = \{\mathbf{y}_a\in\mathbb{R}^2\,,\ \mathbf{Y}_a\cdot\mathbf{y}_a = 0\},$$

and

$$\begin{aligned}\hat{Q}(\mathbf{Y}_a,h_a,\mathbf{y}_a;\mathbf{x}) &\simeq \int d\omega_a \hat{q}^{(0)}(\mathbf{Y}_a+\frac{\mathbf{y}_a}{2},\omega_a+\frac{h_a}{2})\overline{\hat{q}^{(0)}(\mathbf{Y}_a-\frac{\mathbf{y}_a}{2},\omega_a-\frac{h_a}{2})}\\ &\quad\times e^{i\omega_a\frac{\mathbf{x}-\mathbf{Y}_a}{|\mathbf{x}-\mathbf{Y}_a|}\cdot\mathbf{y}_a - ih_a|\mathbf{x}-\mathbf{Y}_a|}\\ &\simeq \frac{1}{(2\pi)^2}\int d\omega_a\int d\tau_a\int_{\mathbf{Y}_a^\perp} d\sigma(\boldsymbol{\kappa}_a)\mathcal{W}_q(\mathbf{Y}_a,\omega_a;\boldsymbol{\kappa}_a,\tau_a)\\ &\quad\times e^{i(\omega_a\frac{\mathbf{x}-\mathbf{Y}_a}{|\mathbf{x}-\mathbf{Y}_a|}-\boldsymbol{\kappa}_a)\cdot\mathbf{y}_a+(\tau_a-|\mathbf{x}-\mathbf{Y}_a|)h_a},\end{aligned}$$

where $\mathcal{W}_q$ is the Wigner transform of $q^{(0)}$:

$$\begin{aligned}\mathcal{W}_q(\mathbf{Y}_a,\omega_a;\boldsymbol{\kappa}_a,\tau_a) &= \int dh_a \int_{\mathbf{Y}_a^\perp} d\sigma(\mathbf{y}_a)\hat{q}^{(0)}(\mathbf{Y}_a+\frac{\mathbf{y}_a}{2},\omega_a+\frac{h_a}{2})\overline{\hat{q}^{(0)}(\mathbf{Y}_a-\frac{\mathbf{y}_a}{2},\omega_a-\frac{h_a}{2})}\\ &\quad\times e^{i\boldsymbol{\kappa}_a\cdot\mathbf{y}_a-ih_a\tau_a}. \qquad (5.18)\end{aligned}$$

Therefore, we get

$$\begin{aligned}\mathbb{E}[\mathcal{I}_{\rm CIR}(\mathbf{x})] &= \frac{1}{(2\pi)^3(\frac{1}{X_d^2}+\frac{1}{X_c^2})^{\frac12}(\tau_c^2+\frac{1}{\Omega_d^2})^{\frac12}}\int_{\partial\Omega} d\sigma(\mathbf{Y}_a)\int d\omega_a\int_{\mathbf{Y}_a^\perp} d\sigma(\boldsymbol{\kappa}_a)\int d\tau_a\\ &\quad\times\mathcal{W}_q(\mathbf{Y}_a,\omega_a;\boldsymbol{\kappa}_a,\tau_a)\\ &\quad\times\exp\Big(-\frac{\big|\boldsymbol{\kappa}_a-\omega_a\big(\frac{\mathbf{x}-\mathbf{Y}_a}{|\mathbf{x}-\mathbf{Y}_a|}-(\frac{\mathbf{Y}_a}{|\mathbf{Y}_a|}\cdot\frac{\mathbf{x}-\mathbf{Y}_a}{|\mathbf{x}-\mathbf{Y}_a|})\frac{\mathbf{Y}_a}{|\mathbf{Y}_a|}\big)\big|^2}{2(\frac{1}{X_d^2}+\frac{1}{X_c^2})}-\frac{(\tau_a-|\mathbf{Y}_a-\mathbf{x}|)^2}{2(\tau_c^2+\frac{1}{\Omega_d^2})}\Big).\end{aligned}$$

Since, for any s,

$$\mathcal{W}_q(\mathbf{Y}_a,\omega_a;\boldsymbol{\kappa}_a+s\mathbf{Y}_a,\tau_a)=\mathcal{W}_q(\mathbf{Y}_a,\omega_a;\boldsymbol{\kappa}_a,\tau_a),$$

we obtain the following result.

PROPOSITION 5.4.2. *We have*

$$\begin{aligned}\mathbb{E}[\mathcal{I}_{\rm CIR}(\mathbf{x})] &= \frac{1}{(2\pi)^3(\frac{1}{X_d^2}+\frac{1}{X_c^2})^{\frac12}(\tau_c^2+\frac{1}{\Omega_d^2})^{\frac12}}\int_{\partial\Omega} d\sigma(\mathbf{Y}_a)\int d\omega_a\int_{\mathbf{Y}_a^\perp} d\sigma(\boldsymbol{\kappa}_a)\int d\tau_a\\ &\quad\times\mathcal{W}_q(\mathbf{Y}_a,\omega_a;\boldsymbol{\kappa}_a,\tau_a)\exp\Big(-\frac{\big|\boldsymbol{\kappa}_a-\omega_a\frac{\mathbf{x}-\mathbf{Y}_a}{|\mathbf{x}-\mathbf{Y}_a|}\big|^2}{2(\frac{1}{X_d^2}+\frac{1}{X_c^2})}-\frac{(\tau_a-|\mathbf{Y}_a-\mathbf{x}|)^2}{2(\tau_c^2+\frac{1}{\Omega_d^2})}\Big). \qquad (5.19)\end{aligned}$$

Formula (5.19) shows that the coherent part (*i.e.*, the expectation) of the CINT-Radon functional is a smoothed version of the Wigner transform of the pre-processed data. It selects a band of directions and time delays that are centered around the direction and the time delay between the search point $\mathbf{x}$ and the point $\mathbf{Y}_a$ of the sensor array.

We observe that:

- if $\Omega_d > \tau_c^{-1}$ and $X_d > X_c$ then the cut-off parameters Ω_d and X_d have no influence on the coherent part of the functional which does not depend on (Ω_d, X_d).
- if $\Omega_d < \tau_c^{-1}$ and $X_d < X_c$ then CINT has an influence and reduces the resolution of the coherent part of the functional (it enhances the smoothing of the Wigner transform).

We next compute the covariance of the CINT-Radon functional. If

$$\omega_1=\omega_a+\frac{h_a}{2},\quad \omega_2=\omega_a-\frac{h_a}{2},\qquad \omega_3=\omega_b+\frac{h_b}{2},\quad \omega_4=\omega_b-\frac{h_b}{2},$$

$$\mathbf{y}_1=\mathbf{Y}_a+\frac{\mathbf{y}_a}{2},\quad \mathbf{y}_2=\mathbf{Y}_a-\frac{\mathbf{y}_a}{2},\qquad \mathbf{y}_3=\mathbf{Y}_b+\frac{\mathbf{y}_b}{2},\quad \mathbf{y}_4=\mathbf{Y}_b-\frac{\mathbf{y}_b}{2},$$

then

$$\mathbb{E}\big[e^{i\omega_1\nu(\mathbf{y}_1)-i\omega_2\nu(\mathbf{y}_2)}\overline{e^{i\omega_3\nu(\mathbf{y}_3)-i\omega_4\nu(\mathbf{y}_4)}}\big]\simeq\exp\Big(-\frac{(h_a-h_b)^2\tau_c^2}{2}-\frac{|\mathbf{y}_a-\mathbf{y}_b|^2}{2X_c^2}\Big),$$

and therefore,

$$\begin{aligned}\mathbb{E}[\mathcal{I}_{\rm CIR}(\mathbf{x})\overline{\mathcal{I}_{\rm CIR}(\mathbf{x}')}] &= \frac{1}{(2\pi)^4}\iiint d\sigma(\mathbf{Y}_a)dh_a d\sigma(\mathbf{y}_a)d\sigma(\mathbf{Y}_b)dh_b d\sigma(\mathbf{y}_b)\\ &\quad\times\hat{Q}(\mathbf{Y}_a,h_a,\mathbf{y}_a;\mathbf{x})\overline{\hat{Q}(\mathbf{Y}_b,h_b,\mathbf{y}_b;\mathbf{x}')}\\ &\quad\times\exp\Big(-\frac{(h_a^2+h_b^2)}{2\Omega_d^2}-\frac{(|\mathbf{y}_a|^2+|\mathbf{y}_b|^2)}{2X_d^2}\Big)\\ &\quad\times\exp\Big(-\frac{(h_a-h_b)^2\tau_c^2}{2}-\frac{|\mathbf{y}_a-\mathbf{y}_b|^2}{2X_c^2}\Big).\end{aligned}$$

Using (5.17) we can see that, if $\Omega_d<\tau_c^{-1}$ and $X_d<X_c$, then we have

$$\mathbb{E}[\mathcal{I}_{\rm CIR}(\mathbf{x})]=\frac{1}{(2\pi)^2}\iiint d\sigma(\mathbf{Y}_a)dh_a d\sigma(\mathbf{y}_a)\hat{Q}(\mathbf{Y}_a,h_a,\mathbf{y}_a;\mathbf{x})\exp\Big(-\frac{h_a^2}{2\Omega_d^2}-\frac{|\mathbf{y}_a|^2}{2X_d^2}\Big).$$

Using

$$1-\exp\Big(-\frac{(h_a-h_b)^2\tau_c^2}{2}-\frac{|\mathbf{y}_a-\mathbf{y}_b|^2}{2X_c^2}\Big)\simeq\frac{(h_a-h_b)^2\tau_c^2}{2}+\frac{|\mathbf{y}_a-\mathbf{y}_b|^2}{2X_c^2},$$

it follows that

$$\mathrm{Var}\big(\mathcal{I}_{\rm CIR}(\mathbf{x})\big)=\mathbb{E}[|\mathcal{I}_{\rm CIR}(\mathbf{x})|^2]-|\mathbb{E}[\mathcal{I}_{\rm CIR}(\mathbf{x})]|^2\quad\sim\quad\Big((\Omega_d\tau_c)^2+\big(\frac{X_d}{X_c}\big)^2\Big)\big|\mathbb{E}\big[\mathcal{I}_{\rm CIR}(\mathbf{x})\big]\big|^2.$$

Therefore, the following proposition, where the SNR is defined analogously to (5.16), holds.

PROPOSITION 5.4.3. *When $\Omega_d<\tau_c^{-1}$ and $X_d<X_c$, we have*

$$\mathrm{SNR}_{\rm CIR}\sim\frac{1}{\sqrt{(\Omega_d\tau_c)^2+\big(\frac{X_d}{X_c}\big)^2}}. \tag{5.20}$$

Note that the SNR is greater than one when $\Omega_d<\tau_c^{-1}$ and $X_d<X_c$.

To conclude, we notice that the values of the parameters $X_d\simeq X_c$ and $\Omega_d\simeq\tau_c^{-1}$ achieve a good trade-off between resolution and stability. When taking smaller values $\Omega_d<\tau_c^{-1}$ and $X_d<X_c$ one increases the signal-to-noise ratio but one also reduces the resolution. In practice, these parameters are difficult to estimate directly from the data, so it is better to determine them adaptively, by optimizing over Ω_d and X_d the quality of the resulting image. This is exactly what is done in adaptive CINT [**41**].

5.4.4. Two Particular Cases. We now discuss the following two particular cases:

(i) If we take $X_d\to 0$ then the CINT functional has the form

$$\mathcal{I}_{\rm CIR}(\mathbf{x})=\frac{1}{(2\pi)^2}\int_{\mathbb{R}}\int_{\mathbb{R}}d\omega_1 d\omega_2\int_{\partial\Omega}d\sigma(\mathbf{y})e^{-\frac{(\omega_1-\omega_2)^2}{2\Omega_d^2}}\hat{q}(\mathbf{y},\omega_1)e^{-i\omega_1|\mathbf{y}-\mathbf{x}|}\overline{\hat{q}(\mathbf{y},\omega_2)}e^{i\omega_2|\mathbf{y}-\mathbf{x}|}. \tag{5.21}$$

This case could correspond to the situation in which X_c is very small, which means that the signals recorded by different sensors are so noisy that they are independent from each other.

If $\Omega_d > B$, then (5.21) is equivalent to the incoherent matched field functional

$$\mathcal{I}_{\mathrm{CIR}}(\mathbf{x}) \simeq \int_{\partial\Omega} d\sigma(\mathbf{Y}_a)\big|q(\mathbf{Y}_a, |\mathbf{Y}_a - \mathbf{x}|)\big|^2.$$

If $\Omega_d \leq B$ (or, more generally, for any Ω_d), then (5.21) is a smoothed (in time) version of this functional given by

$$\mathcal{I}_{\mathrm{CIR}}(\mathbf{x}) = \frac{\Omega_d}{\sqrt{2\pi}} \int_{\partial\Omega} d\sigma(\mathbf{Y}_a) \int_{\mathbb{R}} dt\big|q(\mathbf{Y}_a, |\mathbf{Y}_a - \mathbf{x}| + t)\big|^2 \exp\Big(-\frac{\Omega_d^2 t^2}{2}\Big).$$

(ii) If we take $X_d \to \infty$ then the CINT functional has the form

$$\begin{aligned}\mathcal{I}_{\mathrm{CIR}}(\mathbf{x}) &= \frac{1}{(2\pi)^2} \int_{\mathbb{R}}\int_{\mathbb{R}} d\omega_1 d\omega_2 \iint_{\partial\Omega\times\partial\Omega} d\sigma(\mathbf{y}_1)d\sigma(\mathbf{y}_2) e^{-\frac{(\omega_1-\omega_2)^2}{2\Omega_d^2}} \\ &\quad \times \hat{q}(\mathbf{y}_1, \omega_1) e^{-i\omega_1|\mathbf{y}_1-\mathbf{x}|} \overline{\hat{q}(\mathbf{y}_2, \omega_2)} e^{i\omega_2|\mathbf{y}_2-\mathbf{x}|}. \end{aligned} \tag{5.22}$$

This case could correspond to the situation in which X_c is very large, which means that the signals recorded by different sensors are strongly correlated with one another. This is a typical weak noise case.
If $\Omega_d > B$, then (5.21) is equivalent to the coherent matched field function (or square KM functional):

$$\mathcal{I}_{\mathrm{CIR}}(\mathbf{x}) \simeq \Big|\int_{\partial\Omega} d\sigma(\mathbf{Y}_a) q(\mathbf{Y}_a, |\mathbf{Y}_a - \mathbf{x}|)\Big|^2.$$

If $\Omega_d \leq B$ (or, more generally, for any Ω_d), then (5.22) is a smoothed (in time) version of this functional:

$$\mathcal{I}_{\mathrm{CIR}}(\mathbf{x}) = \frac{\Omega_d}{\sqrt{2\pi}} \int_{\mathbb{R}} dt\Big|\int_{\partial\Omega} d\sigma(\mathbf{Y}_a) q(\mathbf{Y}_a, |\mathbf{Y}_a - \mathbf{x}| + t)\Big|^2 \exp\Big(-\frac{\Omega_d^2 t^2}{2}\Big).$$

5.5. CINT-Radon Algorithm in a Bounded Domain

When considering photoacoustics in a bounded domain, we developed in [**9**] an approach involving the line Radon transform of the initial condition. We will consider homogeneous Dirichlet conditions:

$$\begin{cases} \dfrac{\partial^2 p}{\partial t^2}(\mathbf{x}, t) - c(\mathbf{x})^2 \Delta p(\mathbf{x}, t) = 0, \quad \mathbf{x} \in \Omega, \\ p(\mathbf{x}, 0) = p_0(\mathbf{x}), \qquad \dfrac{\partial p}{\partial t}(\mathbf{x}, 0) = 0, \quad \mathbf{x} \in \Omega, \\ p(\mathbf{y}, t) = 0, \quad \mathbf{y} \in \partial\Omega. \end{cases}$$

Here, Ω is not necessarily a disk. Let $\boldsymbol{n}$ denote the outward normal to $\partial\Omega$. When $c(\mathbf{x}) = c_0$, we can express the line Radon transform of the initial condition $p_0(\mathbf{x})$ in terms of the Neumann measurements $\partial_n p(\mathbf{y}, t) = \boldsymbol{n}(\mathbf{y}) \cdot \boldsymbol{\nabla} p(\mathbf{y}, t)$ on $\partial\Omega \times [0, T]$:

$$\mathcal{R}[p_0](\boldsymbol{\theta}, s) = \mathcal{W}[\partial_n p](\boldsymbol{\theta}, s),$$

where the line Radon transform is defined by

$$\mathcal{R}[p_0](\boldsymbol{\theta}, r) := \int_{\mathbb{R}} p_0(r\boldsymbol{\theta} + s\boldsymbol{\theta}^{\perp}) ds, \quad \boldsymbol{\theta} \in \mathbb{S}^1, \quad r \in \mathbb{R},$$

and

$$\mathcal{W}[g](\boldsymbol{\theta}, s) := \int_0^T \int_{\partial\Omega} g(\mathbf{x}, t) H\left(\frac{\mathbf{x} \cdot \boldsymbol{\theta}}{c_0} + t - s\right) d\sigma(\mathbf{x}) dt, \quad \boldsymbol{\theta} \in \mathbb{S}^1, \quad s \in \mathbb{R}.$$

Here H denotes the Heaviside function. We then invert the Radon transform using the back-projection algorithm

$$p_0 = \mathcal{R}^\star \mathcal{B}\mathcal{W}[\partial_n p],$$

where $\mathcal{R}^\star$ is the adjoint Radon transform:

$$\mathcal{R}^\star[f](\mathbf{x}) = \frac{1}{2\pi}\int_{\mathbb{S}^1} f(\boldsymbol{\theta}, \mathbf{x}\cdot\boldsymbol{\theta})d\sigma(\boldsymbol{\theta}) = \frac{1}{(2\pi)^2}\int_{\mathbb{S}^1}\int_{\mathbb{R}} \hat{f}(\boldsymbol{\theta},\omega)e^{-i\omega\mathbf{x}\cdot\boldsymbol{\theta}}d\omega d\sigma(\boldsymbol{\theta}), \quad \mathbf{x}\in\Omega,$$

and $\mathcal{B}$ is a ramp filter

$$\mathcal{B}[g](\boldsymbol{\theta}, s) = \frac{1}{4\pi}\int_{\mathbb{R}} |\omega|\hat{g}(\boldsymbol{\theta},\omega)e^{-i\omega s}d\omega, \quad \boldsymbol{\theta}\in\mathbb{S}^1.$$

Here, the hat stands for the Fourier transform (5.2) in the second (shift) variable. In the Fourier domain, the inversion reads

$$p_0(\mathbf{x}) = \frac{1}{(2\pi)^2}\int_{\mathbb{S}^1}\int_{\mathbb{R}} \widehat{\mathcal{B}\mathcal{W}[\partial_n p]}(\boldsymbol{\theta},\omega)e^{-i\omega\mathbf{x}\cdot\boldsymbol{\theta}}d\omega d\sigma(\boldsymbol{\theta}), \quad \mathbf{x}\in\Omega.$$

Therefore, a natural idea to extend the CINT imaging to bounded media is to consider the imaging functional:

$$\begin{aligned}\mathcal{I}_{\mathrm{CIR}}(\mathbf{x}) \quad &:= \frac{1}{(2\pi)^4}\int_{\mathbb{S}^1}\int_{\mathbb{S}^1}\int_{\mathbb{R}}\int_{\mathbb{R}} e^{-\frac{(\omega_2-\omega_1)^2}{2\Omega_d^2}} e^{-\frac{|\boldsymbol{\theta}_2-\boldsymbol{\theta}_1|^2}{2\Theta_d^2}} \\ &\times \widehat{\mathcal{B}\mathcal{W}[\partial_n p]}(\boldsymbol{\theta}_1,\omega_1)e^{-i\omega_1\mathbf{x}\cdot\boldsymbol{\theta}_1}\overline{\widehat{\mathcal{B}\mathcal{W}[\partial_n p]}}(\boldsymbol{\theta}_2,\omega_2)e^{i\omega_2\mathbf{x}\cdot\boldsymbol{\theta}_2}d\omega_1 d\omega_2 d\sigma(\boldsymbol{\theta}_1)d\sigma(\boldsymbol{\theta}_2).\end{aligned}$$

The stability and resolution analysis in Section 5.4 applies immediately to $\mathcal{I}_{\mathrm{CIR}}$.

5.6. Numerical Illustrations

In this section we present numerical experiments to illustrate the performance of the CINT-Radon algorithms and to compare them with the Kirchhoff-Radon. The wave equation (direct problem) is solved via a Lie-splitting method. It can be rewritten as a first order PDE:

$$\partial_t \mathbf{P} = A\mathbf{P} + B\mathbf{P},$$

where $\mathbf{P} = \begin{pmatrix} p \\ \partial p/\partial t \end{pmatrix}$, $A = \begin{pmatrix} 0 & 1 \\ c_0^2\Delta & 0 \end{pmatrix}$, and $B = \begin{pmatrix} 0 & 0 \\ (c^2-c_0^2)\Delta & 0 \end{pmatrix}$. The operator A is solved exactly in the Fourier space while the operator B is treated explicitly with a finite difference method and a PML formulation in the case of free space. The inverse circular Radon formula is discretized as in [**69**].

In Figure 5.1, we consider 6 point sources which emit pulses of the form

$$f(t) = \cos(2\pi\omega_0 t)t\delta_\omega \exp(-\pi t^2\delta_\omega^2), \quad \text{with} \quad \delta_\omega = 10, \quad \omega_0 = 3\delta_\omega.$$

We use the random velocity c_1, visualized in Figure 5.1. Figure 5.2 presents the pressure $p(\mathbf{y}, t)$ computed without and with noise, and the reconstruction of the source locations obtained by the Kirchhoff migration functional $\mathcal{I}_{\mathrm{KM}}$. Figure 5.2 illustrates that in the presence of noise, $\mathcal{I}_{\mathrm{KM}}$ becomes very instable and fails to really localize the targets. The images obtained by $\mathcal{I}_{\mathrm{CI}}$ are plotted in Figure 5.3 and compared to those obtained by $\mathcal{I}_{\mathrm{KM}}$. Note that $\mathcal{I}_{\mathrm{CI}}$ presents better stability properties when X_d and Ω_d become small as predicted by the theory.

We now consider the case of extended targets and test the imaging functional $\mathcal{I}_{\mathrm{CIR}}$. We use the random velocity c_2 shown in Figure 5.1. Reconstructions of the

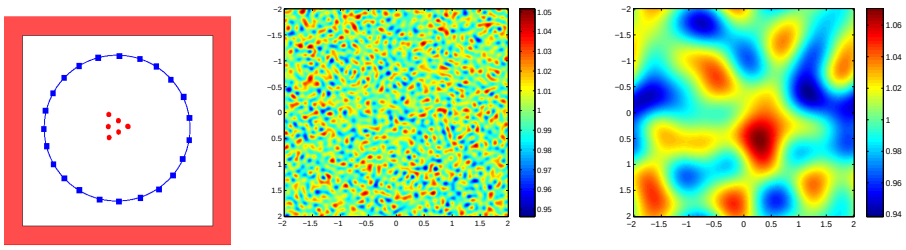

FIGURE 5.1. Left: Positions of the sensors; Center: random velocity c_1 with high frequencies; Right: random velocity c_2 with low frequencies.

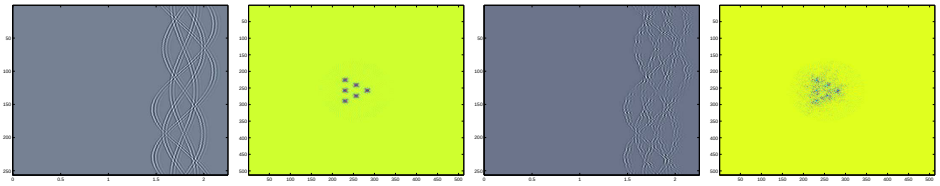

FIGURE 5.2. Test1: measured data $p(\mathbf{y}, t)$ and source localization using Kirchhoff migration $\mathcal{I}_{\mathrm{KM}}$ with (right) and without (left) noise.

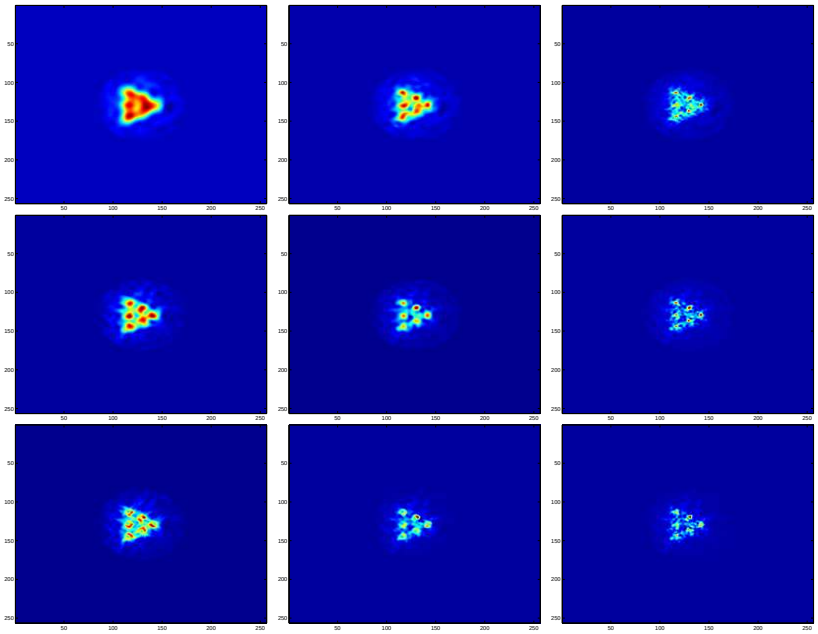

FIGURE 5.3. Test1: source localization using the standard CINT functional $\mathcal{I}_{\mathrm{CI}}$, with parameters X_d and Ω_d given by $X_d = 0.25, 0.5, 1$ (from left to right) and $\Omega_d = 25, 50, 100$ (from top to bottom).

initial pressure obtained by $\mathcal{I}_{\text{KRM}}$ are plotted in Figures 5.4 and 5.6. Figures 5.4 and 5.6 clearly highlight the fact that the noise significantly affects the reconstruction. In fact, the whole line is not found.

On the other hand, plots of $\mathcal{I}_{\text{CIR}}$ presented in Figures 5.5 and 5.7 provide more stable reconstructions of $p_0(\mathbf{x})$. However, note that choosing small values of the parameters X_d and Ω_d can affect the reconstruction in the sense that $\mathcal{I}_{\text{CIR}}$ becomes very different from the expected value, p_0^2, when X_d and Ω_d tend to zero. This is a manifestation of the trade-off between resolution and stability discussed in Section 5.4.

In the case of a bounded domain, we consider the low frequency cluttered speed of Figure 5.1, on a square medium, with homogeneous Dirichlet conditions. We illustrate the performance of $\mathcal{I}_{\text{CIR}}$ on the Shepp-Logan phantom. Figure 5.8 shows the reconstruction using the inverse Radon transform algorithm. We notice that the outer interface appears twice. In fact, $\mathcal{I}_{\text{CIR}}$ can correct this effect. Figure 5.9 shows results for different values of Θ_d and Ω_d. The imaging functional $\mathcal{I}_{\text{CIR}}$ can get the outer interface correctly but seems to focus too much on it. To check if $\mathcal{I}_{\text{CIR}}$ reconstructs the inside of the target with the good contrast, we show in Figure 5.10 the same images with a colormap saturated at 80% of their maximum values.

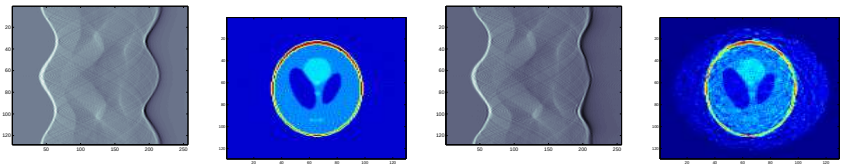

FIGURE 5.4. Test2: measured data $p(\mathbf{y}, t)$ and reconstruction of p_0 using $\mathcal{I}_{\text{KRM}}$ with (right) and without (left) noise.

5.7. Conclusion

In this chapter we have introduced new CINT-Radon type imaging functionals in order to correct the effect on photoacoustic images of random fluctuations of the background sound speed around a known constant value. We have provided a stability and resolution analysis of the proposed algorithms and found the values of the cut-off parameters which achieve a good trade-off between resolution and stability. We have presented numerical reconstructions of both small and extended targets and compared our algorithms with Kirchhoff-Radon migration functionals. The CINT-Radon imaging functionals give better reconstruction than Kirchhoff-Radon migration, specially for extended targets in the presence of low-frequency medium noise.

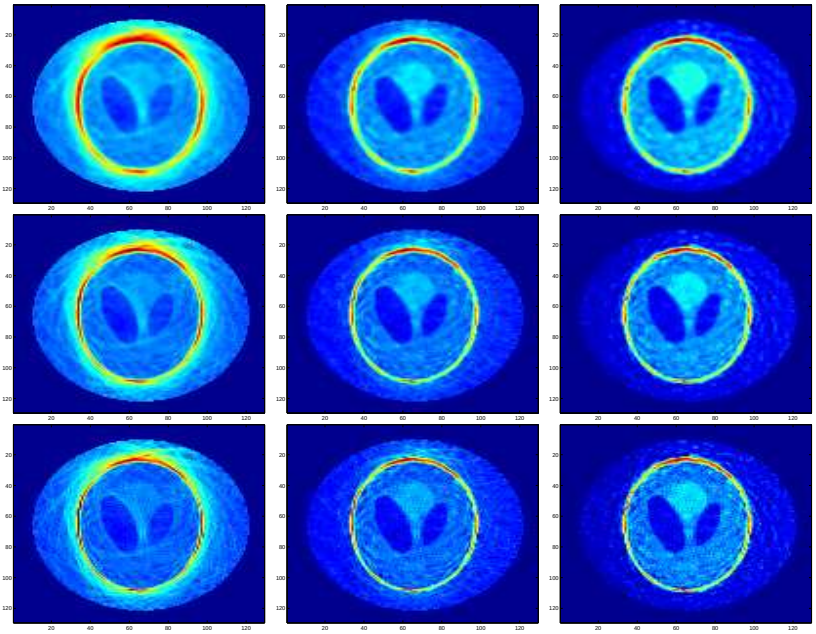

FIGURE 5.5. Test2: source localization using $\mathcal{I}_{\text{CIR}}$, with X_d and Ω_d given by $X_d = 0.5, 1, 2$ (from left to right) and $\Omega_d = 50, 100, 200$ (from top to bottom).

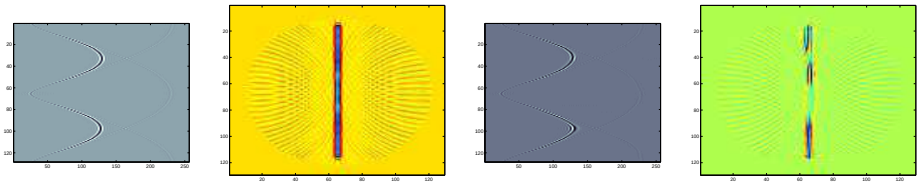

FIGURE 5.6. Test3: measured data $p(\mathbf{y}, t)$ and reconstruction of p_0 using $\mathcal{I}_{\text{KRM}}$ with (right) and without (left) noise.

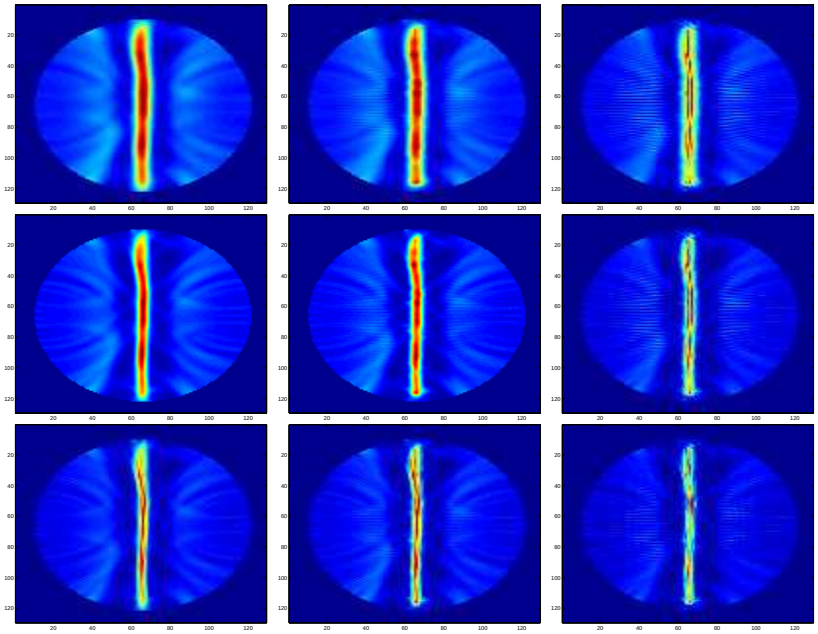

FIGURE 5.7. Test3 : source localization using $\mathcal{I}_{\mathrm{CIR}}$, with X_d and Ω_d given by $X_d = 0.5, 1, 2$ (from left to right) and $\Omega_d = 50, 100, 200$ (from top to bottom).

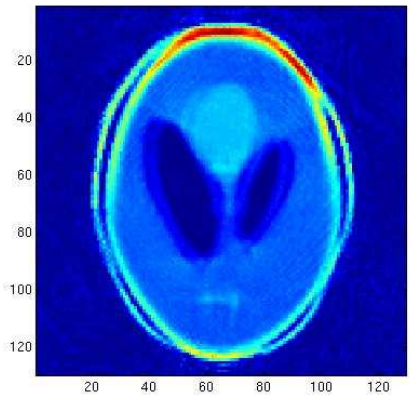

FIGURE 5.8. Reconstruction of an extended target using line Radon transform in the case of imposed boundary conditions.

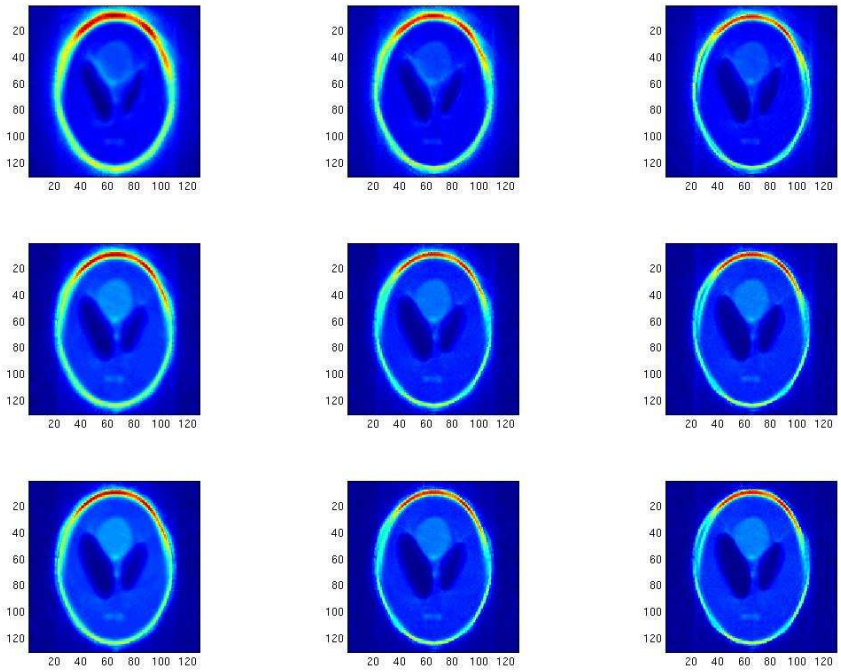

FIGURE 5.9. Extended target reconstruction with boundary conditions using $\mathcal{I}_{\mathrm{CIR}}$, with Θ_d and Ω_d given by $\Theta_d = 1, 3, 6$ (from top to bottom) and $\Omega_d = 50, 100, 200$ (from left to right).

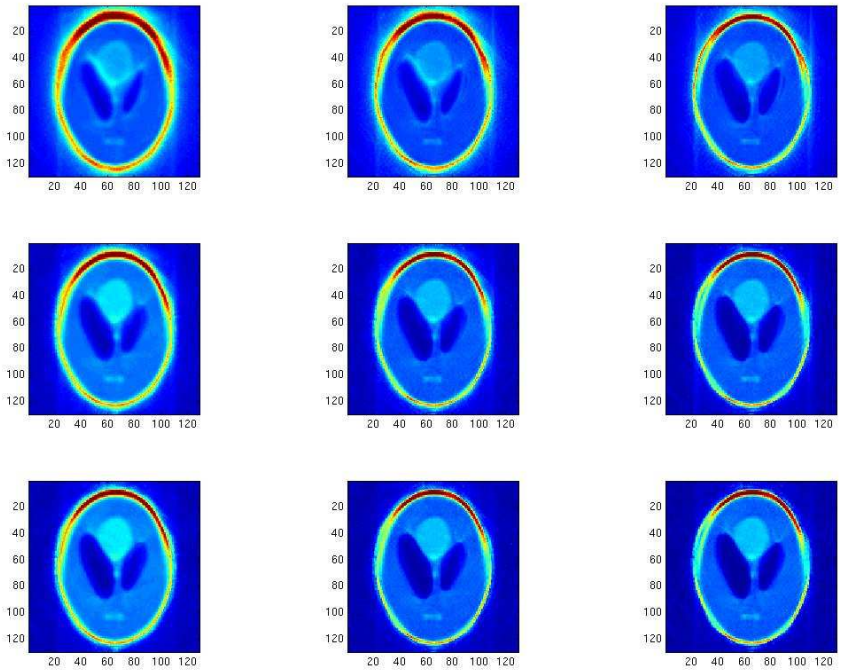

FIGURE 5.10. Extended target reconstruction with boundary conditions using $\mathcal{I}_{\mathrm{CIR}}$, with Θ_d and Ω_d given by $\Theta_d = 1, 3, 6$ (from top to bottom) and $\Omega_d = 50, 100, 200$ (from left to right). Colormaps are saturated at 80% of the maximum values of the images.

CHAPTER 6

Inverse Transport Theory of Photoacoustics

6.1. Introduction

Photoacoustic imaging is a recent medical imaging technique combining the large contrast between healthy and un-healthy tissues of their optical parameters with the high spatial resolution of acoustic (ultrasonic) waves. Electromagnetic radiation, sent through a domain of interest, generates some heating and a resulting thermal expansion of the underlying tissues. The mechanical displacement of the tissues generates acoustic waves, which then propagate through the medium and are recorded by an array of detectors (ultrasound transducers). The photoacoustic effect is now being actively investigated for its promising applications in medical imaging.

In an idealized setting revisited below, the electromagnetic source is a very short pulse that propagates through the domain at a scale faster than that of the acoustic waves. The measured acoustic signals may then be seen as being emitted by unknown initial conditions. A first step in the inversion thus consists in reconstructing this initial condition by solving an inverse source problem for a wave equation. This inversion is relatively simple when the sound speed is constant and full measurements are available. It becomes much more challenging when only partial measurements are available and the sound speed is not constant; see, e.g., Chapters 1 and 3.

A second step consists of analyzing the initial condition reconstructed in the first step and extracting information about the optical coefficients of the domain of interest. The second step is much less studied. The energy deposited by the radiation is given by the product of $\sigma_a(x)$, the attenuation in the tissue and of $I(x)$, the radiation intensity. The question is therefore what information on the medium may be extracted from $\sigma_a I$. The product can be plotted as a proxy for σ_a when I is more or less uniform. This, however, generates image distortions as has been reported, e.g., in [**101**]. The extraction of, e.g., σ_a from $\sigma_a I$ remains an essentially unsolved problem.

Two different regimes of radiation propagation should then be considered. In thermoacoustic tomography (TAT), low frequency (radio-frequency) waves with wavelengths much larger than the domain of interest, are being used. We do not consider this modality here. Rather, we assume that high frequency radiation is generated in the near infra red (NIR) spectrum. NIR photons have the advantage that they propagate over fairly large distances before being absorbed. Moreover, their absorption properties have a very large contrast between healthy and cancerous tissues. In this regime, $I(x)$ may be interpreted as a spatial density of photons propagating in the domain of interest. The density of photons is then modeled

by a transport equation that accounts for photon propagation, absorption, and scattering; see (6.11) below.

This chapter concerns the reconstruction of the optical parameters in a steady-state transport equation from knowledge of $H(x) := \sigma_a(x)I(x)$. The derivation of the transport equation given in (6.11) below is addressed in section 6.2. We are concerned here with the setting of measurements of $H(x)$ for different radiation patterns. Our most general measurement operator A is then the operator which to arbitrary radiation patterns at the domain's boundary maps the deposited energy $H(x)$.

We analyze the reconstruction of the absorption and scattering properties of the photons from knowledge of A. The main tool used in the analysis is the decomposition of A into singular components, in a spirit very similar to what was done, e.g., in [**26, 25, 54**] (see also [**24**]) in the presence of boundary measurements rather than internal measurements. The most singular component is related to the ballistic photons. We show that the analysis of that component allows us to reconstruct the attenuation coefficient σ_a and the spatial component σ_s of the scattering coefficient. The anisotropic behavior of scattering is partially determined by the second most singular term in A, which accounts for photons having scattered only once in the domain. Although the full phase function of the scattering coefficient cannot be reconstructed with the techniques described in this chapter, we show that the anisotropy coefficient $g(x)$ that appears in the classical Henyey-Greenstein phase function is uniquely determined by the measurements in spatial dimensions $n = 2$ and $n = 3$. Moreover, all the parameters that can be reconstructed are obtained with Hölder-type stability. We present the stability results in detail.

When scattering is very large, then radiation is best modeled by a diffusion equation characterized by two unknown coefficients, the diffusion coefficient $D(x)$ and the attenuation coefficient $\sigma_a(x)$. This regime is briefly mentioned in section 6.2.8.

The rest of the chapter is structured as follows. Section 6.2 is devoted to the derivation of the stationary inverse transport problem starting from the transient equation for the short electromagnetic pulse. The main uniqueness and stability results are also presented in detail in this section. The derivation of the uniqueness and stability results is postponed to the technical sections 6.3 and 6.4. The former section is devoted to the decomposition of the albedo operator into singular components. Useful results on the transport equation are also recalled. The latter section presents in detail the proofs of the stability results given in section 6.2.

6.2. Derivation and Main Results

6.2.1. Transport and Inverse Wave Problem. The propagation of radiation is modeled by the following radiative transfer equation

$$\frac{1}{c}\frac{\partial}{\partial t}u(t,x,v) + Tu(t,x,v) = S(t,x,v), \quad t \in \mathbb{R},\ x \in \mathbb{R}^n,\ v \in \mathbb{S}^{n-1}. \tag{6.1}$$

We assume here that $S(t,x,v)$ is compactly supported in $t \geq 0$ and in x outside of a bounded domain of interest X we wish to probe. The domain X is assumed to be an open subset of $\mathbb{R}^n$ with C^1 boundary. For the sake of simplicity, X is also assumed to be convex although all uniqueness and stability results in this chapter remain valid when X is not convex. Here, c is light speed, $\mathbb{S}^{n-1}$ is the unit sphere

in $\mathbb{R}^n$ and T is the transport operator defined as

$$Tu = v \cdot \nabla_x u + \sigma(x,v)u - \int_{\mathbb{S}^{n-1}} k(x,v',v)u(t,x,v')dv', \tag{6.2}$$

where $\sigma(x,v)$ is the total attenuation coefficient and $k(x,v',v)$ is the scattering coefficient. Both coefficients are assumed to be non-negative and bounded (by a constant $M < \infty$) throughout the chapter. We define

$$\sigma_s(x,v) = \int_{\mathbb{S}^{n-1}} k(x,v,v')dv', \qquad \sigma_a(x,v) = \sigma(x,v) - \sigma_s(x,v). \tag{6.3}$$

We also refer to σ_s as a scattering coefficient and define σ_a as the intrinsic attenuation coefficient. We assume that for (almost) all $(x,v) \in \mathbb{R}^n \times \mathbb{S}^{n-1}$, we have $\sigma_a(x,v) \geq \sigma_0 > 0$. We also assume that $k(x,v,v') = 0$ for (almost) all $x \notin X$.

The optical coefficients $k(x,v',v)$ and $\sigma(x,v)$ are the unknown coefficients inside X that we would like to reconstruct by probing the domain X by radiation modeled by $S(t,x,v)$. In photo-acoustics, the emitted radiation generates some heating inside the domain X. Heating then causes some dilation, which mechanically induces acoustic waves. Such acoustic waves are measured at the boundary of the domain X. After time reversion, the latter measurements allow us to infer the intensity of the source of heating. This gives us internal measurements of the solution u of the transport equation (6.1). The objective of this chapter is to understand which parts of the optical parameters may be reconstructed from such information and with which stability.

Before doing so, we need an accurate description of the propagation of the acoustic waves generated by the radiative heating. The proper model for the acoustic pressure is given by the following wave equation (see Chapter 1)

$$\Box p(t,x) = \beta \frac{\partial}{\partial t} H(t,x), \tag{6.4}$$

where $\Box$ is the d'Alembertian defined as

$$\Box p = \frac{1}{c_s^2(x)} \frac{\partial^2 p}{\partial t^2} - \Delta p, \tag{6.5}$$

with c_s the sound speed, where β is a coupling coefficient assumed to be constant and known, and where $H(t,x)$ is the thermal energy deposited by the radiation given by

$$H(t,x) = \int_{\mathbb{S}^{n-1}} \sigma_a(x,v')u(t,x,v')dv'. \tag{6.6}$$

Not surprisingly, the amount of heating generated by radiation is proportional to the amount of radiation u and to the rate of (intrinsic) absorption σ_a.

As it stands, the problem of the reconstruction of the source term $H(t,x)$ inside X from measurements of $p(t,x)$ on the boundary ∂X is ill-posed, because H is $(n+1)-$dimensional whereas information on $(t,x) \in \mathbb{R}_+ \times \partial X$ is $n-$dimensional. What allows us to simplify the inverse acoustic problem is the difference of time scales between the sound speed c_s and the light speed c.

To simplify the analysis, we assume that c_s is constant and rescale time so that $c_s = 1$. Then c in (6.1) is replaced by $\frac{c}{c_s}$, which in water is of order $2.3\,10^8/1.5\,10^3 \approx 1.5\,10^5 := \frac{1}{\varepsilon} \gg 1$. The transport scale is therefore considerably faster than the acoustic scale. As a consequence, when the radiation source term $S(t,x,v)$ is supported on a scale much faster than the acoustic scale, then u is also supported on

a scale much faster than the acoustic scale and as a result $H(t,x)$ can be approximated by a source term supported at $t=0$.

More specifically, let us assume that the source of radiation is defined at the scale $\varepsilon = \frac{c_s}{c}$ so that S is replaced by

$$S_\varepsilon(t,x,v) = \frac{1}{\varepsilon}\rho\big(\frac{t}{\varepsilon}\big)S_0(x,v), \tag{6.7}$$

where $\rho \geq 0$ is a function compactly supported in $t \in (0,\infty)$ such that $\int_{\mathbb{R}_+}\rho(t)dt = 1$. The transport solution then solves

$$\frac{1}{c}\frac{\partial}{\partial t}u_\varepsilon(t,x,v) + Tu_\varepsilon(t,x,v) = S_\varepsilon(t,x,v).$$

With $c_s = 1$, we verify that u_ε is given by

$$u_\varepsilon(t,x,v) = \frac{1}{\varepsilon}u\big(\frac{t}{\varepsilon},x,v\big), \tag{6.8}$$

where u solves (6.1) with $S(t,x,v) = \rho(t)S_0(x,v)$. Because $\sigma_a \geq \sigma_0 > 0$, we verify that u decays exponentially in time. This shows that u_ε lives at the time scale ε so that $H_\varepsilon(t,x) = \int_{\mathbb{S}^{n-1}}\sigma_a(x,v)u_\varepsilon(t,x,v)dv$ is also primarily supported in the vicinity of $t=0$.

Let us formally derive the equation satisfied by p_ε when $\varepsilon \to 0$. Let $\varphi(t,x)$ be a test function and define $(\cdot,\cdot)$ as the standard inner product on $\mathbb{R}\times\mathbb{R}^n$. Then we find that

$$(\Box p_\varepsilon,\varphi) = \beta(\frac{\partial H_\varepsilon}{\partial t},\varphi) = -\beta(H_\varepsilon,\frac{\partial\varphi}{\partial t}) = -\beta(H,\frac{\partial\varphi}{\partial t}(\varepsilon t))),$$

where $H(t,x) = \int_{\mathbb{S}^{n-1}}\sigma_a(x,v)u(t,x,v)dv$ with u defined in (6.8) and where we have used the change of variables $t \to \varepsilon t$. The latter term is therefore equal to

$$-\beta(H,\frac{\partial\varphi}{\partial t}(0)) = -\beta\frac{\partial\varphi}{\partial t}(0)\int_{\mathbb{R}\times\mathbb{S}^{n-1}}\sigma_a(x,v)u(t,x,v)dtdv,$$

up to a small term for φ sufficiently smooth. We thus find that p_ε converges weakly as $\varepsilon \to 0$ to the solution p of the following wave equation

$$\begin{aligned}
&\Box p = 0 && t>0, \quad x\in\mathbb{R}^n\\
&p(0,x) = H_0(x) := \int_{\mathbb{R}\times\mathbb{S}^{n-1}}\sigma_a(x,v)u(t,x,v)dtdv, && x\in\mathbb{R}^n\\
&\frac{\partial p}{\partial t}(0,x) = 0 && x\in\mathbb{R}^n.
\end{aligned} \tag{6.9}$$

The inverse problem for the wave equation is now well-posed. The objective is to reconstruct $H_0(x)$ for $x\in X$ from measurements of $p(t,x)$ for $t\geq 0$ and $x\in\partial X$. Such an inverse problem has been extensively studied in the literature. We refer the reader to, e.g., [**123**] for a recent inversion with (known) variable sound speed.

In this chapter, we assume that $H_0(x)$ has been reconstructed accurately as a functional of the radiation source $S_0(x,v)$. Our objective is to understand which parts of the optical parameters $\sigma(x,v)$ and $k(x,v',v)$ can be reconstructed from knowledge of $H_0(x)$ for a given set of radiations $S_0(x,v)$. Note that we will allow ourselves to generate many such $S_0(x,v)$ and thus consider a multi-measurement setting.

The time average $u(x,v) := \int u(t,x,v)dt$ satisfies a closed-form steady state transport equation given by

$$Tu = S_0(x,v), \qquad (x,v) \in \mathbb{R}^n \times \mathbb{S}^{n-1}, \tag{6.10}$$

as can be seen by averaging (6.1) in time since $\int \rho(t)dt = 1$.

6.2.2. Inverse Transport with Internal Measurements. Since $S_0(x,v)$ is assumed to be supported outside of the domain X and scattering $k(x,v',v) = 0$ outside of X, the above transport equation may be replaced by a boundary value problem of the form

(6.11)
$$\begin{aligned} &v \cdot \nabla_x u + \sigma(x,v)u - \int_{\mathbb{S}^{n-1}} k(x,v',v)u(x,v')dv' = 0, \qquad && (x,v) \in X \times \mathbb{S}^{n-1} \\ &u(x,v) = \phi(x,v) && (x,v) \in \Gamma_-, \end{aligned}$$

where the sets of outgoing and incoming boundary radiations are given by

$$\Gamma_\pm = \{(x,v) \in \partial X \times \mathbb{S}^{n-1}, \quad \pm v \cdot \nu(x) > 0\}, \tag{6.12}$$

where $\nu(x)$ is the outward normal to X at $x \in \partial X$ and $\phi(x,v)$ is an appropriate set of incoming radiation conditions obtained by solving $v \cdot \nabla_x u + \sigma_a(x,v)u = S_0$ outside of X assuming that $\sigma_a(x,v)$ is known outside of X.

We are now ready to state the inverse transport problem of interest in this chapter. It is well known that (6.11) admits a unique solution in $L^1(X \times \mathbb{S}^{n-1})$ when $\phi(x,v) \in L^1(\Gamma_-, d\xi)$, where $d\xi = |v \cdot \nu(x)| d\mu(x)dv$ with $d\mu$ the surface measure on ∂X. We thus define the albedo operator as

$$\begin{aligned} A: \quad L^1(\Gamma_-, d\xi) &\to L^1(X) \\ \phi(x,v) &\mapsto A\phi(x) = H(x) := \int_{\mathbb{S}^{n-1}} \sigma_a(x,v)u(x,v)dv. \end{aligned} \tag{6.13}$$

The inverse transport problem with angularly averaged internal measurements thus consists of understanding what can be reconstructed from the optical parameters $\sigma(x,v)$ and $k(x,v',v)$ from complete or partial knowledge of the albedo operator A. We also wish to understand the stability of such reconstructions.

6.2.3. Albedo Operator and Decomposition. The inverse transport problem and its stability properties are solved by looking at a decomposition of the albedo operator into singular components. Let $\alpha(x,x',v')$ be the Schwartz kernel of the albedo operator A, i.e., the distribution such that

$$A\phi(x) = \int_{\Gamma_-} \alpha(x,x',v')\phi(x',v')d\mu(x')dv'. \tag{6.14}$$

The kernel $\alpha(x,x',v')$ corresponds to measurements of $H(x)$ at $x \in X$ for a radiation condition concentrated at $x' \in \partial X$ and propagating with direction $v' \in \mathbb{S}^{n-1}$. Such a kernel can thus be obtained as a limit of physical experiments with sources concentrated in the vicinity of (x',v') and detectors concentrated in the vicinity of x.

The kernel $\alpha(x,x',v')$ accounts for radiation propagation inside X, including all orders of scattering of the radiation with the underlying structure. It turns out that we can extract from $\alpha(x,x',v')$ singular components that are not affected by

multiple scattering. Such singular components provide useful information on the optical coefficients. Let us define the ballistic part of transport as the solution of

$$v \cdot \nabla_x u_0 + \sigma(x,v)u_0 = 0, \quad \text{in } X \times \mathbb{S}^{n-1}, \qquad u_0 = \phi, \quad \text{on } \Gamma_-. \tag{6.15}$$

Then for $m \geq 1$, we define iteratively

$$v\cdot\nabla_x u_m + \sigma(x,v)u_m = \int k(x,v',v)u_{m-1}(x,v')dv', \quad \text{in } X\times\mathbb{S}^{n-1}, \quad u_m = 0, \quad \text{on } \Gamma_-. \tag{6.16}$$

This allows us to decompose the albedo operator as

$$A = A_0 + A_1 + \mathcal{G}_2, \tag{6.17}$$

where A_k for $k = 0, 1$ are defined as A in (6.13) with u replaced by u_k and where $\mathcal{G}_2$ is defined as $A - A_0 - A_1$. Thus, A_0 is the contribution in A of particles that have not scattered at all with the underlying structure while A_1 is the contribution of particles that have scattered exactly once.

Let α_k for $k = 0, 1$ be the Schwartz kernel of A_k and Γ_2 the Schwartz kernel of $\mathcal{G}_2$ using the same convention as in (6.14). We define $\tau_\pm(x,v)$ for $x \in X$ and $v \in \mathbb{S}^{n-1}$ as $\tau_\pm(x,v) = \inf\{s \in \mathbb{R}_+ | x \pm sv \notin X\}$. Thus, $\tau_\pm(x,v)$ indicates the time of escape from X of a particle at x moving in direction $\pm v$. On ∂X, we also define $\delta_{\{x\}}(y)$ as the distribution such that $\int_{\partial X} \delta_{\{x\}}(y)\phi(y)d\mu(y) = \phi(x)$ for any continuous function ϕ on ∂X. Finally, we define the following terms that quantify attenuation. We define the function $E(x_0, x_1)$ on $X \times \partial X$ as

$$E(x_0,x_1) = \exp\Big(-\int_0^{|x_0-x_1|} \sigma\big(x_0 - s\frac{x_0-x_1}{|x_0-x_1|}, \frac{x_0-x_1}{|x_0-x_1|}\big)ds\Big). \tag{6.18}$$

We still denote by E the function defined above for x_1 in X. Then by induction on m, we define

$$E(x_1,\dots,x_m) = E(x_1,\dots,x_{m-1})E(x_{m-1},x_m). \tag{6.19}$$

The latter term measures the attenuation along the broken path $[x_1, \dots, x_m]$.

Then we have the following result.

THEOREM 6.2.1. *Let α_0, α_1, and Γ_2 be the Schwartz kernels defined as above. Then we have:*

$$\begin{aligned}
\alpha_0(x,x',v') &= \sigma_a(x,v')\exp\Big(-\int_0^{\tau_-(x,v')} \sigma(x-sv',v')ds\Big)\delta_{\{x-\tau_-(x,v')v'\}}(x') \\
\alpha_1(x,x',v') &= |\nu(x')\cdot v'| \\
&\quad \int_0^{\tau_+(x',v')} \sigma_a(x,v)\frac{E(x,x'+t'v',x')}{|x-x'-t'v'|^{n-1}}k(x'+t'v',v',v)\big|_{v=\frac{x-x'-t'v'}{|x-x'-t'v'|}}dt'.
\end{aligned} \tag{6.20}$$

Moreover, we have the bound

$$\begin{aligned}
\frac{\Gamma_2(x,x',v')}{|\nu(x')\cdot v'|} &\in L^\infty(X\times\Gamma_-) \quad \textit{when} \quad n = 2 \\
\frac{|x-x'-((x-x')\cdot v')v'|^{n-3}\Gamma_2(x,x',v')}{|\nu(x')\cdot v'|} &\in L^\infty(X\times\Gamma_-) \quad \textit{when} \quad n \geq 3.
\end{aligned} \tag{6.21}$$

This theorem will be proved in section 6.3. The results show that α_0 is more singular than α_1 and Γ_2. It turns out that α_1 is also more singular than Γ_2 in the sense that it is asymptotically much larger than Γ_2 in the vicinity of the support of the ballistic part α_0. That this is the case is the object of the following result (see also Lemma 6.3.2 (6.48) and (6.50) for "$m = 1$"). For any topological space Y, we denote by $\mathcal{C}_b(Y)$ the set of the bounded continuous functions from Y to $\mathbb{R}$.

THEOREM 6.2.2. *Let us assume that $\sigma \in \mathcal{C}_b(X \times \mathbb{S}^{n-1})$ and that $k \in \mathcal{C}_b(X \times \mathbb{S}^{n-1} \times \mathbb{S}^{n-1})$. For $(x', v') \in \Gamma_-$, let $x = x' + t_0' v'$ for some $t_0' \in (0, \tau_+(x', v'))$. Let $v'^{\perp} \in \mathbb{S}^{n-1}$ be such that $v' \cdot v'^{\perp} = 0$. Then we have the following asymptotic expansion:*

$$
\begin{aligned}
&\frac{\alpha_1(x + \varepsilon v'^{\perp}, x', v')}{E(x, x')|\nu(x') \cdot v'|} = \Big(\ln \frac{1}{\varepsilon}\Big)\big(\chi(x, v', v') + \chi(x, v', -v')\big) + o\Big(\ln \frac{1}{\varepsilon}\Big) \\
&\frac{\alpha_1(x + \varepsilon v'^{\perp}, x', v')}{E(x, x')|\nu(x') \cdot v'|} = \frac{1}{\varepsilon^{n-2}} \int_0^{\pi} \sin^{n-3}\theta \chi(x, v', v(\theta)) d\theta + o\Big(\frac{1}{\varepsilon^{n-2}}\Big),
\end{aligned}
\tag{6.22}
$$

for $n = 2$ and $n \geq 3$, respectively, where we have defined the functions $\chi(x, v', v) = \sigma_a(x, v) k(x, v', v)$ and $v(\theta) = \cos\theta v' + \sin\theta v'^{\perp}$.

Theorem 6.2.2 will be proved in section 6.3.

We thus observe that α_1 blows up a priori faster than Γ_2 as $\varepsilon \to 0$, i.e., as the observation point x becomes closer to the segment where the ballistic term α_0 is supported. This singularity allows us to obtain information on the optical coefficients that is not contained in the ballistic part α_0. Moreover, because of the singular behavior of α_1, such information can be reconstructed in a stable manner.

6.2.4. Stability Estimates. As mentioned above, the singular behaviors of α_0 and α_1 allow us to extract them from the full measurements α. Moreover, such an extraction can be carried out in a stable fashion, in the sense that small errors in the measurement of the albedo operator translates into small errors in the extraction of the terms characterizing α_0 and α_1.

More precisely, let A be the albedo operator corresponding to optical parameters (σ, k) and $\tilde{A}$ the operator corresponding to the optical parameters $(\tilde{\sigma}, \tilde{k})$. From now on, a term superimposed with the $\tilde{}$ sign means a term calculated using the optical parameters $(\tilde{\sigma}, \tilde{k})$ instead of (σ, k). For instance $\tilde{E}(x, y)$ is the equivalent of $E(x, y)$ defined in (6.18) with (σ, k) replaced by $(\tilde{\sigma}, \tilde{k})$.

We first derive the stability of useful functionals of the optical parameters in terms of errors made on the measurements. Let us assume that A is the "real" albedo operator and that $\tilde{A}$ is the "measured" operator. We want to obtain error estimates on the useful functionals of the optical parameters in terms of appropriate metrics for $A - \tilde{A}$. We obtain the following two results. The first result pertains to the stability of the ballistic term in the albedo operator:

THEOREM 6.2.3. *Let A and $\tilde{A}$ be two albedo operators and $(x', v') \in \Gamma_-$. Then we obtain that*

$$
\begin{aligned}
&\int_0^{\tau_+(x', v')} \Big|\sigma_a(x' + tv', v') e^{-\int_0^t \sigma(x' + sv', v') ds} - \tilde{\sigma}_a(x' + tv', v') e^{-\int_0^t \tilde{\sigma}(x' + sv', v') ds}\Big| dt \\
\leq\ & \|A - \tilde{A}\|_{\mathcal{L}(L^1(\Gamma_-, d\xi); L^1(X))}.
\end{aligned}
\tag{6.23}
$$

Theorem 6.2.3 is proved in section 6.4.1.

The stability result obtained from the single scattering component is based on a singular behavior obtained in the vicinity of the ballistic component. Such a behavior cannot be captured by the L^1 norm used above. Instead, we define $\Gamma_1 = \alpha - \alpha_0$ as the Schwartz kernel of the albedo operator where the ballistic part has been removed, i.e., for measurements that are performed away from the support of the ballistic part. Our stability results are obtained in terms of errors on Γ_1 rather than on A. We can then show the following stability result.

THEOREM 6.2.4. *Let us assume that $(\sigma, \tilde{\sigma}) \in \mathcal{C}_b(X \times \mathbb{S}^{n-1})^2$ and that $(k, \tilde{k}) \in \mathcal{C}_b(X \times \mathbb{S}^{n-1} \times \mathbb{S}^{n-1})^2$. Let $(x, x') \in X \times \partial X$ and define $v' = \frac{x-x'}{|x-x'|}$. Let $v'^{\perp} \in \mathbb{S}^{n-1}$ such that $v' \cdot v'^{\perp} = 0$. In dimension $n = 2$, we have*

(6.24)
$$\begin{aligned} &\Big|E(x,x')(\chi(x,v',v') + \chi(x,v',-v')) - \tilde{E}(x,x')(\tilde{\chi}(x,v',v') + \tilde{\chi}(x,v',-v'))\Big| \\ \leq\ &\Big\| \frac{(\Gamma_1 - \tilde{\Gamma}_1)(x,x',v')}{|\nu(x') \cdot v'| w_2(x,x',v')} \Big\|_{L^\infty(X \times \Gamma_-)}, \end{aligned}$$

where $w_2(x,x',v') = 1 + \ln\big(\frac{|x-x'-\tau_+(x',v')v'| - (x-x'-\tau_+(x',v')v')\cdot v'}{|x-x'| - (x-x')\cdot v'}\big)$. When $n \geq 3$, we have

(6.25)
$$\begin{aligned} &\Big| \int_0^\pi \sin^{n-3}(\theta) \Big(E(x,x')\chi(x,v',v(\theta)) - \tilde{E}(x,x')\tilde{\chi}(x,v',v(\theta)) \Big) d\theta \Big| \\ &\leq \Big\| \frac{(\Gamma_1 - \tilde{\Gamma}_1)(x,x',v')}{|\nu(x') \cdot v'| w_n(x,x',v')} \Big\|_{L^\infty(X \times \Gamma_-)}, \end{aligned}$$

where $w_n(x,x',v') = |x - x' - ((x-x')\cdot v')v'|^{2-n}$ and where we use the same notation as in Theorem 6.2.2.

Theorem 6.2.4 is proved in section 6.4.2.

Such results do not grant uniqueness of the reconstruction of the optical parameters in the most general setting. However, they do provide stable, unique, reconstructions in several settings of interest.

6.2.5. Scattering-Free Setting. Let us first assume that $k \equiv 0$ so that $\sigma \equiv \sigma_a$. Then knowledge of the albedo operator uniquely determines $\sigma_a(x,v)$ for all $x \in X$ and $v \in \mathbb{S}^{n-1}$.

Indeed, we deduce from Theorem 6.2.3 that

$$\sigma_a(x' + tv', v') e^{-\int_0^t \sigma_a(x'+sv',v')ds} = -\frac{d}{dt}\Big(e^{-\int_0^t \sigma_a(x'+sv',v')ds} \Big)$$

is uniquely determined and hence $e^{-\int_0^t \sigma_a(x'+sv',v')ds}$ since the latter equals 1 when $t = 0$. Taking the derivative of the negative of the logarithm of the latter expression gives us $\sigma(x' + tv', v')$ for all $(x', v') \in \Gamma_-$ and $t > 0$ and hence $\sigma(x,v)$ for all $(x,v) \in X \times \mathbb{S}^{n-1}$.

Moreover, we have the following stability result.

THEOREM 6.2.5. *Recalling that $\sigma_a(x,v)$ is bounded from above and below by positive constants, we find that when $k \equiv 0$,*

$$\|\sigma_a - \tilde{\sigma}_a\|_{L^\infty(\mathbb{S}^{n-1}; L^1(X))} \leq C \|A - \tilde{A}\|_{\mathcal{L}(L^1(\Gamma_-, d\xi); L^1(X))}. \tag{6.26}$$

Here, C is a constant that depends on the uniform bound M.

The above theorem is proved in section 6.4.1. Note that the above result is local in x' and v'. In other words, $\sigma_a(x,v')$ is uniquely determined by $\{\alpha(y, x - \tau_-(x,v')v', v')|y = x+tv' \text{ for } -\tau_-(x,v') < t < \tau_+(x,v')\}$, that is by the experiment that consists of sending a beam of radiation in direction v' passing through the point x (at least asymptotically since such a transport solution is not an element in $L^1(X \times \mathbb{S}^{n-1})$).

6.2.6. Reconstruction of the Spatial Optical Parameters. We now assume that $k \neq 0$. Then the ballistic component of A and the estimate in Theorem 6.2.3 allow us to uniquely reconstruct both $\sigma_a(x,v)$ and $\sigma(x,v)$ under the assumption that

$$\sigma_a(x,v) = \sigma_a(x,-v), \qquad \sigma(x,v) = \sigma(x,-v). \tag{6.27}$$

We recall that $\sigma_a(x,v)$ is bounded from below by $\sigma_0 > 0$. For technical reasons, we also assume that $\sigma(x,v)$ is known in the δ_0-vicinity of ∂X, i.e., for all $(x,v) \in \mathbb{R}^n \times \mathbb{S}^{n-1}$ such that $\text{dist}(x, \partial X) < \delta_0$ for some $\delta_0 > 0$. Such a hypothesis is not very restrictive from a practical viewpoint.

We denote by $W^{-1,1}(X)$ the Banach space of the continuous linear functionals on the Banach space $W_0^{1,\infty}(X) := \{\phi \in L^\infty(X) \mid \text{supp}\phi \subset X,\ \nabla\phi \in L^\infty(X, \mathbb{C}^n)\}$ (where the gradient ∇ is understood in the distributional sense).

Under the above assumptions, we have the following result.

THEOREM 6.2.6. *The coefficients $\sigma_a(x,v)$ and $\sigma(x,v)$ are uniquely determined by the albedo operator A. Moreover, we have the following stability estimate*

$$\begin{aligned} &\|\sigma - \tilde{\sigma}\|_{L^\infty(\mathbb{S}^{n-1}; W^{-1,1}(X))} \\ &+ \|\sigma_a - \tilde{\sigma}_a\|_{L^\infty(\mathbb{S}^{n-1}; L^1(X))} \leq C\|A - \tilde{A}\|_{\mathcal{L}(L^1(\Gamma_-, d\xi); L^1(X))}. \end{aligned} \tag{6.28}$$

The constant C depends on the parameter δ_0 as well as the uniform bounds σ_0 and M.

This theorem is proved in section 6.4.1. The above result is also local in x' and v'. In other words, $\sigma_a(x,v')$ and $\sigma(x,v')$ are uniquely determined by $\{\alpha(y, x - \tau_-(x,v')v', v')|y = x + tv' \text{ for } -\tau_-(x,v') < t < \tau_+(x,v')\}$, i.e., by the experiment that consists of sending a beam of radiation in direction v' passing through the point x.

Stability estimates may be obtained in stronger norms for σ provided that a priori regularity assumptions be imposed. We show the

COROLLARY 6.2.7. *Let us assume that σ and $\tilde{\sigma}$ are bounded in $L^\infty(\mathbb{S}^{n-1}, W^{r,p}(X))$ by C_0 for $p > 1$ and $r > -1$. Then for all $-1 \leq s \leq r$, we have*

$$\|\sigma - \tilde{\sigma}\|_{L^\infty(\mathbb{S}^{n-1}; W^{s,p}(X))} \leq C\|A - \tilde{A}\|^{\frac{1}{p}\frac{r-s}{1+r}}_{\mathcal{L}(L^1(\Gamma_-, d\xi); L^1(X))}, \tag{6.29}$$

where the constant C depends on C_0 and on the uniform bounds σ_0 and M.

The corollary is proved in section 6.4.1.

6.2.7. Application to Henyey-Greenstein Kernels. Let us assume that $\sigma \in \mathcal{C}_b(X \times \mathbb{S}^{n-1})$ and that $k \in \mathcal{C}_b(X \times \mathbb{S}^{n-1} \times \mathbb{S}^{n-1})$ and let us assume again that $\sigma(x)$ is known in the δ_0-vicinity of ∂X, i.e., for all $x \in \mathbb{R}^n$ such that $\text{dist}(x, \partial X) < \delta_0$ for some $\delta_0 > 0$.

The stability estimate (6.23) allows one to uniquely reconstruct σ_a and σ under the symmetry hypothesis (6.27), which is quite general physically. Indeed, even when attenuation is anisotropic, there is no reason to observe different attenuations in direction v and direction $-v$. The stability estimate in Theorem 6.2.4 provides additional information on the optical coefficients, but not enough to fully reconstruct the scattering kernel $k(x, v', v)$.

In dimension $n = 2$, we gain information only on $k(x, v', v') + k(x, v', -v')$. In dimension $n \geq 3$, we garner information about $\int_0^\pi \chi(x, v', \cos\theta v' + \sin\theta v'^{\perp})d\theta$ for all $v'^{\perp}$ orthogonal to v'. The integration in θ means that one dimension of information is lost in the measurements. Thus, $3n-3$ dimensions of information are available on the $(3n-2)-$dimensional object $k(x, v', v)$.

Let us consider the case of an isotropic absorption $\sigma_a = \sigma_a(x)$ and isotropic scattering in the sense that $k(x, v', v) = k(x, v' \cdot v)$. In such a setting, $k(x, v' \cdot v)$ becomes $(n+1)-$dimensional. Yet, available data in dimension $n \geq 2$ give us information on

$$\sigma_g(x) := k(x, -1) + k(x, 1), \text{ when } n = 2, \tag{6.30}$$

$$\sigma_g(x) := \int_0^\pi k(x, \cos\theta) \sin^{n-3}\theta d\theta, \text{ when } n \geq 3. \tag{6.31}$$

This is different information from the normalization in (6.3)

$$\sigma_s(x) = \int_{\mathbb{S}^{n-1}} k(x, v' \cdot v)dv' = |\mathbb{S}^{n-2}| \int_0^\pi k(x, \cos\theta) \sin^{n-2}\theta d\theta.$$

As a consequence, if $k(x, \cos\theta)$ is of the form $\sigma_s(x)f(x, \cos\theta)$, where $f(x, \cos\theta)$ is parameterized by one function $g(x)$, then we have a chance of reconstructing $g(x)$ from knowledge of $\sigma_g(x)$ and $\sigma_s(x)$ provided $\sigma_s(x) > 0$ (where $\sigma_s = \sigma - \sigma_a$).

This occurs for the classical Henyey-Greenstein (HG) phase function in dimensions $n = 2$ and $n = 3$, where

$$k(x, \lambda) := \sigma_s(x) \frac{1 - g^2(x)}{2\pi(1 + g(x)^2 - 2g(x)\lambda)}, \text{ when } n = 2, \tag{6.32}$$

$$k(x, \lambda) := \sigma_s(x) \frac{1 - g^2(x)}{4\pi(1 + g(x)^2 - 2g(x)\lambda)^{\frac{3}{2}}}, \text{ when } n \geq 3, \tag{6.33}$$

where $g \in C_b(X)$ and $0 \leq g(x) < 1$ for a.e. $x \in X$. Note that

$$\sigma_g(x) = \sigma_s(x)h(g(x)), \tag{6.34}$$

for $x \in X$ where the function $h : [0, 1) \to \mathbb{R}$ is given by

$$h(\kappa) := \frac{1 + \kappa^2}{\pi(1 - \kappa^2)}, \text{ when } n = 2, \tag{6.35}$$

$$h(\kappa) := \int_0^\pi \frac{1 - \kappa^2}{4\pi(1 + \kappa^2 - 2\kappa\cos(\theta))^{\frac{3}{2}}} d\theta, \text{ when } n \geq 3. \tag{6.36}$$

THEOREM 6.2.8. *In the HG phase function in dimension $n = 2, 3$, the parameter $g(x)$ is uniquely determined by the data provided $\sigma_s(x) > 0$ for a.e. $x \in X$.*

Theorem 6.2.8 follows from Theorems 6.2.6, 6.2.4, and from (6.30), (6.31), (6.34) and the following Lemma.

LEMMA 6.2.9. *The function h is strictly increasing on $[0, 1)$, $\dot{h}(0) = 0$, $\ddot{h}(0) > 0$, $\lim_{g\to 1^-}(1-g)h(g) = c(n)$, where $\dot{h}(g) = \frac{dh}{dg}(g)$ and $c(2) = \pi^{-1}$ and $c(3) = (2\pi)^{-1}$.*

Considering (6.35), Lemma 6.2.9 in dimension $n = 2$ is trivial. The proof of Lemma 6.2.9 in dimension $n = 3$ is given in section 6.4.2.

Moreover we have the following stability estimates.

THEOREM 6.2.10. *In dimension $n \geq 2$, we have*

(6.37)
$$\|\sigma_g(x) - \tilde{\sigma}_g(x)\|_{L^1(X)} \leq C\Big(\Big\|\frac{(\Gamma_1 - \tilde{\Gamma}_1)(x, x', v')}{|\nu(x') \cdot v'| w_n(x, x', v')}\Big\|_\infty + \|A - \tilde{A}\|_{\mathcal{L}(L^1(\Gamma_-, d\xi); L^1(X))}\Big),$$

where $w_n(x, x', v')$ is defined in Theorem 6.2.4, and where the constant C depends on δ_0, σ_0 and M.

In addition, for the HG phase function in dimension $n = 2, 3$, we have the following stability estimate: assume $\min(\sigma_s(x), \tilde{\sigma}_s(x)) \geq \sigma_{s,0} > 0$ and $(h(g(x)), h(\tilde{g}(x))) \in W^{1,\infty}(X)^2$, then

(6.38)
$$\|h(g(x)) - h(\tilde{g}(x))\|_{L^1(X)} \leq C\Big(\Big\|\frac{(\Gamma_1 - \tilde{\Gamma}_1)(x, x', v')}{|\nu(x') \cdot v'| w_n(x, x', v')}\Big\|_\infty + \|A - \tilde{A}\|_{\mathcal{L}(L^1(\Gamma_-, d\xi); L^1(X))}\Big),$$

where the constant C depends on δ_0, σ_0, $\sigma_{s,0}$, M and $\min(\|h(g)\|_{W^{1,\infty}(X)}, \|h(\tilde{g})\|_{W^{1,\infty}(X)})$.

Theorem 6.2.10 is proved in section 6.4.2.

The sensitivity of the reconstruction of $g(x)$ degrades as g converges to 0 in the sense that $C(G_0) \to \infty$ as $G_0 \to 0$, $G_0 = \max(\|g\|_\infty, \|\tilde{g}\|_\infty)$, where C is the constant that appears on the right-hand side of (6.38) when we replace $h(g(x)) - h(\tilde{g}(x))$ by $g - \tilde{g}$ on the left-hand side of (6.38). On the other hand, $C(g_0) \to 0$ when $g_0 \to 1$, $g_0 = \min(\|g\|_\infty, \|\tilde{g}\|_\infty)$, so that reconstructions of $g(x)$ are very accurate for $g(x)$ close to 1, i.e., in the case of very anisotropic media.

More precisely, using the properties of the function h, one can replace the left-hand side of (6.38) by $\|g^2 - \tilde{g}^2\|_{L^1(X)}$ (resp. $\|g - \tilde{g}\|_{L^1(X)}$, resp. $\|\frac{1}{1-g} - \frac{1}{1-\tilde{g}}\|_{L^1(X)}$) provided that $\max(\|g\|_\infty, \|\tilde{g}\|_\infty) \leq G_0 < 1$ (resp. $0 < g_0 < \min(\|g\|_\infty, \|\tilde{g}\|_\infty)$ and $\max(\|g\|_\infty, \|\tilde{g}\|_\infty) \leq G_0 < 1$, resp. $\min(\|g\|_\infty, \|\tilde{g}\|_\infty) \geq g_0 > 0$) for some constant G_0 (resp. (g_0, G_0), resp. g_0) and the constant C on the right hand side of (6.38) then depends also on G_0 (resp. (g_0, G_0), resp. g_0).

6.2.8. Reconstructions in the Diffusive Regime. When scattering is large so that the mean free path $\frac{1}{\sigma}(x)$ is small and intrinsic attenuation $\sigma_a(x)$ is small, then radiation inside the domain X is best modeled by a diffusion equation

$$\begin{aligned} &-\nabla \cdot D(x)\nabla I(x) + \sigma_a(x) I(x) = 0 \qquad && x \in X \\ &I(x) = \phi(x) && x \in \partial X, \end{aligned} \tag{6.39}$$

where $I(x) = \int_{S^{n-1}} u(x, v) dv$ is the spatial density of photons and $D(x)$ is the diffusion coefficient. We refer the reader to, e.g., [**24, 61**] for references on the diffusion approximation. When scattering is, e.g., isotropic, i.e., when $k(x, \theta', \theta) = k(x)$, then we find that $D(x) = \frac{1}{n\sigma_s(x)}$, where σ_s is introduced in (6.3) and n is the spatial dimension.

When $D(x)$ is known, then the reconstruction of $\sigma_a(x)$ may be easily obtained by using only one measurement. Indeed, the measurement $H(x) = \sigma_a(x) I(x)$ so that $I(x)$ may be obtained by solving (6.39). Once $I(x)$ is known, it will be positive in X provided that $\phi(x)$ is non trivial and non-negative. Then $\sigma_a(x)$ is obtained by

dividing H by I. When $\phi(x)$ is bounded from below by a positive constant, then we see that the reconstruction of σ_a is unique and clearly stable.

When $(D(x), \sigma_a(x))$ are both unknown, then multiple (at least two) measurements are necessary. This problem will be analyzed elsewhere.

This concludes the section on the derivation and the display of the main results. The mathematical proofs are presented in the following two sections.

6.3. Transport Equation and Estimates

In this section, we prove several results on the decomposition of the albedo operator (Lemmas 6.3.1, 6.3.2 and 6.3.3) and prove Theorems 6.2.1 and 6.2.2.

We first recall the well-posedness of the boundary value problem (6.11) (here $\sigma \in L^\infty(X \times \mathbb{S}^{n-1})$, $k \in L^\infty(X \times \mathbb{S}^{n-1} \times \mathbb{S}^{n-1})$ and $\sigma_a \geq \sigma_0 > 0$) and give a decomposition of the albedo operator. The boundary value problem (6.11) is equivalent to the integral equation

$$(I - K)u = J\phi \tag{6.40}$$

for $u \in L^1(X \times \mathbb{S}^{n-1})$ and $\phi \in L^1(\Gamma_-, d\xi)$, where K is the bounded operator in $L^1(X \times \mathbb{S}^{n-1})$ defined by

$$Ku = \int_0^{\tau_-(x,v)} E(x, x - tv) \int_{\mathbb{S}^{n-1}} k(x - tv, v', v) u(x - tv, v') dv' dt, \tag{6.41}$$

for a.e. $(x, v) \in X \times \mathbb{S}^{n-1}$ and for $u \in L^1(X \times \mathbb{S}^{n-1})$, and J is the bounded operator from $L^1(\Gamma_-, d\xi)$ to $L^1(X \times \mathbb{S}^{n-1})$ defined by

$$J\phi(x, v) = e^{-\int_0^{\tau_-(x,v)} \sigma(x - pv, v) dp} \phi(x - \tau_-(x, v)v, v), \tag{6.42}$$

for a.e. $(x, v) \in X \times \mathbb{S}^{n-1}$.

Since $\sigma_a = \sigma - \sigma_s \geq 0$, it turns out that $I - K$ is invertible in $L^1(X \times S^{n-1})$ [**25**, Lemma 2.4], so that the albedo operator $A : L^1(\Gamma_-, d\xi) \to L^1(X)$ is well-defined by (6.13) and so that the solution u of (6.11) with boundary condition $\phi \in L^1(\Gamma_-, d\xi)$ satisfies

$$u = \sum_{m=0}^{n} K^m J\phi + K^{n+1}(I - K)^{-1} J\phi. \tag{6.43}$$

It follows that

$$\begin{aligned} A\phi &= \int_{\Gamma_-} \left(\sum_{m=0}^{n} \alpha_m(x, x', v') \right) \phi(x', v') d\mu(x') dv' \\ &\quad + \int_{X \times \mathbb{S}^{n-1}} \gamma_{n+1}(x, y, w)((I - K)^{-1} J\phi)(y, w) dy dw, \end{aligned} \tag{6.44}$$

where γ_m, $m \geq 0$, is the distributional kernel of $K^{\bar{m}} : L^1(X \times \mathbb{S}^{n-1}) \to L^1(X)$ defined by

$$K^{\bar{m}} u(x) = \int_{\mathbb{S}^{n-1}} \sigma_a(x, v) K^m u(x, v) dv, \tag{6.45}$$

for a.e. $x \in X$ and $u \in L^1(X \times \mathbb{S}^{n-1})$, and where α_m, $m \geq 0$, is the distributional kernel of $K^{\bar{m}} J : L^1(\Gamma_-, d\xi) \to L^1(X)$.

We give the explicit expression of the distributional kernels α_m, $m \geq 2$, and γ_m, $m \geq 3$ in Lemma 6.3.1 and study the boundedness of α_m in Lemma 6.3.2 and

of γ_{n+1} in Lemma 6.3.3. We then prove Theorems 6.2.1 and 6.2.2 and Lemmas 6.3.2 and 6.3.3. The proof of Lemma 6.3.1 is given in the appendix. For $w \in \mathbb{R}^n$, $w \neq 0$, we set $\hat{w} := \frac{w}{|w|}$.

LEMMA 6.3.1. *For $m \geq 2$ and a.e. $(z_0, z_m, v_m) \in X \times \Gamma_-$, we have*

$$\begin{aligned}(6.46)\qquad \alpha_m(z_0, z_m, v_m) = |\nu(z_m)\cdot v_m| \int_{X^{m-1}} \int_0^{\tau_+(z_m,v_m)} [\sigma_a(z_0, v_0) \\ \times \frac{E(z_0, \dots, z_{m-1}, z_m + t'v_m, z_m) k(z_m + t'v_m, v_m, v_{m-1})}{|z_m + t'v_m - z_{m-1}|^{n-1} \Pi_{i=0}^{m-2} |z_i - z_{i+1}|^{n+1}} \\ \times \Pi_{i=1}^{m-1} k(z_i, v_i, v_{i-1})\big]_{\substack{v_i = z_i \widehat{-z_{i+1}},\ i=0\dots m-2, \\ v_{m-1} = z_{m-1} \widehat{-z_m} - t'z_m}} dt' dz_1 \dots dz_{m-1}.\end{aligned}$$

For $m \geq 3$ and a.e. $(z_0, z_m, v_m) \in X \times X \times \mathbb{S}^{n-1}$, we have

$$\begin{aligned}(6.47)\quad \gamma_m(z_0, z_m, v_m) = \int_{X^{m-1}} \frac{E(z_0, \dots, z_m)}{\Pi_{i=1}^m |z_i - z_{i-1}|^{n-1}} \\ \times [\sigma_a(z_0, v_0) \Pi_{i=1}^m k(z_i, v_i, v_{i-1})]_{v_i = z_i \widehat{-z_{i+1}},\ i=0\dots m-1}\, dz_1 \dots dz_{m-1}.\end{aligned}$$

LEMMA 6.3.2. *For $n = 2$,*

$$(6.48)\qquad \frac{\alpha_1(x, x', v')}{|\nu(x')\cdot v'| \ln\left(\frac{|x-x'-\tau_+(x',v')v'| - (x-x'-\tau_+(x',v')v')\cdot v'}{|x-x'| - (x-x')\cdot v'}\right)} \in L^\infty(X \times \Gamma_-),$$

$$(6.49)\qquad \frac{\alpha_2(x, x', v')}{|\nu(x')\cdot v'|} \in L^\infty(X \times \Gamma_-).$$

For $n \geq 3$, we have

$$(6.50)\qquad \frac{|x - x' - ((x-x')\cdot v')v'|^{n-1-m} \alpha_m(x, x', v')}{|\nu(x')\cdot v'|} \in L^\infty(X \times \Gamma_-),\ 1 \leq m \leq n-2,$$

$$(6.51)\qquad \frac{\alpha_{n-1}(x, x', v')}{|\nu(x')\cdot v'| \ln\left(\frac{1}{|x-x'-((x-x')\cdot v')v'|}\right)} \in L^\infty(X \times \Gamma_-),$$

$$(6.52)\qquad \frac{\alpha_n(x, x', v')}{|\nu(x')\cdot v'|} \in L^\infty(X \times \Gamma_-).$$

We do not use (6.48) and (6.50) for $m = 1$ in order to prove (6.21). However we will use them in the proof of the stability estimates given in Theorem 6.2.4.

LEMMA 6.3.3. *For $n \geq 2$, we have*

$$(6.53)\qquad \gamma_{n+1} \in L^\infty(X \times X \times \mathbb{S}^{n-1}).$$

In addition, we have

$$(6.54)\qquad \bar{K}^{n+1}(I-K)^{-1} J\phi(x) = \int_{\Gamma_-} \Gamma_{n+1}(x, x', v')\phi(x', v') d\mu(x') dv',$$

for a.e. $x \in X$ and for $\phi \in L^1(\Gamma_-, d\xi)$, where

$$(6.55)\qquad \frac{\Gamma_{n+1}(x, x', v')}{|\nu(x')\cdot v'|} \in L^\infty(X \times \Gamma_-).$$

Proof of Theorem 6.2.1. The equality (6.20) for α_0 follows from the definition of the operator J (6.42). From (6.45), (6.41) and (6.42) it follows that

$$\begin{aligned}\bar{K}J\phi(x) &= \int_{\mathbb{S}^{n-1}} \sigma_a(x,v) \int_0^{\tau_-(x,v)} \int_{\mathbb{S}^{n-1}} E(x, x-tv, x-tv-\tau_-(x-tv,v')v') \\ &\times k(x-tv,v',v)\phi(x-tv-\tau_-(x-tv,v')v',v')dv'dtdv, \end{aligned} \tag{6.56}$$

for a.e. $x \in X$ and $\phi \in L^1(\Gamma_-, d\xi)$. Performing the change of variables $z = x - tv$ ($dz = t^{n-1}dtdv$, $t = |z-x|$) on the right-hand side of (6.56), we obtain

$$\begin{aligned}\bar{K}J\phi(x) &= \int_{X\times\mathbb{S}^{n-1}} \frac{\sigma_a(x,\widehat{x-z})}{|x-z|^{n-1}} E(x,z,z-\tau_-(z,v')v') \\ &\times k(z,v',\widehat{x-z})\phi(z-\tau_-(z,v')v',v')dv'dz, \end{aligned} \tag{6.57}$$

for a.e. $x \in X$ and $\phi \in L^1(\Gamma_-, d\xi)$. Performing the change of variables $z = x' + tv'$ ($x' \in \partial X$, $t > 0$, $dz = |\nu(x')\cdot v'|dtd\mu(x')$) on the right hand side of (6.57), we obtain

$$\begin{aligned}\bar{K}J\phi(x) &= \int_{\Gamma_-} \int_0^{\tau_+(x',v')} \frac{\sigma_a(x, x-\widehat{x'-t'v'})}{|x-x'-t'v'|^{n-1}} E(x, x'+t'v', x') \\ &\times k(x'+t'v', v', x-\widehat{x'-t'v'})\phi(x',v')dtd\xi(x',v'), \end{aligned} \tag{6.58}$$

for a.e. $x \in X$ and $\phi \in L^1(\Gamma_-, d\xi)$, which yields (6.20) for α_1.

Now set $\Gamma_2 := \sum_{m=2}^n \alpha_m + \Gamma_{n+1}$ when $n \geq 2$. Taking account of Lemma 6.3.2 (6.49)–(6.52) and Lemma 6.3.3 (6.55), we obtain (6.21). □

Proof of Theorem 6.2.2. We assume that $\sigma \in \mathcal{C}_b(X \times \mathbb{S}^{n-1})$ and $k \in \mathcal{C}_b(X \times \mathbb{S}^{n-1} \times \mathbb{S}^{n-1})$. Let $(x',v') \in \Gamma_-$ and let $t_0' \in (0, \tau_+(x',v'))$ and let $v'^{\perp}$ be such that $v' \cdot v'^{\perp} = 0$. Set $x = x' + t_0'v'$. From (6.20), it follows that

$$\frac{\alpha_1(x+\varepsilon v'^{\perp}, x', v')}{|\nu(x')\cdot v'|} = (L_+ + L_-)(\varepsilon), \qquad \text{where} \tag{6.59}$$

$$L_+(\varepsilon) := \int_0^{t_0'} \frac{E(x+\varepsilon v'^{\perp}, x'+t'v', x')}{((t'-t_0')^2+\varepsilon^2)^{\frac{n-1}{2}}} \sigma_a(x+\varepsilon v'^{\perp}, v_{t',\varepsilon}) k(x'+t'v', v', v_{t',\varepsilon}) dt', \tag{6.60}$$

$$L_-(\varepsilon) := \int_{t_0'}^{\tau_+(x',v')} \frac{E(x+\varepsilon v'^{\perp}, x'+t'v', x')}{((t'-t_0')^2+\varepsilon^2)^{\frac{n-1}{2}}} \sigma_a(x+\varepsilon v'^{\perp}, v_{t',\varepsilon}) k(x'+t'v', v', v_{t',\varepsilon}) dt', \tag{6.61}$$

for $\varepsilon \in (0, \tau_+(x, v'^{\perp}))$, where $v_{t',\varepsilon} = \frac{(t_0'-t')}{\varepsilon}\widehat{v'} + v'^{\perp}$ for $t' \in \mathbb{R}$.

We prove (6.22) for $n = 2$. Consider the function $\operatorname{arcsinh} : \mathbb{R} \to \mathbb{R}$ defined by $\operatorname{arcsinh}(y) := \ln(y + \sqrt{1+y^2})$, for $y \in \mathbb{R}$. Then performing the change of variables $\eta := \frac{\operatorname{arcsinh}(\frac{t_0'-t'}{\varepsilon})}{\operatorname{arcsinh}(\frac{t_0'}{\varepsilon})}$ on the right hand side of (6.60) and performing the change of variables $\eta := \frac{\operatorname{arcsinh}(\frac{t'-t_0'}{\varepsilon})}{\operatorname{arcsinh}(\frac{\tau_+(x',v')-t_0'}{\varepsilon})}$ on the right hand side of (6.61), we obtain

$$L_\pm(\varepsilon) := \operatorname{arcsinh}(\frac{s_\pm}{\varepsilon}) L'_\pm(\varepsilon), \tag{6.62}$$

for $\varepsilon \in (0, \tau_+(x, v'^{\perp}))$, where

$$s_+ := t'_0,\ s_- := \tau_+(x', v') - t'_0, \tag{6.63}$$

$$L'_{\pm}(\varepsilon) := \int_0^1 E(x + \varepsilon v'^{\perp}, x' + t'_{\pm}(\eta, \varepsilon)v', x') \tag{6.64}$$
$$\sigma_a(x + \varepsilon v'^{\perp}, v_{\pm}(\eta, \varepsilon))k(x' + t'_{\pm}(\eta, \varepsilon)v', v', v_{\pm}(\eta, \varepsilon))d\eta$$

$$t'_{\pm}(\eta, \varepsilon) := t'_0 \mp \varepsilon \sinh\Big(\eta \operatorname{arcsinh}(\frac{s_{\pm}}{\varepsilon})\Big), \tag{6.65}$$

$$v_{\pm}(\eta, \varepsilon) := \frac{\pm \sinh\big(\eta \operatorname{arcsinh}(\frac{s_{\pm}}{\varepsilon})\big)\, v' + v'^{\perp}}{\sqrt{\sinh\big(\eta \operatorname{arcsinh}(\frac{s_{\pm}}{\varepsilon})\big)^2 + 1}}, \tag{6.66}$$

for $\eta \in (0, 1)$ (we recall that $\sinh(y) = \frac{e^y - e^{-y}}{2}$, $y \in \mathbb{R}$). Note that using the definition of sinh and arcsinh, we obtain

$$|\varepsilon \sinh\Big(\eta \operatorname{arcsinh}(\frac{s_{\pm}}{\varepsilon})\Big)| \leq \frac{e^{\eta \ln(s_{\pm} + \sqrt{s_{\pm}^2 + 1})} \varepsilon^{1-\eta}}{2}, \tag{6.67}$$

for $\eta \in (0, 1)$. Therefore using (6.65) we obtain

$$t'_{\pm}(\eta, \varepsilon) \to t'_0, \text{ as } \varepsilon \to 0^+ \tag{6.68}$$

for $\eta \in (0, 1)$ and $i = 1, 2$. Note also that from (6.66) it follows that

$$v_{\pm}(\eta, \varepsilon) = \frac{\pm v' + \sinh\big(\eta \operatorname{arcsinh}(\frac{s_{\pm}}{\varepsilon})\big)^{-1} v'^{\perp}}{\sqrt{1 + \sinh\big(\eta \operatorname{arcsinh}(\frac{s_{\pm}}{\varepsilon})\big)^{-2}}} \underset{\varepsilon \to 0^+}{\longrightarrow} \pm v', \tag{6.69}$$

for $\eta \in (0, 1)$ (we used the limit $\sinh\big(\eta \operatorname{arcsinh}(\frac{s}{\varepsilon})\big) \to +\infty$ as $\varepsilon \to 0^+$ which holds for any positive real numbers s and η).

Using (6.64), (6.68), (6.69) and continuity and boundedness of σ and k and σ_a, and using Lebesgue dominated convergence theorem, we obtain

$$L'_{\pm}(\varepsilon) \to \sigma_a(x, \pm v')E(x, x')k(x' + t'_0 v', v', \pm v') \text{ as } \varepsilon \to 0^+. \tag{6.70}$$

Finally note that

$$\operatorname{arcsinh}(\frac{s_{\pm}}{\varepsilon}) = \ln\big(\frac{1}{\varepsilon}\big) + o\Big(\frac{1}{\varepsilon}\Big), \text{ as } \varepsilon \to 0^+. \tag{6.71}$$

Combining (6.59), (6.62), (6.70) and (6.71), we obtain (6.22) for $n = 2$.

We prove (6.22) for $n \geq 3$. Performing the change of variables $\eta = \frac{t' - t'_0}{\varepsilon}$ on the right-hand side of (6.60), we obtain

$$L_+(\varepsilon) = \varepsilon^{2-n} \int_{-\frac{t'_0}{\varepsilon}}^0 E(x + \varepsilon v'^{\perp}, x' + t'_3(\varepsilon, \eta)v', x') \tag{6.72}$$
$$\frac{\sigma_a(x + \varepsilon v'^{\perp}, v)}{\sqrt{\eta^2 + 1}^{n-1}} k(x' + t'_3(\varepsilon, \eta)v', v', v)_{|v = -\widehat{\eta v' + v'^{\perp}}} d\eta,$$

for $\varepsilon \in (0, \tau_+(x, v'^{\perp}))$, where $t'_3(\varepsilon, \eta) = t'_0 + \varepsilon\eta$ for $\eta \in \mathbb{R}$. Note that

$$t'_3(\varepsilon, \eta) \to t'_0, \text{ as } \varepsilon \to 0^+. \tag{6.73}$$

Therefore, using the Lebesgue dominated convergence theorem and continuity and boundedness of (σ, k, σ_a), we obtain

$$L_+(\varepsilon) = \varepsilon^{2-n} E(x, x') \int_{-\infty}^0 \frac{\sigma_a(x, v)k(x, v', v)_{|v = -\widehat{\eta v' + v'^{\perp}}}}{\sqrt{\eta^2 + 1}^{n-1}} d\eta + o(\varepsilon^{2-n}), \tag{6.74}$$

as $\varepsilon \to 0^+$. Similarly performing the change of variables $\eta = \frac{t'-t'_0}{\varepsilon}$ on the right hand side of (6.61), and using Lebesgue dominated convergence theorem and continuity and boundedness of (σ, k, σ_a), we obtain

$$L_-(\varepsilon) = \varepsilon^{2-n} E(x,x') \int_0^{+\infty} \frac{\sigma_a(x,v)k(x,v',v)_{|v=-\widehat{\eta v'+v'}^{\perp}}}{\sqrt{\eta^2+1}^{n-1}} d\eta + o(\varepsilon^{2-n}), \tag{6.75}$$

as $\varepsilon \to 0^+$. Note that performing the change of variables $\cos(\theta) = \frac{-\eta}{\sqrt{1+\eta^2}}$, $\theta \in (0,\pi)$, $(\eta = -\frac{\cos(\theta)}{\sin(\theta)}$, $d\eta = \frac{1}{\sin(\theta)^2} d\theta)$ we have

$$\int_{-\infty}^{+\infty} \frac{\sigma_a(x,v)k(x,v',v)_{|v=-\widehat{\eta v'+v'}^{\perp}}}{\sqrt{\eta^2+1}^{n-1}} d\eta = \int_0^{\pi} \sin(\theta)^{n-3} \sigma_a(x,v(\theta))k(x,v',v(\theta))d\theta. \tag{6.76}$$

Adding (6.74) and (6.75) and using (6.76) and (6.59), we obtain (6.22) for $n \geq 3$.□

Proof of Lemma 6.3.2. First note that from (6.20) and (6.46), it follows that

$$\alpha_m(x,x',v') \leq \|\sigma_a\|_\infty \|k\|_\infty^m |\nu(x') \cdot v'| I_{m,n}(x,x',v'), \tag{6.77}$$

for a.e. $(x,x',v') \in X \times \Gamma_-$ and for $m \in \mathbb{N}$, $m \geq 1$, where

$$I_{1,n}(z_0,x',v') = \int_0^{\tau_+(x',v')} \frac{dt'}{|z_0 - x' - t'v'|^{n-1}}, \tag{6.78}$$

$$I_{m+1,n}(z_0,x',v') = \int_{X^m} \int_0^{\tau_+(x',v')} \frac{dt' dz_1 \dots dz_m}{|x' + t'v' - z_m|^{n-1} \Pi_{i=1}^m |z_i - z_{i-1}|^{n-1}}, \tag{6.79}$$

for $(z_0,x',v') \in X \times \Gamma_-$ and $m \geq 1$.

We prove (6.48) and (6.49). Let $n = 2$. Let $(x,x',v') \in X \times \Gamma_-$ be such that $x \neq x' + \lambda v'$ for any $\lambda \in \mathbb{R}$. Set $(w)_\perp := w - (w \cdot v')v'$ for any $w \in \mathbb{R}^n$. Using (6.78) and using the equality $|x - x' - t'v'|^2 = (t' - (x-x') \cdot v')^2 + |(x-x')_\perp|^2$, we obtain

$$I_{1,n}(x,x',v') = \int_{-(x-x')\cdot v'}^{\tau_+(x',v')-(x-x')\cdot v'} \frac{1}{(|(x-x')_\perp|^2 + t^2)^{\frac{n-1}{2}}} dt, \tag{6.80}$$

$$= \ln\Big(\frac{|x - x' - \tau_+(x',v')v'| - (x - x' - \tau_+(x',v')v') \cdot v'}{|x-x'| - (x-x') \cdot v'} \Big), \tag{6.81}$$

where we used that $\int_0^x \frac{dt}{\sqrt{1+t^2}} = \ln\big(x + \sqrt{1+x^2}\big)$. Estimate (6.48) follows from (6.77) and (6.81).

Let $(x,x',v') \in X \times \Gamma_-$ be such that $x \neq x' + \lambda v'$ for any $\lambda \in \mathbb{R}$. Using (6.81) (with "$x = z$") and (6.79), we obtain

$$\begin{aligned} I_{2,n}(x,x',v') &= \int_X \frac{\ln\Big(\frac{|z-x'-\tau_+(x',v')v'| - (z-x'-\tau_+(x',v')v')\cdot v'|}{|z-x'| - (z-x')\cdot v'} \Big)}{|x-z|} dz \\ &= I'_{2,n}(x, x' + \tau_+(x',v')v', v') - I'_{2,n}(x,x',v'), \end{aligned} \tag{6.82}$$

where

$$I'_{2,n}(x,a,v') = \int_X \frac{\ln(|z-a| - (z-a)\cdot v')}{|x-z|} dz, \tag{6.83}$$

for $a \in \bar{X}$. We prove

$$\sup_{(x,a,v') \in X \times \bar{X} \times \mathbb{S}^{n-1}} |I'_{2,n}(x,a,v')| < \infty. \tag{6.84}$$

Then estimate (6.49) follows from (6.77), (6.82) and (6.84).

Let $(x,a,v') \in X \times \bar{X} \times \mathbb{S}^{n-1}$. Note that by using (6.83), we obtain

$$\begin{aligned} |I'_{2,n}(x,a,v')| &\leq C \int_X \frac{(|z-a| + (z-a)\cdot v')^{\frac{1}{8}}}{|x-z|(|z-a|^2 - ((z-a)\cdot v')^2)^{\frac{1}{8}}} dz \\ &\leq (2D)^{\frac{1}{8}} C \int_X \frac{1}{|x-z|(|z-a|^2 - ((z-a)\cdot v')^2)^{\frac{1}{8}}} dz, \end{aligned} \tag{6.85}$$

where $C := \sup_{r\in(0,6D)} r^{\frac{1}{8}} |\ln(r)| < \infty$ and D denotes the diameter of X. Consider $v'^{\perp} \in \mathbb{S}^{n-1}$ a unit vector orthogonal to v' and perform the change of variable $z = a + \lambda_1 v' + \lambda_2 v'^{\perp}$, then we obtain

$$|I'_{2,n}(x,a,v')| \leq (2D)^{\frac{1}{8}} C \int_{[-D,D]^2} \frac{d\lambda_1 d\lambda_2}{((\lambda_{1,x}-\lambda_1)^2 + (\lambda_{2,x}-\lambda_2)^2)^{\frac{1}{2}} |\lambda_2|^{\frac{1}{4}}}, \tag{6.86}$$

where $\lambda_{1,x} v' + \lambda_{2,x} v'^{\perp} = x - a$. Then note that

$$\int_{-D}^{D} \frac{d\lambda_1}{((\lambda_{1,x}-\lambda_1)^2 + (\lambda_{2,x}-\lambda_2))^{\frac{1}{2}}} = \ln\left(\frac{D - \lambda_{1,x} + ((\lambda_2-\lambda_{2,x})^2 + (D-\lambda_{1,x})^2)^{\frac{1}{2}}}{-D - \lambda_{1,x} + ((\lambda_2-\lambda_{2,x})^2 + (D+\lambda_{1,x})^2))^{\frac{1}{2}}} \right), \tag{6.87}$$

Combining (6.86) and (6.87), we obtain

$$\begin{aligned} |I'_{2,n}(x,a,v')| &\leq C' \int_{-D}^{D} \frac{(D-\lambda_{1,x} + ((\lambda_2-\lambda_{2,x})^2 + (D-\lambda_{1,x})^2)^{\frac{1}{2}})^{\frac{1}{8}} d\lambda_2}{|\lambda_2|^{\frac{1}{4}}(-(D+\lambda_{1,x}) + \sqrt{(\lambda_2-\lambda_{2,x})^2 + (D+\lambda_{1,x})^2})^{\frac{1}{8}}} \\ &\leq C'' \int_{-D}^{D} \frac{(D+\lambda_{1,x} + ((\lambda_2-\lambda_{2,x})^2 + (D+\lambda_{1,x})^2)^{\frac{1}{2}})^{\frac{1}{8}}}{|\lambda_2|^{\frac{1}{4}}|\lambda_2-\lambda_{2,x}|^{\frac{1}{4}}} d\lambda_2 \\ &\leq C''' \int_{-D}^{D} \frac{d\lambda_2}{|\lambda_2|^{\frac{1}{4}}|\lambda_2-\lambda_{2,x}|^{\frac{1}{4}}} = C'''|\lambda_{2,x}|^{\frac{1}{2}} \int_{-\frac{D}{|\lambda_{2,x}|}}^{\frac{D}{|\lambda_{2,x}|}} \frac{ds}{|s|^{\frac{1}{4}}|s-1|^{\frac{1}{4}}}, \end{aligned} \tag{6.88}$$

where $C' := (2D)^{\frac{1}{8}} C^2$, $C'' := (12D^2)^{\frac{1}{8}} C^2$ and $C''' := (72D^3)^{\frac{1}{8}} C^2$. Finally note that

$$|\lambda_{2,x}|^{\frac{1}{2}} \int_{|s|\leq \frac{D}{|\lambda_{2,x}|}} \frac{1}{|s|^{\frac{1}{4}}|s-1|^{\frac{1}{4}}} ds \leq C_1(\lambda_{2,x}) + C_2(\lambda_{2,x}), \quad \text{where} \tag{6.89}$$

$$C_1(\lambda_{2,x}) := |\lambda_{2,x}|^{\frac{1}{2}} \int_{|s|\leq 2} |s|^{-\frac{1}{4}}|s-1|^{-\frac{1}{4}} ds \leq D^{\frac{1}{2}} \int_{|s|\leq 2} |s|^{-\frac{1}{4}}|s-1|^{-\frac{1}{4}} ds \tag{6.90}$$

$$\begin{aligned} C_2(\lambda_{2,x}) &:= |\lambda_{2,x}|^{\frac{1}{2}} \int_{2\leq|s|\leq \max(2,\frac{D}{|\lambda_{2,x}|})} |s|^{-\frac{1}{4}}|s-1|^{-\frac{1}{4}} ds \leq |\lambda_{2,x}|^{\frac{1}{2}} 2^{\frac{1}{4}} \int_{2\leq|s|\leq \max(2,\frac{D}{|\lambda_{2,x}|})} |s|^{-\frac{1}{2}} ds \\ &\leq \left(|\lambda_{2,x}| \max(2, \frac{D}{|\lambda_{2,x}|})\right)^{\frac{1}{2}} \leq (2D)^{\frac{1}{2}}. \end{aligned} \tag{6.91}$$

Combining (6.88)–(6.91) we obtain (6.84).

The statements (6.50)–(6.52) follow from (6.77) and the following statements (6.92)–(6.94)

$$|x-x'-((x-x')\cdot v')v'|^{n-1-m} I_{m,n}(x,x',v') \in L^\infty(X\times\Gamma_-), \tag{6.92}$$

$$\frac{I_{n-1,n}(x,x',v')}{\ln\left(\frac{1}{|x-x'-((x-x')\cdot v')v'|}\right)} \in L^\infty(X\times\Gamma_-), \tag{6.93}$$

$$I_{n,n}(x,x',v') \in L^\infty(X\times\Gamma_-), \tag{6.94}$$

for $(m,n)\in\mathbb{N}\times\mathbb{N}$, $n\geq 3$, $1\leq m\leq n-2$ and where $I_{m,n}$ is defined by (6.78) and (6.79).

We prove (6.92)–(6.94), which will complete the proof of Lemma 6.3.2. We proceed by induction on m. We prove (6.92) for $m=1$. Let $n\geq 3$. Note that formula (6.80) still holds. Note also that

$$|w-\lambda v'|^2 = |w_\perp|^2 + |w\cdot v'-\lambda|^2 \geq 2^{-1}(|w_\perp|+|w\cdot v'-\lambda|)^2, \tag{6.95}$$

for $(w,\lambda)\in\mathbb{R}^n\times(-D,D)$, $|w|\leq 2D$. Therefore

$$\int_{-2D}^{2D}\frac{d\lambda}{|w-\lambda v'|^{n-1}} \leq \int_{-2D}^{2D}\frac{2^{\frac{n-1}{2}}d\lambda}{(|w_\perp|+|\lambda|)^{n-1}} \leq \frac{2^{\frac{n+1}{2}}}{(n-2)|w_\perp|^{n-2}}. \tag{6.96}$$

Thus (6.92) for $m=1$ follows from (6.96) and (6.80).

Let $m\in\mathbb{N}$, $m\geq 1$ be such that (6.92)–(6.94) hold for any $n\geq 3$. We prove that (6.92)–(6.94) hold for any $n\geq 3$ and for "m"$=m+1$. Let (x,x',v') be such that $x\neq x'+\lambda v'$ for any $\lambda\in\mathbb{R}$. From (6.78) and (6.79) it follows that

$$I_{m+1,n}(x,x',v') \leq \int_X \frac{I_{m,n}(z,x',v')}{|x-z|^{n-1}}dz. \tag{6.97}$$

Assume that $m+1\leq n-1$. Then from (6.97) and (6.92) for (m,n) it follows that there exists a constant C (which does not depend on (x,x',v')) such that

$$I_{m+1,n}(x,x',v') \leq C\int_X \frac{1}{|x-z|^{n-1}|(z-x')_\perp|^{n-1-m}}dz. \tag{6.98}$$

Performing the change of variables $z-x'=z'+\lambda v'$, $z'\cdot v'=0$, we obtain

$$I_{m+1,n}(x,x',v') \leq C\int_{\substack{z'\cdot v'=0\\ |z'|\leq D}}\left(\int_{-D}^{D}\frac{d\lambda}{|x-x'-z'-\lambda v'|^{n-1}}\right)\frac{dz'}{|z'|^{n-1-m}}. \tag{6.99}$$

Combining (6.99) and (6.96) (with "$w=x-x'-z'$"), we obtain

$$I_{m+1,n}(x,x',v') \leq \frac{2^{\frac{n+1}{2}}C}{n-2}I''_{m+1,n}(x,x',v'), \quad \text{where} \tag{6.100}$$

$$\begin{aligned} I''_{m+1,n}(x,x',v') &:= \int_{\substack{z'\cdot v'=0\\ |z'|\leq D}}\frac{dz'}{|(x-x')_\perp - z'|^{n-2}|z'|^{n-1-m}} \\ &= \int_{z'\in B_{n-1}(0,D)}\frac{dz'}{||(x-x')_\perp|e_1-z'|^{n-2}|z'|^{n-1-m}}, \end{aligned} \tag{6.101}$$

and $e_1=(1,0,\ldots,0)\in\mathbb{R}^{n-1}$ and $B_{n-1}(0,D)$ denotes the Euclidean ball of $\mathbb{R}^{n-1}$ of center 0 and radius D. Using spherical coordinates $z'=|(x-x')_\perp|e_1+r\Omega$,

$(r,\Omega)\in(0,+\infty)\times\mathbb{S}^{n-2}$ and $\Omega=(\sin(\theta),\cos(\theta)\Theta)$ $((\theta,\Theta)\in(-\frac{\pi}{2},\frac{\pi}{2})\times\mathbb{S}^{n-3})$ we obtain

$$I''_{m+1,n}(x,x',v')\leq|\mathbb{S}^{n-3}|\int_{-\frac{\pi}{2}}^{\frac{\pi}{2}}\cos^{n-3}(\theta)$$
$$\times\Big(\int_0^{2D}\frac{dr}{(|r+|(x-x')_\perp|\sin(\theta)|^2+|(x-x')_\perp|^2\cos(\theta)^2)^{\frac{n-1-m}{2}}}\Big)d\theta \tag{6.102}$$

(by convention $|\mathbb{S}^0|:=2$). Note that by performing the change of variables "$r=r+|(x-x')_\perp|\sin(\theta)$" and using the estimate $a^2+b^2\geq 2^{-1}(a+b)^2$, we obtain

$$\int_0^{2D}\frac{dr}{(|r+|(x-x')_\perp|\sin(\theta)|^2+|(x-x')_\perp|^2\cos(\theta)^2)^{\frac{n-1-m}{2}}}$$
$$\leq\int_{-3D}^{3D}\frac{2^{\frac{n-1}{2}}dr}{(|r|+|(x-x')_\perp|\cos(\theta))^{n-1-m}}=\int_0^{3D}\frac{2^{\frac{n+1}{2}}dr}{(r+|(x-x')_\perp|\cos(\theta))^{n-1-m}}$$
$$\leq\begin{cases}\dfrac{2^{\frac{n+1}{2}}}{(n-m-2)(|(x-x')_\perp|\cos(\theta))^{n-2-m}},\ \text{if } m+1<n-1,\\ 2^{\frac{n+1}{2}}\ln\Big(\dfrac{3D+|(x-x')_\perp|\cos(\theta)}{|(x-x')_\perp|\cos(\theta)}\Big),\ \text{if } m+1=n-1,\end{cases} \tag{6.103}$$

for $\theta\in(-\frac{\pi}{2},\frac{\pi}{2})$. Assume $m+1<n-1$. Then combining (6.102) and (6.103), we obtain

$$I''_{m+1,n}(x,x',v')\leq\frac{2^{\frac{n+1}{2}}|\mathbb{S}^{n-3}|}{(n-2-m)|(x-x')_\perp|^{n-2-m}}\int_{-\frac{\pi}{2}}^{\frac{\pi}{2}}\cos^{m-1}(\theta)d\theta. \tag{6.104}$$

Therefore using also (6.100) we obtain that (6.92) holds for "m"$=m+1<n-1$. Assume $m+1=n-1$. Then note that

$$\ln\Big(\frac{3D+|(x-x')_\perp|\cos(\theta)}{|(x-x')_\perp|\cos(\theta)}\Big)\leq\ln\Big(\frac{4D}{|(x-x')_\perp|\cos(\theta)}\Big)$$
$$\leq\ln(4D)+\ln(\frac{1}{|(x-x')_\perp|})-\ln(\cos(\theta)), \tag{6.105}$$

for $\theta\in(-\frac{\pi}{2},\frac{\pi}{2})$. Combining (6.102), (6.103) and (6.105), we obtain

$$I''_{m+1,n}(x,x',v')\leq 2^{\frac{n+1}{2}}|\mathbb{S}^{n-3}|\left(C_1+C_2\ln(\frac{1}{|(x-x')_\perp|})\right), \tag{6.106}$$

where $C_1:=\int_{-\frac{\pi}{2}}^{\frac{\pi}{2}}\cos^{n-3}(\theta)(\ln(4D)-\ln(\cos(\theta)))d\theta<\infty$ and $C_2:=\int_{-\frac{\pi}{2}}^{\frac{\pi}{2}}\cos^{n-3}(\theta)d\theta$. Therefore using also (6.100), we obtain that (6.93) holds for "m"$=m+1=n-1$.

Assume that $m+1=n$. From (6.97) and (6.93) for $(n-1,n)$ it follows that there exists a constant C (which does not depend on (x,x',v')) such that

$$I_{m+1,n}(x,x',v')\leq C\int_X\frac{\left|\ln\left(\frac{1}{|(z-x')_\perp|}\right)\right|}{|x-z|^{n-1}}dz. \tag{6.107}$$

Performing the change of variables $z-x'=z'+\lambda v'$, $z'\cdot v'=0$, we obtain

$$I_{m+1,n}(x,x',v')\leq C\int_{\substack{z'\cdot v'=0\\ |z'|\leq D}}\left(\int_{-D}^{D}\frac{d\lambda}{|x-x'-z'-\lambda v'|^{n-1}}\right)\left|\ln\left(\frac{1}{|z'|}\right)\right|dz'. \tag{6.108}$$

Combining (6.108) and (6.96) (with "$w = x - x' - z'$"), we obtain

$$I_{m+1,n}(x,x',v') \leq \frac{2^{\frac{n+1}{2}}C}{n-2} I''_{n,n}(x,x',v'), \tag{6.109}$$

where

$$\begin{aligned} I''_{n,n}(x,x',v') &:= \int_{\substack{z'\cdot v'=0 \\ |z'|\leq D}} \frac{\left|\ln\left(\frac{1}{|z'|}\right)\right|}{|(x-x')_\perp - z'|^{n-2}} dz' \\ &= \int_{z'\in B_{n-1}(0,D)} \frac{\left|\ln\left(\frac{1}{|z'|}\right)\right|}{||(x-x')_\perp|e_1 - z'|^{n-2}} dz' \\ &\leq \int_{z'\in B_{n-1}(0,D)} \frac{C'}{|z'|^{\frac{1}{2}}||(x-x')_\perp|e_1 - z'|^{n-2}} dz', \end{aligned} \tag{6.110}$$

and $C' := \sup_{r\in(0,D)} r^{\frac{1}{2}}|\ln(r)|$, $e_1 = (1,0,\ldots,0) \in \mathbb{R}^{n-1}$, and where $B_{n-1}(0,D)$ denotes the Euclidean ball of $\mathbb{R}^{n-1}$ of center 0 and radius D. Using spherical coordinates $z' = |(x-x')_\perp|e_1 + r\Omega$, $(r,\Omega) \in (0,+\infty)\times\mathbb{S}^{n-2}$ and $\Omega = (\sin(\theta), \cos(\theta)\Theta)$ ($(\theta,\Theta) \in (-\frac{\pi}{2},\frac{\pi}{2})\times\mathbb{S}^{n-3}$), and using the estimate $||(x-x')_\perp|e_1 + r\Omega| \geq |r + |(x-x')_\perp|\sin(\theta)|$, we obtain

$$I''_{n,n}(x,x',v') \leq |\mathbb{S}^{n-3}| \int_{-\frac{\pi}{2}}^{\frac{\pi}{2}} \cos^{n-3}(\theta) \left(\int_0^{2D} \frac{C'}{|r + |(x-x')_\perp|\sin(\theta)|^{\frac{1}{2}}} dr \right) d\theta. \tag{6.111}$$

Note that

$$\int_0^{2D} \frac{C'}{|r + |(x-x')_\perp|\sin(\theta)|^{\frac{1}{2}}} dr \leq \int_{-3D}^{3D} \frac{C'}{|r|^{\frac{1}{2}}} dr < \infty, \tag{6.112}$$

for $\theta \in (-\frac{\pi}{2},\frac{\pi}{2})$. Combining (6.109), (6.111) and (6.112), we obtain

$$I_{m+1,n}(x,x',v') \leq \frac{2^{\frac{n+1}{2}}CC'|\mathbb{S}^{n-3}|}{n-2} \int_{-\frac{\pi}{2}}^{\frac{\pi}{2}} \cos^{n-3}(\theta) d\theta \int_{-3D}^{3D} r^{-\frac{1}{2}} dr. \tag{6.113}$$

Therefore (6.94) holds for "m"$= m+1 = n$. □

Proof of Lemma 6.3.3. We first prove the estimates (6.114) and (6.115) given below

$$\int_X \frac{dz_1}{|z_0 - z_1||z_1 - z|^{n-1}} \leq C_2 - C_2' \ln(|z_0 - z|), \text{ when } n = 2 \tag{6.114}$$

$$\int_X \frac{dz_1}{|z_0 - z_1|^m|z_1 - z|^{n-1}} \leq \frac{C_n}{|z_0 - z|^{m-1}}, \text{ when } n \geq 3, \tag{6.115}$$

for $(z_0,z) \in X^2$ and for $m \in \mathbb{N}$ such that $z_0 \neq z$ and $2 \leq m \leq n-1$, where the positive constants C_n, C_2' do not depend on (z_0,z).

Let $(z_0,z) \in X^2$ and let $m \in \mathbb{N}$ be such that $z_0 \neq z$ and $1 \leq m \leq n-1$. Performing the change of variables $z_1 = z + r_1\Omega_1$, $(r_1,\Omega_1) \in (0,D)\times\mathbb{S}^{n-1}$ (where D denotes the diameter of X), we obtain

$$\begin{aligned} \int_X \frac{dz_1}{|z_0 - z_1|^m|z_1 - z|^{n-1}} &\leq \int_0^D \int_{\mathbb{S}^{n-1}} \frac{d\Omega_1}{|r\Omega - r_1\Omega_1|^m} dr_1 \\ &\leq \int_0^D \int_{\mathbb{S}^{n-1}} \frac{d\Omega_1}{|re_1 - r_1\Omega_1|^m} dr_1 \end{aligned} \tag{6.116}$$

where $e_1 = (1, 0, \dots, 0) \in \mathbb{R}^n$ (we also used a rotation that maps Ω to the vector e_1) and

$$r = |z - z_0|,\ \Omega = \frac{z_0 - z}{|z_0 - z|}. \tag{6.117}$$

Performing the change of variables $\Omega_1 = (\sin(\theta_1), \cos(\theta_1)\Theta_1)$, $(\theta_1, \Theta_1) \in (-\frac{\pi}{2}, \frac{\pi}{2}) \times \mathbb{S}^{n-2}$), on the right hand side of (6.116) we obtain

$$\int_0^D \int_{\mathbb{S}^{n-1}} \frac{d\Omega_1}{|re_1 - r_1\Omega_1|^m} dr_1 = c(n) \int_0^D \int_{-\frac{\pi}{2}}^{\frac{\pi}{2}} \frac{\cos(\theta_1)^{n-2} d\theta_1}{(r^2 + r_1^2 - 2rr_1 \sin(\theta_1))^{\frac{m}{2}}} dr_1, \tag{6.118}$$

where $c(n) := |\mathbb{S}^{n-2}|$ (by convention $c(2) := 2$).

Consider the case $n = 2$ and $m = 1$. Using (6.118) and the estimate $(r^2 + r_1^2 - 2rr_1 \sin(\theta_1))^{\frac{1}{2}} \geq 2^{-\frac{1}{2}}(|r_1 - r\sin(\theta_1)| + r|\cos(\theta_1)|)$, we obtain

$$\begin{aligned} S(r) &:= \int_0^D \int_{-\frac{\pi}{2}}^{\frac{\pi}{2}} \frac{d\theta_1}{(r^2 + r_1^2 - 2rr_1 \sin(\theta_1))^{\frac{m}{2}}} dr_1 \\ &\leq \int_0^{2\pi} \int_0^D \frac{\sqrt{2} dr_1}{|r_1 - r\sin(\theta_1)| + r|\cos(\theta_1)|} d\theta_1 \\ &\leq \int_0^{2\pi} \int_{-2D}^{2D} \frac{\sqrt{2} dr_1}{|r_1| + r|\cos(\theta_1)|} d\theta_1 \leq \int_0^{2\pi} \int_0^{2D} \frac{2^{\frac{3}{2}} dr_1}{r_1 + r|\cos(\theta_1)|} d\theta_1 \end{aligned} \tag{6.119}$$

$$\leq 2^{\frac{3}{2}} \int_0^{2\pi} \ln\left(\frac{2D + r|\cos(\theta_1)|}{r|\cos(\theta_1)|}\right) d\theta_1 \leq 2^{\frac{3}{2}} \int_0^{2\pi} \ln\left(\frac{4D}{r|\cos(\theta_1)|}\right) d\theta_1 \leq C_1 - 2^{\frac{7}{2}} \pi \ln(r), \tag{6.120}$$

where $C_1 := 2^{\frac{3}{2}} \int_0^{2\pi} (\ln(4D) - \ln(|\cos(\theta_2)|)) d\theta_2 < \infty$. Estimate (6.114) follows from (6.116), (6.118) and (6.120).

Consider the case $n \geq 3$ and $2 \leq m \leq n - 1$. Note that

$$r\cos(\theta_1) \leq \sqrt{r^2 + r_1^2 - 2rr_1 \sin(\theta_1)}, \tag{6.121}$$

for $(r, r_1, \theta_1) \in (0, +\infty)^2 \times (-\frac{\pi}{2}, \frac{\pi}{2})$. Combining (6.118) and (6.121), we obtain

$$\begin{aligned} &\int_0^D \int_{\mathbb{S}^{n-1}} \frac{d\Omega_1}{|re_1 - r_1\Omega_1|^m} dr \leq \frac{c(n)}{r^{m-2}} \int_0^D \int_{-\frac{\pi}{2}}^{\frac{\pi}{2}} \frac{\cos(\theta_1)^{n-m} d\theta_1}{(r^2 + r_1^2 - 2rr_1 \sin(\theta_1))} dr_1 \\ &\leq \frac{c(n)}{r^{m-2}} \int_0^D \int_{-\frac{\pi}{2}}^{\frac{\pi}{2}} \frac{\cos(\theta_1) d\theta_1}{(r^2 + r_1^2 - 2rr_1 \sin(\theta_1))} dr_1 = \frac{c(n)}{r^{m-1}} \int_0^D \frac{\ln\left(\frac{r + r_1}{r - r_1}\right)}{r_1} dr_1 \\ &= \frac{c(n)}{r^{m-1}} \int_0^{\frac{D}{r}} \frac{\ln\left(\frac{1+\eta}{1-\eta}\right)}{\eta} d\eta \end{aligned} \tag{6.122}$$

(we perform the change of variables $r_1 = r\eta$, $dr_1 = rd\eta$). Finally (6.115) follows from (6.122) and (6.116) and the estimate $\int_0^{+\infty} \frac{\ln(\frac{1+\eta}{1-\eta})}{\eta} d\eta < +\infty$.

We are now ready to prove (6.53). Let $n \geq 2$. From (6.47), it follows that

$$|\gamma_{n+1}(z_0, z_{n+1}, v_{n+1})| \leq \|\sigma_a\|_\infty \|k\|^{n+1}_{L^\infty(X \times \mathbb{S}^{n-1} \times \mathbb{S}^{n-1})} R(z_0, z_{n+1}), \tag{6.123}$$

for a.e. $(z_0, z_{n+1}, v_{n+1}) \in X \times X \times \mathbb{S}^{n-1}$, where

$$R(z_0, z_{n+1}) = \int_{X^n} \frac{1}{\Pi_{i=1}^{n+1} |z_i - z_{i-1}|^{n-1}} dz_1 \dots dz_n, \tag{6.124}$$

for $(z_0, z_{n+1}) \in X \times X$.

Assume $n = 2$. Combining (6.114) and (6.124) we obtain

$$R(z_0, z_3) \leq \int_X \frac{C - C' \ln(|z_3 - z_1|)}{|z_1 - z_0|} dz_1. \tag{6.125}$$

Performing the change of variables $z_1 = z_0 + r_1\Omega_1$, on the right hand side of (6.125), we obtain

$$R(z_0, z_3) \leq \int_0^D \int_{\mathbb{S}^1} (C - C' \ln(|r_1\Omega_1 + z_0 - z_3|)) d\Omega_1 dr_1. \tag{6.126}$$

Assume $n \geq 3$. Using (6.124) and (6.115), we obtain

$$R(z_0, z_{n+1}) \leq C \int_{X^2} \frac{1}{|z_{n+1} - z_n|^{n-1} |z_n - z_{n-1}|^{n-1} |z_{n-1} - z_0|} dz_n dz_{n-1}, \tag{6.127}$$

where C does not depend on (z_0, z_{n+1}). Performing the change of variables $z_i = z_{i+1} + r_i\Omega_i$, $(r_i, \Omega_i) \in (0, +\infty) \times \mathbb{S}^{n-1}$, $i = n-1, n$, we obtain

$$\begin{aligned} R(z_0, z_{n+1}) &\leq \int_{(0,D)^2 \times (\mathbb{S}^{n-1})^2} \frac{dr_{n-1} dr_n d\Omega_{n-1} d\Omega_n}{|z_{n+1} - z_0 + r_n\Omega_n + r_{n-1}\Omega_{n-1}|} \\ &= \int_{(0,D)\times\mathbb{S}^{n-1}} \int_{(0,D)\times\mathbb{S}^{n-1}} \frac{dr_{n-1} d\Omega_{n-1}}{||z_{n+1} - z_0 + r_n\Omega_n|e_1 + r_{n-1}|} dr_n d\Omega_n, \end{aligned} \tag{6.128}$$

where $e_1 = (1, 0, \dots, 0) \in \mathbb{R}^n$. Performing the change of variables $\Omega = (\sin(\theta), \cos(\theta)\Theta)$, $(\theta, \Theta) \in (-\frac{\pi}{2}, \frac{\pi}{2}) \times \mathbb{S}^{n-2}$, we obtain

$$\int_0^D \int_{\mathbb{S}^{n-1}} \frac{d\Omega}{||w|e_1 - r\Omega|} dr \leq c(n) S(|w|), \tag{6.129}$$

for $w \in \mathbb{R}^n$, $w \neq 0$, where $c(n) := |\mathbb{S}^{n-2}|$ and $S(|w|)$ is defined by (6.119). Therefore from (6.129), (6.120) and (6.128), it follows that

$$R(z_0, z_{n+1}) \leq \int_{(0,D)\times\mathbb{S}^{n-1}} (C - C' \ln(|z_{n+1} - z_0 + r_n\Omega_n|)) dr_n d\Omega_n, \tag{6.130}$$

where the positive constants C, C' do not depend on (z_0, z_{n+1}).

Finally from (6.126) and (6.130), it follows that

$$R(z_0, z_{n+1}) \leq \int_{(0,D)\times\mathbb{S}^{n-1}} (C - C' \ln(|z_{n+1} - z_0 + r_n\Omega_n|)) dr_n d\Omega_n, \tag{6.131}$$

for $n \geq 2$ and for $(z_0, z_{n+1}) \in X^2$, $z_0 \neq z_{n+1}$, where the positive constants C, C' do not depend on (z_0, z_{n+1}).

Let $n \geq 2$ and let $(z_0, z_{n+1}) \in X^2$, $z_0 \neq z_{n+1}$. From (6.131) and the estimate $|r_n + (z_0 - z_{n+1}) \cdot \Omega_n| \leq |r_n\Omega_n + z_0 - z_{n+1}|$ it follows that

$$\begin{aligned} R(z_0, z_{n+1}) &\leq c(n)CD - C' \int_{\mathbb{S}^{n-1}} \int_0^D \ln(|r_n + (z_0 - z_{n+1}) \cdot \Omega_n|) dr_n d\Omega_n \\ &\leq c(n)(CD - C' \int_{-2D}^{2D} \ln(|r_n|) dr_n) = c(n)(CD - 2C' \int_0^{2D} \ln(r_n) dr_n), \end{aligned} \tag{6.132}$$

where $c(n) := |\mathbb{S}^{n-1}|$. Statement (6.53) follows from (6.123) and (6.132).

We prove (6.54). We first obtain

$$\bar{K}^{n+1}(I-K)^{-1}J\phi(x)=\int_{X\times\mathbb{S}^{n-1}}\gamma_{n+1}(x,x',v')(I-K)^{-1}J\phi(x,v)dv, \tag{6.133}$$

for a.e. $x\in X$ and for $\phi\in L^1(\Gamma_-,d\xi)$. Therefore using (6.53) we obtain

$$\|\bar{K}^{n+1}(I-K)^{-1}J\phi(x)\|_{L^\infty(X)}\leq C\|\phi\|_{L^1(\Gamma_-,d\xi)}, \tag{6.134}$$

for $\phi\in L^1(\Gamma_-,d\xi)$, where $C:=\|\gamma_{n+1}\|_{L^\infty(X\times X\times\mathbb{S}^{n-1})}\|(I-K)^{-1}J\|_{\mathcal{L}(L^1(\Gamma_-,d\xi),L^1(X\times\mathbb{S}^{n-1}))}$. Therefore there exists a (unique) function $\Phi\in L^\infty(X\times\Gamma_-)$ such that

$$\bar{K}^{n+1}(I-K)^{-1}J\phi(x)=\int_{\Gamma_-}\Phi(x,x',v')\phi(x',v')d\xi(x',v'). \tag{6.135}$$

Set $\Gamma_{n+1}(x,x',v'):=|\nu(x')\cdot v'|\Phi(x,x',v')$ for a.e. $(x,x',v')\in X\times\Gamma_-$ and recall the definition of $d\xi$. Then (6.54) follows from (6.135). □

6.4. Derivation of Stability Estimates

6.4.1. Estimates for Ballistic Part.

Proof of Theorem 6.2.3. Let $\phi\in L^\infty(X)$, $\|\phi\|_{L^\infty(X)}\leq 1$ and $\psi\in L^1(\Gamma_-,d\xi)$, $\|\psi\|_{L^1(\Gamma_-,d\xi)}\leq 1$. We have :

$$\left|\int_X\phi(x)\left[\left(A-\widetilde{A}\right)\psi\right](x)dx\right|\leq\|A-\widetilde{A}\|_{\mathcal{L}(L^1(\Gamma_-,d\xi),L^1(X))}. \tag{6.136}$$

Using (6.136) and the decomposition of the albedo operator (see Theorem 6.2.1) we obtain

$$|\Delta_0(\phi,\psi)|\leq\|A-\widetilde{A}\|_{\mathcal{L}(L^1(\Gamma_-,d\xi),L^1(X))}+|\Delta_1(\phi,\psi)|\,, \tag{6.137}$$

where

$$\Delta_0(\phi,\psi)=\int_{X\times\mathbb{S}^{n-1}}\phi(x)\left(\sigma_a(x,v')E(x,x-\tau_-(x,v')v')\right.$$

$$\left.-\widetilde{\sigma}_a(x,v')\tilde{E}(x,x-\tau_-(x,v')v')\right)\psi(x-\tau_-(x,v')v',v')dv'dx, \tag{6.138}$$

$$\Delta_1(\phi,\psi)=\int_X\phi(x)\int_{\Gamma_-}(\Gamma_1-\tilde{\Gamma}_1)(x,x',v')\psi(x',v')d\mu(x')dv'dx, \tag{6.139}$$

and where $\Gamma_1=\alpha_1+\Gamma_2$ (and $\tilde{\Gamma}_1=\tilde{\alpha}_1+\tilde{\Gamma}_2$).

Note that performing the change of variables $x=x'+tv'$ on the right-hand side of (6.138), we obtain

$$\Delta_0(\phi,\psi)=\int_{\Gamma_-}\int_0^{\tau_+(x',v')}\phi(x'+tv')(\eta-\tilde{\eta})(t;x',v')dt\psi(x',v')d\xi(x',v'), \tag{6.140}$$

where

$$\eta(t;x',v')=\sigma_a(x'+tv',v')e^{-\int_0^t\sigma(x'+sv',v')ds},\ \tilde{\eta}(t;x',v')=\tilde{\sigma}_a(x'+tv',v')e^{-\int_0^t\tilde{\sigma}(x'+sv',v')ds}. \tag{6.141}$$

We use the following result: For any function $G\in L^1(\Gamma_-,d\xi)$ and for a.e. $(x_0',v_0')\in\Gamma_-$ there exists a sequence of functions $\psi_{\varepsilon,x_0',v_0'}\in L^1(\Gamma_-,d\xi)$ (which does not depend on the function G), $\|\psi_{\varepsilon,x_0',v_0'}\|_{L^1(\Gamma_-,d\xi)}=1$, $\psi_{\varepsilon,x_0',v_0'}\geq 0$ and

$\text{supp}\psi_{\varepsilon,x_0',v_0'} \subseteq \{(x',v') \in \Gamma_- \mid |x'-x_0'|+|v-v_0'|<\varepsilon\}$ such that the following limit holds

$$\int_{\Gamma_-} G(x',v')\psi_{\varepsilon,x_0',v_0'}(x',v')d\xi(x',v') \to G(x_0',v_0'), \text{ as } \varepsilon \to 0^+ \tag{6.142}$$

(we refer the reader to [**106**, Corollary 4.2] for the proof of this statement). In particular, the limits (6.142) holds for some sequence $\psi_{\varepsilon,x_0',v_0'}$ when (x_0',v_0') belongs to the Lebesgue set of G denoted by $\mathcal{L}(G)$ and the complement of $\mathcal{L}(G)$ is a negligible subset of Γ_- (see [**106**]).

Let $\mathcal{L} := \cap_{m\in\mathbb{N}\cup\{0\}}\mathcal{L}(G_m)$ where G_m is the measurable function on Γ_- defined by

$$G_m(x',v') = \int_0^{\tau_+(x',v')} t^m(\eta-\tilde{\eta})(t;x',v')dt, \tag{6.143}$$

for $m \in \mathbb{N}\cup\{0\}$. Note that the complement of $\mathcal{L}$ is still negligible. Let $(x_0',v_0') \in \mathcal{L}$ and let $\phi \in C_0(0,\tau_+(x_0',v_0'))$ where $C_0(0,\tau_+(x_0',v_0'))$ denotes the set of continuous and compactly supported functions on $(0,\tau_+(x_0',v_0'))$. Consider the sequence $(\phi_m) \in (L^\infty(X))^{\mathbb{N}}$ defined by

$$\phi_m(x) = \chi_{[0,\frac{1}{m+1})}(|x'|)\phi(t), \tag{6.144}$$

for $x \in X$ and $m \in \mathbb{N}$ where $x = x_0' + tv_0' + x'$, $x'\cdot v_0' = 0$, where $\chi_{[0,\frac{1}{m+1})}(t) = 0$ when $t \geq \frac{1}{m+1}$ and $\chi_{[0,\frac{1}{m+1})}(t) = 1$ otherwise. The support of ϕ_m concentrates around the line which passes through x_0' with direction v_0'. From (6.140), (6.142), (6.143) (and the Stone-Weierstrass theorem), we obtain that

$$\lim_{\varepsilon\to 0^+}\Delta_0(\phi_m,\psi_{\varepsilon,x_0',v_0'}) = \int_0^{\tau_+(x_0',v_0')}\phi_m(x_0'+tv_0')(\eta-\tilde{\eta})(t;x_0',v_0')dt. \tag{6.145}$$

For the single-scattering part, using (6.21) and (6.48) and (6.50) for $m=1$ we obtain:

$$|\Delta_1(\phi_m,\psi_{\varepsilon,x_0',v_0'})| \leq C\int_{\Gamma_-}\Phi_m(x',v')\psi_{\varepsilon,x_0',v_0'}(x',v')d\xi(x',v') \tag{6.146}$$

where $C = \|\frac{(\Gamma_1-\tilde{\Gamma}_1)(x,x',v')}{|\nu(x')\cdot v'|w_n(x,x',v')}\|_\infty$ and Φ is the function from Γ_- to $\mathbb{R}$ defined by

$$\Phi_m(x',v') = \int_X w_n(x,x',v')|\phi_m(x)|dx \tag{6.147}$$

(where $w_n(x,x',v')$ is defined in Theorem 6.2.4). From the definition of w_n, it follows that Φ_m is a bounded and continuous function on Γ_-. Therefore using Lebesgue dominated convergence theorem, we obtain

$$\lim_{\varepsilon\to 0^+}\int_{\Gamma_-}\Phi_m(x',v')\psi_{\varepsilon,x_0',v_0'}(x',v')d\xi(x',v') = \Phi_m(x_0',v_0') = \int_X w_n(x,x_0',v_0')|\phi_m(x)|dx. \tag{6.148}$$

Then using (6.144), (6.148) and Lebesgue convergence theorem, we obtain $\lim_{m\to+\infty}\int_X w_n(x,x_0',v_0')|\phi_m(x)|dx = 0$. Therefore taking account of (6.146) and (6.148), we obtain

$$\lim_{m\to+\infty}\lim_{\varepsilon\to 0^+}\Delta_1(\phi_m,\psi_{\varepsilon,x_0',v_0'}) = 0. \tag{6.149}$$

Combining (6.137) (with $\psi = \psi_{\varepsilon,x',v'}$), (6.145), (6.144), (6.149), we obtain

$$\left| \int_0^{\tau_+(x',v')} \phi(t)(\eta - \tilde{\eta})(t;x',v')dt \right| \leq \|\mathcal{A} - \widetilde{\mathcal{A}}\|_{\mathcal{L}(L^1(\Gamma_-,d\xi),L^1(X))}, \tag{6.150}$$

for $(x',v') \in \mathcal{L}$ and $\phi \in C_0(0,\tau_+(x',v'))$. From the density of $C_0(0,\tau_+(x',v'))$ in $L^1(0,\tau_+(x',v'))$, it follows that (6.150) also holds for $\phi \in L^1(0,\tau_+(x',v'))$. Applying (6.150) on $\phi(t) := \mathrm{sign}(\eta - \tilde{\eta})(t;x',v')$ for a.e. $t \in (0,\tau_+(x',v'))$ (where $\mathrm{sign}(s) = 1$ when $s \geq 0$ and $\mathrm{sign}(s) = -1$ otherwise), we obtain (6.23). □

Proof of Theorem 6.2.5. Let us define

$$\zeta(t) := \zeta(t;x',v') = e^{-\int_0^t \sigma_a(x'+sv',v')ds}, \quad \eta(t) := \eta(t;x',v') = \sigma_a(x'+tv',v')\zeta(t;x',v').$$

Note that $\eta(t) = \dfrac{d}{dt}\zeta(t)$. Then,

$$|\zeta(t) - \tilde{\zeta}(t)| = \Big| \int_0^t \frac{d}{dt}(\zeta - \tilde{\zeta})(s)ds \Big| \leq \int_0^t |\eta - \tilde{\eta}|(s)ds \leq \|A - \tilde{A}\|_{\mathcal{L}(L^1(\Gamma_-,d\xi);L^1(X))},$$

thanks to (6.23). The point-wise (in t) control on $\zeta(t)$ and the estimate (6.23) for $\eta(t)$ show by application of the triangle inequality and the fact that $\zeta(t)$ is bounded from below by the positive constant $e^{-M\mathrm{diam}(X)}$ that

$$\int_0^{\tau_+(x',v')} \Big|\sigma_a(x'+tv',v') - \tilde{\sigma}_a(x'+tv',v')\Big| dt \leq C\|A - \tilde{A}\|_{\mathcal{L}(L^1(\Gamma_-,d\xi);L^1(X))}. \tag{6.151}$$

Here, the constant C depends on M and is of order $e^{M\mathrm{diam}(X)}$. Not surprisingly, reconstructions deteriorate when the optical depth $M\mathrm{diam}(X)$ of the domain increases. This shows that

$$\int_X \big|\sigma_a(x,v') - \tilde{\sigma}_a(x,v')\big| dx \leq C\|A - \tilde{A}\|_{\mathcal{L}(L^1(\Gamma_-,d\xi);L^1(X))}.$$

This concludes the proof of the theorem. □

Proof of Theorem 6.2.6. Let $\mathcal{G} := \{(t,x',v') \in (0,+\infty)\times\Gamma_- \mid t \in (0,\tau_+(x',v'))\}$ and let $h \in L^\infty(\mathcal{G})$ be defined by

$$h(t;x',v') = -\int_0^t \sigma(x'+sv',v')ds + \int_t^{\tau_+(y',v')} \sigma(y'+sv',v')ds, \tag{6.152}$$

for $(t,x',v') \in \mathcal{G}$. The function $\tilde{h} \in L^\infty(\mathcal{G})$ is defined similarly.

We first prove a stability estimate (6.158) on h, $\tilde{h}$. Let $(y_0,v_0) \in \Gamma_-$, $t \in (0,\tau_+(y_0,v_0))$. Set $(y_1,v_1) := (y_0 + \tau_+(y_0,v_0)v_0, -v_0)$ and $t_1 = \tau_+(y_0,v_0) - t$. Due to the symmetry of σ_a, σ with respect to the speed variable v (σ_a, $\widetilde{\sigma}_a$ bounded from below), we obtain:

$$\frac{\eta(t;y_0,v_0)}{\eta(t_1;y_1,v_1)} = e^{h(t;y_0,v_0)}, \ \frac{\tilde{\eta}(t;y_0,v_0)}{\tilde{\eta}(t_1;y_1,v_1)} = e^{\tilde{h}(t;y_0,v_0)}, \tag{6.153}$$

where η is defined by (6.141). Note that from (6.152), it follows that $|h(t;y_0,v_0)| \leq \|\sigma\|_\infty \tau_+(y_0,v_0) \leq D\|\sigma\|_\infty$ where D denotes the diameter of X. A similar estimate is valid for $\tilde{h}$ and $\tilde{\sigma}$. Therefore using the fact that $|a - \tilde{a}| \leq e^{-\min(a,\tilde{a})}|e^a - e^{\tilde{a}}|$ for $\tilde{a} = h(t)$, we obtain

$$|h - \widetilde{h}|(t;y_0,v_0) \leq e^{D\max(\|\sigma\|_\infty,\|\tilde{\sigma}\|_\infty)} \left| \frac{\eta(t;y_0,v_0)}{\eta(t_1;y_1,v_1)} - \frac{\widetilde{\eta}(t;y_0,v_0)}{\widetilde{\eta}(t_1;y_1,v_1)} \right|. \tag{6.154}$$

Note that from (6.141) it follows that

$$0 < \sigma_0 e^{-D\|\sigma\|_\infty} \leq \eta(s;y,v) \leq \|\sigma_a\|_\infty. \tag{6.155}$$

for $(y,v) \in \Gamma_-$ and $s \in (0, \tau_+(y,v))$, where D is the diameter of X. A similar estimate is valid for $(\tilde{\sigma}_a, \tilde{\eta})$. Therefore using the equality $\frac{a}{b} - \frac{\tilde{a}}{\tilde{b}} = \frac{(a-\tilde{a})\tilde{b}+(b-\tilde{b})\tilde{a}}{b\tilde{b}}$ (for $a = \eta(t;y_0,v_0)$, $b = \eta(t_1;y_1,v_1)$), we obtain

$$\begin{aligned}
&\left| \frac{\eta(t;y_0,v_0)}{\eta(t_1;y_1,v_1)} - \frac{\widetilde{\eta}(t;y_0,v_0)}{\widetilde{\eta}(t;y_1,v_1)} \right| \\
&\leq \frac{e^{D(\|\sigma\|_\infty+\|\tilde{\sigma}\|_\infty)}}{\sigma_0\widetilde{\sigma_0}} \Big(\eta(t;y_0,v_0)|\eta-\tilde{\eta}|(t_1;y_1,v_1) + \eta(t_1;y_1,v_1)|\eta-\tilde{\eta}|(t;y_0,v_0) \Big) \\
&\leq \frac{e^{D(\|\sigma\|_\infty+\|\tilde{\sigma}\|_\infty)}}{\sigma_0\widetilde{\sigma_0}} \Big(\|\sigma_a\|_\infty|\eta-\tilde{\eta}|(t_1;y_1,v_1) + \|\widetilde{\sigma}_a\|_\infty|\eta-\tilde{\eta}|(t;y_0,v_0) \Big). \qquad (6.156)
\end{aligned}$$

Using (6.156), integrating in the t variable ($t_1 = \tau_+(y_0,v_0) - t$) and using (6.23), we obtain

$$\begin{aligned}
\int_0^{\tau_+(y_0,v_0)} \left| \frac{\eta(t;y_0,v_0)}{\eta(t_1;y_1,v_1)} - \frac{\widetilde{\eta}(t;y_0,v_0)}{\widetilde{\eta}(t_1;y_1,v_1)} \right| dt \quad &\leq \quad \frac{e^{D(\|\sigma\|_\infty+\|\tilde{\sigma}\|_\infty)}}{\sigma_0\widetilde{\sigma_0}} \left(\|\sigma_a\|_\infty + \|\widetilde{\sigma}_a\|_\infty\right) \\
&\times \|\mathcal{A} - \widetilde{\mathcal{A}}\|_{\mathcal{L}(L^1(\Gamma_-,d\xi),L^1(X))}. \qquad (6.157)
\end{aligned}$$

Combining (6.154) and (6.157) we obtain

$$\int_0^{\tau_+(y_0,v_0)} |h - \widetilde{h}|(t;y_0,v_0)dt \leq C\|\mathcal{A} - \widetilde{\mathcal{A}}\|_{\mathcal{L}(L^1(\Gamma_-,d\xi),L^1(X))} \tag{6.158}$$

for a.e. $(y_0,v_0) \in \Gamma_-$, where the constant C depends only on D, $\|\sigma\|_\infty$, $\|\tilde{\sigma}\|_\infty$, $\|\sigma_a\|_\infty$ and $\|\tilde{\sigma}_a\|_\infty$. We now prove (6.161). Estimate (6.161) is, in particular, a consequence of the identities

$$\frac{dh(t;y_0,v_0)}{dt} = -2\sigma(y_0+sv_0,v_0), \ \frac{d\widetilde{h}(t;y_0,v_0)}{dt} = -2\widetilde{\sigma}(y_0+sv_0,v_0),$$

for a.e. $(y_0,v_0) \in \Gamma_-$ and $t \in (0, \tau_+(y_0,v_0))$.

Consider the operator $T_{\delta\sigma(.,v)}$ associated with $\delta\sigma = \sigma - \widetilde{\sigma}$:

$$T_{\delta\sigma(.,v)} : W_0^{1,\infty}(X) \to \mathbb{R}, \ \phi \mapsto \int_X \delta\sigma(x,v)\varphi(x)dx$$

for $v \in \mathbb{S}^{n-1}$. Using the change of variable $x = y + tv$ ($dx = |\nu(y)\cdot v|dtdy$, $y \in \partial X_-(v) := \{x' \in \partial X \mid \nu(x')\cdot v < 0\}$, $t \in (0, \tau_+(y,v))$) we have

$$\left|\langle T_{\delta\sigma(.,v)}, \varphi\rangle\right| = \left| \int_{\partial X_-(v)} |\nu(y)\cdot v| \int_0^{\tau_+(y,v)} \delta\sigma(y+tv,v)\varphi(y+tv)dtd\mu(y) \right|,$$

and using integration by part in the inner integral we have:

$$\begin{aligned}
\left|\langle T_{\delta\sigma(.,v)}, \varphi\rangle\right| &\leq \int_{\partial X_-(v)} \frac{|\nu(y)\cdot v|}{2} \left| \int_0^{\tau_+(y,v)} (h-\tilde{h})(t;y,v) v\cdot\nabla\varphi(y+tv)dt \right| d\mu(y) \qquad (6.159) \\
&\leq \frac{1}{2}\|\nabla\varphi\|_\infty \int_{\partial X_-(v)} \int_0^{\tau_+(y,v)} \left| h - \widetilde{h} \right| (t;y,v)dtd\mu(y) \\
&\leq C\|\mathcal{A} - \widetilde{\mathcal{A}}\|_{\mathcal{L}(L^1(\Gamma_-,d\xi),L^1(X))} \|\varphi\|_{W_0^{1,\infty}(X)}, \qquad (6.160)
\end{aligned}$$

for a.e. $v \in \mathbb{S}^{n-1}$ (we used (6.158)). Identifying $\delta\sigma$ and $T_{\delta\sigma}$, we obtain

$$\|\sigma - \widetilde{\sigma}\|_{L^\infty(\mathbb{S}^{n-1}, W^{-1,1}(X))} \leq C\|\mathcal{A} - \widetilde{\mathcal{A}}\|_{\mathcal{L}(L^1(\Gamma_-, d\xi), L^1(X))}. \tag{6.161}$$

We prove the following estimate

$$\|\sigma_a - \tilde{\sigma}_a\|_{L^\infty(\mathbb{S}^{n-1}, L^1(X))} \leq C\|A - \tilde{A}\|_{\mathcal{L}(L^1(\Gamma_-); L^1(X))}, \tag{6.162}$$

where C depends on the uniform bounds σ_0 and M. Combining (6.161) and (6.162), we obtain (6.28), which completes the proof of Theorem 6.2.6. The estimate on $\sigma_a(x, v')$ comes from an estimate on $\int_0^t \sigma(x' + sv', v')ds$ by the triangle inequality. The latter is given by

$$2\int_0^t \sigma(x' + sv', v')ds = \int_0^{\tau_+(x',v')} \sigma(x' + sv', v')ds + \Big(\int_0^t - \int_t^{\tau_+(x',v')}\Big)\sigma(x' + sv', v')ds.$$

We just obtained control of

$$\Big(\int_0^t - \int_t^{\tau_+(x',v')}\Big)(\sigma - \tilde{\sigma})(x' + sv', v')ds,$$

in the L^1 sense in the $t-$variable. It thus remains to control the constant term $\int_0^{\tau_+(x',v')}(\sigma - \tilde{\sigma})(x' + sv', v')ds$.

Note that the latter term is nothing but the X-ray transform (Radon transform when $n = 2$) of σ along the line of direction v' passing through x'. In the setting of measurements that are supposed to be accurate in $\mathcal{L}(L^1(\Gamma_-, d\xi); L^1(X))$, the line integral is not directly captured as it corresponds to a measurement performed at a point $x = x' + \tau_+(x', v')v'$. This is the reason why we assume that σ is known in the $\delta-$vicinity of ∂X.

Knowledge of σ and $\tilde{\sigma}$ in the δ_0-vicinity of ∂X allows one to control $\int_0^{\tau_+(x',v')} \sigma(x' + sv', v')ds$ by $\|A - \tilde{A}\|_{\mathcal{L}(L^1(\Gamma_-, d\xi); L^1(X))}$. When the X-ray transform of σ is well captured by available measurements, as for instance in the presence of boundary measurements [**24**], then δ_0 can be set to 0.

More precisely, we find that

$$\int_0^{\tau_+(x',v')} (\sigma - \tilde{\sigma})(x' + sv', v')ds = \int_0^{\tau_+(x',v')} \phi(s)(\sigma - \tilde{\sigma})(x' + sv', v')ds,$$

where $\phi(s) \in C_0^\infty(0, \tau_+(x', v'))$ is equal to 1 for $\delta_0 < s < \tau_+(x', v') - \delta_0$. Integrating by parts, this shows that

$$\begin{aligned}&\Big|\int_0^{\tau_+(x',v')} (\sigma - \tilde{\sigma})(x' + sv', v')ds\Big| \\ &\leq \|(\sigma - \tilde{\sigma})(x' + tv', v')\|_{W_t^{-1,1}(0,\tau_+(x',v'))}\|\phi\|_{W^{1,\infty}(0,\tau_+(x',v'))} \leq C\|A - \tilde{A}\|_{\mathcal{L}(L^1(\Gamma_-,d\xi);L^1(X))},\end{aligned}$$

thanks to estimate (6.158). By Lipschitz regularity of the exponential, we thus have that

$$\int_0^{\tau_+(x',v')} \Big|e^{-\int_0^t \sigma(x'+sv',v')} - e^{-\int_0^t \tilde{\sigma}(x'+sv',v')}\Big|dt \leq C\|A - \tilde{A}\|_{\mathcal{L}(L^1(\Gamma_-,d\xi);L^1(X))}. \tag{6.163}$$

The stability result (6.162) on $\sigma_a(x, v')$ follows from (6.23) and the triangle inequality as in the proof of Theorem 6.2.5. □

Proof of Corollary 6.2.7. Let $p > 1$. We first derive (6.29) from the following estimate

$$\|\sigma - \widetilde{\sigma}\|_{L^\infty(\mathbb{S}^{n-1}, W^{-1,p}(X))} \leq C\|\mathcal{A} - \widetilde{\mathcal{A}}\|^{\frac{1}{p}}_{\mathcal{L}(L^1(\Gamma_-, d\xi), L^1(X))}. \tag{6.164}$$

Assuming that $\sigma - \widetilde{\sigma}$ is bounded by C_0 in $L^\infty\left(\mathbb{S}^{n-1}, W^{r,p}(X)\right)$, then using (6.164) and using the complex interpolation result [**34**, Theorem 6.4.5 pp. 153], we obtain

$$\|\sigma - \tilde{\sigma}\|_{W^{s,p}(X)} \leq \|\sigma - \tilde{\sigma}\|^{1-\theta}_{W^{-1,p}(X)} \|\sigma - \tilde{\sigma}\|^{\theta}_{W^{r,p}(X)} \leq C'\|\mathcal{A} - \widetilde{\mathcal{A}}\|^{\frac{1-\theta}{p}}_{\mathcal{L}(L^1(\Gamma_-, d\xi), L^1(X))}, \tag{6.165}$$

for $-1 \leq s \leq r$, where $s = (1-\theta) \times (-1) + r\theta$ and $C' = C^{1-\theta} C_0^\theta$. This proves (6.29).

We prove (6.164). From (6.152), it follows that $|h - \tilde{h}|(t; x', v') \leq (|h| + |\tilde{h}|)(t; y_0, v_0) \leq D(\|\sigma\|_\infty + \|\tilde{\sigma}\|_\infty)$, where D is the diameter of X. Hence we obtain

$$\left|h - \widetilde{h}\right|^p (t; x', v') \leq D^{p-1}(\|\sigma\|_\infty + \|\tilde{\sigma}\|_\infty)^{p-1} |h - \tilde{h}|(t; x', v'), \tag{6.166}$$

for $(x', v') \in \Gamma_-$ and $t \in (0, \tau_+(x', v'))$. Using (6.159) and Hölder inequality, and using (6.166), we obtain

$$\begin{aligned} \left|\int_X (\sigma - \tilde{\sigma})(x, v)\varphi(x) dx\right| &\leq \frac{1}{2}\left(\int_{\partial X_-(v)} \int_0^{\tau_+(y,v)} |h - \widetilde{h}|^p (t; y, v) dt d\mu(y)\right)^{\frac{1}{p}} \|\nabla\varphi\|_{L^{p'}(X)} \\ &\leq C\|\mathcal{A} - \widetilde{\mathcal{A}}\|^{\frac{1}{p}}_{\mathcal{L}(L^1(\Gamma_-, d\xi), L^1(X))} \|\varphi\|_{W^{1,p'}(X)}, \end{aligned} \tag{6.167}$$

for a.e. $v \in \mathbb{S}^{n-1}$ and for $\varphi \in W_0^{1,p'}(X) := \{\psi \in L^{p'}(X) \mid \text{supp}\psi \subset X,\ \nabla\psi \in L^{p'}(X, \mathbb{C}^n)\}$ where ${p'}^{-1} + p^{-1} = 1$. Estimate (6.167) proves (6.164). □

6.4.2. Estimates for Single Scattering.

Proof of Theorem 6.2.4. Let $(x, x') \in X \times \partial X$. Set $v' = \widehat{x - x'}$ and let ${v'}^\perp \in \mathbb{S}^{n-1}$ be such that $v' \cdot {v'}^\perp = 0$. Let $t_0' = |x - x'|$, then $x = x' + t_0' v'$. First assume $n = 2$. Using the equality $\alpha_1 = \Gamma_1 - \Gamma_2$, and using (6.21), (6.48), we obtain

$$\begin{aligned} \frac{|\alpha_1 - \tilde{\alpha}_1|(x + \varepsilon {v'}^\perp, x', v')}{|\nu(x') \cdot v'| \left(1 + \ln\left(\frac{|(t_0' - \tau_+(x', v'))v' + \varepsilon {v'}^\perp| + (\tau_+(x', v') - t_0')}{|t_0' v' + \varepsilon {v'}^\perp| - t_0'}\right)\right)} \\ \leq \left\|\frac{(\Gamma_1 - \tilde{\Gamma}_1)(z, z', w')}{|\nu(z') \cdot w'| w_2(z, z', w')}\right\|_\infty + \frac{\left\|\frac{(\Gamma_2 - \tilde{\Gamma}_2)(z, z', w')}{|\nu(z') \cdot w'|}\right\|_\infty}{1 + \ln\left(\frac{|(t_0' - \tau_+(x', v'))v' + \varepsilon {v'}^\perp| + (\tau_+(x', v') - t_0')}{|t_0' v' + \varepsilon {v'}^\perp| - t_0'}\right)} \end{aligned} \tag{6.168}$$

for $\varepsilon > 0$. Therefore using (6.168) as $\varepsilon \to 0^+$ and (6.22), we obtain (6.24).

Assume $n \geq 3$. Using the equality $\alpha_1 = \Gamma_1 - \Gamma_2$, and using (6.21), (6.50) (for "$m = 1$"), we obtain

$$\begin{aligned} \varepsilon^{n-2} \frac{|\alpha_1 - \tilde{\alpha}_1|(x + \varepsilon {v'}^\perp, x', v')}{|\nu(x') \cdot v'|} &\leq \left\|\frac{(\Gamma_1 - \tilde{\Gamma}_1)(z, z', w')}{|\nu(z') \cdot w'| w_n(z, z', w')}\right\|_{L^\infty(X \times \Gamma_-)} \\ &+ \varepsilon \left\|\frac{|z - z' - ((z - z') \cdot w')w'|^{n-3}(\Gamma_2 - \tilde{\Gamma}_2)(z, z', w')}{|\nu(z') \cdot w'|}\right\|_{L^\infty(X \times \Gamma_-)} \end{aligned} \tag{6.169}$$

for $\varepsilon > 0$. Therefore using (6.169) as $\varepsilon \to 0^+$ and (6.22), we obtain (6.25). □

Proof of Lemma 6.2.9. First consider the case $n = 2$. The statement in Lemma 6.2.9 is a straightforward consequence of (6.35) and we have the following inversion formula:

$$g = \Big(\frac{\pi h(g) - 1}{\pi h(g) + 1}\Big)^{\frac{1}{2}}, \ g \in [0, 1). \tag{6.170}$$

Let now $n = 3$. Using (6.36) and the identity $\cos(\theta) = 1 - 2\sin^2(\frac{\theta}{2})$, $\theta \in \mathbb{R}$, we obtain

$$2\pi h(g) = \frac{1+g}{(1-g)^2} \int_0^{\pi} \frac{1}{2} \Big(1 + \frac{4g}{(1-g)^2} \sin^2\big(\frac{\theta}{2}\big)\Big)^{-\frac{3}{2}} d\theta,$$

for $g \in [0, 1)$. Performing the change of variables $\theta = 2\arcsin(\frac{t}{\sqrt{1+t^2}})$ ($d\theta = \frac{2dt}{1+t^2}$), we obtain

$$2\pi h(g) = \frac{1+g}{(1-g)^2} \int_0^{+\infty} (1+t^2)^{\frac{1}{2}} \Big(1 + \Big(\frac{1+g}{1-g}\Big)^2 t^2\Big)^{-\frac{3}{2}} dt.$$

Performing the change of variables $v = \frac{1+g}{1-g}t$, we obtain

$$\begin{aligned} 2\pi h(g) &= \int_0^{+\infty} \sqrt{\frac{\Big(\frac{1}{1-g}\Big)^2 + \Big(\frac{1}{1+g}\Big)^2 v^2}{(1+v^2)^3}} dv \\ &= \frac{1}{1-g} \int_0^{+\infty} \sqrt{\frac{1 + \Big(\frac{1-g}{1+g}\Big)^2 v^2}{(1+v^2)^3}} dv, \end{aligned} \tag{6.171}$$

for $g \in [0, 1)$. Note that from the above, it follows that $2\pi h(g) = \frac{1}{1-g} + o(\frac{1}{1-g})$ as $g \to 1^-$ (where we used the integral value $\int_0^{+\infty} \frac{dv}{(1+v^2)^{\frac{3}{2}}} = \Big[\frac{v}{\sqrt{1+v^2}}\Big]_0^{+\infty} = 1$).

Differentiating (6.171) with respect to g, we obtain

$$\begin{aligned} 2\pi \dot{h}(g) = \frac{1}{(1-g)^3} \int_0^{+\infty} &\frac{dv}{(1+v^2)^{\frac{3}{2}} \sqrt{\omega_1^2(g) + \omega_2^2(g) v^2}} \\ &- \frac{1}{(1+g)^3} h_2(g), \end{aligned} \tag{6.172}$$

for $g \in [0, 1)$, where $\dot{h} = \frac{dh}{dg}$, $\omega_1(g) := \frac{1}{1-g}$, $\omega_2(g) := \frac{1}{1+g}$, and

$$h_2(g) := \int_0^{+\infty} \frac{v^2 dv}{(1+v^2)^{\frac{3}{2}} \sqrt{\omega_1^2(g) + \omega_2^2(g) v^2}}. \tag{6.173}$$

Integrating by parts, we obtain

$$h_2(g) \ = \ \int_0^{+\infty} \frac{\omega_1^2(g) dv}{(1+v^2)^{\frac{1}{2}} \left(\omega_1^2(g) + \omega_2^2(g) v^2\right)^{\frac{3}{2}}}, \tag{6.174}$$

for $g \in [0, 1)$, where we use that a primitive of the function $r(v) := v(1+v^2)^{-\frac{3}{2}}$ is given by the function $R(v) := -(1+v^2)^{-\frac{1}{2}}$ and where we used that the derivative of the function $s(v) := \left(\omega_1^2(g) + \omega_2^2(g) v^2\right)^{-\frac{1}{2}}$ is given by $\dot{s}(v) = \omega_1^2(g) \left(\omega_1^2(g) + \omega_2^2(g) v^2\right)^{-\frac{3}{2}}$.

Performing the change of variables "v"$= \frac{1-g}{1+g}v$ on the right hand side of (6.174), we obtain

$$h_2(g) = \omega_2^2(g) \int_0^{+\infty} (1+v^2)^{-\frac{3}{2}} \left(1 + \left(\frac{1+g}{1-g}\right)^2 v^2\right)^{-\frac{1}{2}} dv, \tag{6.175}$$

for $g \in [0,1)$. Combining (6.172) and (6.175), we obtain

$$\begin{aligned} 2\pi \dot{h}(g) &= \frac{1}{(1-g)^2}\Big[\int_0^{+\infty} (1+v^2)^{-\frac{3}{2}} \Big(1 + \left(\frac{1-g}{1+g}\right)^2 v^2\Big)^{-\frac{1}{2}} dv \\ &\quad - \left(\frac{1-g}{1+g}\right)^2 \int_0^{+\infty} (1+v^2)^{-\frac{3}{2}} \Big(1 + \left(\frac{1+g}{1-g}\right)^2 v^2\Big)^{-\frac{1}{2}} dv\Big], \end{aligned} \tag{6.176}$$

for $g \in [0,1)$. Using the estimate $1 + \left(\frac{1+g}{1-g}\right)^2 v^2 > 1 + \left(\frac{1-g}{1+g}\right)^2 v^2$ for $v \in (0,+\infty)$ and $g \in (0,1)$, we obtain that the second integral on the right hand side of (6.176) is less than the first integral on the right-hand side of (6.176) for $g \in (0,1)$. Therefore using also that the second integral is multiplied by $\left(\frac{1-g}{1+g}\right)^2 (< 1)$, we obtain $\dot{h}(g) > 0$ for $g \in (0,1)$, which proves that h is strictly increasing on $(0,1)$. □

Proof of Theorem 6.2.10. We prove (6.37). From (6.24), (6.25), (6.30) and (6.31), it follows that

$$|E(x,x')\sigma_g(x) - \tilde{E}(x,x')\sigma_g(x)| \leq \left\| \frac{(\Gamma_1 - \tilde{\Gamma}_1)(x,x',v')}{|\nu(x')\cdot v'| w_n(x,x',v')} \right\|_\infty, \tag{6.177}$$

for $(x,x') \in X \times \Gamma_-$. Using (6.177) and the estimate $\min(E(x,x'), \tilde{E}(x,x')) \geq e^{-D\max(\|\sigma\|_\infty, \|\tilde{\sigma}\|_\infty)}$ (see (6.18)) where D is the diameter of X, we obtain

$$\begin{aligned} &|\sigma_g - \tilde{\sigma}_g|(x) \leq \\ &e^{D\max(\|\sigma\|_\infty, \|\tilde{\sigma}\|_\infty)} \Big(\left\| \frac{(\Gamma_1 - \tilde{\Gamma}_1)(x,x',v')}{|\nu(x')\cdot v'| w_n(x,x',v')} \right\|_\infty + |E - \tilde{E}|(x,x') \Big), \end{aligned} \tag{6.178}$$

for $(x,x') \in X \times \Gamma_-$ (we used the identity $ab - \tilde{a}\tilde{b} = (a-\tilde{a})b + (b-\tilde{b})\tilde{a}$ for $a := \sigma_g(x)$ and $b := E(x,x')$). Let $(x',v') \in \Gamma_-$. Integrating (6.178) over the line which passes through x' with direction v' and using the stability estimate (6.163) and (6.18), we obtain

$$\begin{aligned} &\int_0^{\tau_+(x',v')} |\sigma_g - \tilde{\sigma}_g|(x'+tv')dt \leq \\ &C \left\| \frac{(\Gamma_1 - \tilde{\Gamma}_1)(x,x',v')}{|\nu(x')\cdot v'| w_n(x,x',v')} \right\|_\infty + C\|A - \tilde{A}\|_{\mathcal{L}(L^1(\Gamma_-, d\xi), L^1(X))}, \end{aligned} \tag{6.179}$$

where $C = e^{D\max(\|\sigma\|_\infty, \|\tilde{\sigma}\|_\infty)} \max(D, C)$ and C is the constant on the right-hand side of (6.163). Integrating (6.179) over $\partial X_-(v') := \{x' \in \partial X \mid v' \cdot \nu(x') < 0\}$ with measure $|\nu(x')\cdot v'| d\mu(x')$, we obtain (6.37). We now prove (6.38). Assume $\|h(g)\|_{W^{1,\infty}(X)} \leq \|h(\tilde{g})\|_{W^{1,\infty}(X)}$. Using (6.34) and $\min(\sigma_s, \tilde{\sigma}_s) \geq \sigma_{s,0}$, we obtain

$$\|h(g) - h(\tilde{g})\|_{L^1(X)} \leq \frac{1}{\sigma_{s,0}} \Big(\|(\sigma_s - \tilde{\sigma}_s)h(g)\|_{L^1(X)} + \|\sigma_g - \tilde{\sigma}_g\|_{L^1(X)} \Big) \tag{6.180}$$

(we used the identity $ab-\tilde{a}\tilde{b}=(a-\tilde{a})b+(b-\tilde{b})\tilde{a}$ for $a=\sigma_s$ and $b=h(g)$). Using the identity $\sigma_s=\sigma-\sigma_a$, we have

$$\|(\sigma_s-\tilde{\sigma}_s)h(g)\|_{L^1(X)}\leq\|\sigma_a-\tilde{\sigma}_a\|_{L^1(X)}\|h(g)\|_{L^\infty(X)}+\|(\sigma-\tilde{\sigma})h(g)\|_{L^1(X)}$$
$$\leq\|\sigma_a-\tilde{\sigma}_a\|_{L^1(X)}\|h(g)\|_{L^\infty(X)}+\|\sigma-\tilde{\sigma}\|_{W^{-1,1}(X)}\|\nabla h(g)\|_{L^\infty(X)} \tag{6.181}$$

(we used the fact that $\sigma=\tilde{\sigma}$ at the vicinity of the boundary ∂X). Finally combining (6.180), (6.181), (6.37) and (6.28), we obtain (6.38). □

Appendix

For $m\geq 2$, let β_m denotes the distributional kernel of the operator K^m where K is defined by (6.41). We first give the explicit expression of β_2, β_3. Then by induction we give the explicit expression of the kernel β_m. Finally we prove Lemma 6.3.1.

From (6.41) it follows that

$$K^2\psi(x,v)=\int_0^{\tau_-(x,v)}\int_{\mathbb{S}^{n-1}}k(x-tv,v_1,v)\int_0^{\tau_-(x-tv,v_1)}E(x,x-tv,x-tv-t_1v_1)$$
$$\times\int_{\mathbb{S}^{n-1}}k(x-tv-t_1v_1,v',v_1)\psi(x-tv-t_1v_1,v')dv'dt_1dv_1dt, \tag{6.182}$$

for a.e. $(x,v)\in X\times\mathbb{S}^{n-1}$ and for $\psi\in L^1(X\times\mathbb{S}^{n-1})$. Performing the change of variables $x'=x-tv-t_1v_1$ ($dx'=t_1^{n-1}dt_1dv_1$) on the right hand side of (6.182), we obtain

$$\begin{aligned}K^2\psi(x,v)&=\int_0^{\tau_-(x,v)}\int_X k(x-tv,\widehat{x-tv-x'},v)E(x,x-tv,x')\\&\times\int_{\mathbb{S}^{n-1}}k(x',v',\widehat{x-tv-x'})\psi(x',v')dv'dx'dt,\end{aligned} \tag{6.183}$$

for a.e. $(x,v)\in X\times\mathbb{S}^{n-1}$ and for $\psi\in L^1(X\times\mathbb{S}^{n-1})$. Therefore

$$\beta_2(x,v,x',v')=\int_0^{\tau_-(x,v)}E(x,x-tv,x')\frac{k(x-tv,v_1,v)k(x',v',v_1)_{|v_1=\widehat{x-tv-x'}}}{|x-tv-x'|^{n-1}}dt, \tag{6.184}$$

for a.e. $(x,v,x',v')\in X\times\mathbb{S}^{n-1}\times X\times\mathbb{S}^{n-1}$. From (6.184) and (6.41) it follows that

$$K^3\psi(x,v)=\textstyle\int_{(0,\tau_-(x,v))\times\mathbb{S}^{n-1}}E(x,x-tv)k(x-tv,v_1,v)$$
$$\times\textstyle\int_{X\times\mathbb{S}^{n-1}}\beta_2(x-tv,v_1,x',v')\psi(x',v')dx'dv'dv_1dt$$

$$=\int_{X\times\mathbb{S}^{n-1}}\psi(x',v')\int_0^{\tau_-(x,v)}\int_{\mathbb{S}^{n-1}}k(x-tv,v_1,v)\int_0^{\tau_-(x-tv,v_1)}\frac{E(x,x-tv,x-tv-t_1v_1,x')}{|x-tv-t_1v_1-x'|^{n-1}}$$
$$\times k(x-tv-t_1v_1,v_2,v_1)k(x',v',v_2)_{v_2=x-t\widehat{v-t_1v_1-x'}}dt_1dv_1dtdx'dv', \tag{6.185}$$

for a.e. $(x,v)\in X\times\mathbb{S}^{n-1}$ and for $\psi\in L^1(X\times\mathbb{S}^{n-1})$. Therefore performing the change of variables $z=x-tv-t_1v_1$ ($dz=t_1^{n-1}dt_1dv_1$) on the right hand side of (6.184) we obtain

$$\beta_3(x,v,x',v')=\int_0^{\tau_-(x,v)}\int_X\frac{E(x,x-tv,z,x')k(x',v',\widehat{z-x'})}{|x-tv-z|^{n-1}|z-x'|^{n-1}}$$
$$\times k(x-tv,\widehat{x-tv-z},v)k(z,\widehat{z-x'},\widehat{x-tv-z})dtdz, \tag{6.186}$$

for a.e. $(x,v,x',v') \in X \times \mathbb{S}^{n-1} \times X \times \mathbb{S}^{n-1}$. Then by induction we have

$$\beta_m(x,v,z_m,v_m) = \int_0^{\tau_-(x,v)} \int_{X^{m-2}} \frac{E(x,x-tv,z_2,\dots,z_m)}{|x-tv-z_2|^{n-1}\Pi_{i=2}^{m-1}|z_i-z_{i+1}|^{n-1}} \times k(x-tv,v_1,v)\Pi_{i=2}^m k(z_i,v_i,v_{i-1})_{|v_1=x\widehat{-tv-z_2},\ v_i=z_i\widehat{-z_{i+1}},\ i=2\dots m-1} dt dz_2 \dots dz_{m-1}, \tag{6.187}$$

for a.e. $(x,v,x',v') \in X \times \mathbb{S}^{n-1} \times X \times \mathbb{S}^{n-1}$.

We prove (6.46) for $m=2$. From (6.184), (6.45) and (6.42) it follows that

$$\bar{K^2}J\psi(x) = \int_{\mathbb{S}^{n-1}} \sigma_a(x,v) \int_{X\times\mathbb{S}^{n-1}} \int_0^{\tau_-(x,v)} E(x,x-tv,y) \frac{k(x-tv,v_1,v)k(y,v',v_1)_{|v_1=x\widehat{-tv-y}}}{|x-tv-y|^{n-1}} dt \times E(y,y-\tau_-(y,v')v')\psi(y-\tau_-(y,v')v',v')dy dv' dv, \tag{6.188}$$

for a.e. $x \in X$ and for $\psi \in L^1(\Gamma_-, d\xi)$. Then performing the change of variable $z = x - tv$ ($t = |x-z|$, $v = \widehat{x-z}$ and $dz = t^{n-1}dtdv$) on the right hand side of (6.188), we obtain

$$\bar{K^2}J\psi(x) = \int_{X\times X\times\mathbb{S}^{n-1}} \sigma_a(x,\widehat{x-z})E(x,z,y) \frac{k(z,v_1,v)k(y,v',v_1)_{|v_1=\widehat{z-y}}}{|x-z|^{n-1}|z-y|^{n-1}} \times E(y,y-\tau_-(y,v')v')\psi(y-\tau_-(y,v')v',v')dz dy dv', \tag{6.189}$$

for a.e. $x \in X$ and for $\psi \in L^1(\Gamma_-, d\xi)$. Performing the change of variables $y = x' + t'v'$ ($x' \in \partial X$, $t' > 0$, $dz = |\nu(x')\cdot v'|d\mu(x')dt'$) on the right hand side of (6.189), we obtain $\bar{K^2}J\psi(x) = \int_{\Gamma_-} \alpha_2(x,x',v')\psi(x',v')d\mu(x')dv'$ for a.e. $x \in X$ and for $\psi \in L^1(\Gamma_-, d\xi)$, which proves (6.46) for $m=2$.

Then we prove (6.47) before proving (6.46) for $m \geq 3$. Let $m \geq 3$. From (6.187) and the definition of the operator $\bar{K^m}$ (6.45), it follows that

$$\begin{aligned}
\bar{K^m}\psi(z_0) &= \int_{\mathbb{S}^{n-1}} \sigma_a(z_0,v_0) \int_{X\times\mathbb{S}^{n-1}} \beta_m(z_0,v_0,z_m,v_m)\psi(z_m,v_m)dz_m dv_m dv_0 \\
&= \int_{\mathbb{S}^{n-1}} \sigma_a(z_0,v_0) \int_{X\times\mathbb{S}^{n-1}} \int_0^{\tau_-(z_0,v_0)} \int_{X^{m-2}} E(z_0,z_0-tv_0,z_2,\dots,z_m) \\
&\times \frac{k(z_0-tv_0,v_1,v_0)\Pi_{i=2}^m k(z_i,v_i,v_{i-1})_{|v_1=z_0\widehat{-tv_0}-z_2,\ v_i=z_i\widehat{-z_{i+1}},\ i=2\dots m-1}}{|z_0-tv_0-z_2|^{n-1}\Pi_{i=2}^{m-1}|z_i-z_{i+1}|^{n-1}} \\
&\times dt dz_2 \dots dz_{m-1}\psi(z_m,v_m)dz_m dv_m dv_0,
\end{aligned}$$

for a.e. $z_0 \in X$ and for $\psi \in L^1(X\times\mathbb{S}^{n-1})$. Therefore performing the change of variables $z_1 = z_0 - tv_0$ ($dz_1 = t^{n-1}dtdv_0$, $t = |z_0 - z_1|$ and $v_0 = \widehat{z_0 - z_1}$) on the right hand side of the above equation we obtain $\bar{K^m}\psi(z_0) = \int_{X\times\mathbb{S}^{n-1}} \gamma_m(z_0,z_m,v_m)\psi(z_m,v_m)$ $dz_m dv_m$, for a.e. $z_0 \in X$ and for $\psi \in L^1(X\times\mathbb{S}^{n-1})$, which proves (6.47).

We prove (6.46). Let $m \geq 3$. From (6.47), (6.45) and (6.42), it follows that

$$\begin{aligned}
\bar{K^m}J\psi(z_0) &= \int_{X\times\mathbb{S}^{n-1}} \gamma_m(z_0,z_m,v_m) \\
&\times E(z_m,z_m-\tau_-(z_m,v_m)v_m)\psi(z_m-\tau_-(z_m,v_m)v_m,v_m)dz_m dv_m \\
&= \int_{X\times\mathbb{S}^{n-1}} \int_{X^{m-1}} \frac{E(z_0,\dots,z_m,z_m-\tau_-(z_m,v_m)v_m)}{\Pi_{i=1}^m|z_i-z_{i-1}|^{n-1}}\psi(z_m-\tau_-(z_m,v_m)v_m,v_m) \\
&\times \left[\sigma_a(z_0,v_0)\Pi_{i=1}^m k(z_i,v_i,v_{i-1})\right]_{v_i=z_i\widehat{-z_{i+1}},\ i=0\dots m-1} dz_1\dots dz_{m-1}dz_m dv_m,
\end{aligned}$$

for a.e. $z_0 \in X$ and for $\psi \in L^1(\Gamma_-, d\xi)$. Then performing the change of variables $z_m = \text{“}z_m\text{”} + t'v_m$ ($\text{“}z_m\text{”} \in \partial X$, $t' > 0$, $dz_m = |\nu(\text{“}z_m\text{”}) \cdot v_m| d\mu(\text{“}z_m\text{”})dt'$), we obtain $\bar{K^m} J\psi(z_0) = \int_{\Gamma_-} \alpha_m(z_0, z_m, v_m)\psi(z_m, v_m)d\mu(z_m)dv_m$ for a.e. $z_0 \in X$ and for $\psi \in L^1(\Gamma_-, d\xi)$, which proves (6.46). □

CHAPTER 7

Stability and Resolution Analysis for a Topological Derivative Based Imaging Functional

7.1. Problem Formulation

Consider an acoustic anomaly with constant bulk modulus K and volumetric mass density ρ. The background medium Ω is smooth and homogeneous with bulk modulus and density equal to one. Suppose that the operating frequency ω is such that ω^2 is not an eigenvalue for the operator $-\Delta$ in $L^2(\Omega)$ with homogeneous Neumann boundary conditions. The scalar acoustic pressure u generated by the Neumann data g in the presence of the anomaly D is the solution to the Helmholtz equation:

(7.1)
$$\begin{cases} \nabla \cdot \Big(\mathbf{1}_{\Omega\setminus\overline{D}}(\mathbf{x}) + \rho^{-1}\mathbf{1}_D(\mathbf{x})\Big)\nabla u + \omega^2\big(\mathbf{1}_{\Omega\setminus\overline{D}}(\mathbf{x}) + K^{-1}\mathbf{1}_D(\mathbf{x})\big)u = 0 \ \text{ in } \Omega, \\ \dfrac{\partial u}{\partial \nu} = g \ \text{ on } \partial\Omega, \end{cases}$$

while the background solution U satisfies

(7.2)
$$\begin{cases} \Delta U + \omega^2 U = 0 \ \text{ in } \Omega, \\ \dfrac{\partial U}{\partial \nu} = g \ \text{ on } \partial\Omega. \end{cases}$$

Here, ν is the outward normal to $\partial\Omega$ and $\mathbf{1}_D$ is the characteristic function of D.

The problem under consideration is the following one: given the field u measured at the surface of the domain Ω, we want to estimate the location of the anomaly D.

Recently, the concept of topological derivative has been applied in the imaging of small anomalies. See, for instance, [**64, 65, 68, 38, 105, 84, 83**]. The concept first appeared in shape optimization [**66, 121, 48**]. However, the use of the topological based imaging functional has been heuristic. As far as we know, it lacks mathematical justification. A stability and resolution investigation is also missing in the literature.

The goal of this chapter is threefold: (i) to explain why the concept of topological derivative works for imaging small acoustic anomalies, (ii) to compare the topological derivative based imaging functional with other widely used imaging approaches such as MUltiple Signal Classification (MUSIC), backpropagation, and Kirchhoff migration, and (iii) to carry out a detailed stability and resolution analysis for the topological derivative based algorithm. Both medium and measurement noises are considered.

The chapter is organized as follows. In Section 7.2, we recall an asymptotic expansion of the boundary pressure perturbations. In Section 7.3, we introduce the topological derivative based imaging functional and prove that it attains its maximum at the location of the anomaly. Sections 7.4 and 7.5 are devoted to a stability and resolution analysis of the topological derivative based functional in the presence of medium and measurement noise, respectively. In Section 7.6, we review MUSIC, backpropagation, and Kirchhoff migration imaging approaches. In Section 7.7, we perform a variety of numerical tests to compare the topological derivative based imaging functional with MUSIC and backpropagation. The chapter ends with a short discussion.

7.2. Asymptotic Analysis of the Boundary Pressure Perturbations

Suppose that the anomaly is $D = \mathbf{z}_a + \delta B$, where $\mathbf{z}_a$ is the "center" of D, B is a smooth reference domain which contains the origin, and δ, the characteristic size of D, is a small parameter.

In this section, we provide an asymptotic expansion of the boundary pressure perturbations, $u - U$, as δ goes to zero. For doing so, we need to introduce a few auxiliary functions that can be computed either analytically or numerically.

For B a smooth bounded domain in $\mathbb{R}^d$ and $0 < k \neq 1 < +\infty$ a material parameter, let $\hat{\mathbf{v}} = \hat{\mathbf{v}}(k, B)$ be the solution to

$$
\begin{cases}
\Delta \hat{\mathbf{v}} = \mathbf{0} \quad \text{in } \mathbb{R}^d \setminus \overline{B}, \\
\Delta \hat{\mathbf{v}} = \mathbf{0} \quad \text{in } B, \\
\hat{\mathbf{v}}|_- - \hat{\mathbf{v}}|_+ = \mathbf{0} \quad \text{on } \partial B, \\
k \dfrac{\partial \hat{\mathbf{v}}}{\partial \nu}\Big|_- - \dfrac{\partial \hat{\mathbf{v}}}{\partial \nu}\Big|_+ = \mathbf{0} \quad \text{on } \partial B, \\
\hat{\mathbf{v}}(\boldsymbol{\xi}) - \boldsymbol{\xi} \to \mathbf{0} \quad \text{as } |\boldsymbol{\xi}| \to +\infty.
\end{cases}
\tag{7.3}
$$

Here we denote

$$
v|_\pm(\boldsymbol{\xi}) := \lim_{t \to 0^+} v(\boldsymbol{\xi} \pm t \boldsymbol{\nu}_{\boldsymbol{\xi}}), \quad \boldsymbol{\xi} \in \partial B,
$$

and

$$
\frac{\partial v}{\partial \nu}\bigg|_\pm (\boldsymbol{\xi}) := \lim_{t \to 0^+} \boldsymbol{\nu}_{\boldsymbol{\xi}}^T \nabla v(\boldsymbol{\xi} \pm t \boldsymbol{\nu}_{\boldsymbol{\xi}}), \quad \boldsymbol{\xi} \in \partial B,
$$

if the limits exist, where $\boldsymbol{\nu}_{\boldsymbol{\xi}}$ is the outward unit normal to ∂B at $\boldsymbol{\xi}$ and T stands for the transpose (so that $\boldsymbol{a}^T \boldsymbol{b}$ is the scalar product of the two vectors $\boldsymbol{a}$ and $\boldsymbol{b}$). Recall that $\hat{\mathbf{v}}$ plays the role of the first-order corrector in the theory of homogenization [**107**].

Define the polarization tensor $\mathbf{M}(k, B) = (M_{pq})_{p,q=1}^d$ by

$$
M_{pq}(k, B) := (k - 1) \int_B \frac{\partial \hat{v}_q}{\partial \xi_p}(\boldsymbol{\xi}) \, d\boldsymbol{\xi},
\tag{7.4}
$$

where $\hat{\mathbf{v}} = (\hat{v}_1, \ldots, \hat{v}_d)^T$ is the solution to (7.3).

The formula of the polarization tensor for ellipses will be useful. Let B be an ellipse whose semi-axes along the x_1- and x_2-axes and of length a and b,

respectively. Then, $\mathbf{M}(k,B)$ takes the form

$$\mathbf{M}(k,B) = (k-1)|B| \begin{pmatrix} \dfrac{a+b}{a+kb} & 0 \\ 0 & \dfrac{a+b}{b+ka} \end{pmatrix}. \tag{7.5}$$

For $\omega \geq 0$, let for $\mathbf{x} \neq 0$,

$$\Gamma_\omega(\mathbf{x}) = \begin{cases} \dfrac{e^{i\omega|\mathbf{x}|}}{4\pi|\mathbf{x}|}, & d=3, \\ \dfrac{i}{4}H_0^{(1)}(\omega|\mathbf{x}|), & d=2, \end{cases} \tag{7.6}$$

which is the outgoing fundamental solution for the Helmholtz operator $-(\Delta+\omega^2)$ in $\mathbb{R}^d$. Here, $H_0^{(1)}$ is the Hankel function of the first kind of order zero.

Let $\mathcal{S}_\Omega^\omega$ be the single-layer potential for $\Delta+\omega^2$, that is,

$$\mathcal{S}_\Omega^\omega[\varphi](\mathbf{x}) = \int_{\partial\Omega} \Gamma_\omega(\mathbf{x}-\mathbf{y})\varphi(\mathbf{y})\,d\sigma(\mathbf{y}), \quad \mathbf{x} \in \mathbb{R}^d, \tag{7.7}$$

for $\varphi \in L^2(\partial\Omega)$. Let the integral operator $\mathcal{K}_\Omega^\omega$ be defined by

$$\mathcal{K}_\Omega^\omega[\varphi](\mathbf{x}) = \int_{\partial\Omega} \frac{\partial\Gamma_\omega(\mathbf{x}-\mathbf{y})}{\partial\nu(\mathbf{y})}\varphi(\mathbf{y})d\sigma(\mathbf{y}), \quad \mathbf{x} \in \partial\Omega.$$

It is well-known that the normal derivative of $\mathcal{S}_\Omega^\omega$ obeys the following jump relation:

$$\frac{\partial(\mathcal{S}_\Omega^\omega[\varphi])}{\partial\nu}\bigg|_\pm(\mathbf{x}) = \Big(\pm\frac{1}{2}\mathcal{I} + (\mathcal{K}_\Omega^{-\omega})^*\Big)[\varphi](\mathbf{x}) \quad \text{a.e. } \mathbf{x} \in \partial\Omega, \tag{7.8}$$

for $\varphi \in L^2(\partial\Omega)$, where $(\mathcal{K}_\Omega^{-\omega})^*$ is the L^2-adjoint of $\mathcal{K}_\Omega^{-\omega}$; that is,

$$(\mathcal{K}_\Omega^{-\omega})^*[\varphi](\mathbf{x}) = \int_{\partial\Omega} \frac{\partial\Gamma_\omega(\mathbf{x}-\mathbf{y})}{\partial\nu(\mathbf{x})}\varphi(\mathbf{y})d\sigma(\mathbf{y}).$$

For $\mathbf{z} \in \Omega$, let us now introduce the Neumann function for $-(\Delta+\omega^2)$ in Ω corresponding to a Dirac mass at $\mathbf{z}$. That is, N_ω is the solution to

$$\begin{cases} -(\Delta_x+\omega^2)N_\omega(\mathbf{x},\mathbf{z}) = \delta_\mathbf{z} & \text{in } \Omega, \\ \dfrac{\partial N_\omega}{\partial\nu} = 0 & \text{on } \partial\Omega. \end{cases} \tag{7.9}$$

We will need the following lemma from [**19**, Proposition 2.8].

LEMMA 7.1. *The following identity relating the fundamental solution Γ_ω to the Neumann function N_ω holds:*

$$\Big(-\frac{1}{2}\mathcal{I} + \mathcal{K}_\Omega^\omega\Big)[N_\omega(\cdot,\mathbf{z})](\mathbf{x}) = \Gamma_\omega(\mathbf{x}-\mathbf{z}), \quad \mathbf{x} \in \partial\Omega,\ \mathbf{z} \in \Omega. \tag{7.10}$$

In (7.10), $\mathcal{I}$ denotes the identity. Assuming that ω^2 is not an eigenvalue for the operator $-\Delta$ in $L^2(\Omega)$ with homogeneous Neumann boundary conditions, we can prove, using the theory of relatively compact operators, the existence and uniqueness of a solution to (7.1) at least for δ small enough [**128**]. Moreover, the following asymptotic formula for boundary pressure perturbations that are due to the presence of a small acoustic anomaly holds [**128, 17**].

THEOREM 7.2. *Let u be the solution of (7.1) and let U be the background solution. Suppose that $D = \mathbf{z}_a + \delta B$, with $0 < (K, \rho) \neq (1, 1) < +\infty$. Suppose that $\omega\delta \ll 1$.*

(i): *For any $\mathbf{x} \in \partial\Omega$,*

$$\begin{aligned} u(\mathbf{x}) &= U(\mathbf{x}) - \delta^d \Big(\nabla U(\mathbf{z}_a)^T \mathbf{M}(1/\rho, B) \nabla_{\mathbf{z}} N_\omega(\mathbf{x}, \mathbf{z}_a) \\ &\qquad + \omega^2 (K^{-1} - 1) |B| U(\mathbf{z}) N_\omega(\mathbf{x}, \mathbf{z}_a) \Big) + o(\delta^d), \end{aligned} \tag{7.11}$$

where $\mathbf{M}(1/\rho, B)$ is the polarization tensor associated with B and $1/\rho$.

(ii): *Let w be a smooth function such that $(\Delta + \omega^2) w = 0$ in Ω. The weighted boundary measurements $I_w[U, \omega]$ defined by*

$$I_w[U, \omega] := \int_{\partial\Omega} (u - U)(\mathbf{x}) \frac{\partial w}{\partial \nu}(\mathbf{x}) \, d\sigma(\mathbf{x}) \tag{7.12}$$

satisfies

$$I_w[U, \omega] \simeq -\delta^d \Big(\nabla U(\mathbf{z}_a)^T \mathbf{M}(1/\rho, B) \nabla w(\mathbf{z}_a) + \omega^2 (K^{-1} - 1) |B| U(\mathbf{z}_a) w(\mathbf{z}_a) \Big). \tag{7.13}$$

Combining (7.11) and Lemma 7.1, the following corollary immediately holds.

COROLLARY 7.3. *For any $\mathbf{x} \in \partial\Omega$,*

$$\begin{aligned} (-\frac{1}{2}\mathcal{I} + \mathcal{K}_\Omega^\omega)[u - U](\mathbf{x}) &= -\delta^d \Big(\nabla U(\mathbf{z}_a)^T \mathbf{M}(1/\rho, B) \nabla_{\mathbf{z}} \Gamma_\omega(\mathbf{x} - \mathbf{z}_a) \\ &\qquad + \omega^2 (K^{-1} - 1) |B| U(\mathbf{z}) \Gamma_\omega(\mathbf{x} - \mathbf{z}_a) \Big) + o(\delta^d). \end{aligned} \tag{7.14}$$

7.3. Topological Derivative Based Imaging Functional

Suppose that $K > 1$ and $\rho > 1$ (one of the two inequalities could be an equality). To locate the anomaly D, we consider the quadratic misfit

$$\mathcal{E}[U](\mathbf{z}^S) = \frac{1}{2} \int_{\partial\Omega} |(-\frac{1}{2}\mathcal{I} + \mathcal{K}_\Omega^\omega)[u_{\mathbf{z}^S} - u_{\text{meas}}](\mathbf{x})|^2 \, d\sigma(\mathbf{x}) \tag{7.15}$$

over the search points $\mathbf{z}^S$, where $u_{\mathbf{z}^S}$ is the solution of (7.1) with $D' = \mathbf{z}^S + \delta' B'$, $K' > 1$, $\rho' > 1$, B' being chosen a priori, and δ' being small. If $K < 1$ and $\rho < 1$, then we choose $K' < 1$ and $\rho' < 1$. According to Theorem 7.2, the synthetic field $u_{\mathbf{z}^S}$ can be expanded with respect to δ' as

$$\begin{aligned} u_{\mathbf{z}^S}(\mathbf{x}) &= U(\mathbf{x}) - (\delta')^d \Big(\nabla U(\mathbf{z}^S)^T \mathbf{M}(1/\rho', B') \nabla_{\mathbf{z}} N_\omega(\mathbf{x}, \mathbf{z}^S) \\ &\qquad + \omega^2 (K'^{-1} - 1) |B'| U(\mathbf{z}^S) N_\omega(\mathbf{x}, \mathbf{z}^S) \Big) + o\big((\delta')^d\big). \end{aligned}$$

Therefore, in view of Corollary 7.3, the quadratic misfit function can be expanded as powers of δ' as

$$\begin{aligned}
\mathcal{E}[U](\mathbf{z}^S) &= \frac{1}{2}\int_{\partial\Omega} \big|(-\frac{1}{2}\mathcal{I}+\mathcal{K}_\Omega^\omega)[u_{\mathbf{z}^S}-U+U-u_{\rm meas}](\mathbf{x})\big|^2\, d\sigma(\mathbf{x})\\
&= \frac{1}{2}\int_{\partial\Omega} \big|(-\frac{1}{2}\mathcal{I}+\mathcal{K}_\Omega^\omega)[U-u_{\rm meas}](\mathbf{x})\big|^2\, d\sigma(\mathbf{x})\\
&-(\delta')^d{\rm Re}\Big\{\nabla U(\mathbf{z}^S)^T\mathbf{M}(1/\rho',B')\int_{\partial\Omega}\nabla_{\mathbf{z}}\Gamma_\omega(\mathbf{x}-\mathbf{z}^S)\overline{\big((-\frac{1}{2}\mathcal{I}+\mathcal{K}_\Omega^\omega)[U-u_{\rm meas}](\mathbf{x})\big)}\, d\sigma(\mathbf{x})\Big\}\\
&-(\delta')^d\omega^2(K'^{-1}-1)|B'|{\rm Re}\Big\{U(\mathbf{z}^S)\int_{\partial\Omega}\Gamma_\omega(\mathbf{x}-\mathbf{z}^S)\overline{\big((-\frac{1}{2}\mathcal{I}+\mathcal{K}_\Omega^\omega)[U-u_{\rm meas}](\mathbf{x})\big)}\, d\sigma(\mathbf{x})\Big\}\\
&+o\big((\delta\delta')^d+(\delta')^{2d}\big).
\end{aligned}$$

Let w be defined in terms of $u_{\rm meas}-U$ as

$$w(\mathbf{x}) = \overline{\mathcal{S}_\Omega^\omega(-\frac{1}{2}\mathcal{I}+\mathcal{K}_\Omega^\omega)[U-u_{\rm meas}](\mathbf{x})} \quad \text{for } \mathbf{x}\in\Omega, \tag{7.16}$$

where $\mathcal{S}_\Omega^\omega$ is defined by (7.7). From (7.8), it follows that w is the solution of the Helmholtz equation

$$\begin{cases} \Delta w+\omega^2 w=0 \quad \text{in } \Omega,\\ \dfrac{\partial w}{\partial\nu} = (-\dfrac{1}{2}\mathcal{I}+(\mathcal{K}_\Omega^{-\omega})^*)\overline{(-\dfrac{1}{2}\mathcal{I}+\mathcal{K}_\Omega^\omega)[U-u_{\rm meas}]} \quad \text{on } \partial\Omega. \end{cases} \tag{7.17}$$

The function w is obtained by backpropagating the Neumann data

$$(-\frac{1}{2}\mathcal{I}+(\mathcal{K}_\Omega^\omega)^*)(-\frac{1}{2}\mathcal{I}+\mathcal{K}_\Omega^\omega)[U-u_{\rm meas}]$$

inside the background medium (without any anomaly). Note that $\overline{(\mathcal{K}_\Omega^\omega)^*}=(\mathcal{K}_\Omega^{-\omega})^*$.

Therefore, we can rewrite the expansion of the quadratic misfit function as

$$\begin{aligned}
\mathcal{E}[U](\mathbf{z}^S) &= \frac{1}{2}\int_{\partial\Omega}|(-\frac{1}{2}\mathcal{I}+\mathcal{K}_\Omega^\omega)[U-u_{\rm meas}](\mathbf{x})|^2\, d\sigma(\mathbf{x})\\
&-(\delta')^d{\rm Re}\Big\{\nabla U(\mathbf{z}^S)^T\mathbf{M}(1/\rho',B')\nabla w(\mathbf{z}^S)+\omega^2(K'^{-1}-1)|B'|U(\mathbf{z}^S)w(\mathbf{z}^S)\Big\}\\
&+o((\delta\delta')^d+(\delta')^{2d}).
\end{aligned}$$

By computing the topological derivative for $\mathbf{z}^S\in\Omega$,

$$\mathcal{I}_{\rm TD}[U](\mathbf{z}^S) := -\frac{\partial\mathcal{E}[U]}{\partial(\delta')^d}\Big|_{(\delta')^d=0},$$

i.e., minus the derivative of $\mathcal{E}[U]$ with respect to the volume $(\delta')^d$ at zero, we obtain the values of the topological derivative imaging functional:

$$\mathcal{I}_{\rm TD}[U](\mathbf{z}^S) = {\rm Re}\Big\{\nabla U(\mathbf{z}^S)^T\mathbf{M}(1/\rho',B')\nabla w(\mathbf{z}^S)+\omega^2(K'^{-1}-1)|B'|U(\mathbf{z}^S)w(\mathbf{z}^S)\Big\}. \tag{7.18}$$

The functional $\mathcal{I}_{\rm TD}[U](\mathbf{z}^S)$ gives, at every search point $\mathbf{z}^S\in\Omega$, the sensitivity of the misfit function relative to the insertion of an anomaly $D'=\mathbf{z}^S+\delta'B'$ at the point $\mathbf{z}^S$. The maximum of $\mathcal{I}_{\rm TD}[U](\mathbf{z}^S)$ corresponds to the point at which the insertion of an anomaly centered at that point maximally decreases the misfit function. The location of the maximum of $\mathcal{I}_{\rm TD}[U](\mathbf{z}^S)$ is, therefore, a good estimate

of the location $\mathbf{z}_a$ of the anomaly that determines the measured field $u_{\rm meas}$. In fact, as we show below the functional $\mathcal{I}_{\rm TD}$ attains its maximum at $\mathbf{z}^S = \mathbf{z}_a$.

Substituting (7.11) into (7.16), we find that

$$\begin{aligned} w(\mathbf{z}^S) &= \delta^d\bigg(\nabla\overline{U}(\mathbf{z}_a)^T\mathbf{M}(1/\rho,B)\int_{\partial\Omega}\nabla_{\mathbf{z}}\overline{\Gamma_\omega}(\mathbf{x}-\mathbf{z}_a)\nabla\Gamma_\omega(\mathbf{x}-\mathbf{z}^S)\,d\sigma(\mathbf{x}) \\ &\quad +\omega^2(K^{-1}-1)\overline{U}(\mathbf{z}_a)\int_{\partial\Omega}\overline{\Gamma_\omega}(\mathbf{x}-\mathbf{z}_a)\Gamma_\omega(\mathbf{x}-\mathbf{z}^S)\,d\sigma(\mathbf{x})\bigg)+o(\delta^d), \end{aligned}$$

and, for $j=1,\dots,d$,

$$\begin{aligned} \frac{\partial w(\mathbf{z}^S)}{\partial z_j^S} &= \delta^d\bigg(\nabla\overline{U}(\mathbf{z}_a)^T\mathbf{M}(1/\rho,B)\int_{\partial\Omega}\nabla_{\mathbf{z}}\overline{\Gamma_\omega}(\mathbf{x}-\mathbf{z}_a)\frac{\partial\Gamma_\omega(\mathbf{x}-\mathbf{z}^S)}{\partial z_j^S}\,d\sigma(\mathbf{x}) \\ &\quad +\omega^2(K^{-1}-1)\overline{U}(\mathbf{z}_a)\int_{\partial\Omega}\overline{\Gamma_\omega}(\mathbf{x}-\mathbf{z}_a)\frac{\partial\Gamma_\omega(\mathbf{x}-\mathbf{z}^S)}{\partial z_j^S}\,d\sigma(\mathbf{x})\bigg)+o(\delta^d). \end{aligned}$$

We now explain in more detail why the topological derivative imaging functional attains its highest value at the location $\mathbf{z}_a$ of the anomaly. For simplicity assume that $K=1$ or $\rho=1$.

If $\rho=1$ then

$$\begin{aligned} \mathcal{I}_{\rm TD}[U](\mathbf{z}^S) &= \delta^d\omega^4(K'^{-1}-1)(K^{-1}-1)|B'|{\rm Re}\bigg\{U(\mathbf{z}^S)r_\omega(\mathbf{z}^S,\mathbf{z}_a)\overline{U}(\mathbf{z}_a)\bigg\} \\ &\quad +o(\delta^d), \qquad (7.19) \\ r_\omega(\mathbf{z}^S,\mathbf{z}) &:= \int_{\partial\Omega}\Gamma_\omega(\mathbf{x}-\mathbf{z}^S)\overline{\Gamma_\omega}(\mathbf{x}-\mathbf{z})\,d\sigma(\mathbf{x}). \qquad (7.20) \end{aligned}$$

If $K=1$ then

$$\begin{aligned} \mathcal{I}_{\rm TD}[U](\mathbf{z}^S) &= \delta^d\,{\rm Re}\bigg\{\nabla U(\mathbf{z}^S)^T\mathbf{M}(1/\rho',B')\mathbf{R}_\omega(\mathbf{z}^S,\mathbf{z}_a)\mathbf{M}(1/\rho,B)^T\nabla\overline{U}(\mathbf{z}_a)\bigg\} \\ &\quad +o(\delta^d), \\ \mathbf{R}_\omega(\mathbf{z}^S,\mathbf{z}) &:= \int_{\partial\Omega}\nabla_{\mathbf{z}}\Gamma_\omega(\mathbf{x}-\mathbf{z}^S)\nabla_{\mathbf{z}}\overline{\Gamma_\omega}(\mathbf{x}-\mathbf{z})^T\,d\sigma(\mathbf{x}). \end{aligned}$$

Recall that Helmholtz-Kirchhoff theorem (see, *e.g.*, [**4**]) states that, for $\mathbf{z}$ and $\mathbf{z}^S$ away from the boundary $\partial\Omega$, the quantities $r_\omega(\mathbf{z}^S,\mathbf{z})$ and $\mathbf{R}_\omega(\mathbf{z}^S,\mathbf{z})$ are (approximately) proportional to the imaginary part of Γ_ω:

$$\begin{aligned} &\int_{\partial\Omega}\overline{\Gamma_\omega}(\mathbf{x}-\mathbf{z})\Gamma_\omega(\mathbf{x}-\mathbf{z}^S)\,d\sigma(\mathbf{x})\sim\frac{1}{\omega}{\rm Im}\big\{\Gamma_\omega(\mathbf{z}^S-\mathbf{z})\big\}, \\ &\int_{\partial\Omega}\nabla_{\mathbf{z}}\Gamma_\omega(\mathbf{x}-\mathbf{z}^S)\nabla_{\mathbf{z}}\overline{\Gamma_\omega}(\mathbf{x}-\mathbf{z})^T\,d\sigma(\mathbf{x})\sim\omega\,{\rm Im}\big\{\Gamma_\omega(\mathbf{z}^S-\mathbf{z})\big\}\left(\frac{\mathbf{z}-\mathbf{z}^S}{|\mathbf{z}-\mathbf{z}^S|}\right)\left(\frac{\mathbf{z}-\mathbf{z}^S}{|\mathbf{z}-\mathbf{z}^S|}\right)^T. \end{aligned}$$

Here, $A\sim B$ means $A\simeq CB$ for some constant C.

Let, for simplicity, $(\boldsymbol{\theta}_1,\dots,\boldsymbol{\theta}_n)$ be n equi-distributed directions on the unit sphere and denote by U_j the plane wave

$$U_j(\mathbf{x}) = e^{i\omega\boldsymbol{\theta}_j^T\mathbf{x}},\quad \mathbf{x}\in\Omega,\quad j=1,\dots,n. \qquad (7.21)$$

For sufficiently large n we have

$$\frac{1}{n}\sum_{l=1}^{n} e^{i\omega\boldsymbol{\theta}_l^T\mathbf{x}} \simeq 4(\frac{\pi}{\omega})^{d-2}\,\mathrm{Im}\big\{\Gamma_\omega(\mathbf{x})\big\} = \begin{cases} \mathrm{sinc}(\omega|\mathbf{x}|) & \text{for } d=3,\\ J_0(\omega|\mathbf{x}|) & \text{for } d=2, \end{cases} \tag{7.22}$$

where $\mathrm{sinc}(s) = \sin(s)/s$ is the sinc function and J_0 is the Bessel function of the first kind and of order zero.

When $\rho = 1$, by computing the topological derivatives for the n plane waves, we obtain

$$\begin{aligned} \frac{1}{n}\sum_{j=1}^{n}\mathcal{I}_{\mathrm{TD}}[U_j](\mathbf{z}^S) &\simeq \frac{\delta^d\omega^4}{n}\sum_{j=1}^{n}\mathrm{Re}\big\{e^{i\omega\boldsymbol{\theta}_j^T(\mathbf{z}^S-\mathbf{z}_a)}r_\omega(\mathbf{z}^S,\mathbf{z}_a)\big\}\\ &\sim \omega^{5-d}(\mathrm{Im}\big\{\Gamma_\omega(\mathbf{z}^S-\mathbf{z}_a)\big\})^2. \end{aligned} \tag{7.23}$$

Similarly, when $K = 1$, by computing the topological derivatives for the n plane waves, $U_j, j = 1,\dots,n$, given by (7.21), we obtain

$$\frac{1}{n}\sum_{j=1}^{n}\mathcal{I}_{\mathrm{TD}}[U_j](\mathbf{z}^S) \simeq \delta^d\omega^2\frac{1}{n}\sum_{j=1}^{n}\mathrm{Re}\big\{e^{i\omega\boldsymbol{\theta}_j^T(\mathbf{z}^S-\mathbf{z}_a)}\big[\boldsymbol{\theta}_j^T\mathbf{M}(1/\rho',B')\mathbf{R}_\omega(\mathbf{z}^S,\mathbf{z}_a)\mathbf{M}(1/\rho,B)^T\boldsymbol{\theta}_j\big]\big\}.$$

Using $\rho' = 0$ and B' the unit disk, the polarization tensor $\mathbf{M}(1/\rho', B') = C_d\mathbf{I}$, where C_d is a constant, is proportional to the identity. If, additionally, we assume that $\mathbf{M}(1/\rho, B)$ is approximately proportional to the identity, which occurs in particular when B is a disk or a ball, then

$$\frac{1}{n}\sum_{j=1}^{n}\mathcal{I}_{\mathrm{TD}}[U_j](\mathbf{z}^S) \sim \omega^{5-d}(\mathrm{Im}\big\{\Gamma_\omega(\mathbf{z}^S-\mathbf{z}_a)\big\})^2. \tag{7.24}$$

Therefore, the topological derivative based imaging functional

$$\mathcal{I}_{\mathrm{TD}}(\mathbf{z}^S) := \frac{1}{n}\sum_{j=1}^{n}\mathcal{I}_{\mathrm{TD}}[U_j](\mathbf{z}^S) \tag{7.25}$$

attains its maximum at $\mathbf{z}_a$. Moreover, the resolution for the location estimation is given by the diffraction limit. It is of the order of half the wavelength $\lambda = 2\pi/\omega$.

We conclude this section by making a few remarks:

- In (7.15), we postprocess $u_{\mathbf{z}} - u_{\mathrm{meas}}$ by applying the integral operator $(-\frac{1}{2}\mathcal{I}+\mathcal{K}_\Omega^\omega)$. This postprocessing is essential in order to derive an efficient topological based imaging functional. See Section 7.7.
- The topological derivative based imaging functional cannot detect anomalies close to the boundary.
- The results of this section apply to the Dirichlet problem as well as to the case of a hard anomaly.

7.4. Stability with Respect to Medium Noise

7.4.1. The Topological Derivative in the Presence of Medium Noise. We consider the case in which the medium is randomly heterogeneous around a constant background. Let K be the bulk modulus of the anomaly D. We assume that the density ρ of the anomaly is equal to one (*i.e.*, the same as the density of the background) in order to simplify the analysis, but the results could be extended to the general case in which $\rho \neq 1$. The scalar acoustic pressure u generated by the

Neumann data g in the presence of the anomaly D is the solution to the Helmholtz equation:

$$\begin{cases} \Delta u + \omega^2 n^2(\mathbf{x}) u = 0 \ \text{ in } \Omega, \\ \dfrac{\partial u}{\partial \nu} = g \ \text{ on } \partial\Omega. \end{cases} \tag{7.26}$$

The index of refraction is of the form

$$n^2(\mathbf{x}) = 1 + (K^{-1} - 1)\mathbf{1}_D(\mathbf{x}) + \mu(\mathbf{x}),$$

where 1 stands for the constant background, $(K^{-1}-1)\mathbf{1}_D(\mathbf{x})$ stands for the localized perturbation of the index of refraction due to the anomaly, and $\mu(\mathbf{x})$ stands for the fluctuations of the index of refraction due to clutter. We assume that μ is a random process with Gaussian statistics and mean zero, and that it is compactly supported within Ω. The background solution U, *i.e.*, the field that would be observed without the anomaly, satisfies

$$\begin{cases} \Delta U + \omega^2 (1+\mu) U = 0 \ \text{ in } \Omega, \\ \dfrac{\partial U}{\partial \nu} = g \ \text{ on } \partial\Omega. \end{cases} \tag{7.27}$$

Note that U is not known because it depends on μ, only the background reference solution $U^{(0)}$ can be computed:

$$\begin{cases} \Delta U^{(0)} + \omega^2 U^{(0)} = 0 \ \text{ in } \Omega, \\ \dfrac{\partial U^{(0)}}{\partial \nu} = g \ \text{ on } \partial\Omega. \end{cases} \tag{7.28}$$

If the anomaly is of the form $D = \mathbf{z}_a + \delta B$, then one can show that the field measured at the surface of Ω can be expanded as

$$u_{\text{meas}}(\mathbf{x}) = U(\mathbf{x}) - \delta^d \omega^2 (K^{-1} - 1)|B| U(\mathbf{z}_a) N_\omega(\mathbf{x}, \mathbf{z}_a) + o(\delta^d), \tag{7.29}$$

where N_ω is the unknown Neumann function for $-(\Delta + \omega^2(1+\mu))$ (it is unknown because it depends on μ). It is worth mentioning that we changed the notation in this section: N_ω is the Neumann function for $-(\Delta + \omega^2(1+\mu))$, not for $-(\Delta+\omega^2)$ as in the previous section. The Neumann function for $-(\Delta+\omega^2)$ will be denoted by $N_\omega^{(0)}$ (the superscript (0) indicates the 'zero noise').

We want to compare the measured data with the synthetic field $u_{\mathbf{z}^S}$, which is the solution of

$$\begin{cases} \Delta u_{\mathbf{z}^S} + \omega^2 \big(1 + (K'^{-1} - 1)\mathbf{1}_{D'}(\mathbf{x})\big) u_{\mathbf{z}^S} = 0 \ \text{ in } \Omega, \\ \dfrac{\partial u_{\mathbf{z}^S}}{\partial \nu} = g \ \text{ on } \partial\Omega, \end{cases}$$

with $D' = \mathbf{z}^S + \delta' B'$, K' and B' being chosen a priori, and δ' being a small parameter. We can expand the synthetic field $u_{\mathbf{z}^S}$ in powers of δ' and we find that

$$u_{\mathbf{z}^S}(\mathbf{x}) = U^{(0)}(\mathbf{x}) - (\delta')^d \omega^2 (K'^{-1} - 1)|B'| U^{(0)}(\mathbf{z}^S) N_\omega^{(0)}(\mathbf{x}, \mathbf{z}^S) + o\big((\delta')^d\big).$$

The quadratic misfit functional

$$\mathcal{E}[U^{(0)}](\mathbf{z}^S) = \frac{1}{2} \int_{\partial\Omega} |(-\frac{1}{2}\mathcal{I} + \mathcal{K}_\Omega^{\omega,(0)})[u_{\mathbf{z}^S} - u_{\text{meas}}](\mathbf{x})|^2 \, d\sigma(\mathbf{x})$$

uses the background reference solution $U^{(0)}$ and the known integral operator $\mathcal{K}_\Omega^{\omega,(0)}$ defined in terms of the Green function Γ_ω of the reference background medium. It can be expanded as powers of δ' as

$$\begin{aligned}\mathcal{E}[U^{(0)}](\mathbf{z}^S) &= \frac{1}{2}\int_{\partial\Omega} \big|(-\frac{1}{2}\mathcal{I}+\mathcal{K}_\Omega^{\omega,(0)})[U^{(0)}-u_{\rm meas}](\mathbf{x})\big|^2\, d\sigma(\mathbf{x})\\ &-(\delta')^d\omega^2(K'^{-1}-1)|B'|\mathrm{Re}\Big\{U^{(0)}(\mathbf{z}^S)\int_{\partial\Omega}\Gamma_\omega(\mathbf{x}-\mathbf{z}^S)\overline{\big((-\frac{1}{2}\mathcal{I}+\mathcal{K}_\Omega^{\omega,(0)})[U^{(0)}-u_{\rm meas}](\mathbf{x})\big)}\, d\sigma(\mathbf{x})\Big\}\\ &+o\big((\delta\delta')^d+(\delta')^{2d}\big),\end{aligned}$$

This shows that the computation of the topological derivative gives the imaging functional

$$\mathcal{I}_{\rm TD}[U^{(0)}](\mathbf{z}^S) = \omega^2(K'^{-1}-1)|B'|\mathrm{Re}\big\{U^{(0)}(\mathbf{z}^S)w^{(0)}(\mathbf{z}^S)\big\}, \tag{7.30}$$

where $w^{(0)}$ is given by

$$w^{(0)}(\mathbf{z}^S) = \mathcal{S}_\Omega^{\omega,(0)}\overline{\big((-\frac{1}{2}\mathcal{I}+\mathcal{K}_\Omega^{\omega,(0)})[U^{(0)}-u_{\rm meas}]\big)}(\mathbf{z}^S), \tag{7.31}$$

which is the known solution of

$$\begin{cases}\Delta w^{(0)}+\omega^2 w^{(0)}=0 \quad \text{in } \Omega,\\ \dfrac{\partial w^{(0)}}{\partial\nu} = (-\frac{1}{2}\mathcal{I}+(\mathcal{K}_\Omega^{-\omega,(0)})^*)\overline{(-\frac{1}{2}\mathcal{I}+\mathcal{K}_\Omega^{\omega,(0)})[U^{(0)}-u_{\rm meas}]} \quad \text{on } \partial\Omega.\end{cases}$$

Here, $\mathcal{S}_\Omega^{\omega,(0)}$ is the single-layer potential associated with the Green function Γ_ω of the reference background medium. The function $w^{(0)}$ is known because it depends only on $U^{(0)}$ that can be computed and on $u_{\rm meas}$ that is measured at the boundary.

7.4.2. Stability and Resolution Analysis. Let $\Lambda^{(0)} = (-\frac{1}{2}\mathcal{I}+\mathcal{K}_\Omega^{\omega,(0)})^*(-\frac{1}{2}\mathcal{I}+\mathcal{K}_\Omega^{\omega,(0)})$. We want now to carry out a resolution and stability analysis. Using (7.29) we have

$$\begin{aligned}w^{(0)}(\mathbf{z}^S) &= \int_{\partial\Omega} N_\omega^{(0)}(\mathbf{x},\mathbf{z}^S)\overline{\Lambda^{(0)}[U^{(0)}-U]}(\mathbf{x})\, d\sigma(\mathbf{x})\\ &+\delta^d\omega^2(K^{-1}-1)|B|\overline{U(\mathbf{z}_a)}\int_{\partial\Omega}\Lambda^{(0)}[N_\omega^{(0)}(\cdot,\mathbf{z}^S)](\mathbf{x})\overline{N_\omega(\mathbf{x},\mathbf{z}_a)}\, d\sigma(\mathbf{x})\\ &+o\big(\delta^d\big).\end{aligned} \tag{7.32}$$

This expression shows that clutter noise has two effects:

- First the background field U is not known, so that the backpropagation step transports not only the field due to the anomaly but also the field $U-U^{(0)}$ due to clutter, which generates a contribution (the first term of the right-hand side of (7.32)) which is spatially distributed for $\mathbf{z}^S$ throughout the domain Ω.
- Second the Neumann function N_ω is not known exactly, so that the backpropagation by $N_\omega^{(0)}$ of the field generated by the anomaly is not perfect and may alter the sharp peak around $\mathbf{z}^S\sim\mathbf{z}_a$ that is observed when the two Neumann functions are identical.

In the sequel we study the imaging functional in the weak fluctuation regime (when the standard deviation of μ is small). For this we need to characterize the statistical distribution of the function $w^{(0)}$ defined by (7.32):

- The first term of the right-hand side of (7.32) requires to model the difference $U - U^{(0)}$. If we assume that the random process μ has small amplitude, then we can expand U as $U = U^{(0)} + U^{(1)}$ where $U^{(1)}$ is the solution of

$$\left\{ \begin{array}{l} \Delta U^{(1)} + \omega^2 U^{(1)} = -\omega^2 \mu U^{(0)} \ \text{ in } \Omega, \\ \dfrac{\partial U^{(0)}}{\partial \nu} = 0 \ \text{ on } \partial\Omega. \end{array} \right. \tag{7.33}$$

This is a single scattering approximation for the cluttered field as we have neglected the term $\mu U^{(1)}$ in this equation. Therefore $U^{(1)}$ is given by

$$U^{(1)}(\mathbf{x}) = -\omega^2 \int_\Omega N_\omega^{(0)}(\mathbf{x},\mathbf{y})\mu(\mathbf{y})U^{(0)}(\mathbf{y})\, d\mathbf{y}.$$

- The second term of the right-hand side of (7.32) requires to model the term N_ω. In the weak fluctuation regime, the error in this term is essentially determined by the phase mismatch between $N_\omega(\mathbf{x},\mathbf{z}_a)$ and $\Lambda^{(0)}[N_\omega^{(0)}(\cdot,\mathbf{z}^S)](\mathbf{x})$ when $\mathbf{z}^S$ is close to $\mathbf{z}_a$ (which is the position of the peak). This phase mismatch comes from the random fluctuations of the travel time between $\mathbf{x}$ and $\mathbf{z}_a$ which is approximately equal to the integral of $\mu/2$ along the ray from $\mathbf{x}$ to $\mathbf{z}_a$:

$$\overline{N_\omega(\mathbf{x},\mathbf{z}_a)}\Lambda^{(0)}[N_\omega^{(0)}(\cdot,\mathbf{z}^S)](\mathbf{x}) \simeq \overline{N_\omega^{(0)}(\mathbf{x},\mathbf{z}_a)}\Lambda^{(0)}[N_\omega^{(0)}(\cdot,\mathbf{z}^S)](\mathbf{x})e^{-i\omega T(\mathbf{x})},$$

with

$$T(\mathbf{x}) \simeq \frac{|\mathbf{x}-\mathbf{z}_a|}{2}\int_0^1 \mu\Big(\mathbf{z}_a + \frac{\mathbf{x}-\mathbf{z}_a}{|\mathbf{x}-\mathbf{z}_a|}s\Big)\, ds.$$

Therefore $w^{(0)}$ can be expanded as

$$\begin{aligned} w^{(0)}(\mathbf{z}^S) &= \omega^2 \int_\Omega \mu(\mathbf{y})\overline{U^{(0)}(\mathbf{y})}\Big[\int_{\partial\Omega} N_\omega^{(0)}(\mathbf{x},\mathbf{z}^S)\overline{\Lambda^{(0)}[N_\omega^{(0)}(\cdot,\mathbf{y})](\mathbf{x})}\, d\sigma(\mathbf{x})\Big]\, d\mathbf{y} \\ &\quad + \delta^d\omega^2(K^{-1}-1)|B|\overline{U^{(0)}(\mathbf{z}_a)}\int_{\partial\Omega}\Lambda^{(0)}[N_\omega^{(0)}(\cdot,\mathbf{z}^S)](\mathbf{x})\overline{N_\omega^{(0)}(\mathbf{x},\mathbf{z}_a)}e^{-i\omega T(\mathbf{x})}\, d\sigma(\mathbf{x}). \end{aligned}$$

If the correlation radius of the random process μ is small, then the last integral is self-averaging and therefore

$$\begin{aligned} w^{(0)}(\mathbf{z}^S) &= \omega^2 \int_\Omega \mu(\mathbf{y})\overline{U^{(0)}(\mathbf{y})}\Big[\int_{\partial\Omega} N_\omega^{(0)}(\mathbf{x},\mathbf{z}^S)\overline{\Lambda^{(0)}[N_\omega^{(0)}(\cdot,\mathbf{y})](\mathbf{x})}\, d\sigma(\mathbf{x})\Big]\, d\mathbf{y} \\ &\quad + \delta^d\omega^2(K^{-1}-1)|B|\overline{U^{(0)}(\mathbf{z}_a)}\int_{\partial\Omega}\Lambda^{(0)}[N_\omega^{(0)}(\cdot,\mathbf{z}^S)](\mathbf{x})\overline{N_\omega^{(0)}(\mathbf{x},\mathbf{z}_a)}e^{-\frac{\omega^2\mathrm{Var}(T(\mathbf{x}))}{2}}\, d\sigma(\mathbf{x}). \end{aligned}$$

Let us introduce the kernel

$$Q(\mathbf{z}^S,\mathbf{z}_a) := \mathrm{Re}\Big\{U^{(0)}(\mathbf{z}^S)\overline{U^{(0)}(\mathbf{z}_a)}\int_{\partial\Omega}\Lambda^{(0)}[N_\omega^{(0)}(\cdot,\mathbf{z}^S)](\mathbf{x})\overline{N_\omega^{(0)}(\mathbf{x},\mathbf{z}_a)}\, d\sigma(\mathbf{x})\Big\},$$

and the function

$$Q_0(\mathbf{z}^S) = \frac{\lambda^{3-d}}{\pi 2^{5-d}}|U^{(0)}(\mathbf{z}^S)|^2 \quad \text{for } d = 2 \text{ or } 3. \tag{7.34}$$

As shown in Section 7.3, we have

$$Q(\mathbf{z}^S,\mathbf{z}_a) = \mathrm{Re}\Big\{U^{(0)}(\mathbf{z}^S)\overline{U^{(0)}(\mathbf{z}_a)}\int_{\partial\Omega}\Gamma_\omega(\mathbf{x}-\mathbf{z}^S)\overline{\Gamma_\omega(\mathbf{x}-\mathbf{z}_a)}\, d\sigma(\mathbf{x})\Big\}.$$

Moreover, the function $\mathbf{z}^S \to Q(\mathbf{z}^S, \mathbf{z}_a)$ is maximal for $\mathbf{z}^S = \mathbf{z}_a$, its maximal value is $Q_0(\mathbf{z}_a)$ and the width of the peak of $\mathbf{z}^S \to Q(\mathbf{z}^S, \mathbf{z}_a)$ centered at $\mathbf{z}^S = \mathbf{z}_a$ is of the order of half the wavelength λ. We can express the topological derivative imaging functional in terms of the kernel Q:

(7.35)
$$\begin{aligned}\mathcal{I}_{\mathrm{TD}}[U^{(0)}](\mathbf{z}^S) \quad &\simeq \quad \omega^4(K'^{-1}-1)|B'|\int_\Omega \mu(\mathbf{y})Q(\mathbf{z}^S,\mathbf{y})\,d\mathbf{y} \\ &\quad +\delta^d\omega^4(K'^{-1}-1)(K^{-1}-1)|B'||B|Q(\mathbf{z}^S,\mathbf{z}_a)e^{-\frac{\omega^2\mathrm{Var}(T)}{2}},\end{aligned}$$

where we have assumed that $\mathrm{Var}(T(\mathbf{x}))$ is constant for $\mathbf{x} \in \partial\Omega$ in order to simplify the analysis.

The topological derivative has the form of a peak centered at the location $\mathbf{z}_a$ of the anomaly (second term of the right-hand side of (7.35)) buried in a zero-mean Gaussian field or speckle pattern (first term of the right-hand side of (7.35)) that we can characterize statistically.

On the one hand clutter noise reduces the height of the main peak by the damping factor $e^{-\omega^2\mathrm{Var}(T)/2}$ and on the other hand it induces random fluctuations of the image in the form of a speckle field. The covariance function of the speckle field is

$$\begin{aligned}\mathrm{Cov}\big(\mathcal{I}_{\mathrm{TD}}(\mathbf{z}^S),\mathcal{I}_{\mathrm{TD}}(\mathbf{z}^{S'})\big) \quad &= \quad \omega^8(K'^{-1}-1)^2|B'|^2 \\ &\quad \times\int_\Omega\int_\Omega Q(\mathbf{z}^S,\mathbf{y})C_\mu(\mathbf{y},\mathbf{y}')Q(\mathbf{z}^{S'},\mathbf{y}')\,d\mathbf{y}d\mathbf{y}',\end{aligned}$$

where C_μ is the covariance function of the process μ: $C_\mu(\mathbf{y},\mathbf{y}') = \mathbb{E}[\mu(\mathbf{y})\mu(\mathbf{y}')]$.

If we assume that the process μ is supported and stationary in $\Omega_\mu \subset \Omega$, that the correlation radius l_μ of μ is smaller than the wavelength, and if we denote by σ_μ the standard deviation of μ, then we have

$$\mathrm{Var}(T) \simeq \frac{1}{8}\sigma_\mu^2\mathrm{diam}(\Omega_\mu)l_\mu,$$

and

$$\mathrm{Cov}\big(\mathcal{I}_{\mathrm{TD}}(\mathbf{z}^S),\mathcal{I}_{\mathrm{TD}}(\mathbf{z}^{S'})\big) \simeq \omega^8(K'^{-1}-1)^2|B'|^2\sigma_\mu^2 l_\mu^d\int_{\Omega_\mu} Q(\mathbf{z}^S,\mathbf{y})Q(\mathbf{z}^{S'},\mathbf{y})\,d\mathbf{y}.$$

Since the typical width of the kernel Q is about half-a-wavelength, we can see that the correlation radius of the speckle field is of the order of half the wavelength, that is to say, of the same order as the main peak centered at the anomaly location. Therefore, there is no way to distinguish the main peak from the hot spots of the speckle field based on their shapes. Only the height of the main peak can allow it to be visible out of the speckle field.

It is interesting to notice that the variance of the speckle field depends on the diameter of the heterogeneous region Ω_μ, because $Q(\mathbf{z}^S,\mathbf{y})^2$ decays as $1/|\mathbf{z}^S-\mathbf{y}|^{d-1}$ since $|\mathbf{z}^S-\mathbf{y}| \gg \lambda$, so that

$$\mathrm{Var}\big(\mathcal{I}_{\mathrm{TD}}(\mathbf{z}^S)\big) \simeq \omega^8(K'^{-1}-1)^2|B'|^2\sigma_\mu^2 l_\mu^d Q_0^2(\mathbf{z}_a)\lambda^{d-1}\mathrm{diam}(\Omega_\mu).$$

Therefore, a large heterogeneous domain implies large fluctuations in the topological derivative, and the peak centered at the anomaly location $\mathbf{z}_a$ can be buried in these fluctuations. More quantitatively, the Signal-to-Noise Ratio (SNR) defined

by

$$\mathrm{SNR} = \frac{\mathbb{E}[\mathcal{I}_{\mathrm{TD}}(\mathbf{z}_a)]}{\mathrm{Var}(\mathcal{I}_{\mathrm{TD}}(\mathbf{z}_a))^{1/2}}$$

is equal to

$$\mathrm{SNR} = \frac{(K^{-1}-1)}{\sigma_\mu}\frac{\delta^d|B|}{\lambda^d}\frac{\lambda^{1/2}}{\mathrm{diam}(\Omega_\mu)^{1/2}}\frac{\lambda^{d/2}}{l_\mu^{d/2}}e^{-\frac{\pi^2}{2}\sigma_\mu^2\frac{l_\mu}{\lambda^2}}. \tag{7.36}$$

As shown by (7.36), the SNR is proportional to the contrast $(K^{-1}-1)$ and the volume of the anomaly, $\delta^d|B|$ over the standard deviation the noise, σ_μ. Moreover, it depends on the dimensionless parameters l_μ/λ, $\mathrm{diam}(\Omega_\mu)/\lambda$, and δ/λ.

7.5. Stability with Respect to Measurement Noise

7.5.1. The Topological Derivative in the Presence of Measurement Noise. We consider the case in which the field $u_{\mathrm{meas}}(\mathbf{x})$ measured at the surface of the domain is corrupted by an additive noise that we denote by $\nu_{\mathrm{noise}}(\mathbf{x})$, $\mathbf{x}\in\partial\Omega$. Again, in order to simplify the presentation, we suppose that $\rho = 1$.

If we assume that the surface of the domain Ω is covered with sensors half the wavelength apart from each other and that the additive noises have variance σ_1^2 and are independent from one sensor to the other one, then we can model the additive noise process ν_{noise} by a Gaussian white noise with covariance function

$$\mathbb{E}\big[\nu_{\mathrm{noise}}(\mathbf{x})\overline{\nu_{\mathrm{noise}}(\mathbf{x}')}\big] = \sigma^2_{\mathrm{noise}}\delta(\mathbf{x}-\mathbf{x}'), \qquad \sigma^2_{\mathrm{noise}} = \sigma_1^2\lambda^{d-1}2^{1-d}.$$

The topological derivative imaging functional is

$$\mathcal{I}_{\mathrm{TD}}[U^{(0)}](\mathbf{z}^S) = \omega^2(K'^{-1}-1)|B'|\mathrm{Re}\big\{U^{(0)}(\mathbf{z}^S)\big(w^{(0)}(\mathbf{z}^S)+w_{\mathrm{noise}}(\mathbf{z}^S)\big)\big\},$$

where

$$w_{\mathrm{noise}}(\mathbf{z}^S) = -\mathcal{S}_\Omega^{\omega,(0)}\overline{(-\frac{1}{2}\mathcal{I}+\mathcal{K}_\Omega^{\omega,(0)})[\nu_{\mathrm{noise}}]}(\mathbf{z}^S), \tag{7.37}$$

and

$$w^{(0)}(\mathbf{z}^S) = \mathcal{S}_\Omega^{\omega,(0)}\overline{(-\frac{1}{2}\mathcal{I}+\mathcal{K}_\Omega^{\omega,(0)})[U^{(0)}-(u_{\mathrm{meas}}-\nu_{\mathrm{noise}})]}(\mathbf{z}^S). \tag{7.38}$$

7.5.2. Stability and Resolution Analysis. We find from (7.37) and (7.38) that

$$\begin{aligned}\mathcal{I}_{\mathrm{TD}}[U^{(0)}](\mathbf{z}^S) &= \delta^d\omega^4(K'^{-1}-1)(K^{-1}-1)|B'||B|Q(\mathbf{z}^S,\mathbf{z}_a) - \omega^2(K'^{-1}-1)|B'| \\ &\times\mathrm{Re}\Big\{\int_{\partial\Omega}U^{(0)}(\mathbf{z}^S)\Gamma_\omega(\mathbf{z}^S-\mathbf{y})\overline{(-\frac{1}{2}\mathcal{I}+\mathcal{K}_\Omega^{\omega,(0)})[\nu_{\mathrm{noise}}](\mathbf{y})}\,d\sigma(\mathbf{y})\Big\}.\end{aligned} \tag{7.39}$$

Therefore, the imaging functional $\mathcal{I}_{\mathrm{TD}}$ has the form of a peak centered at the location $\mathbf{z}_a$ of the anomaly. Moreover, (7.39) shows that the peak is buried in a speckle field, as in the case of clutter noise. However, on contrary to the clutter noise, the value of the main peak itself is not reduced by the additive noise, which means that the imaging functional is much more robust with respect to additive measurement noise than with respect to clutter noise. Let us compute the covariance function of the speckle field. We first introduce the auxiliary field defined on $\partial\Omega$:

$$\nu_{\mathrm{noise},1}(\mathbf{y}) = (-\frac{1}{2}\mathcal{I}+\mathcal{K}_\Omega^{\omega,(0)})[\nu_{\mathrm{noise}}](\mathbf{y}).$$

It is a zero-mean with Gaussian statistics and covariance

$$\begin{aligned}\mathbb{E}\big[\nu_{\text{noise},1}(\mathbf{y})\overline{\nu_{\text{noise},1}(\mathbf{y}')}\big] &= \frac{\sigma^2_{\text{noise}}}{4}\delta(\mathbf{y}-\mathbf{y}') - \frac{\sigma^2_{\text{noise}}}{2}\Big(\overline{\frac{\partial\Gamma_\omega(\mathbf{y}'-\mathbf{y})}{\partial\nu(\mathbf{y})}} + \frac{\partial\Gamma_\omega(\mathbf{y}'-\mathbf{y})}{\partial\nu(\mathbf{y}')}\Big)\\ &\quad +\sigma^2_{\text{noise}}\int_{\partial\Omega}\frac{\partial\Gamma_\omega(\mathbf{y}-\mathbf{x})}{\partial\nu(\mathbf{x})}\overline{\frac{\partial\Gamma_\omega(\mathbf{y}'-\mathbf{x})}{\partial\nu(\mathbf{x})}}\,d\sigma(\mathbf{x}).\end{aligned}$$

We next introduce the auxiliary field defined on Ω:

$$\nu_{\text{noise},2}(\mathbf{z}) = \int_{\partial\Omega}\Gamma_\omega(\mathbf{z}-\mathbf{y})\overline{\nu_{\text{noise},1}(\mathbf{y})}\,d\sigma(\mathbf{y}).$$

It is a zero-mean with Gaussian statistics with covariance:

$$\mathbb{E}\big[\nu_{\text{noise},2}(\mathbf{z})\overline{\nu_{\text{noise},2}(\mathbf{z}')}\big] = \int_{\partial\Omega}\int_{\partial\Omega}\Gamma_\omega(\mathbf{z}-\mathbf{y})\overline{\Gamma_\omega(\mathbf{z}'-\mathbf{y}')}\overline{\mathbb{E}\big[\nu_{\text{noise},1}(\mathbf{z})\overline{\nu_{\text{noise},1}(\mathbf{z}')}\big]}\,d\sigma(\mathbf{y})\,d\sigma(\mathbf{y}').$$

Using Helmholtz-Kirchhoff theorem the covariance of $\nu_{\text{noise},2}(\mathbf{z})$ can be expressed as

$$\begin{aligned}\mathbb{E}\big[\nu_{\text{noise},2}(\mathbf{z})\overline{\nu_{\text{noise},2}(\mathbf{z}')}\big] &= \frac{\sigma^2_{\text{noise}}}{4\omega}\text{Im}\big\{\Gamma_\omega(\mathbf{z}-\mathbf{z}')\big\}\\ &\quad -\frac{\sigma^2_{\text{noise}}}{2\omega}\int_{\partial\Omega}\Gamma_\omega(\mathbf{z}-\mathbf{y})\frac{\partial\text{Im}\big\{\Gamma_\omega(\mathbf{z}'-\mathbf{y})\big\}}{\partial\nu(\mathbf{y})}\,d\sigma(\mathbf{y})\\ &\quad -\frac{\sigma^2_{\text{noise}}}{2\omega}\int_{\partial\Omega}\overline{\Gamma_\omega(\mathbf{z}'-\mathbf{y})}\frac{\partial\text{Im}\big\{\Gamma_\omega(\mathbf{z}-\mathbf{y})\big\}}{\partial\nu(\mathbf{y})}\,d\sigma(\mathbf{y})\\ &\quad +\frac{\sigma^2_{\text{noise}}}{\omega^2}\int_{\partial\Omega}\frac{\partial\text{Im}\big\{\Gamma_\omega(\mathbf{z}-\mathbf{y})\big\}}{\partial\nu(\mathbf{y})}\frac{\partial\text{Im}\big\{\Gamma_\omega(\mathbf{z}'-\mathbf{y})\big\}}{\partial\nu(\mathbf{y})}\,d\sigma(\mathbf{y}).\end{aligned}$$

When $\mathbf{z}$ and $\mathbf{z}'$ are far from the boundary, using $\frac{\partial\Gamma_\omega(\mathbf{z}-\mathbf{y})}{\partial\nu(\mathbf{y})} \simeq i\omega\Gamma_\omega(\mathbf{z}-\mathbf{y})$ and Helmholtz-Kirchhoff theorem, we get

$$\mathbb{E}\big[\nu_{\text{noise},2}(\mathbf{z})\overline{\nu_{\text{noise},2}(\mathbf{z}')}\big] = \frac{\sigma^2_{\text{noise}}}{4\omega}\text{Im}\big\{\Gamma(\mathbf{z}-\mathbf{z}')\big\},$$

and therefore

$$\text{Cov}\big(\mathcal{I}_{\text{TD}}(\mathbf{z}^S),\mathcal{I}_{\text{TD}}(\mathbf{z}^{S'})\big) = \frac{1}{8}\omega^4(K'^{-1}-1)^2|B'|^2\sigma^2_{\text{noise}}Q(\mathbf{z}^S,\mathbf{z}^{S'}),$$

for the search points $\mathbf{z}^S,\mathbf{z}^{S'}\in\Omega$. This shows that the typical shape of a hot spot of the speckle field is exactly the form of the main peak. Moreover, the variance of the speckle field is

$$\text{Var}\big(\mathcal{I}_{\text{TD}}(\mathbf{z}^S)\big) = \frac{1}{8}\omega^4(K'^{-1}-1)^2|B'|^2\sigma^2_{\text{noise}}Q_0(\mathbf{z}^S),$$

with Q_0 given by (7.34), which shows that the SNR is equal to

(7.40)
$$\text{SNR} = \frac{2\sqrt{2}\omega^2Q_0(\mathbf{z}_a)^{1/2}(K^{-1}-1)\delta^d|B|}{\sigma_{\text{noise}}} = 2^{d-1}\pi^{3/2}\frac{|U^{(0)}(\mathbf{z}_a)|(K^{-1}-1)}{\sigma_1}\frac{\delta^d|B|}{\lambda^d}.$$

From (7.40), the SNR is proportional to the contrast $(K^{-1}-1)$ and the volume of the anomaly, $\delta^d|B|$, over the standard deviation of the noise, σ_{noise}.

7.6. Other Imaging Algorithms

Consider P well-separated anomalies $D_p = \mathbf{z}_p + \delta B_p$, $p = 1, \ldots, P$. The volumetric mass density and bulk modulus of D_p are denoted by ρ_p and K_p, respectively. Suppose that all the domains B_p are disks.

7.6.1. MUSIC-type Algorithm. Let $(\boldsymbol{\theta}_1, \ldots, \boldsymbol{\theta}_n)$ be n unit vectors in $\mathbb{R}^d$. For $\boldsymbol{\theta} \in \{\boldsymbol{\theta}_1, \ldots, \boldsymbol{\theta}_n\}$, we assume that we are in possession of the boundary data u when the domain Ω is illuminated with the plane wave $U(\mathbf{x}) = e^{i\omega \boldsymbol{\theta}^T \mathbf{x}}$. Therefore, taking the harmonic function $w(\mathbf{x}) = e^{-i\omega \boldsymbol{\theta}'^T \mathbf{x}}$ for $\boldsymbol{\theta}' \in \{\boldsymbol{\theta}_1, \ldots, \boldsymbol{\theta}_n\}$ and using (7.5) shows that the weighted boundary measurement is approximately equal to

$$I_w[U, \omega] \simeq -\sum_{p=1}^{P} |D_p| \omega^2 \Big(2 \frac{\rho_p^{-1} - 1}{\rho_p^{-1} + 1} \boldsymbol{\theta}^T \boldsymbol{\theta}' + K_p^{-1} - 1 \Big) e^{i\omega (\boldsymbol{\theta} - \boldsymbol{\theta}')^T \mathbf{z}_p}.$$

Define the response matrix $\mathbf{A} = (A_{ll'})_{l,l'=1}^n \in \mathbb{C}^{n \times n}$ by

$$A_{ll'} := I_{w_{l'}}[U_l, \omega]. \tag{7.41}$$

It is approximately given by

$$A_{ll'} \simeq -\sum_{p=1}^{P} |D_p| \omega^2 \Big(2 \frac{\rho_p^{-1} - 1}{\rho_p^{-1} + 1} \boldsymbol{\theta}_l^T \boldsymbol{\theta}_{l'} + K_p^{-1} - 1 \Big) e^{i\omega (\boldsymbol{\theta}_l - \boldsymbol{\theta}_{l'})^T \mathbf{z}_p},$$

for $l, l' = 1, \ldots, n$. Introduce the n-dimensional vector fields $\boldsymbol{g}^{(j)}$, defined for $j = 1, \ldots, d+1$, by

$$\boldsymbol{g}^{(j)}(\mathbf{x}) = \big(\mathbf{e}_j^T \boldsymbol{\theta}_1 e^{i\omega \boldsymbol{\theta}_1^T \mathbf{x}}, \ldots, \mathbf{e}_j^T \boldsymbol{\theta}_n e^{i\omega \boldsymbol{\theta}_n^T \mathbf{x}} \big)^T, \quad j = 1, \ldots, d, \tag{7.42}$$

and

$$\boldsymbol{g}^{(d+1)}(\mathbf{x}) = \big(e^{i\omega \boldsymbol{\theta}_1^T \mathbf{x}}, \ldots, e^{i\omega \boldsymbol{\theta}_n^T \mathbf{x}} \big)^T, \tag{7.43}$$

where $(\mathbf{e}_1, \ldots, \mathbf{e}_d)$ is an orthonormal basis of $\mathbb{R}^d$. Let $\mathbf{P}_{\text{noise}} = \mathbf{I} - \mathbf{P}$, where $\mathbf{P}$ is the orthogonal projection onto the range of $\mathbf{A}$. The MUSIC-type imaging functional is defined by

$$\mathcal{I}_{\text{MU}}(\mathbf{z}^S) := \Big(\sum_{j=1}^{d+1} \| \mathbf{P}_{\text{noise}} \boldsymbol{g}^{(j)}(\mathbf{z}^S) \|^2 \Big)^{-1/2}. \tag{7.44}$$

This functional has large peaks only at the locations of the anomalies; see, *e.g.*, [**4**].

7.6.2. Backpropagation-type Algorithms. Let $(\boldsymbol{\theta}_1, \ldots, \boldsymbol{\theta}_n)$ be n unit vectors in $\mathbb{R}^d$. A backpropagation-type imaging functional at a single frequency ω is given by

$$\mathcal{I}_{\text{BP}}(\mathbf{z}^S) := \frac{1}{n} \sum_{l=1}^{n} e^{-2i\omega \boldsymbol{\theta}_l^T \mathbf{z}^S} I_{w_l}[U_l, \omega], \tag{7.45}$$

where $U_l(\mathbf{x}) = w_l(\mathbf{x}) = e^{i\omega \boldsymbol{\theta}_l^T \mathbf{x}}$, $l = 1, \ldots, n$. Suppose that $(\boldsymbol{\theta}_1, \ldots, \boldsymbol{\theta}_n)$ are equidistant points on the unit sphere S^{d-1}. For sufficiently large n, we have (7.22) and it follows that

$$\mathcal{I}_{\text{BP}}(\mathbf{z}^S) \simeq \sum_{p=1}^{P} |D_p| \omega^2 \Big(2 \frac{\rho_p^{-1} - 1}{\rho_p^{-1} + 1} - (K_p^{-1} - 1) \Big) \times \begin{cases} \operatorname{sinc}(2\omega |\mathbf{z}^S - \mathbf{z}_p|) & \text{for } d = 3, \\ J_0(2\omega |\mathbf{z}^S - \mathbf{z}_p|) & \text{for } d = 2. \end{cases}$$

These formulae show that the resolution of the imaging functional is the standard diffraction limit. Note that the above backpropagation-type algorithm is a simplified version of the algorithm studied in [**12, 13**]. In fact, instead of using only the diagonal terms of the response matrix $\mathbf{A}$, defined by (7.41), we can use the whole matrix to define the Kirchhoff migration functional:

$$\mathcal{I}_{\mathrm{KM}}(\mathbf{z}^S) = \sum_{j=1}^{d+1} \sum_{l} \left(\overline{\boldsymbol{g}^{(j)}(\mathbf{z}^S)}^T \boldsymbol{u}_l \right) \left(\overline{\boldsymbol{g}^{(j)}(\mathbf{z}^S)}^T \overline{\boldsymbol{v}_l} \right), \tag{7.46}$$

where $\boldsymbol{u}_l$ and $\boldsymbol{v}_l$ are respectively the left and right singular vectors of $\mathbf{A}$ and $\boldsymbol{g}^{(j)}$ are defined by (7.42) and (7.43).

7.7. Numerical Illustrations

In this section we present results of numerical experiments that give qualitative illustrations of some of the main findings in this chapter. We consider the two-dimensional case ($d = 2$). The domain Ω is the unit disk. We simulate the measurements using a finite-element method to solve the Helmholtz equation. We use a piecewise linear representation of the solution u and piecewise constant representations of the parameter distributions $\mathbf{1}_{\Omega\setminus\overline{D}}(\mathbf{x})+\rho^{-1}\mathbf{1}_D(\mathbf{x})$ and $\mathbf{1}_{\Omega\setminus\overline{D}}(\mathbf{x})+K^{-1}\mathbf{1}_D(\mathbf{x})$. We consider a small anomaly $D = \mathbf{z}_a + \delta B$ with $\mathbf{z}_a = (-0.3, 0.5)$, $\delta = 0.05$, and B being the unit disk. We fix the working frequency ω to be equal to 6, which corresponds to a wavelength $\lambda \simeq 1$. We assume that the measurements corresponding to the plane wave illuminations, $U_l(\mathbf{x}) = e^{i\omega \boldsymbol{\theta}_l^T \mathbf{x}}$, at the equi-distributed directions $\boldsymbol{\theta}_l$, for $l = 1, \ldots, n = 50$.

7.7.1. Bulk Modulus Contrast Only. Here, the parameters of the anomaly are $\rho = 1$ and $K = 1/2$.

7.7.1.1. *Resolution in the Absence of Noise.* Within the above setting, we first present results of the described algorithms in the absence of noise. In Figure 7.1, plots of $\mathcal{I}_{\mathrm{TD}}(\mathbf{z}^S)$, defined by (7.25), with respectively $n = 50$ and $n = 2$ illustrate the efficiency of the proposed topological derivative based imaging procedure. The imaging functional $\mathcal{I}_{\mathrm{TD}}(\mathbf{z}^S)$ reaches its maximum at the location $\mathbf{z}_a$ of the anomaly and behaves, accordingly to (7.23), like $J_0(\omega|\mathbf{z}^S - \mathbf{z}_a|)^2$ if the number n of incident waves is large while for small n, it behaves, as expected, like $J_0(\omega|\mathbf{z}^S - \mathbf{z}_a|)$.

In Figures 7.2 and 7.3, we compare the performance of the topological based imaging functionals with and without postprocessing the data by applying the integral operator $(-\frac{1}{2}\mathcal{I} + \mathcal{K}_\Omega^\omega)$. It is clear that the data postprocessing step is essential, specially if the number n of incident waves is small. In Figure 7.4, we show that this postprocessing is even more essential in the case of multiple anomalies.

In Figure 7.5, we present two MUSIC-type reconstructions. Given the structure of the response matrix $\mathbf{A}$ with $\rho = 1$ (contrast only on the K distribution), it is known that its SVD yields only one significant singular value. See, *e.g.*, [**16, 4**]. Thus, the illumination vectors $\boldsymbol{g}^{(1)}$ and $\boldsymbol{g}^{(2)}$ do not belong to the signal subspace of $\mathbf{A}$. Using these vectors in the projection step generates a blurred MUSIC image (figure on the left). To get a sharp peak, we should project only the illumination vector $\boldsymbol{g}^{(3)}$ (figure on the right), which assumes a priori knowledge of the physical nature of the contrast.

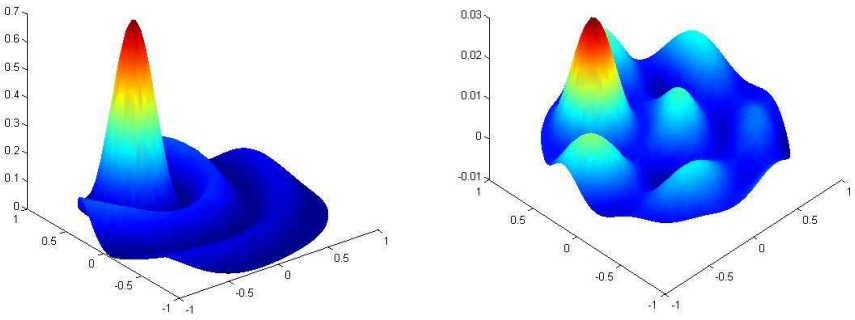

FIGURE 7.1. Plots of $\mathcal{I}_{\mathrm{TD}}(\mathbf{z}^S)$ defined by (7.25) with $n = 50$ (left) and $n = 2$ (right).

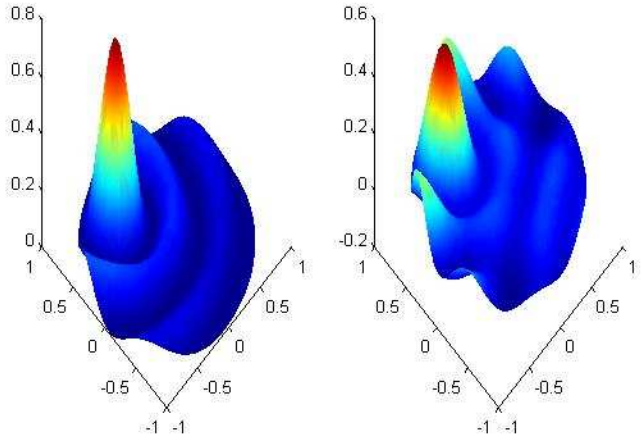

FIGURE 7.2. Comparison for $n = 50$ between topological derivative based images with (left) and without (right) postprocessing the data.

As shown in Figure 7.6, the backpropagation image of the anomaly has the expected behavior of the Bessel function and reaches its maximum at the location of the anomaly.

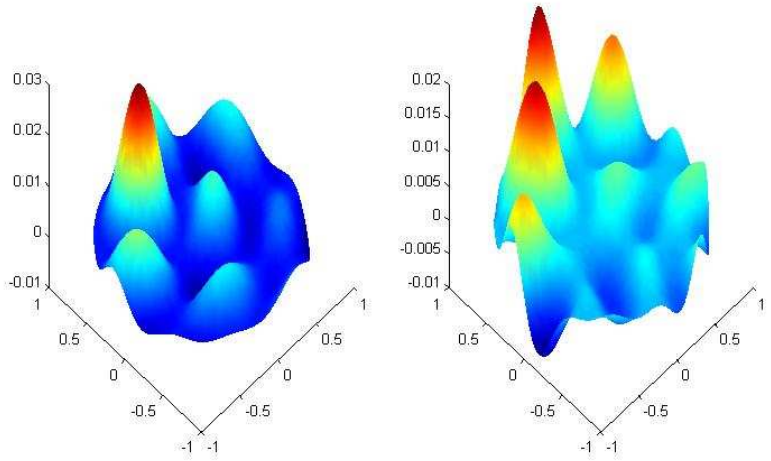

FIGURE 7.3. Comparison for $n = 2$ between topological derivative based images with (left) and without (right) postprocessing the data.

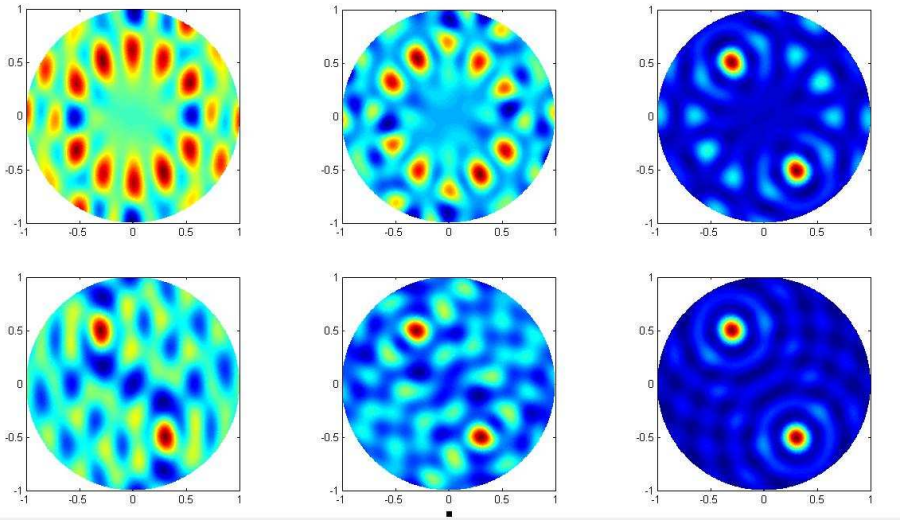

FIGURE 7.4. Comparison between topological derivative based images of multiple anomalies with (second line) and without (first line) postprocessing the data. The first column corresponds to $n = 1$, the second to $n = 2$, and the third to $n = 50$.

7.7.1.2. *Stability with Respect to Measurement and Medium Noises.* We now consider imaging from noisy data. We first add electronic (measurement) noise

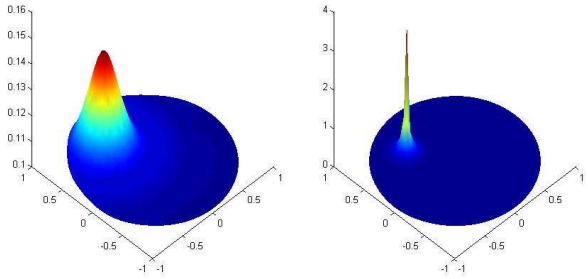

FIGURE 7.5. Left: MUSIC image using the projection of $\boldsymbol{g}^{(1)}, \boldsymbol{g}^{(2)}$, and $\boldsymbol{g}^{(3)}$ on the signal subspace of $\mathbf{A}$. Right: MUSIC image using the projection of $\boldsymbol{g}^{(3)}$ on the signal subspace of $\mathbf{A}$.

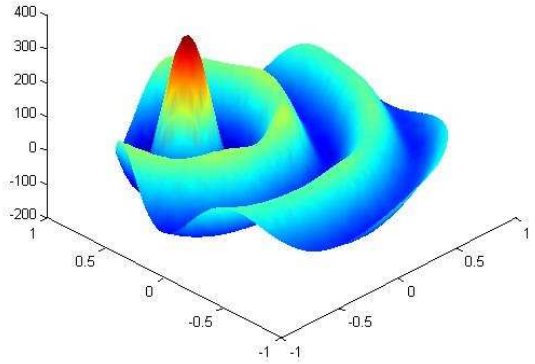

FIGURE 7.6. Plot of $\mathcal{I}_{\mathrm{BP}}(\mathbf{z}^S)$ defined by (7.45) with $n = 50$.

ν_{noise} to the previous measurements $u_{i,\mathrm{meas}}$, $i = 1, \ldots, n$. Here, ν_{noise} is a white Gaussian noise with standard deviation $\sigma\%$ of the L^2 norm of u_{meas} and σ ranges from 0 to 30. We compute $N_r = 250$ realizations of such noise and apply different imaging algorithms. Figure 7.7 presents the results of computational experiments. It clearly shows that the topological derivative based functional performs as good as Kirchhoff migration and much better than MUSIC and backpropagation, specially at high levels of electronic noise. Figure 7.8 shows the dramatic effect of the postprocessing step in the topological derivative based imaging when the number of plane wave illuminations n is small.

We now suppose that the medium bulk modulus is randomly heterogeneous around a constant background: $K^{-1}(\mathbf{x}) = 1 + (K^{-1} - 1)\mathbf{1}_D(\mathbf{x}) + \mu(\mathbf{x})$. To simulate

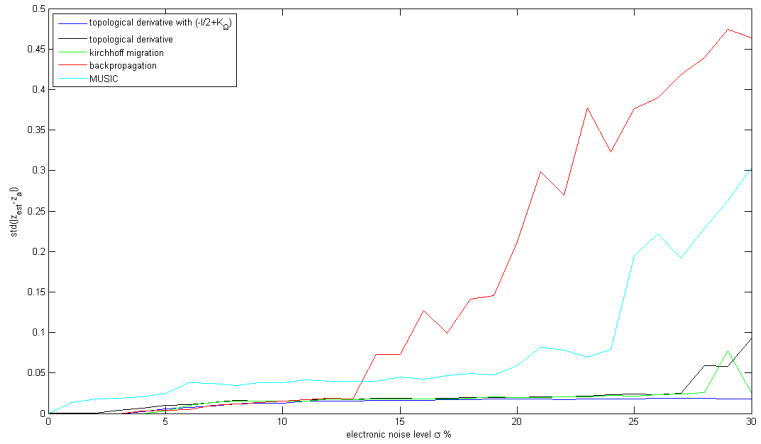

FIGURE 7.7. Standard deviations of localization error with respect to electronic noise level for $\mathcal{I}_{\mathrm{MU}}, \mathcal{I}_{\mathrm{BP}}, \mathcal{I}_{\mathrm{KM}}$, and $\mathcal{I}_{\mathrm{TD}}$ with $n = 50$.

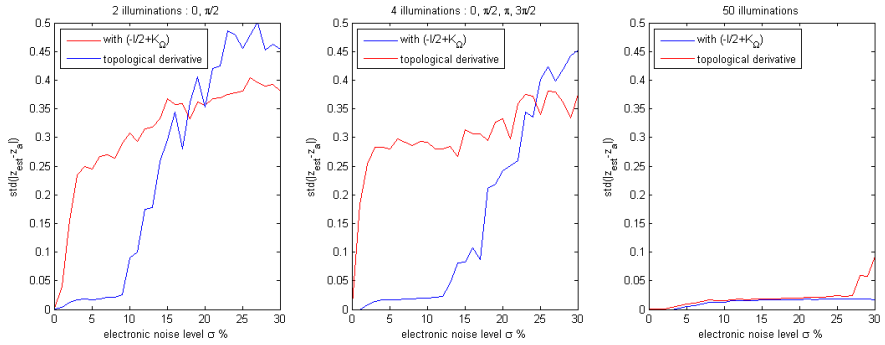

FIGURE 7.8. Effect of the data postprocessing on the standard deviation of localization error with respect to electronic noise level.

μ, we compute a white Gaussian noise in the medium and then apply a low-pass Gaussian filter. The parameters of this filter can be linked to the correlation length l_μ of μ.

Comparisons between the standard deviations of the localization error with respect to clutter noise for the discussed imaging algorithms are given in Figures 7.9 and 7.10. Again, the topological derivative based imaging functional is the most robust functional.

7.7.2. Density Contrast Only. Here, the parameters of the anomaly are $\rho = 1/2$ and $K = 1$.

7.7.2.1. *Resolution in the Absence of Noise.* As shown in Figure 7.11, the topological derivative based imaging functional $\mathcal{I}_{\mathrm{TD}}(\mathbf{z}^S)$ reaches its maximum at the location of the anomaly.

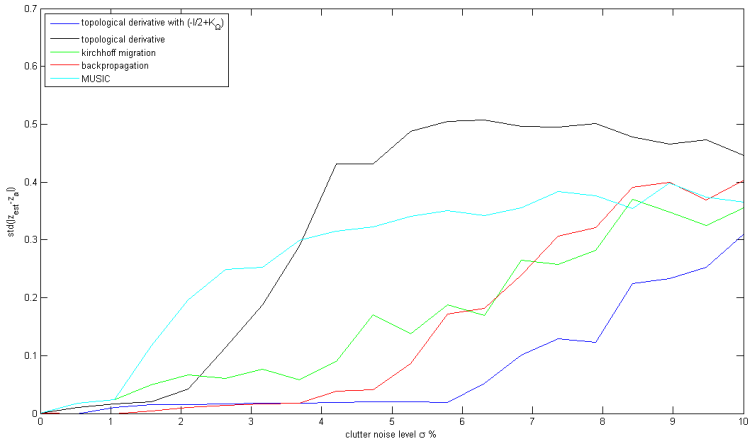

FIGURE 7.9. Standard deviations of localization error with respect to clutter noise for $\mathcal{I}_{\mathrm{MU}}, \mathcal{I}_{\mathrm{BP}}, \mathcal{I}_{\mathrm{KM}}$, and $\mathcal{I}_{\mathrm{TD}}$ with $n = 50$.

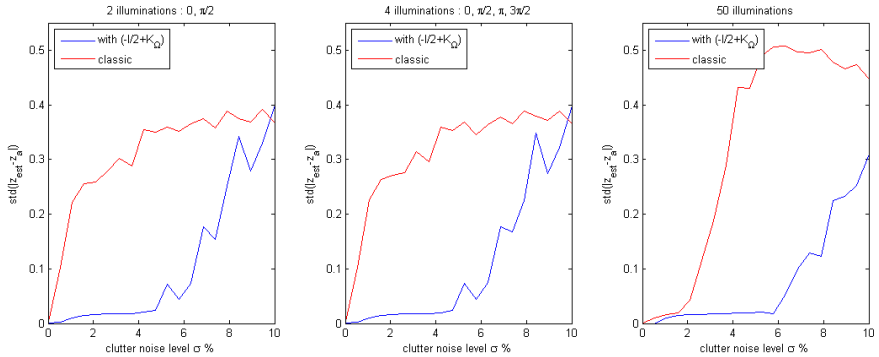

FIGURE 7.10. Effect of the data postprocessing on the standard deviation of localization error with respect to clutter noise.

In Figures 7.12 and 7.13, we compare the performance of the topological based imaging functionals with and without the postprocessing step. In Figure 7.14, we show that this postprocessing is even more critical in the case of multiple anomalies.

Figure 7.15 shows MUSIC images. As expected from the structure of the response matrix with $K = 1$ (ρ contrast only), its SVD yields two significant singular values [**44, 16, 4**]. Thus, the illumination vector $\boldsymbol{g}^{(3)}$ does not belong to the signal subspace of the response matrix $\mathbf{A}$. As before, using this vector in the projection step generates a blurred MUSIC peak (figure on the left). To get a sharp peak, we should only project the illumination vectors $\boldsymbol{g}^{(1)}$ and $\boldsymbol{g}^{(2)}$ (figure on the right).

As shown in Figure 7.16, the backpropagation image has the expected behavior and reaches its maximum at the location of the anomaly. In the case of multiple

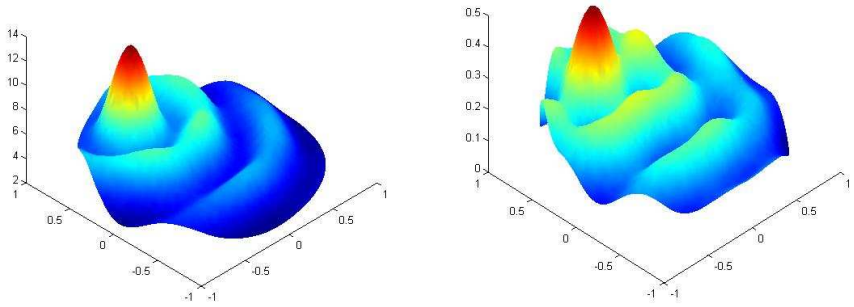

FIGURE 7.11. Plots of $\mathcal{I}_{\mathrm{TD}}(\mathbf{z}^S)$ with (left) $n = 50$ and (right) $n = 2$.

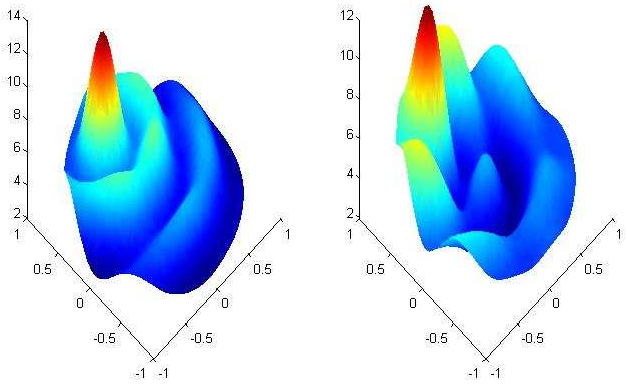

FIGURE 7.12. Comparison for $n = 50$ between topological derivative based images with (left) and without (right) postprocessing the data.

anomalies, the oscillatory pattern of the backpropagation imaging functional can be troublesome.

7.7.2.2. *Stability with Respect to Measurement and Medium Noises.* We carry out the same analysis as in the case of only a bulk modulus contrast. Figure 7.17 gives the standard deviation of the localization error as function of the noise level σ for each algorithm.

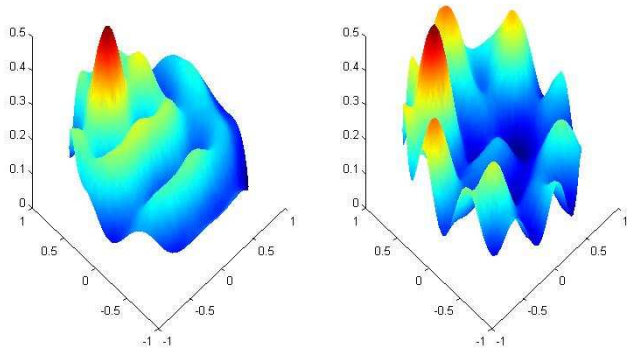

FIGURE 7.13. Comparison for $n = 2$ between topological derivative based images with (left) and without (right) postprocessing the data.

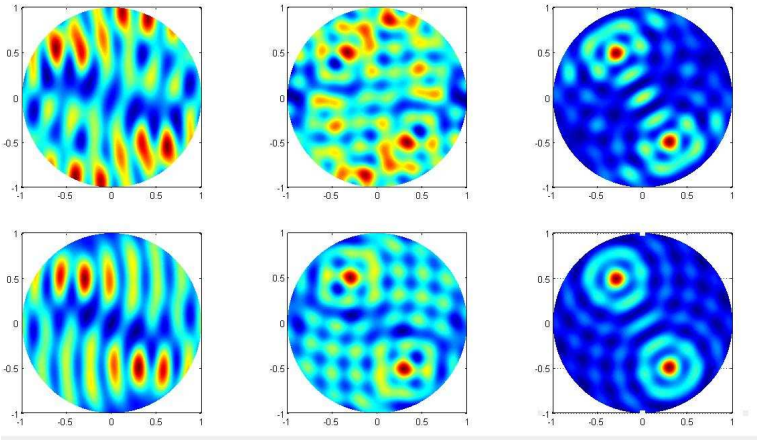

FIGURE 7.14. Comparison between topological derivative based images of multiple anomalies with (second line) and without (first line) postprocessing the data. The first column corresponds to $n = 1$, the second to $n = 2$, and the third to $n = 50$.

Again, the topological derivative algorithm with postprocessing seems to be the most robust. However, the effect of the data postprocessing step seems less dramatic here than in the case of bulk modulus contrast.

Finally, we suppose that the medium density is randomly heterogeneous around a constant background: $\rho^{-1}(\mathbf{x}) = 1+(\rho^{-1}-1)\mathbf{1}_D(\mathbf{x})+\mu(\mathbf{x})$, with μ a random process of mean zero and tunable standard deviation σ. As before, we compute $N_r = 250$ realizations of such clutter and the corresponding measurements. We then apply

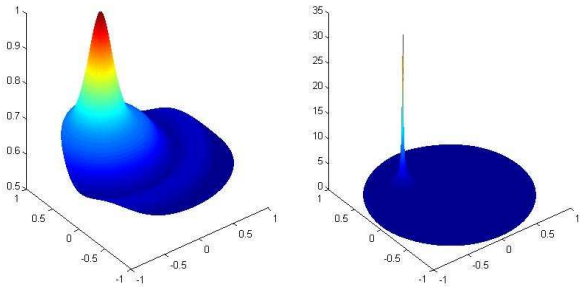

FIGURE 7.15. Left: MUSIC image using projection of $\boldsymbol{g}^{(1)}, \boldsymbol{g}^{(2)}, \boldsymbol{g}^{(3)}$ on the signal subspace of $\mathbf{A}$. Right: image using projection of $\boldsymbol{g}^{(1)}$ and $\boldsymbol{g}^{(2)}$ on the signal subspace of $\mathbf{A}$.

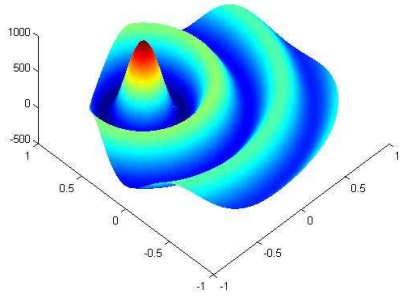

FIGURE 7.16. Backpropagation image.

the localization algorithms. Stability results are given in Figure 7.19. They clearly indicate the robustness of the topological derivative based imaging functional.

7.8. Conclusion

In this chapter we have explained why the concept of topological derivative works for imaging small acoustic anomalies and carried out a stability and resolution analysis in the presence of medium and measurement noises. We have shown that in order to design an efficient topological derivative based imaging functional, we have first to postprocess the data. We have proved that the functional behaves like the square of the imaginary part of the Green function and then attains its maximum at the location of the anomaly with a resolution limit of the order of half-a-wavelength. We have also shown that the topological derivative based imaging functional, compared to other more classical imaging functionals, is more robust in both cases of measurement and medium noise. Another advantage of

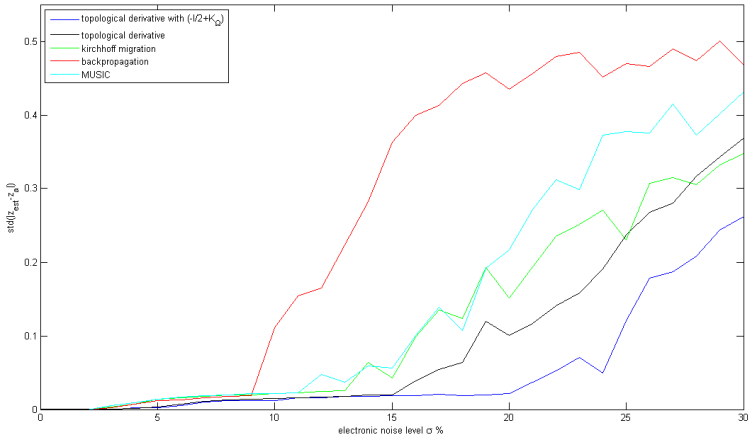

FIGURE 7.17. Standard deviations of localization error with respect to electronic noise level for $\mathcal{I}_{\mathrm{MU}}, \mathcal{I}_{\mathrm{BP}}, \mathcal{I}_{\mathrm{KM}}$, and $\mathcal{I}_{\mathrm{TD}}$ with $n = 50$.

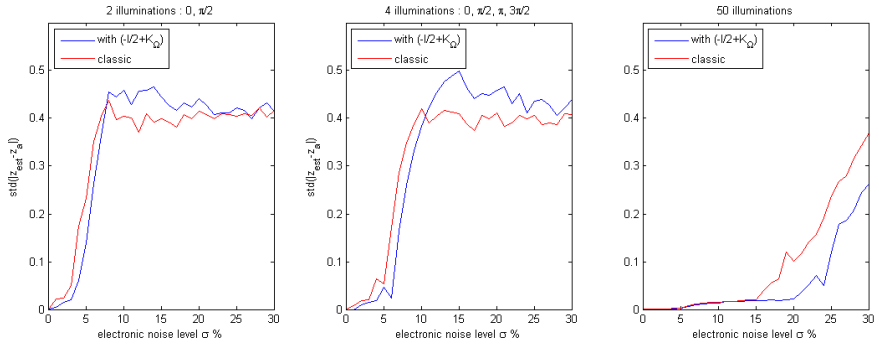

FIGURE 7.18. Standard deviations of localization error with respect to electronic noise level for the topological derivative based functionals with and without postprocessing the data.

the proposed functional is that it works with a very small number of plane wave illuminations. However, its complexity is roughly speaking $O(nm^3)$ while the complexities of MUSIC and backpropagation are respectively $O(n^3 + n^2 m)$ and $O(nm)$, where n is the number of plane wave illuminations and m is the number of space discretization points in the domain Ω. Note that in general $n \ll m$.

Our results in this chapter apply to the electrical impedance tomography problem. In fact, let Γ be the fundamental solution of the Laplacian in $\mathbb{R}^d$ and denote by $\mathcal{K}_\Omega$ the integral operator given by

$$\mathcal{K}_\Omega[\varphi](\mathbf{x}) = \int_{\partial\Omega} \frac{\partial\Gamma(\mathbf{x}-\mathbf{y})}{\partial\nu(\mathbf{y})}\varphi(\mathbf{y})d\sigma(\mathbf{y}), \quad \mathbf{x} \in \partial\Omega.$$

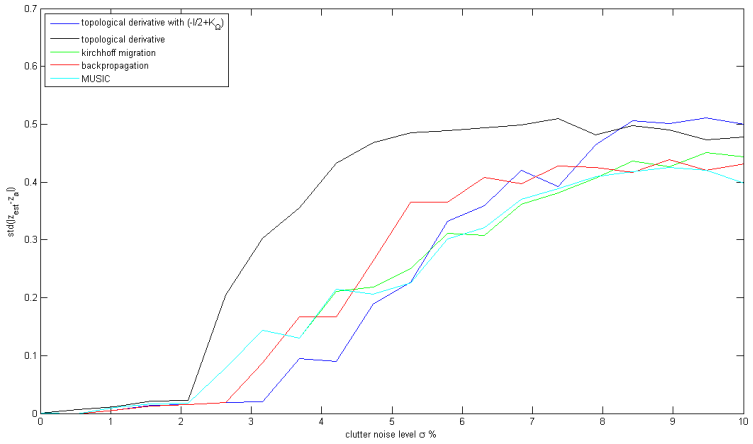

FIGURE 7.19. Standard deviations of the localization error with respect to clutter noise for $\mathcal{I}_{\rm MU}, \mathcal{I}_{\rm BP}, \mathcal{I}_{\rm KM}$, and $\mathcal{I}_{\rm TD}$ with $n = 50$.

Let $\mathcal{I}_{\rm TD}$ be the topological derivative of the misfit

$$\mathcal{E}[U](\mathbf{z}^S) = \frac{1}{2}\int_{\partial\Omega} |(-\frac{1}{2}\mathcal{I} + \mathcal{K}_\Omega)[u_{\mathbf{z}^S} - u_{\rm meas}](\mathbf{x})|^2 \, d\sigma(\mathbf{x}),$$

where $u_{\mathbf{z}^S}$ and $u_{\rm meas}$ are respectively the computed and the measured voltage potential. In exactly the same manner as in this chapter, we can prove that, for $d = 2$,

$$\mathcal{I}_{\rm TD}(\mathbf{z}^S) \sim \int_{\partial\Omega} \nabla\Gamma(\mathbf{x} - \mathbf{z}^S)\nabla\Gamma(\mathbf{x} - \mathbf{z}_a)\, d\sigma(\mathbf{x}) \sim \int_{\partial\Omega} \frac{1}{|\mathbf{x}|^2} \frac{(\mathbf{x} - \mathbf{z}^S)^T}{|\mathbf{x} - \mathbf{z}^S|} \frac{(\mathbf{x} - \mathbf{z}_a)}{|\mathbf{x} - \mathbf{z}_a|}\, d\sigma(\mathbf{x})$$

provided that $\mathrm{dist}(\mathbf{z}^S, \partial\Omega), \mathrm{dist}(\mathbf{z}_a, \partial\Omega) \gg 1$. A similar result holds in three dimensions. Therefore, $\mathcal{I}_{\rm TD}(\mathbf{z}^S)$ yields an image similar to the one proposed in [**98**].

Our results extend to elastic and electromagnetic waves as well as to the transient regime [**103**]. They can also be generalized to imaging functionals based on high-order topological derivatives [**37, 114, 84**], which are based on high-order asymptotic expansions for the boundary pressure perturbations derived in [**17**].

References

[1] M. Agranovsky and P. Kuchment, Uniqueness of reconstruction and an inversion procedure for thermoacoustic and photoacoustic tomography with variable sound speed, Inverse Problems, 23 (2007), 2089-2102.

[2] M. Agranovsky, P. Kuchment, and L. Kunyansky, On reconstruction formulas and algorithms for the thermoacoustic and photoacoustic tomography, to appear in L. H. Wang (Editor) "*Photoacoustic Imaging and Spectroscopy*," CRC Press.

[3] G. Ambartsoumian and S. Patch, Thermoacoustic tomography Implementation of exact backprojection formulas, math.NA/0510638.

[4] H. Ammari, *An Introduction to Mathematics of Emerging Biomedical Imaging*, Math. & Appl., Vol. 62, Springer-Verlag, Berlin, 2008.

[5] H. Ammari, An inverse initial boundary value problem for the wave equation in the presence of imperfections of small volume, SIAM J. Control Optim., 41 (2002), 1194–1211.

[6] H. Ammari, M. Asch, L. Guadarrama Bustos, V. Jugnon, and H. Kang, Transient wave imaging with limited-view data, SIAM J. Imag. Sci, submitted.

[7] H. Ammari, E. Bossy, V. Jugnon, and H. Kang, Mathematical modelling in photo-acoustic imaging of small absorbers, SIAM Rev., 52 (2010), 677–695.

[8] H. Ammari, E. Bossy, V. Jugnon, and H. Kang, Reconstruction of the optical absorption coefficient of a small absorber from the absorbed energy density, SIAM J. Appl. Math., under revision.

[9] H. Ammari, E. Bretin, V. Jugnon, and A. Wahab, Photoacoustic imaging for attenuating acoustic media, in *Mathematical Modeling in Biomedical Imaging II*, Lecture Notes in Mathematics, Springer-Verlag, Berlin, to appear.

[10] H. Ammari, E. Bretin, J. Garnier, and V. Jugnon, Coherent interferometric strategy for photoacoustic imaging, SIAM J. Numer. Anal., submitted.

[11] H. Ammari, J. Garnier, V. Jugnon, and H. Kang, Stability and resolution analysis for a topological derivative based imaging functional, SIAM J. Control Opt., submitted.

[12] H. Ammari, J. Garnier, H. Kang, W.-K. Park, and K. Solna, Imaging schemes for perfectly conducting cracks, SIAM J. Appl. Math., to appear.

[13] H. Ammari, J. Garnier, and K. Solna, A statistical approach to target detection and localization in the presence of noise, Waves in Random and Complex Media, to appear.

[14] H. Ammari, Y. Capdeboscq, H. Kang, and A. Kozhemyak, Mathematical models and reconstruction methods in magneto-acoustic imaging, Euro. J. Appl. Math., 20 (2009), 303–317.

[15] H. Ammari, P. Garapon, L. Guadarrama Bustos, and H. Kang, Transient anomaly imaging by the acoustic radiation force, J. Diff. equat., 249 (2010), 1579–1595.

[16] H. Ammari, E. Iakovleva, and D. Lesselier, A MUSIC algorithm for locating small inclusions buried in a half-space from the scattering amplitude at a fixed frequency, Multiscale Model. Simul., 3 (2005), 597–628.

[17] H. Ammari and H. Kang, *Reconstruction of Small Inhomogeneities from Boundary Measurements*, Lecture Notes in Mathematics, Vol. 1846, Springer-Verlag, Berlin, 2004.

[18] H. Ammari and H. Kang, *Polarization and Moment Tensors: with Applications to Inverse Problems and Effective Medium Theory*, Applied Mathematical Sciences, Vol. 162, Springer-Verlag, New York, 2007.

[19] H. Ammari, H. Kang, and H. Lee, *Layer Potential Techniques in Spectral Analysis*, Mathematical Surveys and Monographs, Vol. 153, American Mathematical Society, Providence RI, 2009.

[20] H. Ammari and A. Khelifi, Electromagnetic scattering by small dielectric inhomogeneities, J. Math. Pures Appl., 82 (2003), 749–842.

[21] H. Ammari and H. Kang, Reconstruction of elastic inclusions of small volume via dynamic measurements, Appl. Math. Opt., 54 (2006), 223–235.
[22] S. R. Arridge, Optical tomography in medical imaging, Inverse Problems, 15 (1999), R41–R93.
[23] M. Asch and G. Lebeau, Geometrical aspects of exact boundary controllability for the wave equation–a numerical study, ESAIM Control Optim. Calc. Var., 3 (1998), 163–212.
[24] G. Bal, Inverse transport theory and applications, Inverse Problems, 25 (2009), 053001.
[25] G. Bal and A. Jollivet, Stability estimates in stationary inverse transport, Inverse Probl. Imaging, 2(4) (2008), pp. 427–454.
[26] ———, *Time-dependent angularly averaged inverse transport*, submitted, (2009).
[27] G. Bal, A. Jollivet, and V. Jugnon, Inverse Transport Theory of Photoacoustics, Inverse Problems, 26 (2010), p. 025011.
[28] C. Bardos, G. Lebeau, and J. Rauch, Sharp sufficient conditions for the observation, control, and stabilization of waves from the boundary, SIAM J. Control Optim., 30 (1992), 1024-1065.
[29] A. Beck and M. Teboulle, A fast iterative shrinkage-thresholding algorithm for linear inverse problems, SIAM J. Imaging Sci., 2 (2009), 183–202.
[30] M. I. Belishev, Recent progress in the boundary control method, Inverse Problems, 23 (2007), R1-R67.
[31] J. Benesty, J. Chen, and Y. Huang, Time-delay estimation via linear interpolation and cross correlation, IEEE Trans. Speech Audio Process., 12 (2004), 509–519.
[32] J. Bercoff, M. Tanter, and M. Fink, Supersonic shear imaging: a new technique for soft tissue elasticity mapping, IEEE Trans. Ultrasonics, Ferro., Freq. Control, 51 (2004), 396–409.
[33] J. Bercoff, M. Tanter, M. Muller, and M. Fink, The role of viscosity in the impulse diffraction field of elastic waves induced by the acoustic radiation force, IEEE Trans. Ultrasonics, Ferro., Freq. Control, 51 (2004), 1523–1536.
[34] J. Bergh and L. Löfström, *Interpolation Spaces*, Springer, New York, 1976.
[35] A. C. Birch and A. G. Kosovichev, Travel time sensitivity kernels, Solar Phys., 192 (2000), 193–201.
[36] N. Bleistein, J. K. Cohen, and J. W. Stockwell Jr., *Mathematics of Multidimensional Seismic Imaging, Migration, and Inversion*, Springer, New York, 2001.
[37] M. Bonnet, Higher-order topological sensitivity for 2-D potential problems. Application to fast identification of inclusions, Inter. J. Solids Struct., 46 (2009), 2275–2292.
[38] M. Bonnet and B. B. Guzina, Sounding of finite solid bodies by way of topological derivative, Int. J. Numer. Meth. Eng., 61 (2004), 2344–2373.
[39] L. Borcea, G. Papanicolaou, and C. Tsogka, Theory and applications of time reversal and interferometric imaging, Inverse Problems, 19 (2003), 134–164.
[40] L. Borcea, G. Papanicolaou, and C. Tsogka, Interferometric array imaging in clutter, Inverse Problems 21 (2005), 14191460.
[41] L. Borcea, G. Papanicolaou, and C. Tsogka, Adaptive interferometric imaging in clutter and optimal illumination, Inverse Problems 22 (2006), 1405–1436.
[42] L. Borcea, G. Papanicolaou, and C. Tsogka, Coherent interferometric imaging in clutter, Geophysics 71 (2006), SI165–SI175.
[43] E. Bossy, K. Daoudi, A.-C. Boccara, M. Tanter, J.-F. Aubry, G. Montaldo, and M. Fink, Time reversal of photoacoustic waves, Appl. Phys. Lett. 89 (2006), 184108.
[44] M. Brühl, M. Hanke, and M. S. Vogelius, A direct impedance tomography algorithm for locating small inhomogeneities, Numer. Math., 93 (2003), 635–654.
[45] P. Burgholzer, H. Grün, M. Haltmeier, R. Nuster, and G. Paltauf, Compensation of acoustic attenuation for high resolution photoacoustic imaging with line detectors, Proc. of SPIE, 6437 (2007), 643724.
[46] S. A. Carp, A. Guerra III, S. Q. Duque, Jr, and V. Venugopalan, Optoacoustic imaging using interferometric measurement of surface displacement, Appl. Phys. Lett., 85 (2004), 5772–5774.
[47] G. C. Carter, Special Issue on Time-Delay Estimation, IEEE Trans. Acoust., Speech, Sig. Process., vol. ASSP-29, June 1981.
[48] J. Céa, S. Garreau, P. Guillaume, and M. Masmoudi, The shape and topological optimization connection, Computer Methods in Applied Mechanics and Engineering, 188 (2001), 703–726.
[49] A. Chambolle, An algorithm for total variation minimization and applications, J. Math. Imag. Vis., 20 (2004), 89–97.

[50] Y. T. Chan and K. C. Ho, A simple and efficient estimator for hyperbolic location, IEEE Trans. Sig. Process., 42 (1994), 1905–1915.
[51] T. K. Chan, Y. Kuga, and A. Ishimaru, Experimental studies on circular sar imaging in clutter using angular correlation function technique, IEEE Trans. Geoscience and Remote Sensing, 37 (1999), 2192–2197.
[52] W. Chen and S. Holm, Fractional Laplacian time-space models for linear and nonlinear lossy media exhibiting arbitrary frequency power-law dependency, J. Acoust. Soc. Amer., 115 (2004), 1424–1430.
[53] J. C. Chen, K. Yao, and R. E. Hudson, Source localization and beamforming, IEEE Sig. Process. Magazine, March 2002, 30–39.
[54] M. Choulli and P. Stefanov, Reconstruction of the coefficients of the stationary transport equation from boundary measurements, Inverse Problems, 12 (1996), pp. L19–L23.
[55] P. Combettes and V. Wajs, Signal recovery by proximal forward-backward splitting, Mult. Model. Simul., 4 (2005), 1168–1200.
[56] B. T. Cox, S. R. Arridge, and P. C. Beard, Gradient-based quantitative photoacoustic image reconstruction for molecular imaging, Proc. of SPIE Vol. 6437 (2007), 64371T, doi:10.1117/12.700031.
[57] B. T. Cox, S. R. Arridge, and P. C. Beard, Photoacoustic tomography with a limited-aperture planar sensor and a reverberant cavity, Inverse Problems 23 (2007), S95-S112.
[58] B. T. Cox, S. R. Arridge, K. Köstli, and P. C. Beard, 2D quantitative photoacoustic image reconstruction of absorption distributions in scattering media using a simple iterative method, Appl. Opt., 45 (2006), 1866–1874.
[59] B. T. Cox, J. G. Laufer, and P. C. Beard, The challenges for quantitative photoacoustic imaging, Proc. of SPIE, 7177 (2009), 717713.
[60] I. Daubechies, M. Defrise and C. De Mol, An iterative thresholding algorithm for linear inverse problems with a sparsity constraint, Comm. Pure Appl. Math., 57 (2004), 1413–1457.
[61] R. Dautray and J.-L. Lions, *Mathematical Analysis and Numerical Methods for Science and Technology. Vol.6*, Springer Verlag, Berlin, 1993.
[62] A. J. Devaney, A filtered backpropagation algorithm for diffraction tomography, Ultrasonic Imaging, 4 (1982), 336–350.
[63] A. J. Devaney, Time reversal imaging of obscured targets from multistatic data, IEEE Trans. Antennas Propagat., 523 (2005), 1600–1610.
[64] N. Dominguez, V. Gibiat and Y. Esquerrea, Time domain topological gradient and time reversal analogy: an inverse method for ultrasonic target detection, Wave Motion, 42 (2005), 31–52.
[65] N. Dominguez and V. Gibiat, Non-destructive imaging using the time domain topological energy method, Ultrasonics, 50 (2010), 172–179.
[66] H. A. Eschenauer, V. V. Kobelev, and A. Schumacher, Bubble method for topology and shape optimization of structures, Struct. Optimization 8 (1994), 42–51.
[67] L. C. Evans, *Partial Differential Equations*, 2nd edition, Graduate Studies in Mathematics, Vol. 19, American Mathematical Society, Providence, RI, 2010.
[68] G. R. Feijóo, A new method in inverse scattering based on the topological derivative, Inverse Probl., 20 (2004), 1819–1840.
[69] D. Finch, M. Haltmeier, and Rakesh, Inversion of spherical means and the wave equation in even dimensions, SIAM J. Appl. Math., 68 (2007), 392–412.
[70] D. Finch, S. Patch, and Rakesh, Determining a function from its mean-values over a family of spheres, SIAM J. Math. Anal., 35 (2004), 1213–1240.
[71] M. Fink, Time-reversal acoustics, in *Inverse Problems, Multi-Scale Analysis and Homogenization,* 151–179, Contemp. Math., Vol. 408, Rhode Island, Providence, 2006.
[72] A. R. Fisher, A. J. Schissler, and J. C. Schotland, Photoacoustic effect of multiply scattered light, Phys. Rev. E, 76 (2007), 036604.
[73] J.-P. Fouque, J. Garnier, G. Papanicolaou, and K. Sølna, *Wave Propagation and Time Reversal in Randomly Layered Media*, Springer, New York, 2007.
[74] A. Funke, J-F. Aubry, M. Fink, A-C. Boccara, E. Bossy, Photoacoustic guidance of high intensity focused ultrasound with selective optical contrasts and time-reveral, Appl. Phys. Lett. 94 (2009), *in press*.
[75] A. Funke, Towards guidance of therapeutical ultrasounds by time reversal and photoacoustics, preprint.

[76] F. G. Friedlander, *The Wave Equation on a Curved Space-Time*, Cambridge University Press, Cambridge, 1975.
[77] R. Glowinski, Ensuring well posedness by analogy; Stokes problem and boundary control for the wave equation, J. Comput. Phys., 103 (1992), 189–221.
[78] C. Haisch, Quantitative analysis in medicine using photoacoustic tomography, Anal. Bioanal. Chem., 393 (2009), 473–479.
[79] M. Haltmeier, R. Kowar, A. Leitao, and O. Scherzer, Kaczmarz methods for regularizing nonlinear ill-posed equations II: Applications, Inverse Problems and Imaging, 1 (2007), 507–523.
[80] M. Haltmeier, T. Schuster, and O. Scherzer, Filtered backprojection for thermoacoustic computed tomography in spherical geometry, Math. Meth. Appl. Sci., 28 (2005), 1919-1937.
[81] M. Haltmeier, O. Scherzer, P. Burgholzer, R. Nuster, and G. Paltauf, Thermoacoustic tomography and the circular Radon transform: exact inversion formula, Math. Model. Meth. Appl. Sci., 17(4) (2007), 635-655.
[82] F. Hetch, O. Pironneau, K. Ohtsuka and A. Le Hyaric, FreeFem++, http://www.freefem.org, 2007.
[83] M. Hintermüller and A. Laurain, Electrical impedance tomography: from topology to shape, Control Cybernet., 37 (2008), 913–933.
[84] M. Hintermüller, A. Laurain, and A. A. Novotny, Second-order topological expansion for electrical impedance tomography, preprint.
[85] L. Hörmander, *The Analysis of Linear Partial Differential Operators. I. Distribution Theory and Fourier Analysis*, Classics in Mathematics, Springer-Verlag, Berlin, 2003.
[86] Y. Huang, J. Benesty, G. W. Elko, and R. M. Mersereau, Real-time passive source localization: a practical linear-correction least-squares approach, IEEE Trans. Speech Audio Process., 9 (2001), 943–956.
[87] L. I. Ignat and E. Zuazua, Convergence of a two-grid algorithm for the control of the wave equation, J. Europ. Math. Soc., 11 (2009), 351–391.
[88] M. R. Islam and B. C. Towe, Bioelectric current image reconstruction from magneto-acoustic measurements, IEEE Trans. Med. Img. 7 (1988), 386–391.
[89] J. Kaipio and E. Somersalo, *Statistical and Computational Inverse Problems*, Applied Mathematical Sciences, Vol. 160, Springer-Verlag, New York, 2005.
[90] A. Katchalov, Y. Kurylev, and M. Lassas, *Inverse Boundary Spectral Problems*, Monographs and Surveys in Pure and Applied Mathematics, Chapman & Hall/CRC, 2001.
[91] A. G. Kosovichev, T. L. Duvall, and P. H. Scherrer, Time-distance inversion methods and results, Solar Phys., 192 (2000), 159–176.
[92] R. Kowar, Integral equation models for thermoacoustic imaging of dissipative tissue, Inverse Problems, 26 (2010), 095005 (18pp).
[93] R. Kowar and O. Scherzer, Photoacoustic imaging taking into account attenuation, in this volume.
[94] R. Kowar, O. Scherzer, and X. Bonnefond, Causality analysis of frequency dependent wave attenuation, Math. Meth. Appl. Sci., to appear.
[95] P. Kuchment and L. Kunyansky, Mathematics of photoacoustics and thermoacoustic tomography, in *Handbook of Mathematical Methods in Imaging* (ed: O. Scherzer), Springer-Verlag, New York, 2011.
[96] P. Kuchment and L. Kunyansky, Mathematics of thermoacoustic tomography, European J. Appl. Math., 19 (2008), 191–224.
[97] L. Kunyansky, Explicit inversion formulas for the spherical mean Radon transform, Inverse Problems, 23 (2007), 373–383.
[98] O. Kwon, J. K. Seo, and J. R. Yoon, A real-time algorithm for the location search of discontinuous conductivities with one measurement, Comm. Pure Appl. Math., 55 (2002), 1–29.
[99] J. Laufer, D. Delpy, C. Elwell, and P. Beard, Quantitative spatially resolved measurement of tissue chromophore concentrations using photoacoustic spectroscopy: application to the measurement of blood oxygenation and haemoglobin concentration, Phys. Med. Biol., 52 (2007), 141–168.
[100] G. Lebeau, Control of hyperbolic equations, Journées Equat. Dérivées Part., 1992, 1–24.
[101] C. H. Li, M. Pramanik, G. Ku, and L. V. Wang, Image distortion in thermoacoustic tomography caused by microwave diffraction, Phys. Rev. E, 77 (2008), 031923.

[102] J.-L. Lions, *Contrôlabilité exacte, Perturbations et Stabilisation de Systèmes Distribués*, Tome 1, Contrôlabilité exacte, Masson, Paris, 1988.

[103] A. Malcolm and B. Guzina, On the topological sensitivity of transient acoustic fields, Wave Motion 45 (2008), 821–834.

[104] K. Maslov, H. F. Zhang, and L. V. Wang, Effects of wavelength-dependent fluence attenuation on the noninvasive photoacoustic imaging of hemoglobin oxygen saturation in subcutaneous vasculature in vivo, Inverse Problems, 23 (2007), S113–S122.

[105] M. Masmoudi, J. Pommier, and B. Samet, The topological asymptotic expansion for the Maxwell equations and some applications, Inverse Probl., 21 (2005), 547–564.

[106] S. R. McDowall, A. Tamasan, and P. Stefanov, Stability of the gauge equivalent classes in stationary inverse transport, submitted, (2009).

[107] G. W. Milton, *The Theory of Composites*, Cambridge Monographs on Applied and Computational Mathematics, Cambridge University Press, 2001.

[108] L. V. Nguyen, A family of inversion formulas in thermoacoustic tomography, Inverse Problems and Imaging, 3 (2009), 649–675.

[109] V. Ntziachristos, J. Ripoll, L. V. Wang, and R. Weissleder, Looking and listening to light: the evolution of whole-body photonic imaging, Nature Biotechnology, 23 (2005), 313–320.

[110] K. Patch and M. Haltmeier, Thermoacoustic tomography - ultrasound attenuation artifacts, IEEE Nuclear Science Symposium Conference, 4 (2006), 2604–2606.

[111] S. K. Patch and O. Scherzer, Guest editors' introduction: Photo- and thermo-acoustic imaging, Inverse Problems 23 (2007), S1–10.

[112] J. Ripoll and V. Ntziachristos, Quantitative point source photoacoustic inversion formulas for scattering and absorbing media, Phys. Rev. E, 71 (2005), 031912.

[113] P. J. La Rivière, J. Zhang, and M. A. Anastasio, Image reconstruction in optoacoustic tomography for dispersive acoustic media, Opt. Lett., 31 (2006), 781–783.

[114] J. Rocha de Faria and A. A. Novotny, On the second order topological asymptotic expansion, Struct. Multidiscip. Optim., 39 (2009), 547–555.

[115] B. J. Roth and P. J. Basser, A model of the stimulation of a nerve fiber by electromagnetic induction, IEEE Trans. Biomed. Eng., 37 (1990), 588–597.

[116] B. J. Roth, P. J. Basser, and J. P. Jr Wikswo, A theoretical model for magneto-acoustic imaging of bioelectric currents, IEEE Trans. Biomed. Eng., 41 (1994), 723–728.

[117] H. C. Schau and A. Z. Robinson, Passive source localization employing intersecting spherical surfaces from time-of-arrival differences, IEEE Trans. Acoust. Speech, Process., 35 (1987), 1223–1225.

[118] M. Sivaramakrishnan, K. Maslov, H. F. Zhang, G. Stoica, and L. V. Wang, Limitations of quantitative photoacoustic measurements of blood oxygenation in small vessels, Phys. Med. Biol., 52 (2007), 1349–1361.

[119] G. T. Schuster, J. Yu, J. Sheng, and J. Rickett, Interferometric daylight seismic imaging, Geophysics Journal International, 157 (2004), 838–852.

[120] R. Snieder, A. Gret, H. Douma, and J. Scales, Coda wave interferometry for estimating nonlinear behavior in seismic velocity, Science, 295 (2002), 2253–2255.

[121] J. Sokołowski and A. Zochowski, On the topological derivative in shape optimization, SIAM J. Control Optim., 37 (1999), 1251–1272.

[122] E. M. Stein, *Harmonic Analysis: Real-Variable Methods, Orthogonality, and Oscillatory Integrals*, Princeton Mathematical Series, Vol. 43, Princeton University Press, Princeton, NJ, 1993.

[123] P. Stefanov and G. Uhlmann, Thermoacoustic tomography with variable sound speed, Inverse Problems, 25 (2009), 075011.

[124] N. V. Sushilov and R. S. C. Cobbold, Frequency-domain wave equation and its time-domain solutions in attenuating media, J. Acoust. Soc. Am., 115 (2004), 1431–1436.

[125] T. L. Szabo. Causal theories and data for acoustic attenuation obeying a frequency power law. *Journal of Acoustical Society of America*, 97 (1995), 14–24.

[126] B. E. Treeby and B. T. Cox, Fast, tissue-realistic models of photoacoustic wave propagation for homogeneous attenuating media, Proc. of SPIE, 7177 (2009), 717716.

[127] J. A. Viator, J. Komadina, L. O. Svaasand, G. Aguilar, B. Choi, and J.S. Nelson, A comparative study of photoacoustic and reflectance methods for determination of epidermal melanin content, J. Invest. Dermatol., 122 (2004), 1432–1439.

[128] M. S. Vogelius and D. Volkov, Asymptotic formulas for perturbations in the electromagnetic fields due to the presence of inhomogeneities, Math. Model. Numer. Anal., 34 (2000), 723–748.
[129] X. Wang, Y. Pang, G. Ku, X. Xie, G. Stoica, and L. V. Wang, Noninvansive laser-induced photoacoustic tomography for structural and functional in vivo imaging of the brain, Nature Biotechnology, 21 (2003), 803–806.
[130] Y. W. Wang, X. Y. Xie, X. D. Wang, G. Ku, K. L. Gill, D. P. O'Neal, G. Stoica, and L. V. Wang, Photoacoustic tomography of a nanoshell contrast agent in the in vivo rat brain, Nano Letters, 4 (2004), 1689–1692.
[131] L. V. Wang and X. Yang, Boundary conditions in photoacoustic tomography and image reconstruction, J. Biomed. Optics, 12 (2007), 014027.
[132] M. Wax and T. Kailath, Optimum localization of multiple sources by passive arrays, IEEE Trans. Acoust. Speech, Process., 31 (1983), 1210–1217.
[133] Y. Xu, L. V. Wang, G. Ambartsoumian, and P. Kuchment, Reconstructions in limited view thermoacoustic tomography, Medical Physics 31 (2004), 724–733.
[134] Y. Xu and L. V. Wang, Reconstructions in limited-view thermoacoustic tomography, Medical Physics, 31 (2004), 724–733.
[135] M. Xu and L. V. Wang, Photoacoustic imaging in biomedicine, Review of Scientific Instruments 77, 041101, 2006.
[136] L. Yin, Q. Wang, Q. Zhang, and H. Jiang, Tomographic imaging of absolute optical absorption coefficient in turbid media using combined photoacoustic and diffusing light measurements, Optics Letters, 32 (2007), 2556–2558.
[137] Z. Yuan and H. Jiang, Quantitative phototacoustic tomography, Phil. Trans. R. Soc. A., 367 (2009), 3043–3054.
[138] Z. Yuan, C. Wu, H. Zhao, and H. Jiang, Imaging of small nanoparticle-containing objects by finite-element-based photoacoustic tomography, Optics Lett. 30 (2005), 3054–3056.
[139] H. F. Zhang, K. Maslov, G. Stoica, and L. V. Wang, Funtional photoacoustic microscopy for high-resolution and noninvansive in vivo imaging, Nature Biotechnology, 24 (2006), 848–851.
[140] E. Zuazua, Propagation, observation, and control of waves approximated by finite difference methods, SIAM Rev., 47 (2005), 197–243.